(A) STRUCTURE AND MOBILITY STUDIES OF SOME LAYER COMPOUNDS AND (B) ELECTRONIC STRUCTURE OF MOLECULES

A Thesis Submitted for the Degree

of

Doctor of Philosophy

to

The Board of the Faculty of Physical Sciences

at

The University of Oxford

R.C.T. Slade,
New College.

March 1978

"The fear of the Lord is the beginning

of knowledge"

Proverbs 1 v 7.

ACKNOWLEDGEMENTS

I am most grateful to my supervisor, Dr. P.G. Dickens, for all his help and encouragement, particularly with the theoretical work, and for the opportunities of collaborative work that he gave me.

I wish to thank Dr. T.K. Halstead for the opportunity to work with him at York University and for his guidance on nmr. I am grateful for the hospitality extended to me by York University during my stay there.

My thanks go to Dr. P. McGeehin of the AERE Harwell for supplying β-alumina samples, to Bruker-Physik AG for running some spectra and for their hospitality and to Dr. B.G. Silbernagel for running some spectra.

I am grateful to Mrs. P. Purcell for typing this thesis.

ABSTRACT

(A) Structure and mobility studies of some layer compounds

(B) Electronic structure of molecules

R.C.T.Slade, New College D.Phil Hilary term 1978

(A) Structure and mobility studies of some layer compounds

^{1}H nmr relaxation times and absorption spectra have been used to study structure and mobility of protons and proton-containing ions in some oxide lattices over a range of temperature.

The absorption spectrum of γ-AlOOH is a doublet arising from pairing of protons bonded to different oxygen atoms. M_2 for GaOOH suggests that the H-atom coordinates differ from the D-atom coordinates in GaOOD.

Hydrogen diffusion occurs in $H_{1.71}MoO_3$ with E_A = 22 kJ mol^{-1} and $\tau_c^o = 10^{-13}$s. Room temperature absorption spectra give information about the anisotropic chemical shielding tensor.

Hydrogen diffusion occurs in $H_{0.36}MoO_3$ with E_A = 11 kJ mol^{-1} and $\tau_c^o = 3 \times 10^{-8}$s.

In NH_4^+ β-alumina translation of NH_4^+ occurs with E_A = 25 kJ mol^{-1} and $\tau_c^o = 1.6 \times 10^{-11}$s.

In H_3O^+ β-alumina a proton motion, possibly an exchange process, occurs with E_A = 25 kJ mol^{-1} and $\tau_c^o = 10^{-10}$s.

(B) Electronic structure of molecules

The importance of electron-electron interactions in determining molecular shape is assessed using one-centre expansion methods in SCF and perturbation method calculations for the water molecule over a range of bond angle.

The perturbation method makes no allowance for differences in electron-electron interactions from those in a spherical system, the molecular puff. The results are very similar at all bond angles to those of SCF calculations, where the differences are included. The salient features of the VSEPR and Walsh-Mulliken schemes are reproduced by both methods.

The equilibrium molecular geometry is a result of a delicate balance of energy terms and does not arise from a minimum in V_{ee}, the total electron-electron interaction energy, nor in sums of molecular orbital energies.

EXTENDED ABSTRACT

(A) Structure and mobility studies of some layer compounds

Proton nmr relaxation time measurements (at a frequency of 16 MHz) and absorption spectra have been used in structural and mobility studies of the compounds GaOOH, γ-AlOOH, $H_{1.71}MoO_3$, $H_{0.36}MoO_3$, NH_4^+ β-alumina and H_3O^+β-alumina.

Absorption spectra have been recorded for the oxide hydroxides GaOOH and γ-AlOOH over a range of temperature. Line narrowing due to proton motion is not observed. The central narrow peak, which is absent at low temperatures, corresponds to less than 1% of the total absorption signal and is ascribed to occluded water molecules.

The second moment of the absorption spectrum for GaOOH (8.5 ± 0.9 G^2) suggests that the hydrogen atom positions are significantly different to the deuterium atom positions in GaOOD.

The absorption spectrum for γ-AlOOH is a doublet and arises from proton pairs with an intra-pair separation of 1.69 Å. The IR spectrum of this compound shows that no OH_2 groups are present. A structural model is proposed to account for pairing of protons bonded to different oxygen atoms.

The hydrogen molybdenum bronzes, H_xMoO_3, are mixed ionic-electronic conductors and are possible electrochromic materials for display devices. Measurements have been made of T_1, T_2, $T_{1\rho}$ and absorption spectra for $H_{1.71}MoO_3$ and $H_{0.36}MoO_3$ over a range of temperature.

In $H_{1.71}MoO_3$ motional narrowing occurs above 150K. At room temperature $T_1 = T_2 = T_{1\rho}$ showing there to be rapid hydrogen diffusion. The motion is characterised by E_A = 22 kJ mol^{-1} and $\tau_c^o = 10^{-13}$s. The estimated room temperature

protonic conductivity is 2 x 10^{-2}ohm^{-1}cm^{-1}, which would classify $H_{1.71}MoO_3$ as a superionic conductor. At room temperature, the motion largely removes dipolar interactions and information about the anisotropic chemical shielding tensor is available from absorption spectra. At low temperatures (in the rigid lattice region), absorption spectra show that 88% of the protons are present in pairs (OH_2 groups coordinated to Mo atoms) and this is confirmed by the approximately Gaussian attenuation of solid echo maxima.

In $H_{0.36}MoO_3$ motional narrowing occurs above 215K, the motion being characterised by E_A= 11 kJ mol^{-1} and τ_c^o = 3 x 10^{-8}s. The estimated room temperature ionic conductivity is 10^{-6}ohm^{-1}cm^{-1}, showing this material to be a poor ionic conductor. Low temperature absorption spectra show that 89% of the protons are present in pairs (the intra-pair separation being 1.94 Å) and the approximately Gaussian attenuation of solid echo maxima confirms this.

β-aluminas are of interest as Na^+β-alumina is the solid electrolyte in the sodium-sulphur battery. Measurements of T_1, T_2 and $T_{1\rho}$ were carried out for the compounds NH_4^+ β-alumina and H_3O^+ β-alumina.

In NH_4^+ β-alumina line narrowing occurs above 250K. At temperatures above 450K $T_1 = T_2 = T_{1\rho}$ showing there to be fast NH_4^+ diffusion. The motion is characterised by E_A= 25 kJ mol^{-1} and τ_c^o = 1.6 x 10^{-11} s. The estimated ionic conductivity at 400K (10^{-4}ohm^{-1}cm^{-1}) is in agreement with the results of conductivity measurements.

In H_3O^+ β-alumina line narrowing occurs above 270K. The motion is characterised by E_A = 25 kJ mol^{-1} and $\tau_c^o \sim 10^{-10}$s, and

is not the conduction mechanism. There is no evidence of H_3O^+ rotation . A proton exchange process may be occurring.

(B) Electronic structure of molecules

The importance of electron-electron interactions in determining molecular shape has been assessed using the water molecule as a simple model system. Molecular orbital calculations have been carried out using the one-centre expansion (OCE) method and basis sets of Slater-type orbitals (STO's). The best known basis set of this kind for water was used for high accuracy calculations, and a subset of this was used for calculations over a range of bond angle. The valence shell was re-expressed in terms of localised bonding and lone pair orbitals.

The water molecule is regarded as a perturbation of a hypothetical spherical entity, the molecular puff, the wave function for which is calculated by SCF methods. Wave functions calculated for the molecule by perturbation of the molecular puff, making no allowance for changes in electron-electron interactions from those in the spherical entity, are compared with those calculated by SCF methods, in which these changes are included, and the agreement is good in all respects. No minimum is found in V_{ee}, the total electron-electron interaction energy, at the equilibrium geometry. These results suggest that electron-electron interactions do not bear primary responsibility for molecular shape.

The salient features of the VSEPR and Walsh-Mulliken schemes are reproduced by both SCF and perturbation method calculations.

The characteristic distribution in space of bonding and lone pairs is reproduced without allowing for differences in electron-electron interactions from those in a spherical system. The success of the VSEPR scheme does not imply a causal relationship with reality. A simple classical model, consisting of summing the repulsions between pairs of electrons placed at the centroids of localised orbitals, gives a minimum close to the equilibrium geometry.

Neither the sum of the molecular orbital energies nor the sum of the valence shell molecular orbital energies shows a minimum. The equilibrium molecular geometry is a result of a delicate balance of energy terms.

CONTENTS

PART A

STRUCTURE AND MOBILITY STUDIES OF SOME LAYER COMPOUNDS

PART B

ELECTRONIC STRUCTURE OF MOLECULES

PART A

STRUCTURE AND MOBILITY STUDIES OF SOME LAYER COMPOUNDS

Chapter 1

INTRODUCTION

1.1 Ionic diffusion in solids.

An atom or ion in a solid is associated with a given lattice site. Translational motion can however occur in solids and such diffusion processes can be studied by nuclear magnetic resonance, tracer diffusion and other methods. In ionic compounds the diffusion is also a mechanism for charge transport and hence there is an associated ionic conductivity.

The self-diffusion coefficient, D, of a species is the diffusion coefficient measured when the system under study is at chemical equilibrium. The diffusion process can be considered as a series of jumps from occupied to unoccupied sites in the lattice. The random walk model (1) predicts that D is related to the jump distance, l, and the average time between random jumps, τ, by

$$D = fl^2/n\tau$$

where n is the number of possible jump paths and f a correlation factor for successive jumps (f = 1 for a truly random process). The temperature dependence of D is usually assumed to have the general form

$$D = D_o \exp(-E_A/RT)$$

where E_A is the activation energy for the process, T the temperature and R the gas constant.

For ionic conductors, a diffusion ceofficient D_q can be calculated from conductivity data using the Nernst-Einstein relationship

$$\frac{\sigma}{D_q} = \frac{Ne^2}{kT}$$

where σ is the conductivity, N is the number of mobile particles per unit volume, e is the charge on a proton and k is the Boltzmann constant. The ratio D/D_q is commonly called the Haven ratio, H_R, and has a particular value for a given mechanism or combination of mechanisms, which makes H_R of considerable diagnostic value. In the best purely ionic conductors, where there is a large number of sites to which an ion can move relative to the number of ions, the difference between these diffusion coefficients is small and, if only self-diffusion data are available, the ionic conductivities may be estimated by assuming $H_R = 1$.

The property of fast ion transport, where the self-diffusion coefficient for one of the ions is anomalously high, is well established. A recent review (2) has proposed that, for a material to be considered to show fast ion transport, it should have $E_A \sim 10$ kJ mol^{-1} ($\sim$0.1 eV) and $D_o \sim 10^{-4} - 10^{-5}$ cm^2 s^{-1}, and therefore a room temperature value of $D \sim 10^{-6}$ cm^2 s^{-1}, with acceptable values of these coefficients being one or two orders of magnitude lower. The corresponding room temperature ionic conductivity is $\sigma \sim 10^{-2}$ ohm^{-1} cm^{-1}. Materials with these properties are called superionic conductors.

1.2 Superionic conductors.

Figure 1.1 summarises the properties of some extensively studied superionic conductors.

The principal techniques which have been used to screen and study materials as superionic conductors are electrical measurements, magnetic resonance, infra-red and Raman spectro-

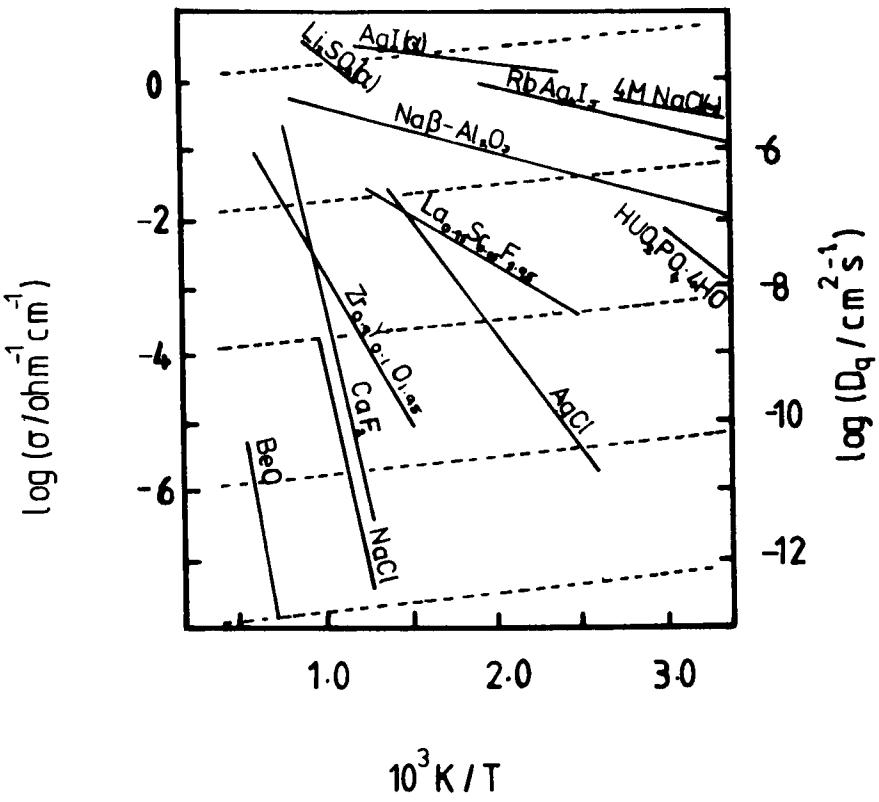

Figure 1.1

Ionic conductivity versus temperature data. The dotted lines refer to conductivities calculated from diffusion coefficients.

scopies and tracer diffusion. The most commonly used are ac conductivity and nuclear magnetic resonance measurements.

For superionic conductors, complicated analysis may be necessary to convert the frequency dependent ac response into meaningful bulk parameters. Complex plane plotting (3) allows representation of the observed response as an R-C network, each component of which can be linked to a particular process in the assembly (e.g. ionic conductivity), hence eliminating interfacial and grain boundary effects from ionic conductivity measurements.

Motional narrowing of nmr lines (4) can be studied as a guide to possible translational motion of ions which have nuclei with magnetic moments, but nmr relaxation time measurements (5) provide a more powerful method to study motions, giving activation energies, self-diffusion coefficients and information about the diffusion/motional process. The theoretical background to these measurements is discussed in Chapter 2.

The majority of known superionic conductors are α- AgI type salts of silver or copper (see e.g. ref.6) in which mobile cations are randomly distributed over an excess of lattice sites and the concentration of mobile species equals the total concentration of mobile cations. The majority of poor ionic conductors have only a small fraction of mobile defects. Fast oxide ion transport has been found in doped group VI A oxides (7), the doping stabilising the fluorite structure (e.g. ZrO_2 + 12% CaO), and doped Bi_2O_3 (8), but otherwise few examples of fast anionic conduction are known. This is not surprising as the larger anions will be less free to move than the cations. Current areas of interest are alkali ion conduction, solid solution

electrodes and electrochromic materials.

Alkali ion conductors are of interest for energy storage devices, such as solid state batteries (9). The highly electropositive alkali ions give large cell voltages and high energy densities. An open framework of ions within which the alkali ion can reside and/or an excess of available sites over the number of mobile ions is required. McGeehin and Hooper (2) give an extensive tabulation of known alkali ion conductors and their measured properties. Interest has centred on sodium compounds such as sodium β- alumina and "nazirpsio" ($Na_3Zr_2PSi_2O_{12}$, ref. 10-11). Lithium ion conductors are also being extensively studied (12 -14).

A particular material may be required either as an electrolyte or as an electrode. An electrolyte must have very low electronic conductivity to be useful. A mixed conductor is suitable for electrode applications since it provides compatibility between the device and the external electronically conducting circuit. Solid solution electrode materials function as a host lattice for reversible incorporation of elements (e.g. H,O,Cu,Li,Na) which may be employed as the electroactive species in a variety of electrochemical devices. Steele (15) has discussed the criteria for materials to function as non-stoichiometric solid solution electrodes.

Applications for hydrogen ion (proton) conductors are easy to envisage, and they would find immediate use in low temperature H_2/O_2 fuel cells. High proton mobilities are found in the solid state (16), hexagonal ice being the classic example. In ice the mobility arises from extensive hydrogen bonded networks, directly

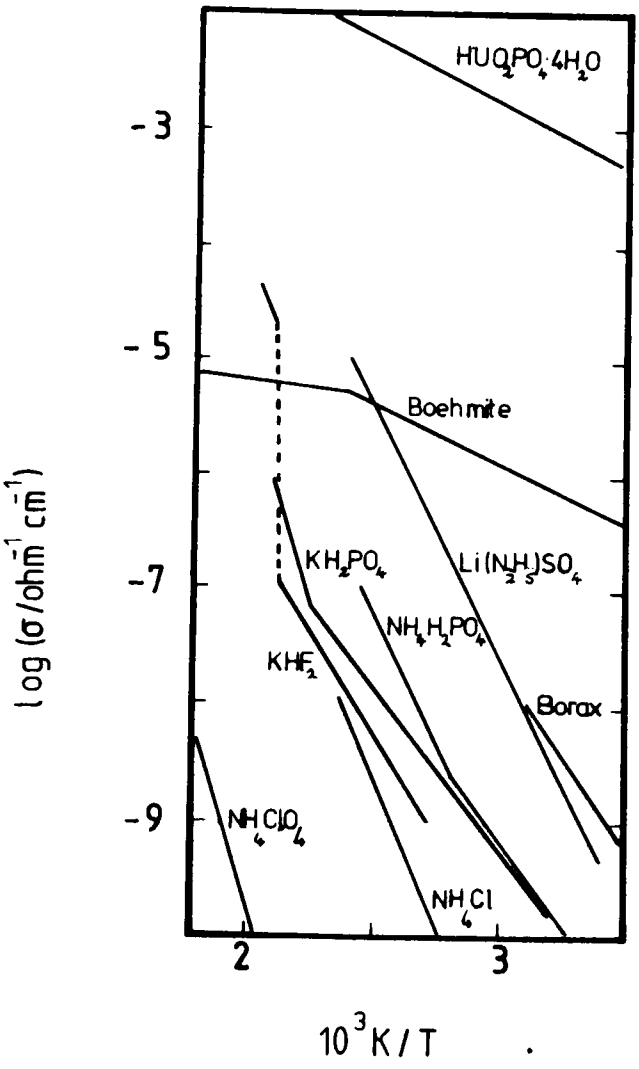

Figure 1·2

Ionic conductivity versus temperature for some proton conductors.

linked throughout the crystal, along which the protons may be transferred by cooperative processes. Glasser (17) has proposed a tentative set of criteria for proton conduction:-

(i) The protons should be involved in hydrogen bonds.

(ii) There should be suitable paths for proton migration in the form of a network of H-bonds.

(iii) The system should not be so rigid that possibilities of molecular rotation are excessively limited.

Figure 1.2 gives measured properties of some proton conductors. Shilton and Howe (18) have recently reported that the compound $HUO_2PO_4 \cdot 4H_2O$ is a fast proton conductor, with $\sigma = 4 \times 10^{-3} ohm^{-1} cm^{-1}$ at room temperature, and Childs and Halstead (19) have used nmr to confirm this. This material could be suitable for solid electrolyte applications.

An electrochromic material is one in which an optical absorption band can be introduced, or an existing one modified, by passage of a current through the material or by application of an electric field. These materials are currently of interest for display devices (20). For good room temperature electrochromic performance, the activation energy for the process must be low and thus the search for good electrochromic materials comes within that for superionic conductors and is akin to that for solid solution electrodes. WO_3 and related films are currently of prime interest (21), incorporation of protons causing a white to blue colouration resulting from hydrogen tungsten bronze formation.

The rapidly growing literature shows that fast ion transport is more often anticipated than established. The study of superionic conductors is confused by the lack of understanding

of their basic properties and the difficulty of performing adequate experimental tests on a whole range of compounds.

1.3 Some hydrogen oxide bronzes and related compounds.

Oxides, oxide bronzes, oxide hydroxides and hydroxides are often closely related in their structures, which can be described in terms of a common structural feature, the MO_6 octahedron (22). These octahedra can be regular, as in ReO_3, or severely distorted, as in V_2O_5. There are no general rules for predicting structure, many compounds, such as aluminium oxide hydroxide, existing in several forms.

Oxide hydroxides of some trivalent metals (23) have an α-form with a tunnel structure and a γ-form with a layer structure. The oxide frameworks for these are illustrated in figure 1.3. Gallium oxide hydroxide (GaOOH) and α-AlOOH (diaspore) are isostructural, complete structure determinations having been carried out by neutron diffraction (24,25). The space group for diaspore is Pbnm, and the structure, for GaOOH, is shown in figure 1.4. The hydrogen is bonded to O1 (at the centre of the tunnel) and hydrogen bonded to O2 (the next nearest oxygen). All the atoms in the structure lie on mirror planes. Unpublished neutron diffraction data (26,27) for γ-AlOOH (boehmite) suggest the space group Cmcm, with the structure as shown in figure 1.5. Random distribution of four hydrogens among eight equivalent sites in the unit cell is suggested. The distance between the two sites 11' (0.78 Å) is too short for simultaneous occupation of both. This could lead to disorder in the zig-zag chains containing the hydrogens. Holm et al. (28) explain the nmr second moment in terms of a zig-zag chain of

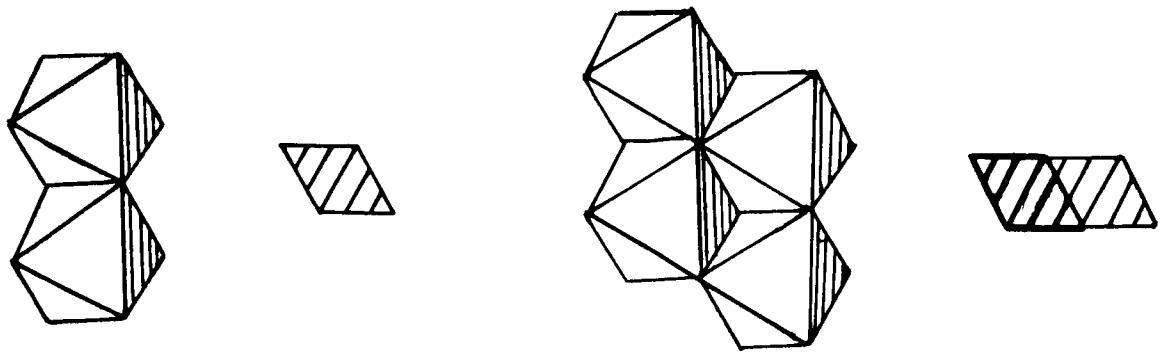

(a) Key

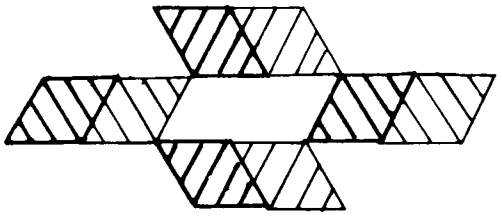

(b) α-form

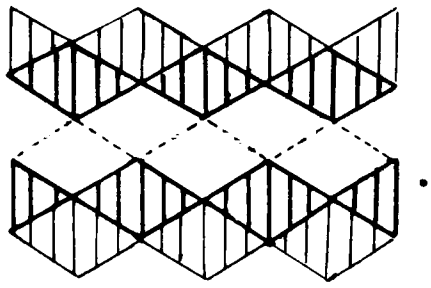

(c) γ-form

Figure 1·3

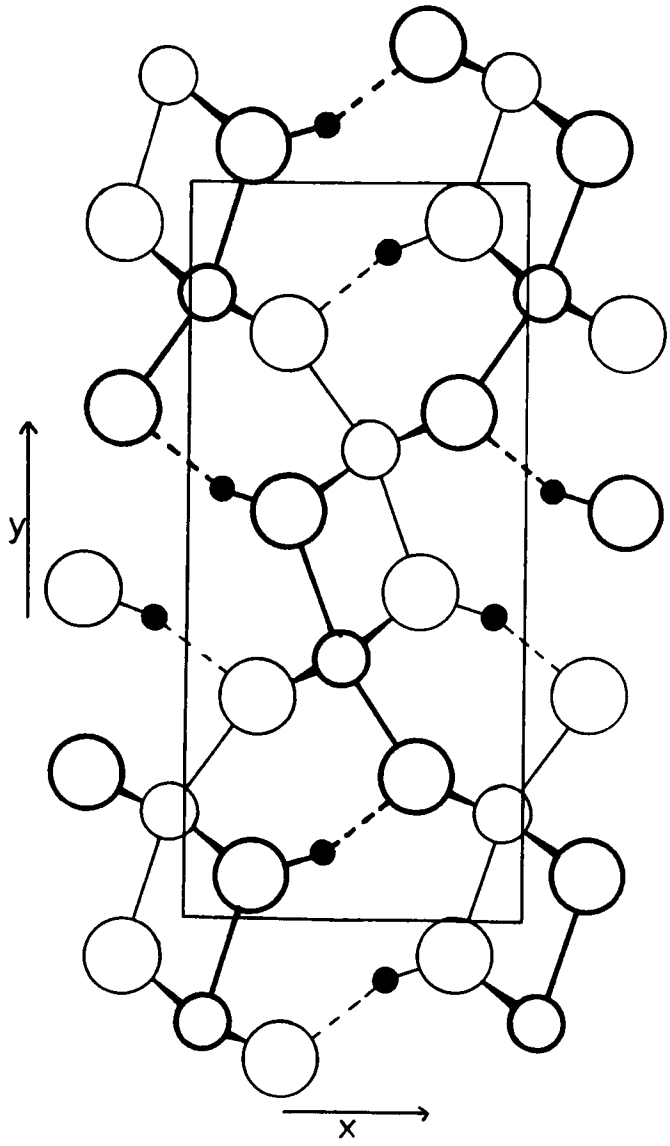

= O — z = - 0·25

= Ga — z = + 0·25

= D

Figure 1·4

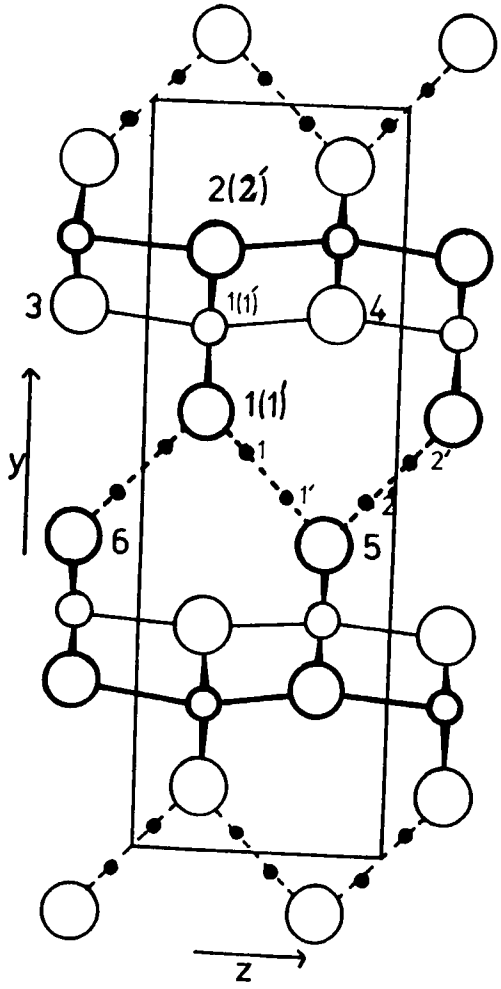

○ = O

○ = Al

• = D

— x = 0·0

— x = 0·5

Figure 1·5

hydroxyl groups, and the infra-red spectrum has been interpreted in similar terms (29,30).

α and γ forms of oxide hydroxides exchange protons rapidly. Gallagher (31) has proposed a mechanism for α forms involving hydrogen bond rupture and rotation of a defect water molecule. Extensive studies have been made of boehmite (γ-AlOOH). Fripiat et al. (32) give an activation energy of 65.5 kJ mol^{-1} and Wei et al. (33) give 53.9 kJ mol^{-1}. A proton delocalisation mechanism involving formation of ionic defects (H_2O^+) has been proposed (34). X-ray powder patterns for boehmite show broad diffuse bands at low angle, characteristic of some disorder, and the fit to neutron diffraction data is unsatisfactory in some respects (35). Fripiat et al. (36) in interpreting their broad-line nmr results propose a proton motion with the surprisingly low activation energy of 7.5 kJ mol^{-1}. These systems are therefore not totally understood and in this work further nmr studies are made of boehmite (a γ form) and GaOOH (an α form).

Oxide bronzes, A_xMO_n, are ternary oxide phases formally derived from oxides MO_n by insertion of an electropositive element A. Alkali metal oxide bronzes are electronic conductors ($A_x^+ MO_n e_x^-$), either metallic (e.g. Na_xWO_3, $x > 0.3$) or semi-conducting (β- $Na_xV_2O_5$), chemically rather inert and show large variations in stoichiometry. The transition metal, M, is usually in a high oxidation state and has a small crystal radius, tunnel and layer structures being found. In hydrogen oxide bronzes, such as H_xWO_3 and H_xMoO_3, the hydrogen is attached to oxygen atoms. The hydrogen tungsten bronzes are more properly formulated as non-stoichiometric oxide hydroxides, $WO_{3-x}(OH)_x$ (37,38), as are

low hydrogen content molybdenum bronzes (39-41). High hydrogen content molybdenum bronzes ($x > 1.55$) may contain OH_2 groups (41). Hydrogen oxide bronzes are oxidized by air.

Hydrogen tunsten bronzes have a high, metal-like, conductivity and have been studied by diffraction (37), nmr (42-44) and neutron inelastic scattering (38). Some disagreement has arisen in values for diffusion parameters as measured by different groups and this is discussed in Chapter 6. The electrical and optical properties of electrochromic WO_3 amorphous films have been extensively studied (21). When the electrolyte is a conductive acid gel (45), H_xWO_3 production is proposed, and it has been shown that electrocolouration takes place only in films containing H_2O (46). Displays based on insertion of other ions, such as Li^+ (47), are also being studied.

The hydrogen molybdenum bronzes, H_xMoO_3, are a series of phases in which the molybdenum oxygen framework is substantially unaltered from that in MoO_3 (48-51). Glemser et al. (48,49) report four phases, $Mo_4O_{10}(OH)_2$ ($x = 0.5$), $Mo_2O_4(OH)_2$ ($x = 1.0$), $Mo_5O_7(OH)_8$ ($x = 1.6$) and $Mo_5O_5(OH)_{10}$ ($x = 2.0$). Birtill has shown that the phase limits are (39)

$x = 0.23 - 0.4$ Blue orthorhombic

$x = 0.85 - 1.04$ Blue monoclinic

$x = 1.55 - 1.72$ Red monoclinic

$x = 2.0$ (possibly a line phase) Green monoclinic.

Wilhelmi (51) suggested that the hydrogen atoms in $Mo_4O_{10}(OH)_2$ are located between the layers of the MoO_3 structure. Complete structure determinations by neutron diffraction (39-41) have shown that, in this phase, the hydrogens are located within the layers. Figure 1.6 shows the structure of MoO_3 (space

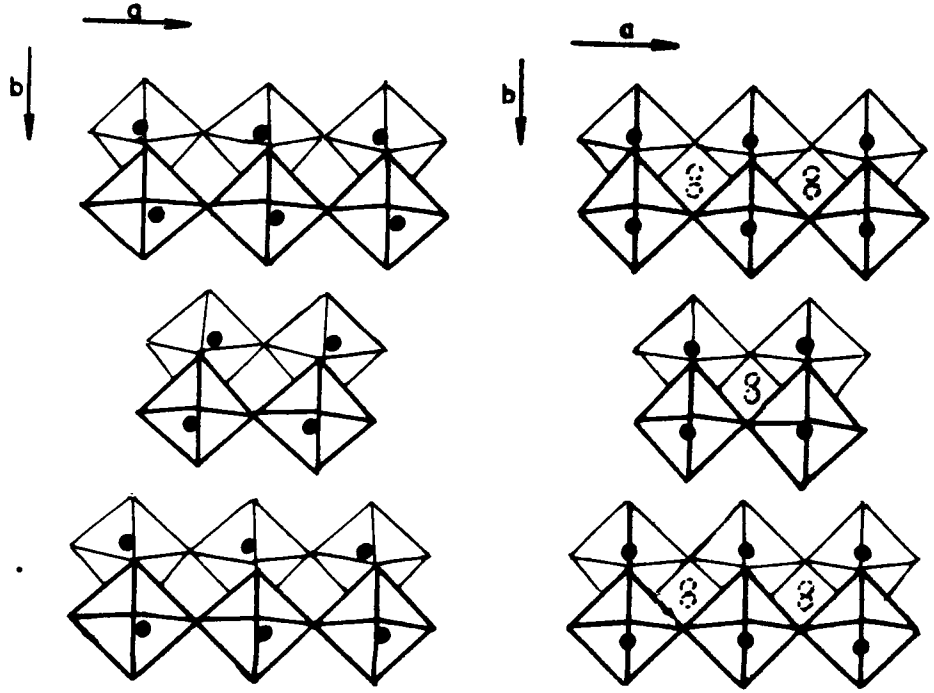

MoO_3 $H_{0.34}MoO_3$

Figure 1.6

group Pbnm) and $H_{0.34}MoO_3$ (space group Cmcm). There is one bridging oxygen per molybdenum, the hydrogen atoms being randomly attached to 34% of these and located almost on the line between them, the separation of these oxygens being 3.0Å and the O-D length 1.06Å (39). Hydrogen positions in the other phases are not known.

The hydrogen molybdenum bronzes are probably metallic conductors (52), show a weak temperature independent paramagnetism and give no esr signal at room or liquid helium temperatures (40,52). This shows the conduction band to be highly delocalised. Reversible electrochemical reduction of MoO_3 occurs at room temperature in aqueous acids (53)

$$\underset{\text{colourless}}{\frac{1}{x}MoO_3} + H^+ + e = \underset{\text{coloured}}{\frac{1}{x}H_xMoO_3}$$

and can provide the basis of an electrochromic system (20). The relationship between bulk H_xMoO_3 and electrochemically reduced MoO_3 films has yet to be investigated.

Neutron inelastic scattering measurements have been carried out on all four hydrogen molybdenum bronze phases (41). The results for $H_{0.34}MoO_3$ are similar to those for $H_{0.4}WO_3$ (38), the hydrogen being present as hydroxyl groups and the main peaks at 1251 cm^{-1} and 1146 cm^{-1} for these compounds being assigned to the M-O-H bending mode (c.f. 1156 cm^{-1} for this mode in the infra-red spectrum of $In(OH)_3$). This band is absent for the other phases, where the results are interpreted in terms of OH_2 groups coordinated to molybdenum atoms. This is found in the molybdic and tungstic acids. The latter compounds, $WO_3.2H_2O$ and $WO_3.H_2O$, were shown to contain OH_2 both by broad-line nmr (54,55) and other techniques (56). Combined infra-red and nmr studies (57) suggest the same is also true for $MoO_3.2H_2O$ and $MoO_3.H_2O$. X-ray work (58,59) suggests the structural relation-

Figure 1.7

(a) molybdic acids

($MoO_3 \cdot H_2O$, $MoO_3 \cdot 2H_2O$)

(b) MoO_3

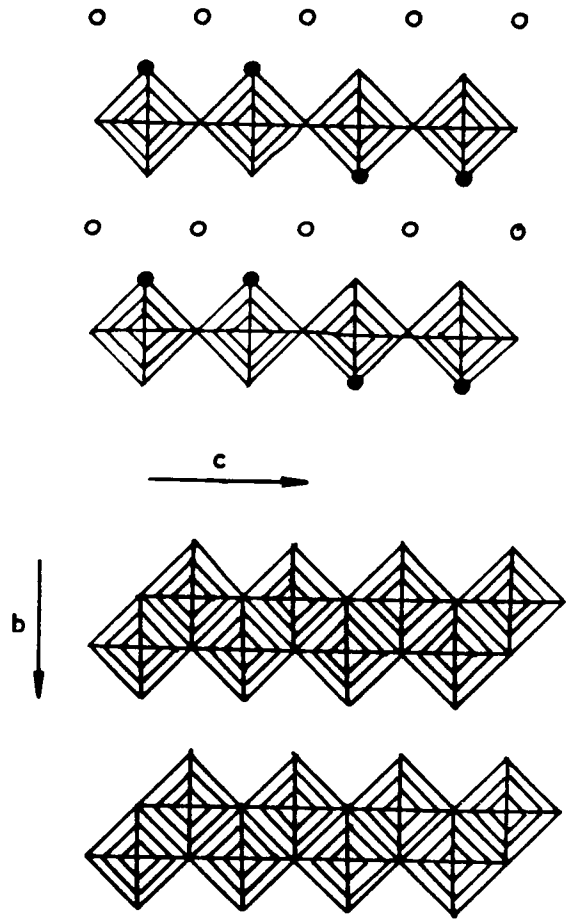

ships between MoO_3, $MoO_3.H_2O$ and $MoO_3.2H_2O$ are as shown in figure 1.7.

In this work the compounds $H_{0.36}MoO_3$ and $H_{1.71}MoO_3$ are studied.

1.4 β-Aluminas.

The name β-alumina is frequently applied indiscriminately to a group of non-stoichiometric layered materials formed in the Na-Al-O system. Interest in these is great as β-alumina is used for passage of ions in the sodium-sulphur battery. It has also been used in other devices (60), such as a sodium-halogen primary battery and a sodium heat engine.

Early X-ray structural investigations (61) and associated chemical analyses showed the formula to be approximately $Na_2O.11Al_2O_3$, and a number of isostructural compounds have been isolated in which sodium has been replaced by other ions (see e.g. ref.62). Four structures are known and these have been labelled β(63), β"(64), β'"(65) and β""(66). The dominant structural motif is sheets of cubic close packed oxygen layers, these being four oxygens thick in β and β" and six oxygens thick in β'" and β"", these latter two only being found in the presence of a small amount of divalent oxide (e.g. MgO). The non-alkali metal atoms are predominantly in the octahedral and tetrahedral interstices in these layers, giving them a spinel-like structure, and hence they are termed spinel blocks. The blocks are separated by Al-O-Al pillars, which provide weak links, and there is thus facile cleavage parallel to the layers. A β' phase has been reported (67), having an identical structure to β but with half

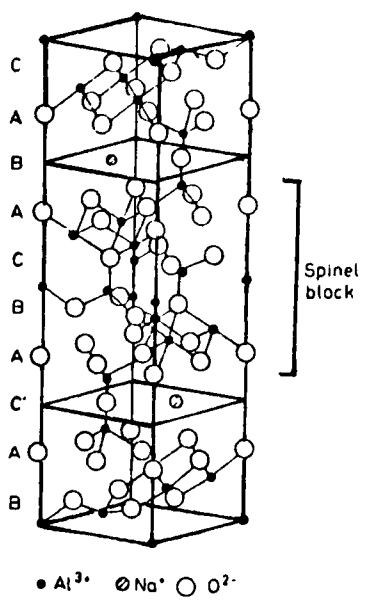

(b) β-alumina

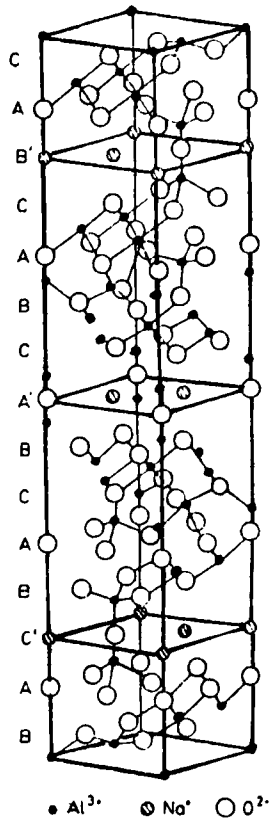

(a)

β''-alumina

Figure 1·8

Figure 1·9

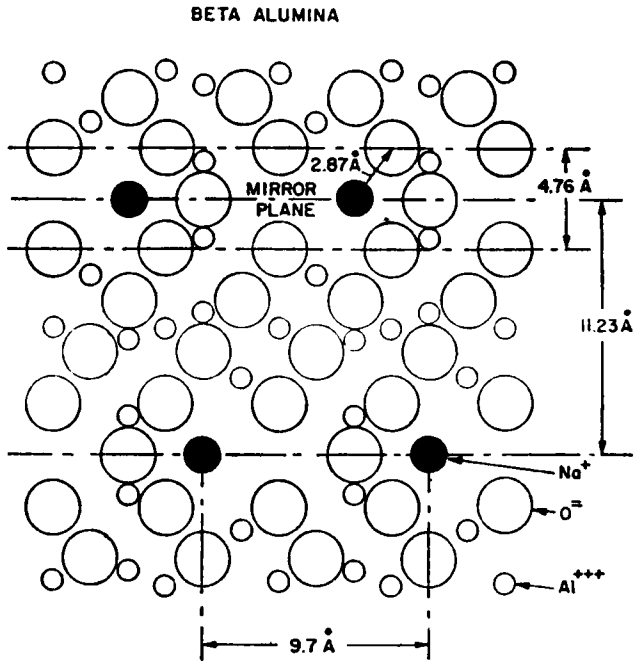

as much sodium again between the layers. Bettman and Terner (65) state that this is a manifestation of the non-stoichiometry of β-alumina and Baughman and Lefever (68) suggest that it is a particularly stable composition in a solid solution range. In this work, the name β-alumina implies a pure β-phase.

Spinel blocks can stack in two ways, adjacent layers being related by two fold or three fold screw axes, giving unit cells with either two or three layers as the repeat distance in the c-direction (perpendicular to the layers). Figure 1.8 shows the structures of β and β" aluminas. The β phase (63) has two sheets in the c-direction in the unit cell (c = 22.7 Å, space group $P6_3/mmc$) and the β"(64) has three (c = 33.8 Å, space group $R\bar{3}m$). In β-alumina the sodium containing plane is a mirror plane, as shown in figure 1.9, whereas in β"-alumina it is not. The available sites for the alkali ion in the interlayer plane are shown in figure 1.10. In β-alumina, the oxygens above and below the Beevers-Ross (BR) site are closer than those above and below the anti-Beevers-Ross (aBR) sites, whereas in β"-alumina the corresponding sites are equivalent.

There is much confusion in the literature concerning the phase diagram for the Na-Al-O system, several different versions being given (62,66,68-72). The β-phase seems to have a composition range, for $Na_2O.xAl_2O_3$, of $x = 5.\dot{3}\dot{3} - 8.25$ at 1400°C, and β" the range x = 7.0 - 8.5. β" is not formed alone but intergrown with the β-phase, electron micrographs of crystals showing this clearly (73). β" is however stabilised by the presence of a small amount of MgO (64). The excess sodium above the ideal formula (x = 11) is found in the interlayer region, but the exact mechanism of stoichiometric variation is a matter of debate.

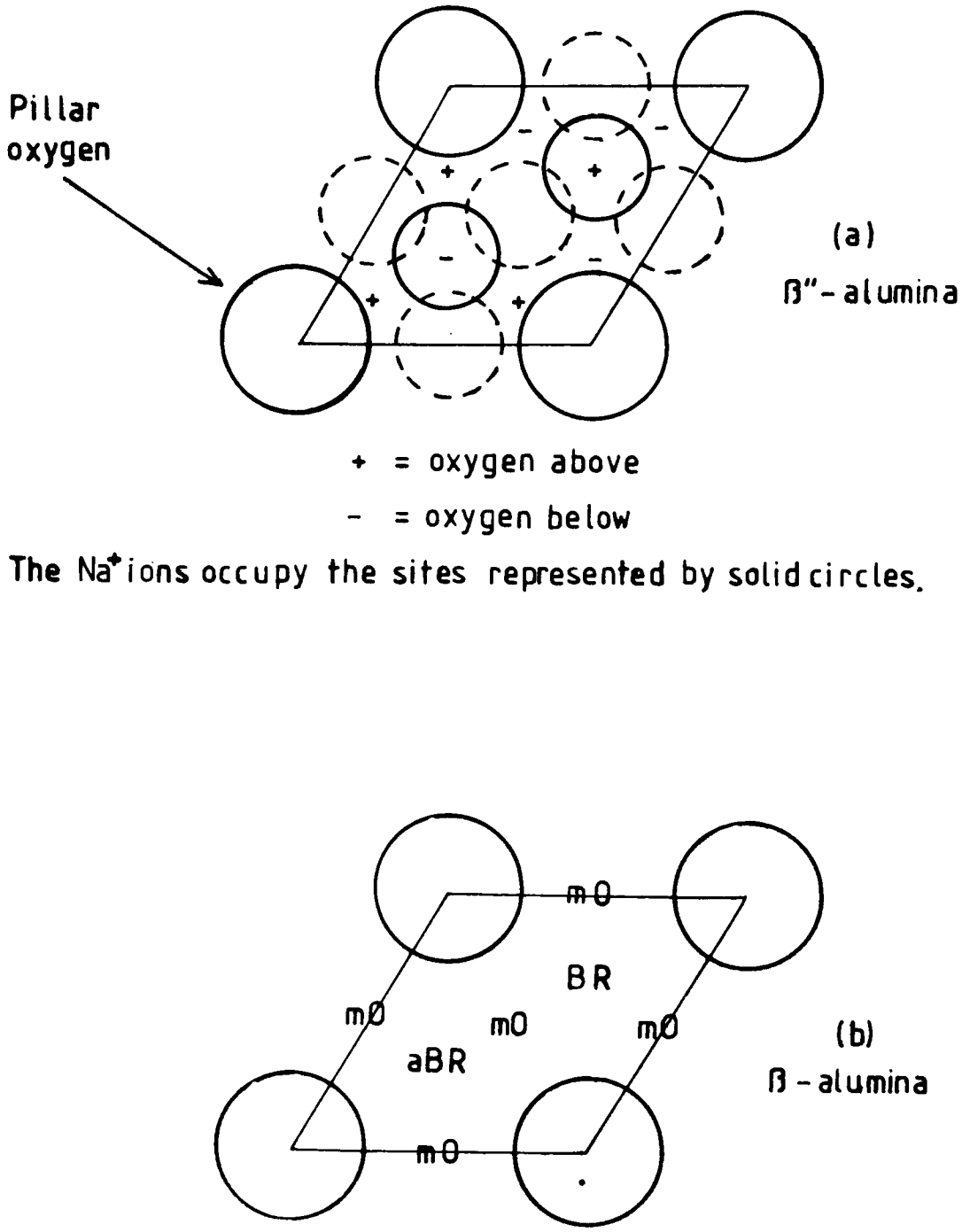

The conduction plane in "β-aluminas"

Figure 1.10

Peters et al. (63) suggest a model based on defect clusters, interaction occurring between Al^{3+} vacancies and sodium ions, but the manner of the c-axis variation with stoichiometry (74) and the mobility of the sodium ions show that this is not the best model. Recent work (75,76) suggests that extra oxygens are inserted in the sodium-containing planes and Roth (77) asserts that oxygen bound in the plane by two Al^{3+} Frenkel defects is the most likely charge compensation mechanism.

The sodium ion in β-alumina can be exchanged with a number of mono and divalent ions. Yao and Kummer (78) worked extensively with molten salts and others have used concentrated acids (79,80). Recent work (81) has shown that exchange in molten salts is not as complete as previous work had suggested and that more than one exchange may be necessary. Lattice constants for a number of exchanged β-aluminas have been reported (62). For alkali ions, the c-axis expands when ions larger than sodium are present. Li^+ also produces an expansion but the structure is slightly different, the Li^+ lying in a potential well closer to one spinel block than the other.

Complete structure determinations give an average picture of the disorder over the available alkali ion sites. The Beevers-Ross position has the highest occupancy in all cases. Na^+ β-alumina (63) has 59% occupancy of the BR sites and no occupation of the aBR sites, and K^+ β-alumina is similar. Ag^+ β-alumina is quite different (75), 52.8% being in BR and 34% in aBR. Tl^+ β-alumina (82) and Rb^+ β-alumina (83) have more complex structures with occupation of more sites unoccupied in simpler cases. In H^+ β-alumina, the hydrogen is directly bonded to a pillar oxygen at low temperatures, but resembles Na^+ β-alumina

at higher temperatures, this being evidence for proton conductivity (84). Saalfeld (85) suggests that H_3O^+ β-alumina ($3H_2O.11Al_2O_3$) is related to this, with hydrogen bonding between the pillar hydroxyl and H_2O on another site.

The ionic diffusion in β-alumina occurs two dimensionally in the interlayer plane, as has been shown elegantly by ion-exchange studies (62). Measured self-diffusion coefficients for some cation substituted β-aluminas are shown in figure 1.11. Figure 1.12 gives the variation in activation energy with ionic radius (as defined in ref. 86). The size of the mobile ion is important, dimensions both above and below a certain limit being unfavourable. If the cation is too small (e.g. Li^+) it sits to one side of the slot between the spinel blocks, with three oxygen nearest neighbours. If the cation is too large, it experiences repulsive forces from the spinel blocks, particularly as it translates to and through the aBR sites. This qualitative picture is borne out by the results of studies of the effect of hydrostatic pressures on ionic conductivity (62).

Several theories have been put forward to explain the fast ion conduction in these materials, and in superionic conductors in general (87). Sato and Kikuchi (88) use path probability methods for a vacancy mechanism of migration where the density of vacancies is high. Rice (89) has put forward a free ion model with thermal activation of localised ions. Van Gool (90) considers migration of domain walls and Roth has proposed a domain structure in β-aluminas to explain the stoichiometry. Domains of between 5 and 10Å width would be required, and these would not be resolved by X-ray techniques. Wang et al. (91) have calculated potential energy curves for various carrier ions.

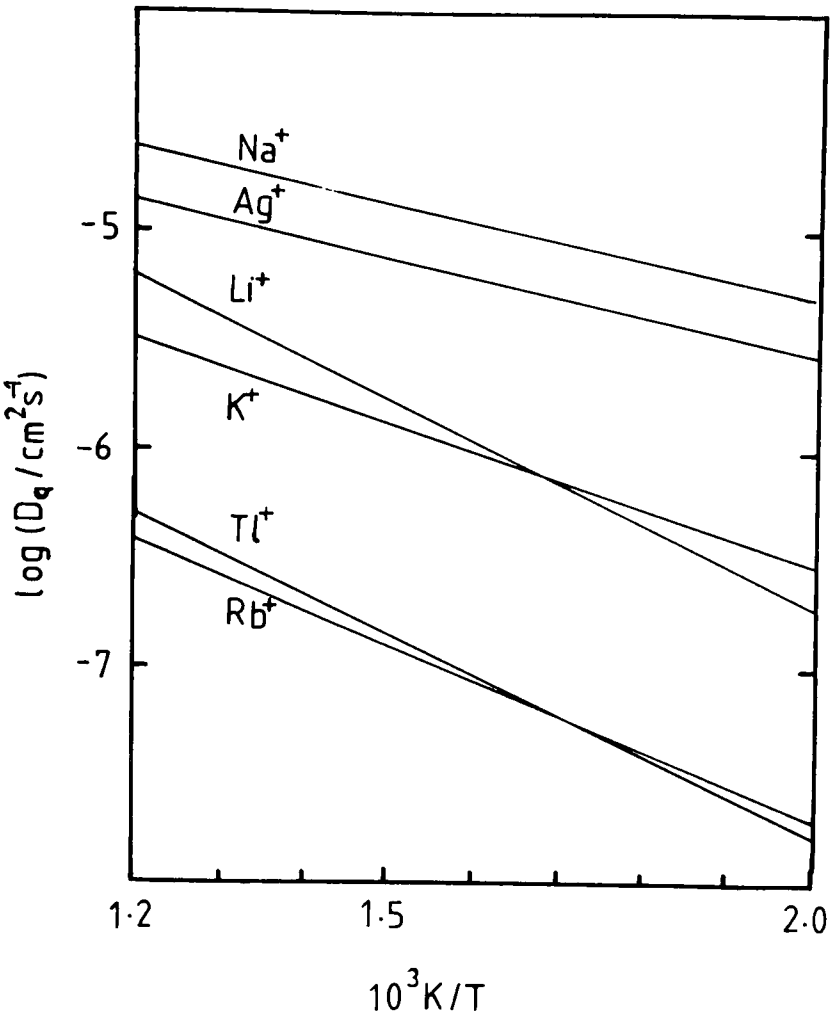

Self-diffusion in some β"-aluminas.

Figure 1·11

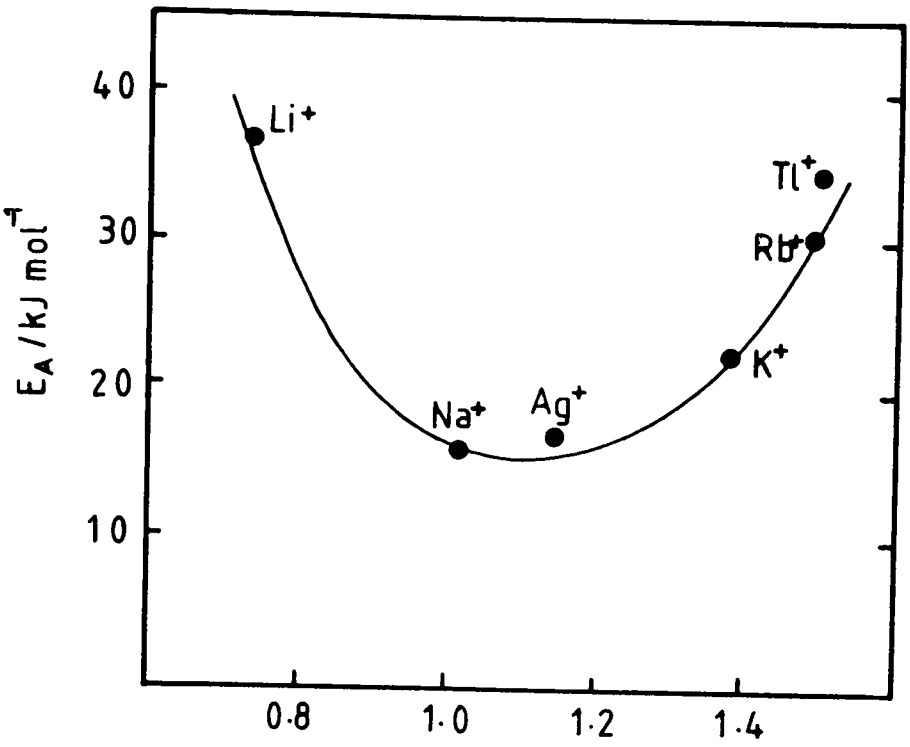

Self-diffusion in some β-aluminas

Figure 1·12

They showed the energy difference between BR and aBR sites in stoichiometric crystals to be ~ 2eV (~ 200kJ mol^{-1}). In non-stoichiometric materials, the extra carrier ions could form interstitialcy pairs and, in this case, the energy barrier for in phase motion of the pairs was comparable to experimental activation energies. Vibrational (attempt) frequencies were also in good agreement with experiment.

The high number of protons per carrier cation in the compounds ammonium β-alumina (NH_4^+ β-alumina) and hydroxonium β-alumina (H_3O^+ β-alumina) increases the sensitivity of nmr measurements and makes them particularly suitable for study using this technique. The only literature report of diffusion measurements are those by dielectric loss on NH_4^+ β-alumina (92). In this work, the author studied these compounds using pulsed nmr.

1.5 The present work.

The nuclear magnetic resonance sensitivity of the proton (the hydrogen nucleus) is the highest known for any stable nucleus. In this work, the mobility of protons and proton-containing ions is studied, in compounds of the types discussed in sections 1.3 and 1.4, by recording nmr relaxation times and absorption spectra over a range of temperature. The theoretical background to these measurements is discussed in Chapter 2.

The specific compounds studied are GaOOH, γ-AlOOH, $H_{1.71}MoO_3$, $H_{0.36}MoO_3$, NH_4^+ β-alumina and H_3O^+ β-alumina.

Chapter 2

Nuclear Magnetic Resonance and Motion in Solids

2.1 Nuclei and magnetic fields.

A nucleus has a magnetic moment $\underline{\mu}$ given by

$$\underline{\mu} = \gamma \hbar \underline{I}$$

where γ is the gyromagnetic ratio for the nucleus, $\underline{I}$ its spin angular momentum and $\hbar$ Dirac's constant. The nucleus has $(2I+1)$ distinct eigenstates, where I is its spin quantum number, which are degenerate in the absence of a magnetic field. In a static field, $\underline{B}_o$, the degeneracy is lifted and, for a given spin-$\frac{1}{2}$ nucleus (e.g. a proton), there are two states with components $\mu_z = + \hbar\gamma/2$ and $\mu_z = -\hbar\gamma/2$ and with corresponding energies

$$U_+ = -\hbar\gamma B_o/2 \qquad U_- = +\hbar\gamma B_o/2$$

where z is the field direction. The magnetic resonance experiment matches the energy gap using radiofrequency (RF) energy of angular frequency ω_o where

$$\omega_o = |\gamma B_o|$$

This is the resonance condition of nmr. The resultant magnetisation, $\underline{M}$, of a macroscopic sample is the vector sum of the individual nuclear moments. At equilibrium the populations of the different energy levels are determined by a Boltzmann distribution, and there is a resultant magnetisation in the z direction.

The equation of motion for a magnetic moment in a static field is

$$\frac{d\underline{\mu}}{dt} = \gamma \underline{\mu} \times \underline{B}_o$$

in a laboratory coordinate frame. In a frame rotating with angular velocity $\underline{\omega}$, the equation of motion is

$$\frac{d\underline{\mu}}{dt} = \gamma \underline{\mu} x (\underline{B}_o + \underline{\omega}/\gamma)$$

and hence the effective field in the rotating frame is $(\underline{B}_o + \underline{\omega}/\gamma)$. If $\underline{\omega} = -\gamma \underline{B}_o$, the moment is static in the rotating frame. The precession frequency for the moment in the laboratory frame is thus ω_o $(= |\gamma B_o|)$, the Larmor frequency.

An oscillating field, $B_x(t) = 2B_1 \cos(\omega t)$, can be considered as the sum of two components, each of amplitude B_1, rotating with angular velocities $\underline{\omega}$ and $-\underline{\omega}$. One of these components will be stationary in the rotating frame of angular velocity $\underline{\omega}$, and hence can be represented by a static vector, length B_1, in that frame. In treatments of resonance, the counter-rotating component may be ignored (93).

A static field in the z-direction and an oscillating field perpendicular to it correspond, in a rotating frame, to an effective field $\underline{B}_{eff}$, given by

$$\underline{B}_{eff} = (B_o - \omega/\gamma)\, \underline{k} + B_1 \underline{i}$$

If the resonance condition is fulfilled $(\omega = \omega_o)$, $\underline{B}_{eff}$ is directed along the x'-axis of the rotating frame and the moment precesses in the $y'z'$ plane, periodically aligned opposed to $\underline{B}_o$. If $\underline{B}_1$ is switched on only for a short time (a pulse), the moment precesses through an angle ϑ given by

$$\vartheta = \gamma B_1 t \quad \text{radians}$$

Chosing t such that $\vartheta = \pi/2$ would turn the moment from the z'-direction into the y'-direction (a 90° pulse) and $\vartheta = \pi$ would invert the moment (a 180° pulse).

Arbitrary orientation of the moment is not in conflict with a quantum mechanical description, the wave function for the spin-state being a linear combination of eigenstates.

The resultant magnetisation, $\underline{M}$, of macroscopic samples is described by the same equations as those for motion of $\underline{\mu}$, except that relaxation terms have to be included when there is interaction between the spins themselves and between the spins and the lattice.

2.2 Transient and steady state responses.

Nuclear magnetic resonance phenomena can be studied either by continuous wave (CW) or pulse methods. Saturation is the equilisation of the populations of occupied energy levels. In CW measurements, low power levels have to be used to avoid loss of signal strength due to this saturation. In pulse techniques, a single 90^{o} pulse is sometimes termed a saturation pulse as, after such a pulse, $M_z = 0$ and hence the populations of occupied levels must be equal. Phenomenological equations describing nmr responses have been given by Bloch (94).

At equilibrium a sample has magnetisation $\underline{M}_o$ ($M_z = M_o$, $M_x = M_y = 0$). After a 90^{o} pulse, the magnetisation is in, say, the y'-direction in the rotating frame and the system is no longer at equilibrium. Bloch assumed that components of $\underline{M}$ decay exponentially to the equilibrium values, the decay constants for components perpendicular to and parallel to $\underline{M}_o$ being T_2 and T_1 such that

$$\frac{dM_z}{dt} = (M_o - M_z)/T_1$$

$$\frac{dM'_x}{dt} = -M'_x/T_2 \qquad \frac{dM'_y}{dt} = -M'_y/T_2$$

The approach to equilibrium is termed relaxation. Relaxation along the field direction alters the energy of the spin system, and hence involves energy flow to or from the other degrees of freedom (termed the lattice), whereas relaxation perpendicular to the field does not. T_1 and T_2 may therefore differ. T_1 is the spin-lattice (or longitudinal) relaxation time and T_2 the spin-spin (or transverse) relaxation time. $T_{1\rho}$, the spin-lattice relaxation time in the rotating frame, is the time constant for decay along $\underline{B}_1$.

The transient response after a 90^o pulse (called the free induction decay) and the steady state response (from CW methods) are related by Fourier transformation (93). If $m(\tau)$ is the transient response, the complex susceptibility, χ, is given by

$$\chi = \int_o^\infty m(\tau) e^{-i\omega\tau} \, d\tau$$

The absorption signal is proportional to the imaginary susceptibility, χ'', and is thus given by

$$\chi'' = \int_o^\infty m(\tau) \sin(\omega\tau) \, d\tau$$

For work on solids, CW instruments are operated in the absorption mode and signals proportional to the first derivative of χ'' are detected and displayed. This technique is termed broad-line nmr. Following the trend set by widespread use of high resolution pulse Fourier transform spectroscopy, transformation of transient signals obtained by pulse methods is becoming increasingly common for solids (95).

2.3 Interactions in solids.

The Hamiltonian operators for the important interactions between nuclei in solids for a system of like spins can be written (in frequency units) as

$$\text{Zeeman:} \quad \hat{H}_z = -\gamma\hbar \sum_i \underline{B}_o \cdot \underline{I}_i$$

$$\text{Dipolar:} \quad \hat{H}_D = (\gamma^2\hbar^2\mu_o/4\pi) \cdot \sum_{i<j} \frac{1}{r_{ij}^3} (A+B+C+D+E+F)$$

where

$$A = (1-3\cos^2\vartheta)\,\hat{I}_{iz}\cdot\hat{I}_{jz}$$

$$B = -\tfrac{1}{4}(1-3\cos^2\vartheta)\,(\hat{I}_{i+}\hat{I}_{j-} + \hat{I}_{i-}\hat{I}_{j+})$$

$$C = -\tfrac{3}{2}\sin\vartheta\cos\vartheta\,(\hat{I}_{i+}\hat{I}_{jz} + \hat{I}_{iz}\hat{I}_{j+})e^{-i\phi}$$

$$D = C^*$$

$$E = -\tfrac{3}{4}\sin^2\vartheta\,\hat{I}_{i+}\hat{I}_{j+}\,e^{-2i\phi}$$

$$F = E^*$$

and $(r_{ij}, \vartheta, \phi)$ denotes the vector between spins i and j. The terms A to F control the selection rules for transitions associated with the dipolar Hamiltonian.

The terms involving A and B correspond to $\Delta I_z = 0$ and together are called the secular Hamiltonian. As this corresponds to zero energy change for the spin system, the secular Hamiltonian is associated with T_2. Experiments where the secular Hamiltonian is averaged to zero give line narrowing, as the dipolar contribution to line broadening is removed (96). In liquids the molecules are in random motion and the time averaged secular Hamiltonian is zero (as $\overline{\cos^2\vartheta} = \frac{1}{3}$). This fact allows the very useful high resolution absorption spectra of liquids. Much work is being devoted to line narrowing experiments in solids (96). Mechanical sample spinning at $\cos^{-1}(1/\sqrt{3})$ (the "magic" angle) to the static field (97) can be used, but, for the widest lines, rotation

frequencies required are too high for mechanical integrity of the spinner. Multiple pulse sequences, such as the well-known WAHUHA sequence (98), rotate the spin coordinates such that the time average of the secular Hamiltonian is zero.

The terms C to F are associated with $\Delta I_z = \pm 1, \pm 2$. They thus involve changes in the energy of the spin system and are associated with T_1.

Molecular motion imparts a time dependence to the co-ordinates $(r_{ij}, \vartheta, \phi)$. The total Hamiltonian can then be represented as the sum of a time dependent and a time independent part.

$$\hat{H} = \hat{H}^o + \hat{H}^1(t)$$

where $\hat{H}^o$ includes the applied field and the time independent parts of $\hat{H}_D$. The shape and structure of the absorption lineshape is determined by $\hat{H}^o$ and the relaxation behaviour depends on $\hat{H}^1(t)$. If the applied field, B_{app}, is very much larger than the local fields, B_L, then $\hat{H}^1(t)$ can be treated as a small perturbation. However, when $B_{app} \sim B_L$ this approach fails. The approach of Slichter and Ailion (99) is to calculate the change in dipolar energy due to jumping. This is then communicated to the sample magnetisation via the Zeeman Hamiltonian by establishment of a common spin temperature for dipolar and Zeeman heat reservoirs, this taking time T_m (thermal mixing time). It is assumed that this is achieved between jumps and hence $\tau \gg T_m$. The related temperature region is called the "strong" collision or low temperature region. As the applied field increases, T_m becomes very long because of the very different spacings of the Zeeman and dipolar energy levels and the concept of a common

spin temperature breaks down ($\tau \ll T_m$). The related region is called the "weak" collision, the motionally narrowed, or the high temperature region, and is treated using perturbation methods.

2.4 Linewidth, second moment and transverse relaxation.

The linewidth and second moment of a broad-line nmr spectrum for a solid and the associated transverse relaxation behaviour are determined by the secular Hamiltonian.

A continuous wave instrument usually gives the derivative of the absorption spectrum and a convenient definition of linewidth, ΔB, is the separation (in gauss) of the points of maximum and minimum slope. When the absorption spectrum itself is observed, a definition of linewidth, $\Delta B_{\frac{1}{2}}$, as the half-width at half intensity is convenient. The ratio of these two linewidths will depend on the actual lineshape. The second moment, for a normalised resonance absorption lineshape $g(B)$ centred at B_o, is defined by

$$M_2 = \int_{-\infty}^{\infty} (B-B_o)^2 \, g(B) \, dB.$$

If nuclei are in relative motion, the local field experienced fluctuates with time and the time average may be much less than the static value. The time average field $\sim \Delta B \sim M_2^{\frac{1}{2}}$ and, assuming fluctuations can be characterised by a correlation time τ_c, a criterion for line narrowing and a reduction in the observed second moment is

$$(\gamma^2 M_2)^{\frac{1}{2}} \tau_c \ll 1.$$

When this condition is not fulfilled (e.g. at lower temperatures), the linewidth is constant with temperature and the lattice is said to be rigid.

The steady state lineshape arising from solution of the Bloch equations is a Lorentzian, and for this lineshape (100)

$$\Delta B_{\frac{1}{2}} = \frac{1}{\gamma T_2} \quad (= \frac{37.4}{T_2} \ \mu s \ G \text{ for protons}).$$

In solids at low temperatures, the lineshape often approximates to a Gaussian . For this lineshape with a system of one magnetic nuclear type (100)

$$M_2 = \frac{\pi}{2\gamma^2} \left(\frac{1}{T_2} \right)^2 \quad (= 2.20 \times 10^3 \left(\frac{1}{T_2}\right)^2 \ \mu s^2 G^2 \text{ for protons})$$

and $\Delta B = 2(M_2)^{\frac{1}{2}}$; $\Delta B = 1.695 \ \Delta B_{\frac{1}{2}}$

Figure 2.1 illustrates the definitions of linewidth for a Gaussian lineshape.

In a rigid dipolar lattice, an exact solution for the nmr lineshape is not obtainable. However, the moments of the resonance absorption are exactly calculable, as shown by van Vleck (101). It can be shown that

$$\gamma^2 M_2 = - \frac{\mathrm{Tr}([\hat{H}_{sec}, \hat{I}]^2)}{\mathrm{Tr}[\hat{I}_x^2]}$$

Evaluation of these traces leads to van Vleck's expressions for M_2 in terms of the microscopic coordinates of magnetic nuclei, A, non-resonant nuclei, B, and a probe resonant nucleus i. M_2 is given by (*for a powder*)

$$M_2 = \frac{3}{5} I_A(I_A+1) \gamma_A^2 \hbar^2 \left(\frac{\mu_o}{4\pi}\right)^2 \sum_A r_{iA}^{-6} + \frac{4}{15} \left(\frac{\mu_o \hbar}{4\pi}\right)^2 \sum_B I_B(I_B+1) \gamma_B^2 r_{iB}^{-6}$$

For a system where the only magnetic nuclei are protons, M_2 for the resonance is

$$M_2 = 358.1 \sum_A r_{iA}^{-6} \quad \text{Å}^6 \ G^2.$$

Thus M_2 is given by the crystal structure.

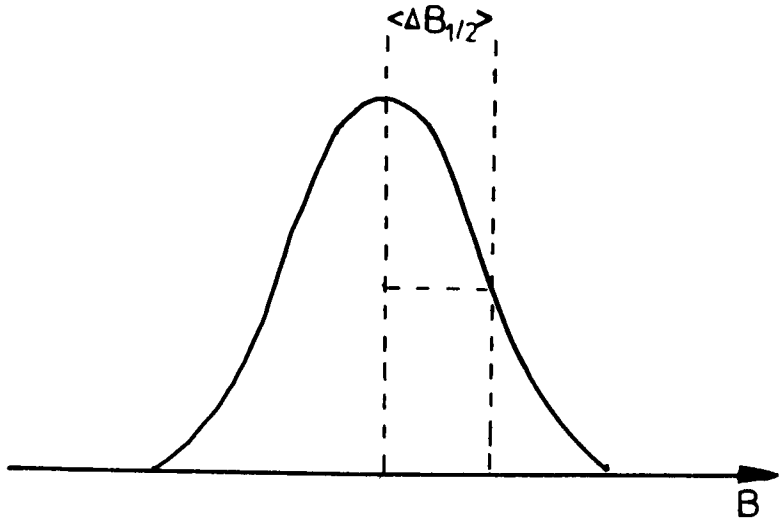

(a) absorption

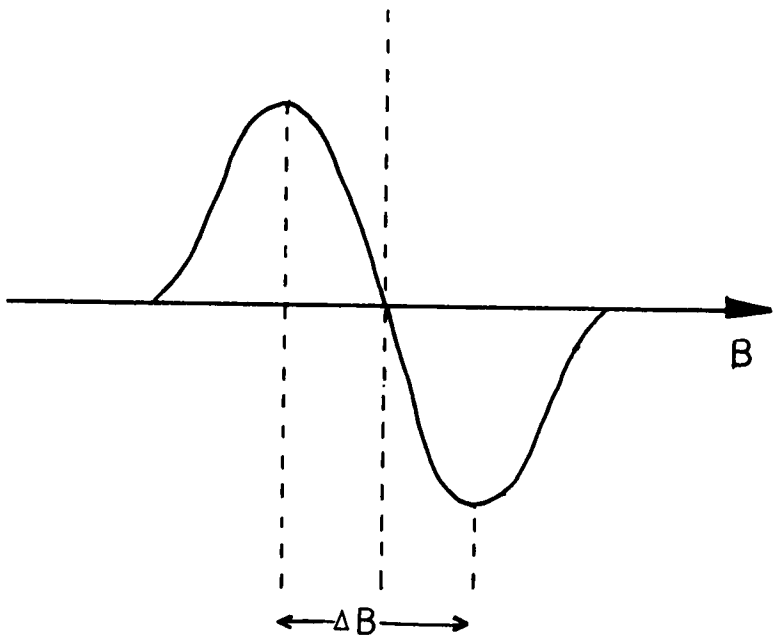

(b) derivative

Linewidths

Figure 2·1

2.5 Lattice dynamics.

Thermal vibrations are of higher frequency than ω_o and do not affect the spin system. The types of motion of interest in nmr of solids are molecular rotation, tumbling and translational diffusion. The atom or molecule is considered to be a vehicle that carries the nucleus from point to point.

The range of frequencies and amplitudes is treated theoretically by using the spectral density, $J(\omega)$. The mean square of the time variation of a random (position) function $f(t)$ is given by $\overline{f(t)f(t)^*}$. Transitions occur at definite frequencies and Fourier transformation for a positional variation over time $-\tau$ to $+\tau$ gives

$$f(\omega) = \int_{-\tau}^{\tau} f(t)e^{i\omega t}\, dt.$$

$f(\omega)$ is another random function and averages to zero, but the mean square, $\overline{f(\omega)f(\omega)^*}$, has a definite value and gives the amplitude at frequency ω from $-\tau$ to $+\tau$. As time becomes infinite, so does the integral above, and the spectral density is

$$J(\omega) = \lim_{\tau\to\infty} \frac{1}{2\tau} f(\omega)\ f(\omega)^*.$$

which is the mean square amplitude per unit time.

Fluctuation problems are treated by introduction of a correlation function $K(\tau)$ where

$$K(\tau) = \overline{f(t)\ f(t+\tau)^*} \quad .$$

The function has a maximum at $\tau=0$ and goes to zero at $\tau=\infty$. For a time less than a critical time, τ_c, called the correlation time, the motion is considered small, while for times greater than τ_c, the correlation is weak. The spectral density and the correlation function are related by Fourier transformation.

$$J(\omega) = \int_{-\infty}^{\infty} K(\tau)e^{i\omega\tau}\, d\tau$$

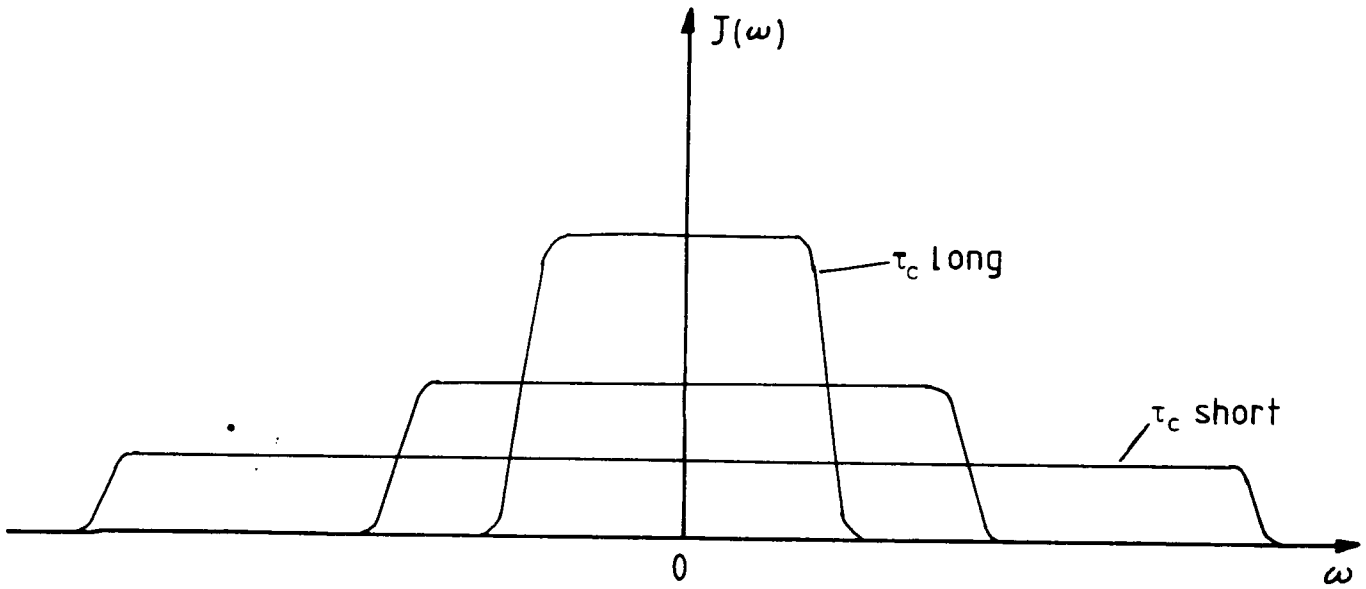

Figure 2·2

The choice of correlation function depends on the physical basis of the motion. It can be difficult to solve the mathematical problem.

The integral of the spectral density is a constant, the shape of the curve varying with τ_c. It is often assumed that the fluctuations can be described by an exponential correlation function

$$K(\tau) = f(0)\ e^{-|\tau|/\tau_c}$$

which corresponds to a field jumping randomly between two values (99). The corresponding spectral density is

$$J(\omega) = K(0)\ 2\tau_c/(1+\omega^2\tau_c^2).$$

The variation of $J(\omega)$ with τ_c for this case is shown in figure 2.2.

The position functions in the dipolar Hamiltonian (section 2.3) are denoted

$$F^0(t) = (1-3\cos^2\vartheta)\ r_{ij}^{-3}$$

$$F^1(t) = \sin\vartheta\cos\vartheta\ r_{ij}^{-3}\ e^{-i\phi}$$

$$F^2(t) = \sin^2\vartheta\ r_{ij}^{-3}\ e^{-2i\phi}$$

and the corresponding spectral densities are J^0, J^1, J^2.

2.6 Theories of relaxation.

The temperature dependence of nmr relaxation times can provide a quantitative measure of the probability per unit time $(1/\tau_c)$ of motional jumps over a wide range of values.

Relaxation in the laboratory frame is usually studied in fields of 10kG or more, and the weak collision case then always applies. This has been treated by many workers, classic papers being by Bloembergen, Purcell and Pound (the BPP theory, see reference 102) and Kubo and Tomita (103). Redfield (104) expresses this in density matrix formalism (105). The magnetic nucleus is treated as taking part in random translational and/or rotational Brownian motion. The formulae deduced for relaxation

times for a system of like spins are

$$\frac{1}{T_1} = \frac{3}{2}\gamma^4\hbar^2 I(I+1)\,[J^1(\omega_o) + J^2(2\omega_o)]$$

$$\frac{1}{T_2} = \gamma^4\hbar^2 I(I+1)\,[\tfrac{3}{8}J^2(2\omega_o) + \tfrac{15}{4}J^1(\omega_o) + \tfrac{3}{8}J^o(0)]$$

For an exponential correlation function (section 2.5) it follows that

$$\frac{1}{T_1} = \frac{2}{3}\gamma^2 CM_2\left(\frac{\tau_c}{1+\omega_o^2\tau_c^2} + \frac{4\,\tau_c}{1+4\omega_o^2\tau_c^2}\right)$$

where C is the fraction of the second moment removed by the motion. A minimum in T_1 is predicted when $\omega_o\tau_c = 0.616$ and its value is

$$(T_1)_{min} = 3\omega_o/(2.84CM_2\gamma^2)$$

which for protons and an instrument frequency of 16MHz (as used in this work) corresponds to

$$(T_1)_{min} = \frac{148}{CM_2}\ msG^2.$$

When $\omega_o\tau_c \gg 1$, this predicts $T_1 \propto \tau_c$, and, when $\omega_o\tau_c \ll 1$, $T_1 \propto \tau_c^{-1}$. If τ_c conforms to a relationship

$$\tau_c = \tau_c^o \exp(E_A/RT)$$

this theory predicts that, for a plot of log T_1 versus $1/T$, the limiting slope on either side of a T_1 minimum gives the activation energy, E_A, for the motional process. This can also be deduced from a similar plot for T_2 in a line narrowing region.

Torrey (106-108) and Resing and Torrey (109) extended the theory to a more quantitative study of relaxation using random walk theory. In evaluating spectral densities, time averages are replaced by ensemble averages by construction of probability functions for random walks to nearest sites, the probability per unit time for a jump being $1/\tau_r$. τ_r is twice the BPPτ_c, since the dipolar interaction between a randomly migrating pair of

spins changes whenever either of the two spins jump . Functions $G(k,y)$ have been tabulated for cubic close packed and body centred cubic lattices

$$G(k,y) = \int_0^\infty J^2_{3/2}(kx)\ \frac{1-(\sin x/x)}{(1-(\sin x/x))^2+y^2}\ \frac{dx}{x}$$

where k is a factor depending on lattice type and $y = \omega\tau_r/2$. Also

$$J^1(\omega) = \frac{8\pi}{15}\ \frac{n\tau_r}{k^3 l^3}\ G(k,y)$$

and $J^2(\omega) = 4J^1(\omega)$, $J^o(\omega) = 6J^1(\omega)$,

where n is the number of nuclear spins per unit cell and l is the jump distance. The general behaviour of T_1 and τ_r is as in BPP theory but

$$(T_1)_{min} = \frac{\omega_o}{0.874 C M_2 \gamma^2}$$

$$= \frac{160}{C M_2}\ \text{msG}^2 \text{ for protons at 16 MHz}$$

As temperature decreases, $\omega_o\tau_c$ becomes longer than unity for a particular type of motion. Thus T_1 becomes long and perhaps awkward to measure. In these circumstances, $T_{1\rho}$ measurements are very useful. These sample local fields fluctuating at low frequencies ($\sim\gamma B_1$) as well as those near the Larmor frequency. Normally in such an experiment, $\gamma B_o \gg \gamma B_1 \gg \gamma B_{local}$, so that at resonance the effective field in the rotating frame is $\underline{B}_1$. This weak collision case has been treated by a number of workers (110-112), Blicharski having given a recent comprehensive treatment similar in form to BPP theory and giving

$$\frac{1}{T_{1\rho}} = \frac{3}{2}\gamma^4\hbar^2 I(I+1)\left[\frac{5}{2}J^1(\omega_o) + \frac{1}{4}J^2(2\omega_o) + \frac{1}{4}J^o(2\omega_1)\right]$$

For an exponential correlation function this predicts similar behaviour to T_1 with

$$(T_{1\rho})_{min} = 2\omega_1/C M_2 \gamma^2$$

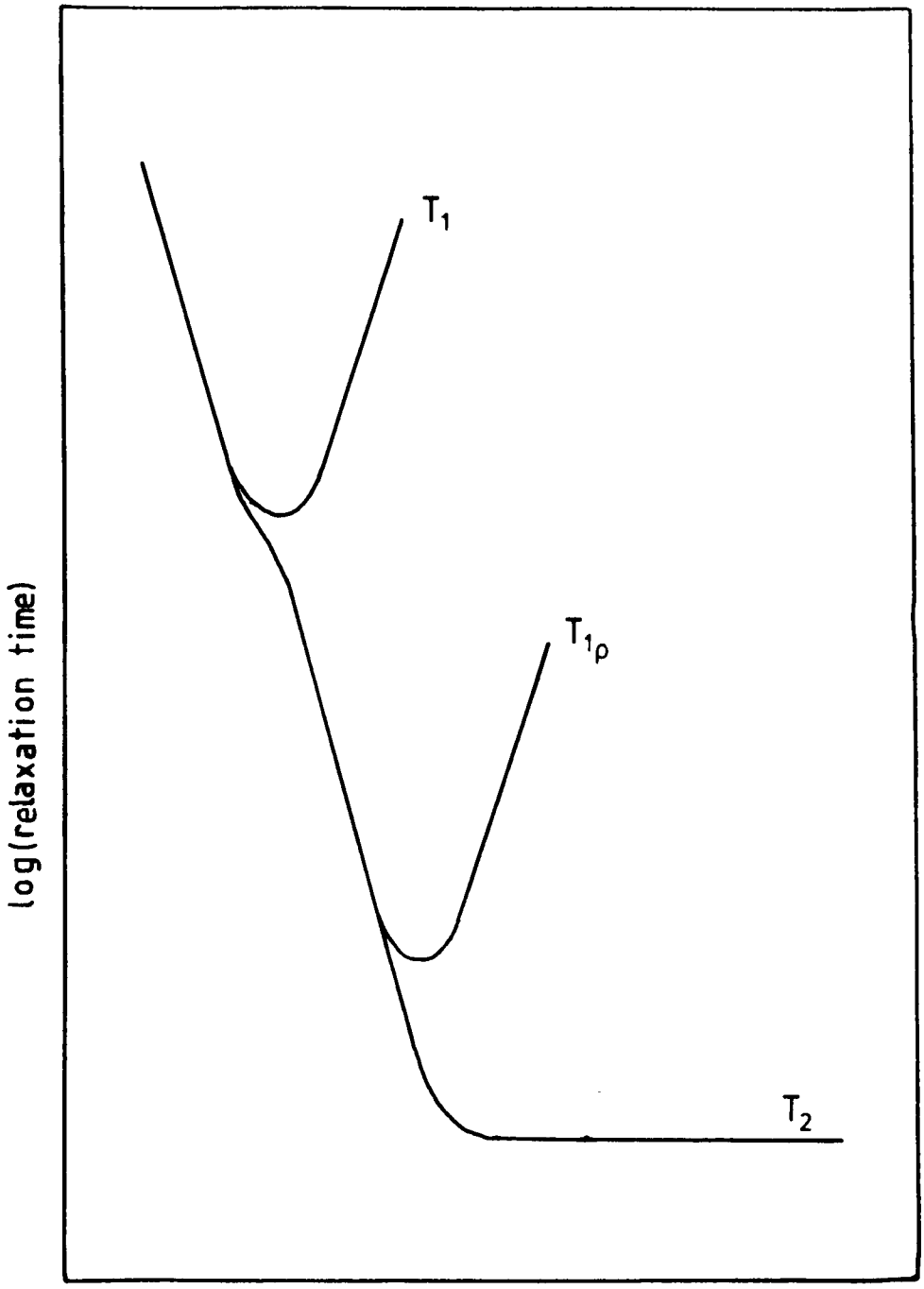

Figure 2·3

The ratio of $(T_1)_{min}$ to $(T_{1\rho})_{min}$ is given for protons by

$$\frac{(T_1)_{min}}{(T_{1\rho})_{min}} = 0.525\ \frac{\omega_o}{\omega_1} \qquad \text{(Torrey's theory: } 0.26\ \frac{\omega_o}{\omega_1}\text{)}$$

At temperatures above the T_1 minumum, the combined theories predict

$$T_1^{-1} = T_2^{-1} = T_{1\rho}^{-1} = \frac{10}{3}\ \gamma^2 CM_2\ \tau_c$$

An idealised behaviour for T_1, T_2 and $T_{1\rho}$ for a translational process is shown in figure 2.3.

Wolf and Jung (113) have developed a comprehensive perturbation formalism, valid for $T_{1\rho}$, from which both the strong and weak collision formulae are obtained as special cases. In the low field transitional region between these two approaches (i.e. when a low field $T_{1\rho}$ minimum is observed), relaxation is not governed by internal motions alone but internal equilibration within the spin system is also important. The Slichter-Ailion formula for random walk processes in the strong collision limit is (99)

$$\frac{1}{T_{1\rho}} = \frac{2(1-p)}{\tau_r}\ \frac{B_L'^2}{B_1^2+B_L'^2}$$

where p is a geometrical factor depending on the type of motion and the structure of the material, and B_L' is the local field in the rotating frame given by (113)

$$B_L' = (\tfrac{1}{5}M_2)^{1/2}.$$

2.7 Solid echoes.

In rigid solids, the instrument dead-time (time to recover from the saturating effect of the pulse, $\sim 4\mu s$) is a significant part of the free induction decay ($\sim 10-40\mu s$) and simple observation of the free induction decay will result in loss of the initial part of the decay. Effective zero time resolution is obtained by the two pulse solid echo technique (114).

Mansfield (115) has shown that the response of a rigid dipolar coupled nuclear spin system to the RF pulse sequence, $90^{o}_{0}o - \tau - 90^{o}_{90}o$ (the second pulse $\pi/2$ out of phase with the first), is given by

$$m(t') = 1 - \frac{\gamma^2 M_2 (\tau - t')^2}{2!} + \frac{\gamma^4 M_4 (\tau - t')^4}{4!} \ldots\ldots + \text{error terms}$$

where $M_2, M_4 \ldots\ldots$ are the van Vleck moments of the absorption lineshape, t' is the time since the second pulse (i.e. $t+\tau$) and the error terms, discussed below, give the attenuation of the echo maximum, which occurs at $t'=\tau$ ($t=2\tau$), and are a measure of the irreversibility of the transverse relaxation. The echo arises from homogeneous dipolar interactions and is different from spin echoes in liquids (see Chapter 3 and ref 116) and quadrupolar echoes in solids (117) which depend on refocussing the spin dephasing caused by static inhomogeneities. Powles and Strange (114) have shown that, in the limit $\tau \to 0$, the echo is identical to the FID (free induction decay) for solids containing single identical interacting spin-$\frac{1}{2}$ nuclei. The pulse sequence and response are shown in figure 2.4.

Errors in the tails of absorption spectra have large effects on M_2 values and the same is true for errors at short time in FID's. M_2 values can be obtained to a predictable accuracy,

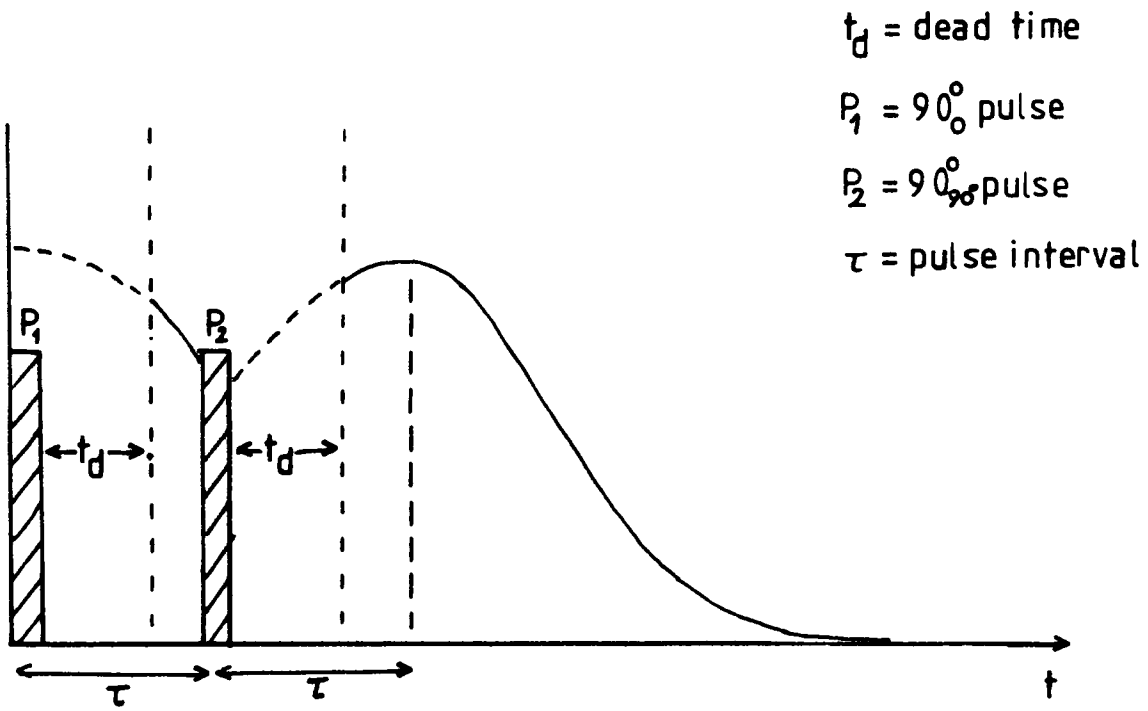

Figure 2·4 Solid echoes

comparable to that of steady state measurements, by curve fitting to solid echo decay shapes (115).

The attenuating error terms have been found to depend on the structure. For systems containing spin-$\frac{1}{2}$ pairs (e.g. $CaSO_4.2H_2O$) the maximum echo amplitude $E(\tau)$ has a Gaussian dependence on τ and has been fitted (118,119) to

$$E(\tau) = 1 - \frac{\gamma^2 M_{2E} \tau^2}{2!} + \frac{\gamma^4 M_{4E} \tau^4}{4!} - \ldots\ldots\ldots$$

the Gaussian decay showing $M_{4E} = 3M_{2E}^2 \ldots\ldots$, and the dependence to be

$$E(\tau) = E(0)\exp(-\tfrac{1}{2}\gamma^2 M_{2E} \tau^2).$$

The Gaussian shape is characteristic of a local field distribution due to a system of interacting species which are more or less uniformly distributed in space. Boden et al. (118,119) have shown that

$$M_{2E} = \frac{16}{18} M_2^{vv} \text{ (inter)}$$

where M_2^{vv} (inter) is the van Vleck intergroup second moment. For a plot of lnE versus τ^2 this corresponds to

$$M_2^{vv}(\text{inter}) = -3.14 \times 10^3 \text{ slope } G^2 \mu s^2.$$

This behaviour contrasts with that predicted (115) and observed (120) for solids containing single identical spins, where the effect of the error terms is to give the maximum at $t < 2\tau$ and attenuation principally by a fourth moment like term $M_{4E}\tau^4$, the attenuation then being distinctly non-Gaussian.

The measurement of M_2^{vv}(inter) is a result of practical importance as this information is not usually determinable in an unambiguous way from either steady state lineshapes or FID's.

2.8 Complications.

For a rigid lattice ($(\gamma^2 M_2)^{\frac{1}{2}} \tau_c > 1$), the free induction decay is non-exponential and hence T_2 cannot be defined in a Bloch-like manner. The decay often approximates to a Gaussian

$$g(t) = g(0) \exp(-\tfrac{1}{2}\gamma^2 M_2 t^2)$$

where M_2 is the second moment of the absorption lineshape, which is also a Gaussian. T_2 is defined conventionally (114,121) as the time for decay to 1/e of the initial amplitude.

A non-exponential correlation function will alter the spin-lattice relaxation behaviour. Hunt and Powles (122) have used such a function, derived from a defect diffusion model, to explain the relaxation in supercooled liquids and glasses. Wolf (123) has proposed a correlation function for random walk and point defect mechanism of self-diffusion which consists of an exponential part multiplied by a power series in t/τ_c, the leading term being the simple exponential correlation function. He argues that this form is crucial for applicability in the strong collision region (113).

There may be more than one correlation time when different motions are present or when there are different environments in the sample (124). The effect of the latter is to broaden and flatten the minima observed.

Rotation can be important in solids. Ammonium salts show minima due to this (e.g. 125). When two different sites are present, two minima in the spin-lattice relaxation behaviour may be observed (126), the total behaviour then being the sum of that for the two different environments. Thus Na_2ReH_9, with one site, shows a single T_1 minimum, while K_2ReH_9, with two

sites, has two, both due to rotation of ReH_9^{2-} (127).

Non-exponential spin-lattice relaxation can arise in a number of ways. One possibility is the superposition of decay processes in a multi-phase system. Another is that it might arise from correlated motion of more than two nuclei in re-orienting groups (such as a methyl group or an ammonium ion). In solids where this is an important relaxation mechanism, the relaxation may be the sum of a number of exponentials, none of which dominates the other. This has been explained by Hilt and Hubbard (128) as resulting from cross-correlation terms due to interaction of one dipole-dipole interaction with another. Intergroup interactions have negligible cross-correlations and hence produce no non-exponential character. Most practical cases fall somewhere between the extremes of relaxation totally determined by intra-group relaxation and relaxation unaffected by cross-correlation.

The semi-classical theory of magnetic resonance discussed here is inappropriate at very low temperatures for simple molecular rotors, such as ammonium ions and methyl groups, where symmetry of rotor states and quantum mechanical effects become important. Studies have been made of both line-shapes and spin-lattice relaxation in.such cases (124), but interpretations vary from author to author. Clough (129) has explained observed non-exponentiality in T_1 behaviour and Morimoto has explained non-exponentiality in $T_{1\rho}$ behaviour (130). NMR can be used to study the effects involved (e.g. quantum mechanical tunnelling (131)).

Relaxation may result from dipolar interactions between unlike spins e.g. between ^{1}H and ^{19}F or between ^{1}H and paramagnetic centres. Relaxation by unlike spins has been treated theoretically by a number of workers (149-152). In many compounds at low temperature the dominant relaxation mechanism is interaction with paramagnetic (impurity) centres. In the presence of such centres, the correlation time, τ, for the local field fluctuations at a nucleus is given by (149,150)

$$\tau^{-1} = \tau_d^{-1} + (T_1^e)^{-1}$$

where T_1^e is the relaxation time of the paramagnetic centre and τ_d is the time between diffusional jumps. When $\tau_d > T_1^e$, relaxation is not governed by diffusion but by relaxation of the paramagnetic centre. τ_d may be less than the experimental T_1 and many jumps occur in a single relaxation time giving an average, exponential, relaxation behaviour. The temperature-dependence of T_1 will then be that of T_1^e, which is much weaker than that of τ_d. If ϑ, the time taken for a nucleus to diffuse between paramagnetic centres (typically $\sim 100\,\tau_d$ if these are impurities), becomes long compared with T_1 (i.e. at very low temperatures), the spatial averaging of relaxation behaviour is no longer performed and this results in a distribution of relaxation rates. The non-exponential relaxation behaviour may then be represented arbitrarily as the sum of two exponentials (e.g. ref.151). Further, as relaxation via dipolar interaction with paramagnetic centres is only effective over a limited distance, at these low temperatures some relaxation must be taking place by spin diffusion (energy exchange through the bonds) to the paramagnetic sinks. The occurrence of weakly temperature-dependent non-

motionally determined T_1 values at low temperatures can limit the use of T_1 measurements for studying motions. Measurements of the relaxation times $T_{1\rho}$ and T_{1D} (the spin-lattice relaxation time in the local dipolar field, see refs.153-154) can extend the temperature range over which information about motions is obtainable.

Chapter 3

Apparatus and Techniques

3.1 The spin-echo spectrometer.

A block diagram of the modified Polaron spin-echo spectrometer and accompanying systems is given in figure 3.1.

Two magnets were available to supply the static magnetic field, B_o. The first, an AEI RS2, was current controlled and kept at a constant temperature using a heat exchanger and recirculatory water system. The second, a Varian Associates Fiedial, was field controlled and cooled by filtered mains water (flow rate $> 2.5\ dm^3\ min^{-1}$).

The probe was of a crossed coil configuration, the coils being wound on PTFE formers as shown in figure 3.2. The transmitter coil was $4\frac{1}{2}$ turns of PTFE insulated multi-strand wire wound in the Helmholtz manner and the receiver coil a ten turn solenoid with diameter 14mm. The probe carriage allowed movement both vertically and horizontally in the magnet pole gap and the probe could thus be positioned in the region of maximum field homogeneity.

The radiofrequency field, B_1, was derived from a crystal controlled continuous wave 16 MHz oscillator. After low power amplification, the oscillator fed two independently adjustable channels. The output from these channels fed a high power transmitter supplied by a variable stabilized power supply. The pulses were then fed through a matching circuit to the transmitter coil of the probe which formed part of a tuned circuit.

The hard-wired pulse programmer was synchronized by a

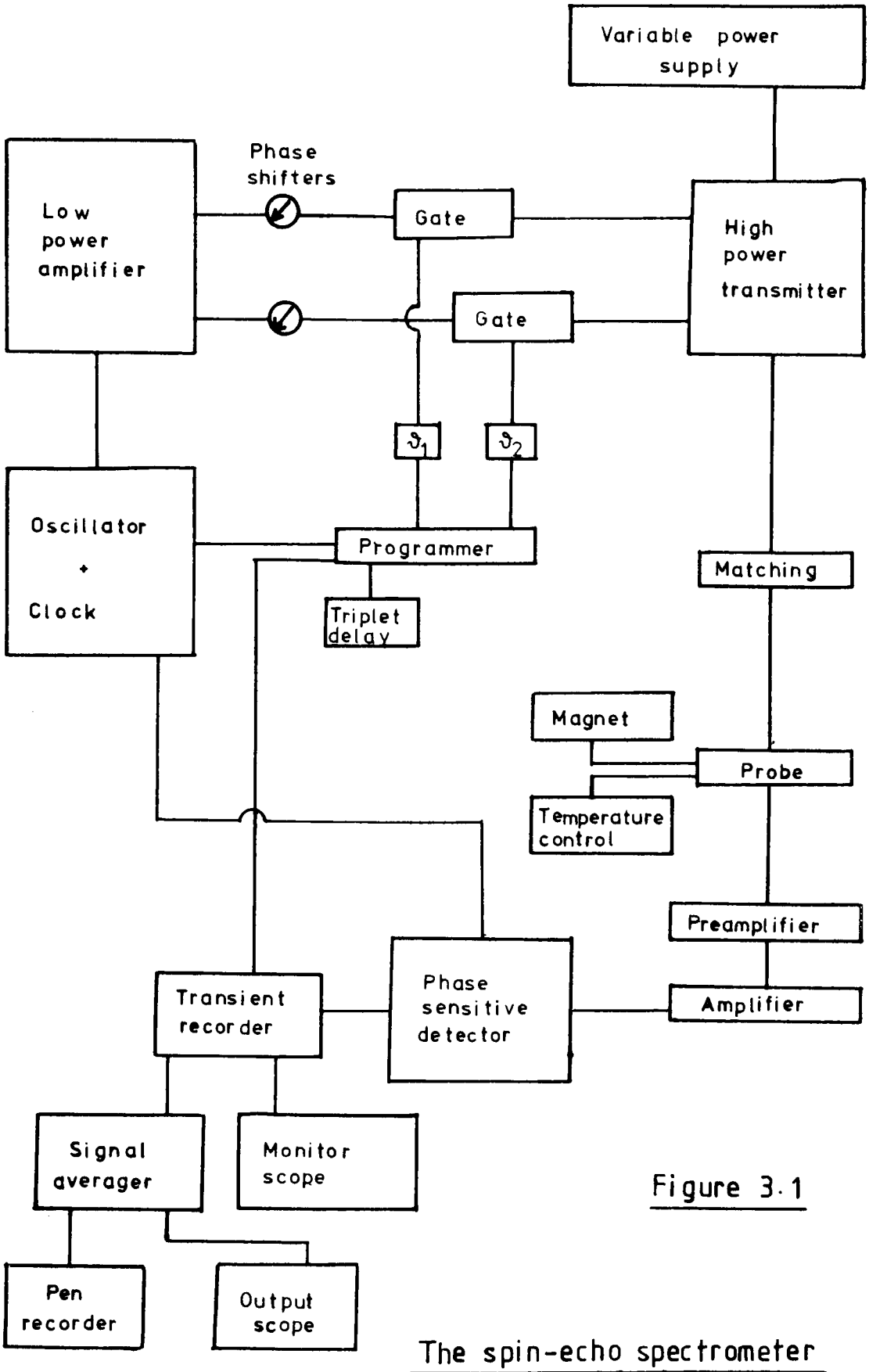

Figure 3.1

The spin-echo spectrometer

FIGURE 3.2 The components of the n.m.r probe

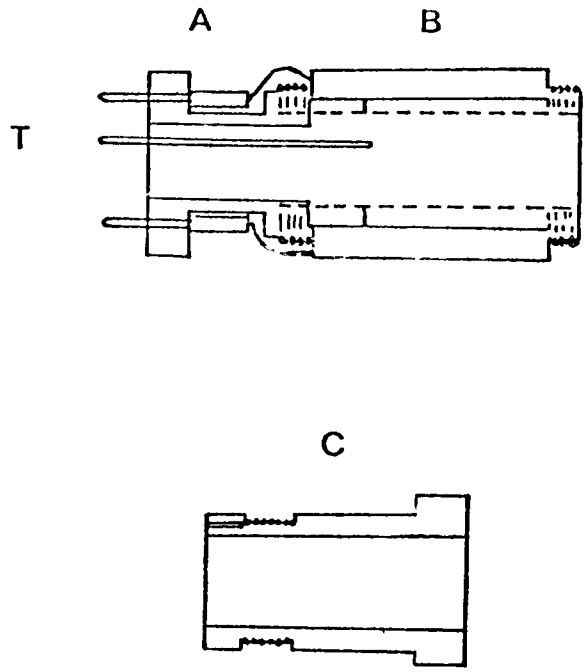

A.B.C Together made up the probe

AB a crossection through the probe with C removed

C is the receiver

B is the transmitter coil

T is the thermocouple

B_1 is the top view of B

1 MHz clock and the following pulse sequences could be selected

(1) Channel 1

(2) Channel 2

(3) Channel 1 - τ - Channel 1

(4) Channel 2 - τ - Channel 1

(5) Channel 1 then the sequence (Channel 1-t-Channel 2-t-Channel 1) after τ and every successive 2τ .

(6) Channel 1 - τ - Channel 2

(7) Channel 1 then, after τ and then after every 2τ , Channel 2.

(8) Channel 1 - t - Channel 2. The length of the second pulse is τ.

(9) Channel 1 followed at τ and then every 2τ by Channel 1-t - Channel 2.

(10) Channel 1 - t - Channel 2 -τ - Channel 2.

τ was set digitally and t continuously (using a triplet delay unit). The length of multi-cycle sequences was controllable, as was the time between sequences.

The nmr signal induced in the receiver coil passed to a low noise pre-amplifier protected from the saturating effect of the transmitter pulse by crossed diodes. The signal was further amplified and phase sensitively detected, the reference signal being derived from the oscillator.

All signals were stored in a transient recorder (see next section) and could be monitored continuously on an oscilloscope.

3.2 Data averaging equipment.

It is advantageous to accumulate several, perhaps hundreds, of similar signals, the technique being known as signal averaging. For a Gaussian noise distribution, the signal to noise ratio is improved by $\sqrt{N}$, where N is the number of accumulations. The spectrometer at York was equipped with a Datalab DL905 transient recorder interfaced with a Datalab DL102 200 point averager. This combination is capable of real time averaging with sampling rates of up to 5MHz.

The DL905 is a digital instrument and the controls and operation are similar to those of an oscilloscope. Signals are sampled at discrete points and the first 1000 points in the memory are reconstructed as a series of analogue values and displayed on an oscilloscope. In signal averaging, the analogue signal is transferred at a fixed rate to the averager. Starting the averager arms the DL905 which, triggered by the programmer, executes a sweep according to the settings of its controls. The recorder then triggers the averager and data transfer occurs, 200 words being synchronously transferred to the averager. These can be the first 200 or every fifth word depending on the averager control settings. The averager then arms the recorder and this process continues until the averager reaches its preset sweep count. The result is then scaled and can be read off a display oscilloscope. An analogue output from the averager can also be fed to a pen-recorder. The resolution in amplitude of the averaged signal can be altered to a maximum of 7 bits (1 in 128) using the averager "scale control" switch.

3.3 Setting up the spectrometer.

Samples were loaded in glass ampoules ($<1cm^3$) which were sealed under vacuum.

Cross-talk between the transmitter and receiver coils was minimised by rotation of the receiver within the probe, which affects the deviation from orthogonality. A high frequency signal generator was used and the cross-talk monitored on an oscilloscope. This procedure helps to minimise the machine dead time which was typically 5-10 μs.

Prior to measurements, the pulses were optimised for shape and power and the magnet was set "on field" for resonance. Transmitter pulses were monitored with a loop situated close to the tuning capacitors and displayed on the HP170 monitor oscilloscope. They were optimised by tuning the low power amplifier, transmitter and matching unit to give the maximum pulse height consistent with a short rise and fall time for the pulse. The magnet was set "on field" by observing the free induction decay (FID) of a sample with a large signal, long T_2 and short T_1. Suitable samples were water, doped with a paramagnetic salt (e.g. $Mn(NO_3)_2$), or an ammonium salt (e.g. $(NH_4)_4Fe(CN)_6 \cdot 3H_2O$). If the magnet was off resonance for protons, a damped oscillation was superimposed on the FID (due to interference as M_x and the reference signal came in and out of phase). The magnet settings were adjusted to give the decay with the longest characteristic decay time. The height of the FID was optimised by tuning the pre-amplifier and the phase shifter for the channel, the resultant FID signal being in phase with the reference signal.

A 90°_0 pulse could be set on Channel 1 using sequence 3 (1 -τ - 1) with $\tau \sim 10T_2$ and $\tau \ll T_1$. The pulse length was varied

so that no decay was observed after the second pulse.

A 90^{o}_{o} pulse could be set on Channel 2 by first setting one on Channel 1 and then using sequence 4 (2 -τ - 1) with $\tau \sim 10T_2$ and $\tau \ll T_1$. The length of the pulse on Channel 2 was adjusted so that no decay was observed after the second pulse.

A 180^{o}_{o} pulse could be set on either channel by first setting up a 90^{o}_{o} pulse and then increasing the pulse length until no FID was observed.

A channel could be set 90^{o} out of phase by setting up a decay and adjusting the phase shifter, and if necessary B_o, so that no FID was observed for any length of pulse.

Typical 90^{o} pulse lengths (t_{90}) with the high power supply at 3.5 kV were 7-8 μs. This corresponds (see section 2.1) to an RF field strength, B_1, of 8.4-7.3G.

3.4 Relaxation time measurements.

All the samples studied gave weak signals and hence use of data averaging equipment was essential.

3.4.1 T_2 measurements.

After a 90^{o}_{o} pulse (e.g. using sequence 1) the resultant magnetisation precesses in the laboratory frame and this is detected by the receiver coil. The signal decays with characteristic time T_2 as the spins dephase from one another. The signal is the free induction decay (FID).

When $T_2 > 200$ μs, the shape of the FID is not determined solely by T_2, but also by static field inhomogeneities. Several pulse sequences have been used to find true T_2's. Hahn's spin echo method (116) is a two pulse sequence but is again limited

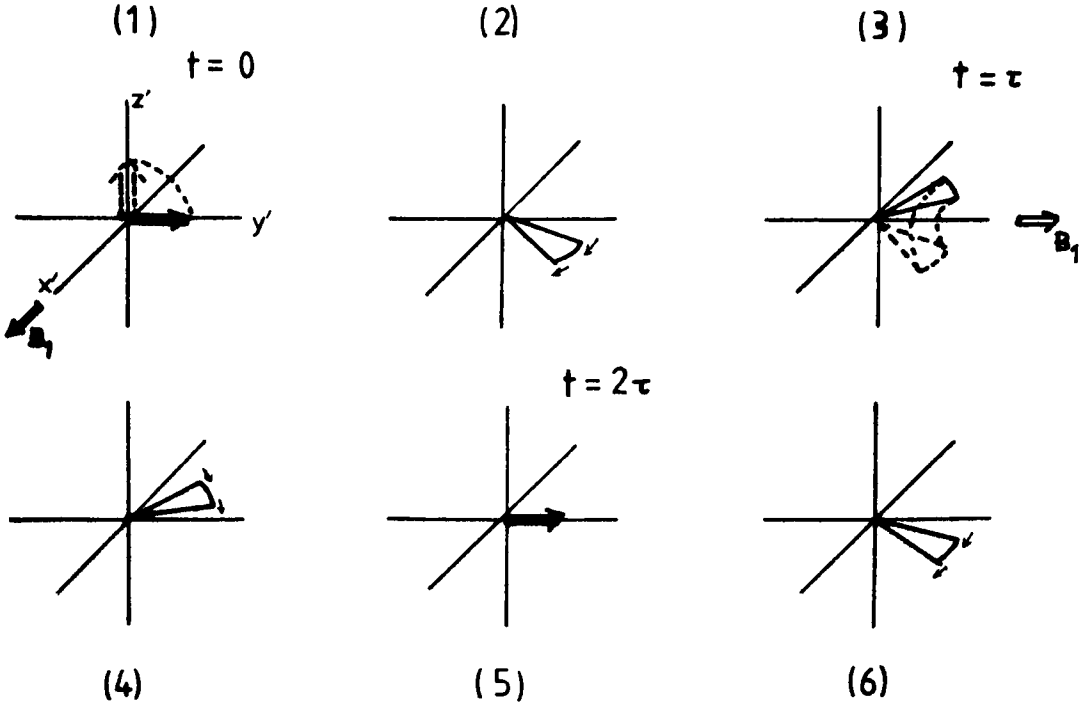

The Carr-Purcell-Meiboom-Gill pulse sequence

Different spins precess at slightly different frequencies in the inhomogeneous magnetic field and therefore dephase. The 180°_{90} pulses lead to rephasing along the y' axis, giving a train of echoes. For simplicity, the rate of rotation of the frame above is taken to be slower than the precession frequency of any of the spins.

$P_1 = 90^{\circ}_{0}$ pulse $\qquad P_{2\to n} = 180^{\circ}_{90}$ pulse

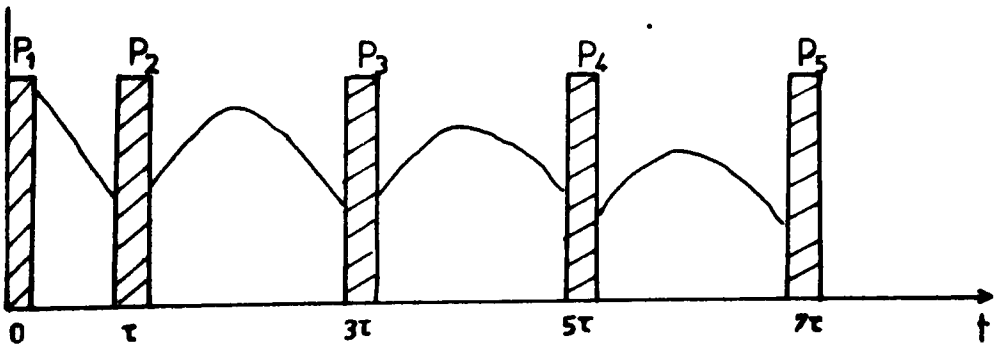

Figure 3.3

by molecular diffusion. Carr and Purcell (132) showed that a simple multiple pulse modification of Hahn's method reduced the effect of diffusion, and Meiboom and Gill (133) modified this to eliminate cumulative errors due to errors in pulse lengths. The CPMG (Carr-Purcell-Meiboom-Gill) method can be used to measure very long T_2's, and sequence 7 of the programmer was suitable for this. A 90°_{0} pulse was set on Channel 1 and a 180°_{90} pulse, $\pi/2$ out of phase with Channel 1, was set on Channel 2. Figure 3.3 illustrates the pulse sequence and its effects. The envelope of the echo maxima gives T_2 directly.

In rigid solids, the FID can be very short ($\sim 10\mu s$), with the result that the early part of the decay is lost in the instrument dead time, and is typically non-exponential. The solid echo technique (ref.114, section 2.7) was used to give effective zero time resolution. In such cases T_2 was defined (as is done conventionally (114,121)), as the time for decay to 1/e of the initial signal height, in this case the echo maximum. Sequence 6 of the programmer was used, Channel 1 having a 90°_{0} pulse and Channel 2 having a 90°_{90} pulse.

3.4.2 T_1 measurements.

Method A

T_1 can be measured by the $90^{\circ}_{0} - \tau - 90^{\circ}_{0}$ method (134), and sequence 3 was suitable for this. The height of the FID after the first pulse is proportional to M_0, the equilibrium magnetisation in the static field direction. The second pulse, after time τ, gives an FID with height proportional to $M_z(\tau)$, the magnetisation in the z-direction after time τ. Thus $(M_0 - M_z(\tau))$ is proportional to the difference in heights of the FID's at

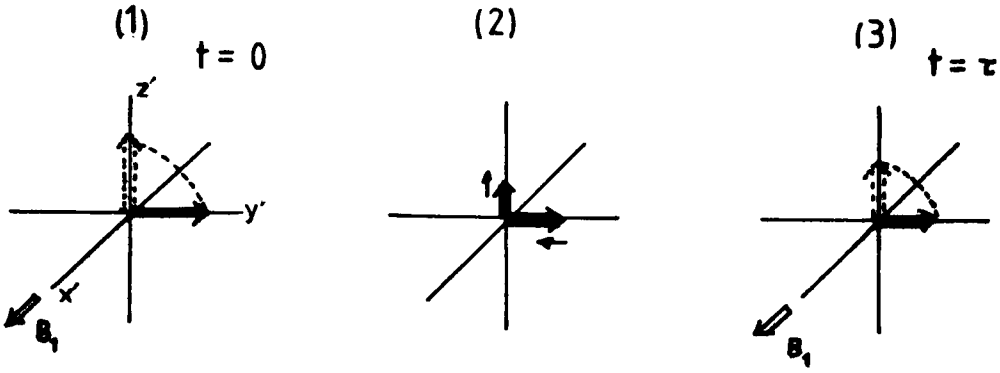

Measurement of T_1 by the 90°-τ-90° method

The second pulse gives an FID with height proportional to $M_z(\tau)$.

$P_1 = P_2 = 90^\circ_0$ pulse

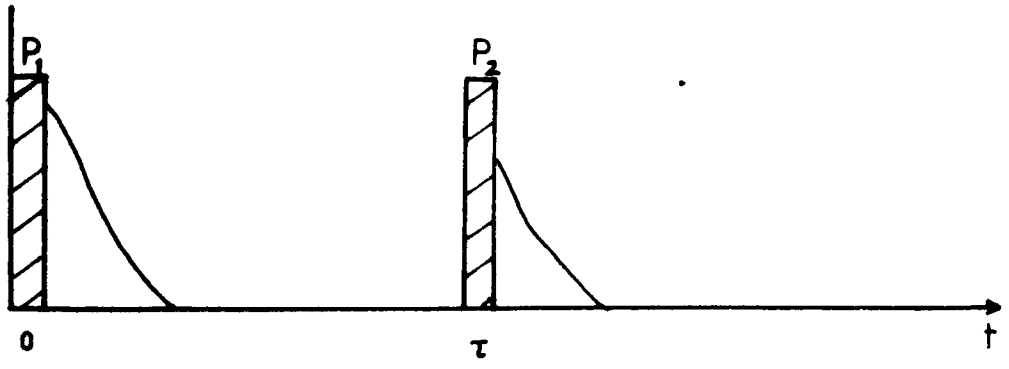

Figure 3.4

$t = 0$ and $t = \tau$. The decay of this quantity with τ has the characteristic time T_1 (see section 2.2). The sequence is illustrated in figure 3.4.

Method B

Normally, when making T_1, T_2 or $T_{1\rho}$ measurements, the repeat time between successive sequences is set at a value $> 6T_1$ to prevent saturation effects. However, with very weak signals, hundreds of sequences might need to be accumulated and considerable time saving in measuring long T_1's is possible by exploiting these saturation effects.

The "progressive saturation" technique has been used in various forms by several workers (135-137), though generally not with pulse spectrometers. For a train of accurately 90°_0 pulses, the magnetisation, M_z, and hence the FID, reaches a constant value which varies with pulse separation τ_s according to (135)

$$M_\infty(\tau_s) = M_0(1 - e^{-\tau_s/T_1}).$$

Sequence 1 could be used for this, by varying the sequence repeat time, or alternatively sequence 9, where τ_s was twice the digitally set τ value and the length of the pulse train was controlled by the sequence length control. Channel 2 had no pulse in this case.

Solid echo read pulses

For samples where the FID was very short (rigid solids), sequence 9 could be used to give a chain of solid echoes, and the decay of the echo height with τ_s used to give T_1. This prevented loss of the main part of the decay and thus reduced the averaging necessary. The 90°_{90} pulse can be regarded as a "read pulse".

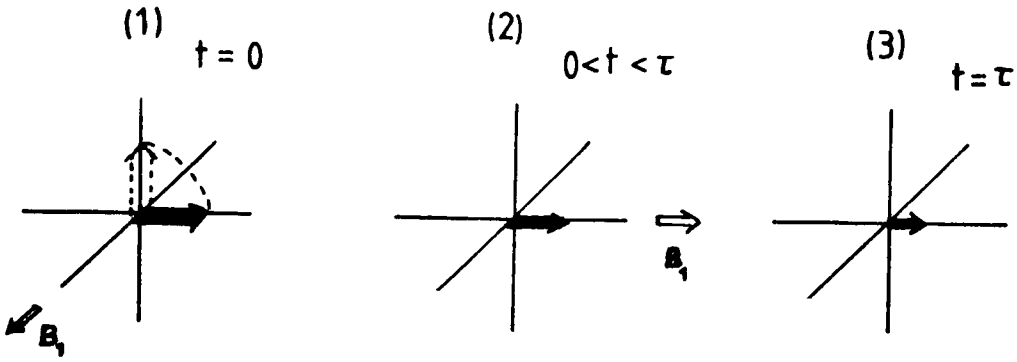

Measurement of $T_{1\rho}$ by Hartmann and Hahn's method

The decay of the height of the FID after the spin-locking pulse with τ gives $T_{1\rho}$.

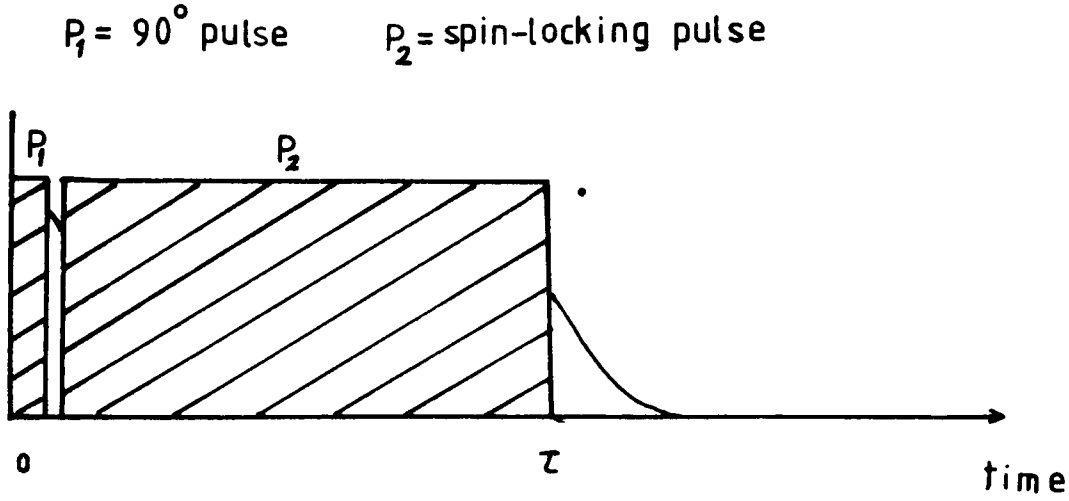

Figure 3.5

3.4.3 $T_{1\rho}$ measurement.

The spin-lattice relaxation time in the rotating frame, $T_{1\rho}$, can be measured by the method of Hartmann and Hahn (138). Sequence 8 of the programmer was used, Channel 1 giving a 90°_{o} pulse and Channel 2 being $\pi/2$ out of phase with Channel 1. The pulse sequence and effect are illustrated in figure 3.5. The first pulse rotates the sample magnetisation onto the X'-axis, and the second is applied along this direction and is termed "spin-locking". The magnetisation (viewed in the rotating frame) relaxes towards a very small value along B_1 while it is spin locked and, after time τ, the B_1 field ceases and the FID then observed gives the remaining magnetisation in the X'-direction. The decay of the initial height of this FID with τ has the characteristic time $T_{1\rho}$.

If the pulses are correctly set up exactly on resonance, for $\tau \ll T_{1\rho}$ the initial FID amplitude after the second, spin-locking, pulse should be the same as that from the first pulse on its own, and for $\tau \gg T_{1\rho}$ the amplitude should be zero. This provides an alternative method for setting the static field exactly on resonance (139), but, because the recovery of the pre-amplifier is impaired by long spin-locking pulses, this method was difficult to use.

3.4.4 Solid echo envelope.

The variation of $E(\tau)$, the echo amplitude (see section 2.7), with τ for solid echo measurements could be followed using sequence 6 of the programmer. For other measurements involving solid echoes, τ was chosen to be twice the instrument dead-time (i.e. $\tau \sim 24\mu s$) so as to both see an echo maximum and have its amplitude the maximum possible (114).

3.5 Temperature control.

Sample temperatures were controlled to ±1K using a proportional temperature controller. A diagram of the probe assembly is given in figure 3.6. The 50W cartridge heater and sensing thermocouple were close together in the copper block. The sample temperature was measured using another thermocouple taped (with PTFE) to the sample. Both thermocouples were copper-constantan with reference junctions at $0^{o}C$. The whole probe assembly was surrounded by a Dewar vessel.

Sample temperatures from room temperature down to liquid nitrogen temperature (77K) were obtained using the cartidge heater and a gas/liquid nitrogen spray produced from a liquid nitrogen "kettle" (a 24 litre Dewar with a 24W heater) and passed through an insulated pipe to the probe. Temperatures above room temperature were produced using the heater alone. The highest temperature which could be attained was limited by the thermal stability of the PTFE probe (i.e. about 500K). At each temperature the sample was equilibrated for at least 30 minutes to eliminate thermal gradients before relaxation measurements were made.

3.6 Statistical analysis of relaxation data.

Relaxation time and solid echo data were analysed using computer programs written by the author.

Relaxation time data at a given temperature were analysed using the program RELAXO listed on microfiche in the programs appendix. Readings were weighted for equal instrumental uncertainties (140). When the decay appeared non-exponential, an iterative least squares fit to two exponentials (using standard

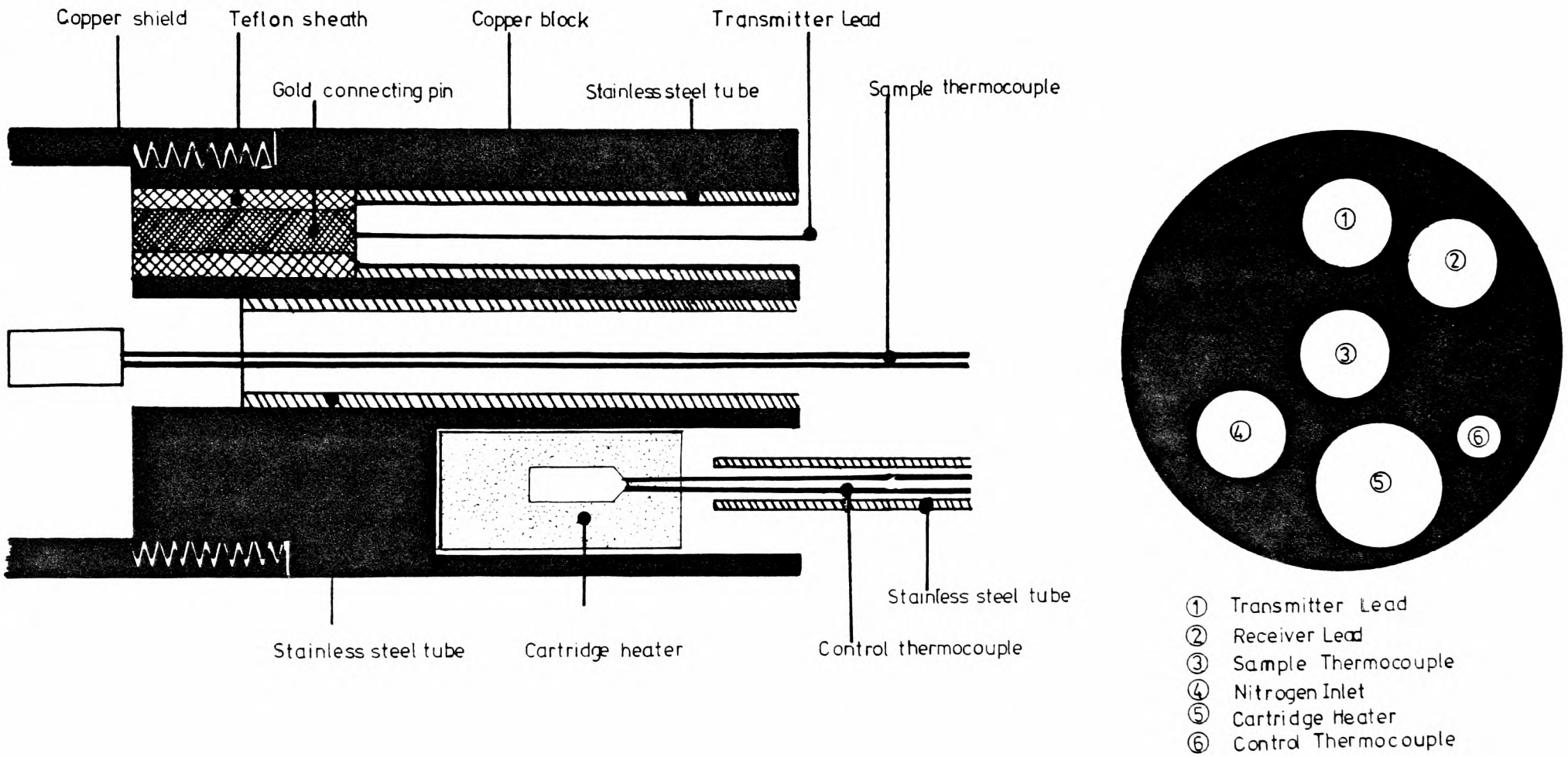

Figure 3.6 The Probe Assembly

techniques (140)) was carried out, requiring, as data, estimated values of the relaxation times and the mole fraction for each decay. Output from RELAXO gives, in the simple case, the relaxation time and its standard deviation. For the two exponential case, the calculated time to decay to 1/e of the initial signal height is given, together with relaxation parameters, standard deviations and mole fractions of the decays.

Second moment (M_2) values were estimated by fitting the top of the solid echo (points from before the maximum until 50% of the decay has occurred) for a given compound to a Gaussian using the program GAUSS which performed an iterative least squares refinement. Estimated values of the height of the echo, the position of the maximum and of M_2 were required as data. M_2 values obtained in this manner were in close agreement with values obtained by continuous-wave methods.

The program MINFIT performed an iterative least squares fit to BPP theory (102) for an observed T_1 minimum. Estimated values of $(T_1)_{min}$, τ_c^o and E_A were required as data. The program gave calculated values and standard deviations for these parameters.

3.7 Broad-line measurements.

Continuous-wave broad-line spectra were recorded in Oxford by the author on a Jeol JMN-4H-100 100MHz high resolution nmr instrument equipped with a broad-line attachment. The probe was of the single coil type and a low frequency modulation (30Hz) was used to obtain the derivative of the absorption signal which was displayed on a pen-recorder. Modulation widths were kept to less than 1/6 of the resonance linewidth to avoid

modulation broadening effects (125).

A temperature range of 160 to 470K was available using a Jeol temperature controller, with a nitrogen "kettle" for temperatures below room temperature, a hot air blasting arrangement for high temperatures,and a combination of both for intermediate temperatures. Samples were contained in 10 mm nmr tubes, sealed under vacuum and equilibrated for at least 30 minutes at each temperature to remove temperature gradients.

Additional continuous-wave broad-line spectra were recorded for the author. Bruker-Physik AG recorded spectra using a 30 MHz instrument at their French laboratory. Dr.B.G. Silbernagel of the Exxon Research and Engineering Company (Linden, New Jersey) recorded spectra on a Varian WL-112 spectrometer operating at 15 MHz.

A Fourier transform spectrometer was used, with the author as observer and adviser, to give broad-line absorption spectra. The instrument used was a Bruker CXP spectrometer at the applications laboratory of Bruker-Physik AG in Karlsruhe. The CXP is designed for multinuclear work on both liquids and solids and has an operating frequency of 90 MHz for protons. The spectrometer is controlled by a digital microprocessor, which is accessed by the operator using an electronic keyboard. The operator issues commands as to pulse sequences, lengths, delays, etc. and RF phases and probe assemblies are adjusted externally. Fourier transformation of accumulated data is accomplished by issuing a command (FT) on the keyboard and adjusting a few external controls.

Continuous-wave instruments give the derivative of an absorption spectrum, whereas Fourier transform spectrometers

give absorption signals. The meaning of the term "linewidth" in these two cases is discussed in section 2.4. Second moment (M_2) values were calculated from these spectra using computer programs written by the author and involving numerical integration using Simpson's rule.

Chapter 4

Preparation and Characterisation of Materials

Samples of gallium oxide hydroxide (GaOOH), boehmite (γ-AlOOH) and hydrogen molybdenum bronzes, H_xMoO_3 (x = 1.71, 0.36), were prepared by the author. Samples of the cation substituted β-aluminas, NH_4^+ β-alumina and H_3O^+ β-alumina, were supplied by Dr. P. McGeehin of the AERE Harwell.

4.1 Oxide hydroxides.

The compounds GaOOH and γ-AlOOH were prepared by hydrothermal treatment of parent oxides. The equipment used for this was an autoclave with a stainless steel lining, giving temperatures up to 400°C and pressures up to 350 atmospheres. Temperature was controlled to $\pm$ 5°C and, for safety, a metal diaphragm, perforating at pressures in excess of 350 atmospheres, was included. Samples were contained in a platinum tube with a platinum lid to prevent contamination by the autoclave, and the apparatus was filled with sufficient water to ensure the presence of liquid water at all stages of the reaction. Products were vacuum dried overnight in a vacuum desiccator.

δ-Ga_2O_3 was prepared from $Ga(NO_3)_3.9H_2O$ (Koch Light laboratories) by heating overnight at 250°C. The X-ray powder pattern for this phase was as reported by Roy et al.(141). This oxide was reacted with water in the autoclave at 250°C and 32 atmospheres pressure for 4 days to produce GaOOH. The X-ray powder pattern for the product was consistent with those previously reported for GaOOH (27,142,143) and corresponded to a pure phase with orthorhombic lattice parameters a = 4.516(4)Å,

b = 9.745Å, c = 2.964(2)Å. Lattice parameter refinement was carried out using a least squares refinement program (27) and the numbers in brackets are the standard deviations of the last figure. The pattern is given in table 4.1. The composition of the product was verified by vacuum decomposition on a microbalance, the observed weight loss being 9.0% and that predicted 8.8%.

γ -Al_2O_3 was prepared by heating ammonium aluminium sulphate (BDH"Analar") to 1000°C under a stream of nitrogen (to remove gaseous products). This was converted to γ-AlOOH by reaction with water in the autoclave at 350°C and 175 atmospheres for 5 days. The X-ray powder pattern, given in table 4.2, was consistent with those previously reported for γ -AlOOH (26,27,144, 145) and corresponds to a pure phase with orthorhombic lattice parameters a = 2.868(1)Å, b = 12.205(9)Å and c = 3.693(2)Å. Diffuse haloes at low angle, observed by other workers (34), suggested some disorder. The product composition was verified by vacuum decomposition on a microbalance, the observed weight-loss being 14.7% and the theoretical 15.0%.

4.2 Hydrogen molybdenum bronzes.

The phases H_xMoO_3 are oxidized in air by a stepwise process with the next lowest hydrogen-content phase being formed and then finally MoO_3 (48,49). The rate of oxidation is proportional to the hydrogen content. Compounds H_xMoO_3 were therefore always handled in an O_2-free atmosphere (glove box or bag).

The hydrogen content of H_xMoO_3 was determined by thermogravimetric dehydration and/or oxidation and by determination of the reducing power of the material.

Table 4.1

X-Ray Powder Pattern for GaOOH

(Debye-Scherrer Camera, CuK_{α} radiation)

Intensity	$2\vartheta/^{\circ}$	$d_{(obs)}/\text{Å}$	$d_{(calc)}/\text{Å}$	h	k	l
W	17.85	4.887	4.860	0	2	0
S	21.70	4.095	4.089	1	1	0
W	27.10	3.290	3.290	1	2	0
M	34.00	2.637	2.633	1	3	0
M	35.53	2.527	2.529	0	2	1
F	36.33	2.473	2.475	1	0	1
VW	36.85	2.439	2.433	0	4	0
M	37.53	2.397	2.399	1	1	1
VW	40.05	2.251	2.256	2	0	0
VW	41.13	2.195	2.206	1	2	1
W	42.33	2.135	2.141	1	4	0
VW	45.85	1.979	1.968	1	3	1
F	48.45	1.879	1.880	0	4	1
MW	51.80	1.765	1.765	2	1	1
VF	52.55	1.741	1.736	1	4	1
M	54.43	1.686	1.684	2	2	1
W	55.50	1.656	1.655	2	4	0
F	56.75	1.622	1.623	0	6	0
W	58.83	1.570	1.571	2	3	1
MW	60.53	1.530	1.531	1	5	1
VW	62.75	1.481	1.481	0	0	2

W = Weak M = Medium S = Strong V = Very F = Faint

The refined orthorhombic lattice parameters are

a = 4.516(4)Å b = 9.745(6)Å c = 2.964(2)Å

Table 4.2

X-Ray Powder Pattern for γ-AlOOH

(Stoe Guinier Camera, CuK_{α} radiation)

Intensity	$2\vartheta/^{\circ}$	d(obs)/Å	d(calc)/Å	h	k	l
MS	14.50	6.109	6.102	0	2	0
S	28.26	3.157	3.154	0	2	1
F	29.51	3.027	3.051	0	4	0
MS	38.46	2.341	2.343	1	3	0
W	49.03	1.858	1.859	1	5	0
S	49.40	1.845	1.846	0	0	2
W	51.74	1.767	1.767	0	2	2
F	55.36	1.660	1.660	1	5	1
M	64.20	1.451	1.450	1	3	2
M	65.05	1.434	1.434	2	0	0
F	67.07	1.395	1.396	2	2	0
VF	67.77	1.383	1.382	1	7	1
W	72.08	1.310	1.310	1	5	2
W	72.35	1.306	1.306	2	2	1
W	85.76	1.133	1.132	2	0	2
W	87.66	1.113	1.113	2	2	2

The refined orthorhombic lattice parameters are

a = 2.868(1)Å b = 12.205(9)Å c = 3.693(2)Å

Thermogravimetric analyses were carried out on a micro-balance connected to a vacuum/gas line. The reactions used were (48)

$$H_xMoO_3 = MoO_{3-x/2} + \frac{x}{2} H_2O \text{ (in vacuo)}$$

$$MoO_{3-x/2} + \frac{x}{4} O_2 = MoO_3.$$

The dehydration is very slow and the method used was slow heating up to 400°C over a period of several hours, followed by several more hours at that temperature until a constant weight was reached. The largest weight changes are the dehydration and subsequent oxidation of the reduced oxide, and these were used to give the most accurate values for x.

The reducing power of samples was determined by the method of Choain and Marion (146), in which Mo(VI-x) reduces the tetrathiocyanoargentate (I) complex ion in alkaline solution to give a silver metal precipitate.

$$Mo(VI-x) + xAg(I) = Mo(VI) + xAg(0).$$

This method is particularly suitable for these compounds as they dissolve rapidly in the oxidising alkaline medium. Determinations by this method were carried out by Mr. Gascoigne of the Inorganic Chemistry laboratory. About 100 mg of sample were dissolved (in an O_2-free glove box) in a solution made by mixing A (40 g dm^{-3} AgSCN, 300 g dm^{-3} KSCN) and B (200 g dm^{-3} KOH, 20 g dm^{-3} KCN) in the ratio 2:1. The mixture was magnetically stirred for 45 minutes to coagulate the silver precipitate. The silver metal was recovered and dissolved in 6M nitric acid, where it was determined bytitration against 0.05M KSCN with ferric ammonium sulphate as indicator.

A sample of red monoclinic phase H_xMoO_3 was prepared by reduction of MoO_3 (A/R grade) with zinc and hydrochloric acid (49). The MoO_3 was mixed with hydrochloric acid (Analar)

and distilled water (50% by volume). Granulated zinc (A/R grade) was gradually added to the magnetically stirred reaction mixture and the temperature kept below 50°C. The MoO_3 eventually turned green, after passing through the colours appropriate to the lower hydrogen-content H_xMoO_3 phases. The product was washed several times with O_2-free distilled water under a nitrogen atmosphere. The green phase is known to decompose to the red by hydrogen evolution above 90°C (49). The red phase was prepared from the green by dehydrogenation at 110°C in vacuo for about 12 hours.

The X-ray powder pattern (given in table 4.3) confirmed the presence of a single phase, all lines being indexable in terms of a monoclinic unit cell, and is consistent with that obtained by Birtill (39). Two separate redox analyses gave $x = 1.70$, thermogravimetric dehydration gave $x = 1.74$ and oxidation of the reduced oxide gave $x = 1.71$. The composition of the red monoclinic phase was thus $H_{1.71}MoO_3$ ($x = 1.713 \pm 0.016$).

A sample of blue orthorhombic phase H_xMoO_3 was prepared from MoO_3, Mo metal and water. Glemser (49) reported this reaction to be,

$$Mo(s) + 11\ MoO_3(s) + 3H_2O(l) = 3Mo_4O_{10}(OH)_2(s) \quad (x = 0.5).$$

Molybdenum (A/R grade) and MoO_3 (A/R grade) powders were ground together in the stoichiometric proportions for the reaction above, and then mixed with distilled water (30% by volume) in a silica tube, which was then cooled in liquid nitrogen, evacuated and sealed. The tube was heated in an oven at 110°C for a month, with regular shaking. Three such preparations were attempted, only one giving a pure orthorhombic phase, the X-ray powder pattern of which is given in table 4.4. The pattern is consistent with those obtained by Kihlborg (50) and Birtill (39)

Table 4.3

X-Ray Powder Pattern for $H_{1.71}MoO_3$

(Debye-Scherrer Camera, CuK_α radiation)

Intensity	$2\vartheta/^\circ$	$d_{(obs)}/\text{Å}$	$d_{(calc)}/\text{Å}$	h	k	l
S	12.85	6.889	6.881	2	0	0
W	22.03	4.036	4.040	0	0	1
S	24.48	3.637	3.639	1	1	0
W	26.28	3.392	3.377	2	0	1
F	30.68	2.914	2.914	3	1	0
M	32.70	2.738	2.730	$\bar{1}$	1	1
F	33.33	2.689	2.678	1	1	1
W	35.50	2.529	2.529	4	0	1
W	37.30	2.411	2.418	$\bar{3}$	1	1
M	39.35	2.290	2.294	6	0	0
W	40.63	2.221	2.224	5	1	0
M	44.83	2.022	2.020	0	0	2
VF	45.33	2.001	2.000	$\bar{5}$	1	1
VF	47.05	1.931	1.935	6	0	1
F	47.70	1.907	1.901	2	0	2
M	48.23	1.887	1.887	0	2	0
F	50.18	1.818	1.820	2	2	0
VF	50.70	1.801	1.800	$\bar{4}$	0	2
F	51.30	1.781	1.781	$\bar{1}$	1	2
MW	52.15	1.754	1.752	1	1	2
MW	52.50	1.743	1.743	7	1	0
W	53.23	1.721	1.721	8	0	0
W	54.88	1.673	1.671	$\bar{2}$	2	1
W	55.80	1.647	1.647	2	2	1
W	56.60	1.627	1.627	3	1	2
W	58.63	1.575	1.575	$\bar{6}$	0	2

The refined monoclinic lattice parameters are

$a = 13.798(8)\text{Å}$ $b = 3.774(2)\text{Å}$ $c = 4.051(2)\text{Å}$

$= 94.202(1)^\circ$.

Table 4.4

X-Ray Powder Pattern for $H_{0.36}MoO_3$

(Debye-Scherrer Camera, CuK_α radiation)

Intensity	$2\vartheta/^\circ$	$d(obs)/\text{Å}$	$d(calc)/\text{Å}$	h	k	l
S	12.60	7.067	7.042	0	2	0
S	23.73	3.750	3.749	1	1	0
S	25.28	3.520	3.521	0	4	0
S	27.00	3.305	3.302	0	2	1
MW	29.83	2.996	3.000	1	3	0
MS	33.88	2.646	2.647	1	1	1
W	35.03	2.558	2.563	0	4	1
S	38.43	2.340	(2.347	1	3	1
			(2.338	0	6	0
MS	39.53	2.288	2.282	1	5	0
MW	45.73	1.988	1.988	0	6	1
M	46.73	1.944	1.947	2	0	0
M	48.80	1.867	1.869	0	0	2
VF	50.60	1.806	1.807	0	2	2
VF	51.20	1.789	1.787	1	7	0
VF	51.95	1.759	1.760	0	8	0
W	53.88	1.703	1.703	2	4	0
MS	54.85	1.674	(1.676	2	2	1
			(1.673	1	1	2
W	55.63	1.651	1.651	0	4	2
M	57.23	1.612	1.612	1	7	1
M	58.05	1.589	(1.593	0	8	1
			(1.586	1	3	2
W	59.60	1.546	1.550	2	4	1
MW	61.98	1.499	1.498	2	6	0
W	63.75	1.463	1.462	0	6	2
W	64.23	1.453	1.452	1	9	0
W	64.48	1.447	1.446	1	5	2
W	66.40	1.408	1.408	0	10	0
W	67.45	1.389	1.390	2	6	1
WM	69.93	1.347	1.348	2	0	2
W	73.25	1.292	(1.241	3	1	0
			(1.292	1	7	2
W	75.57	1.258	1.259	2	4	2

The refined orthorhombic lattice parameters are

$a = 3.891(1)\text{Å}$ $b = 14.084(4)\text{Å}$ $c = 3.738(1)\text{Å}$.

for this phase. The products were vacuum dried overnight.

Thermogravimetric dehydration of the pure blue orthorhombic sample gave x = 0.36 for the product. However analysis by reducing power gave x = 0.5, as would be expected from Glemser's reaction (49). Birtill (39) has suggested that this discrepancy, which is always observed with this preparative method, is due to the actual reaction being

$$\frac{x}{3} H_2O(l) + \frac{x}{6} Mo(s) + (1-\frac{x}{6}) MoO_3 = (1-\frac{x}{6}) H_yMoO_3(s) + \frac{x}{2} MoO_2(s)$$

where $y = 2x/(3-\frac{x}{2})$, and the MoO_2 formed is too amorphous and too small in quantity for detection by powder X-ray techniques. For a mixture made to give x = 0.5, the product would then be $H_{0.364}MoO_3$ and a small amount of MoO_2. This being the case, the proton magnetic relaxation behaviour will be characteristic of the pure phase $H_{0.36}MoO_3$.

4.3 β-aluminas.

Powder samples of ammonium β-alumina (NH_4^+ β-alumina) and hydroxonium β-alumina (H_3O^+ β-alumina) were supplied by Dr. P. McGeehin of the AERE Harwell, and characterised by the author.

NH_4^+ β-alumina was prepared by exchange in a large excess ($\sim 10^3$ times) of NH_4NO_3 melt at 190°C for 24 hours, followed by decantation of the melt and washing with water.

$$2NH_4NO_3 + Na_2O.xAl_2O_3 = (NH_4)_2O.xAl_2O_3 + 2NaNO_3.$$

Kummer (62) implies >98% exchange by this method, but recent work with single crystals (81) shows that this is not the case and more than one exchange may be necessary. The powder supplied had been prepared by a single exchange but was more likely to be

completely exchanged. Analysis for residual sodium by the AERE gave 0.42% by weight, corresponding to 92% exchange for a β-alumina with x = 8.

The powder X-ray pattern recorded for NH_4^+ β-alumina was indexed by the author as that of a pure β phase and is given in table 4.5. The refined hexagonal lattice parameters were a = 5.613(1)Å and c = 22.845(4)Å. Kummer (62) quotes a = 5.596Å and c = 22.888Å for this compound.

Fully hydrogen exchanged β-alumina (H^+ β-alumina) was prepared by first exchanging the sodium for silver and then reducing the product with hydrogen. Na^+ β-alumina was immersed in excess molten $AgNO_3$ at 220°C for 24 hours and then the melt was decanted and the product, Ag^+ β-alumina, washed with water.

$$2AgNO_3 + Na_2O.xAl_2O_3 = Ag_2O.xAl_2O_3 + 2NaNo_3.$$

This material was then reduced with hydrogen at 350°C. H^+ β-alumina absorbs water, on exposure to air, to give H_3O^+ β-alumina. The completion of this reaction was ensured when the sample/silver mixture was boiled in nitric acid to remove the silver.

The X-ray powder pattern for H_3O^+ β-alumina was of poorer quality than that for NH_4^+ β-alumina, the lines being more diffuse. This is a consequence of the reduction stage, silver diffusing into the grain boundaries and causing crumbling, and hence reduction in particle size. The X-ray powder patterns for β and β" phases differ very little (67), most of the lines coinciding. The pattern for a two phase mixture is thus difficult to interpret. All but 3 of the observed lines for the H_3O^+ β-alumina sample could be assigned to a β phase with a = 5.605(2)Å and c = 22.811(19)Å. The additional 3 lines show the presence of

Table 4.5

X-Ray Powder Pattern for NH_4^+ β-alumina

(Stoe Guinier Camera, CuK_α radiation)

Intensity	$2\vartheta/^\circ$	d(obs)/Å	d(calc)/Å	h	k	l
S	7.68	11.509	11.422	0	0	2
MS	15.53	5.707	5.711	0	0	4
W	18.70	4.745	4.754	0	1	1
MS	19.85	4.473	4.473	0	1	2
M	21.70	4.096	4.097	0	1	3
VF	24.00	3.708	3.702	0	1	4
VF	29.82	2.996	2.997	0	1	6
WM	31.32	2.856	2.856	0	0	8
MS	31.87	2.808	2.806	1	1	0
M	33.04	2.711	2.709	1	0	7
S	35.64	2.519	2.519	1	1	4
VW	36.46	2.464	2.462	0	1	8
VW	36.99	2.430	2.430	0	2	0
MS	37.19	2.418	2.417	0	2	1
M	37.84	2.378	2.377	0	2	2
W	38.91	2.314	2.315	0	2	3
W	39.41	2.286	2.284	0	0	10
M	39.89	2.260	2.259	1	1	6
W	40.01	2.253	2.250	1	0	9
W	40.34	2.236	2.236	0	2	4
M	42.11	2.146	2.146	0	2	5
W	43.76	2.069	2.068	0	1	10
MS	44.21	2.049	2.049	0	2	6
MS	46.58	1.950	1.944	0	2	7
M	49.23	1.851	1.851	0	2	8
VF	49.63	1.837	1.837	1	2	0
F	49.83	1.830	1.831	1	2	1
VF	51.13	1.787	1.786	2	1	3
F	51.61	1.771	1.773	0	1	12
			1.772	1	1	10
VF	52.06	1.757	1.755	0	2	9
VF	52.33	1.748	1.749	1	2	4
W	55.18	1.665	1.665	0	2	10
W	55.60	1.653	1.655	1	2	6
			1.653	0	1	13
W	56.35	1.633	1.632	0	0	14
W	56.83	1.620	1.620	3	0	0
MS	57.55	1.601	1.601	1	2	7
M	58.45	1.579	1.579	0	2	11
MW	59.28	1.559	1.559	0	3	4
W	59.85	1.545	1.547	0	1	14
			1.545	1	2	8

Table 4.5 (cont'd)

Intensity	$2\vartheta/^{\circ}$	$d(obs)/\mathring{A}$	$d(calc)/\mathring{A}$	h	k	l
MW	62.30	1.490	1.491	0	3	6
			1.488	1	2	9
W	65.15	1.432	1.432	1	2	10
M	65.55	1.424	1.424	0	2	13
S	66.65	1.403	1.401	2	2	0
WM	67.22	1.393	1.393	2	2	2
WM	68.92	1.363	1.362	2	2	4
M	69.37	1.355	1.355	0	2	14

The refined hexagonal lattice parameters are

$a = 5.613(1)\mathring{A}$ $b = 22.845(4)\mathring{A}$.

some β'' phase, the lines being the strongest 3 non-coincident with those of a β phase. The comparative weakness of these lines suggests that material is predominantly β phase. This interpretation of the powder pattern is given in table 4.6. Saalfeld (147) gives a = 5.600 (1) Å and c = 22.702 (1) Å for a β-phase single crystal.

Two forms of hydroxonium β-alumina exist over the temperature range 20-550°C (155). These may be represented as $n_A H_2O.11Al_2O_3$ (for the low temperature form) and $n_B H_2O.11Al_2O_3$. The low temperature form has a stoichiometry corresponding to replacement of every Na^+ ion in Na^+ β-alumina by an H_3O^+ ion and is designated H_3O^+ β-alumina. The high temperature form contains one water molecule for every two protons in the conducting plane and is termed H^+- H_3O^+ β-alumina. Above about 700°C dehydration is complete and α-Al_2O_3 is obtained on prolonged heating.

$$n_A H_2O.11Al_2O_3 \underset{200\text{-}300^\circ C}{\rightleftharpoons} n_B H_2O.11Al_2O_3 \xrightarrow[>700^\circ C]{} \alpha\text{-}Al_2O_3 + H_2O$$

Ammonium β-alumina is transformed on heating in air above 500°C into a stoichiometric H_3O^+ β-alumina (156), the necessary oxygen atoms coming from the environment (atmosphere, absorbed water, interstitial oxygens). This phase decomposes completely above 850°C and prolonged heating gives α-Al_2O_3.

$$(NH_4)_2O.x\ Al_2O_3 \xrightarrow[>500^\circ C]{} 3H_2O.11Al_2O_3 \xrightarrow[>850^\circ C]{} \alpha\text{-}Al_2O_3$$

Thermal decomposition (by heating to 1000°C on a micro-balance) of two samples of H_3O^+ β-alumina gave weight losses of 7.69% and 7.91%. This corresponds to $(H_3O)_2O.x\ Al_2O_3$ with $x = 6.24 \pm 0.11$. Similarly samples of NH_4^+ β-alumina gave weight losses of 6.01% and 6.28% corresponding to $(NH_4)_2O.xAl_2O_3$ with $x = 8.09 \pm 0.19$. The X-ray powder patterns of the

Table 4.6

X-Ray Powder Pattern for H_3O^+ β-alumina

(Stoe Guinier Camera, CuK_α radiation)

Lines assignable to β-phase.

Intensity	$2\vartheta/^\circ$	d(obs)/Å	d(calc)/Å	h	k	l
S	7.721	11.451	11.405	0	0	2
MS	15.50	5.717	5.703	0	0	4
M	31.91	2.805	2.803	1	1	0
MW	33.13	2.704	2.706	0	1	7
MS	35.67	2.517	2.515	1	1	4
MW	37.14	2.421	2.427	0	2	0
W	37.89	2.375	2.374	0	2	2
F	38.94	2.313	2.312	0	2	3
W	39.39	2.288	2.281	0	0	10
MW	39.91	2.259	2.256	1	1	6
W	42.18	2.142	1.143	0	2	5
W	44.27	2.046	2.046	0	2	6
VW	46.69	1.945	1.947	0	2	7
F	49.31	1.848	1.848	0	2	8
VW	56.86	1.619	1.618	0	3	0
F	57.21	1.610	1.614	0	3	1
W	57.69	1.598	1.599	1	2	7
VW	58.21	1.585	1.583	0	3	3
W	59.33	1.558	1.557	0	3	4
VW	62.32	1.490	1.489	0	3	6
VW	65.71	1.421	1.422	0	2	13

The refined hexagonal lattice parameters are

a = 5.605(2)Å c = 22.811(19)Å

Lines assignable to β″-phase.

Intensity	$2\vartheta/^\circ$	d(obs)/Å	d(calc)/Å	h	k	l
W	34.10	2.629	2.630	0	1	11
W	38.56	2.335	2.335	0	2	4
M	45.74	1.983	1.983	0	2	10

The refined hexagonal lattice parameters are

a = 5.603(2)Å c = 34.423(23)Å.

decomposition products of H_3O^+ and NH_4^+ β-aluminas were identical. The pattern was that of α-alumina (148) with a few non-assignable lines at low angle. This confirmed the absence of Na^+ β-alumina, stable at the decomposition temperature, for both materials and also the absence of Ag^+ β-alumina or Ag metal in the H_3O^+ β-alumina.

Chapter 5

Results of nmr Studies

Tables referred to in this Chapter can be found in Appendix 1.

5.1 Oxide hydroxides.

Broad-line absorption spectra of gallium oxide hydroxide (GaOOH) in the temperature range -100°C to +150°C were recorded on the continuous-wave Jeol instrument in Oxford (see Chapter 3). The instrument was calibrated with a sample of finely ground vacuum-dried ammonium chloride (NH_4Cl) by comparing the line-width obtained with the literature value (125) of 4.8G at room temperature.

The spectra at temperatures below -60°C differed from those at higher temperatures, the latter showing a narrow central peak superimposed on the low temperature broad signal. The narrow peak diminished in intensity with reduction in temperature. The linewidth for the broad signal was constant over the entire temperature range, its value being 8.16 $\pm$ 0.43G. A value of 8.3 $\pm$ 0.9G^2 was calculated for M_2 from the low temperature spectra. Recorded spectra at three different temperatures are shown in figure 5.1.

Additional room temperature continuous-wave broad-line spectra were run for the author by Bruker-Physik AG on an instrument operating at 30 MHz. The linewidth for NH_4Cl was 4.6G. The GaOOH spectrum was similar to that observed in Oxford, with ΔB = 8.08G and M_2 (for the line less central peak) equal to 7.7G^2. The spectrum of boehmite (γ-AlOOH) is shown in figure 5.2. The width of the wide line is 10.9G and M_2

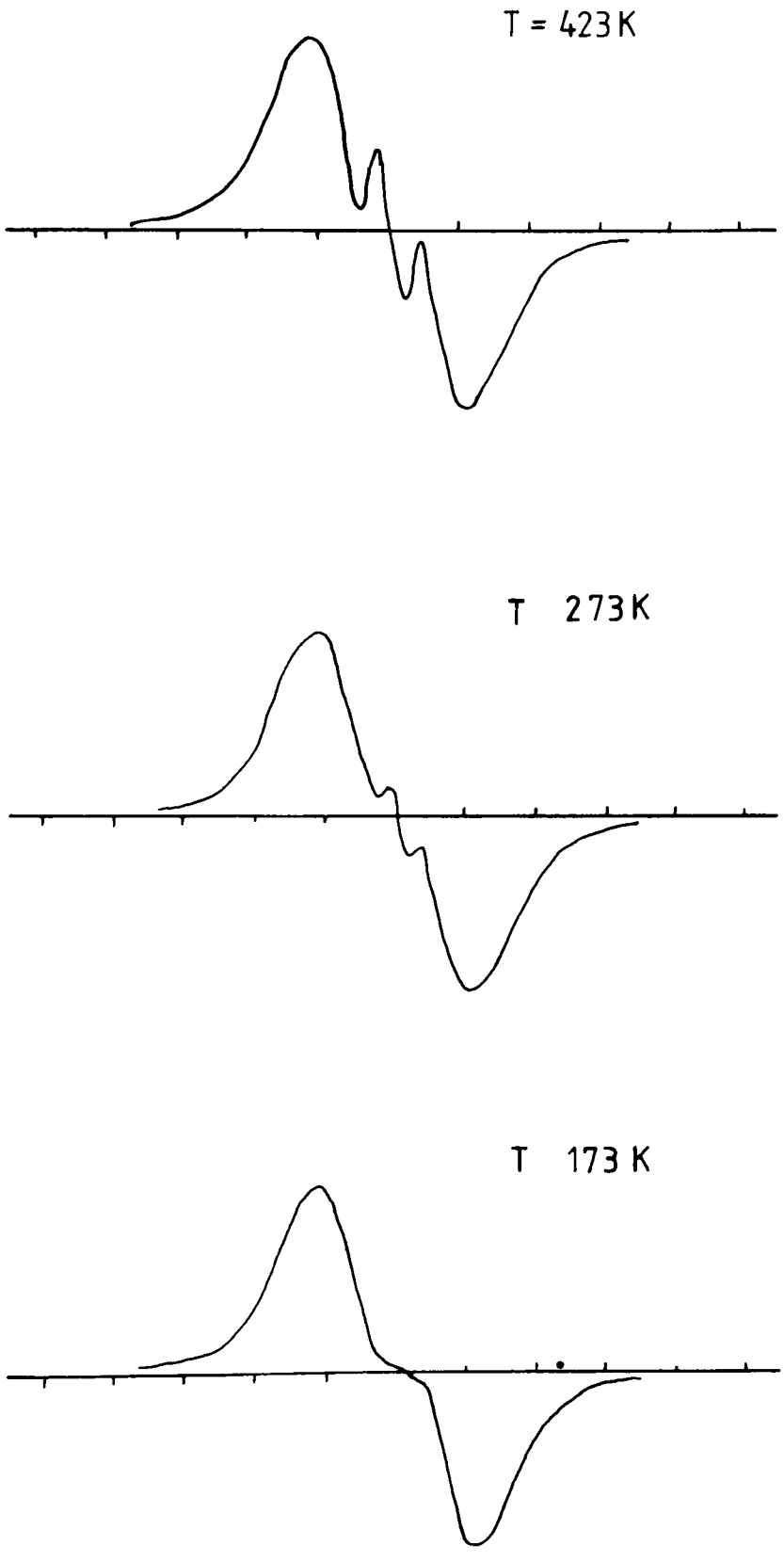

CW Spectra for GaOOH
(Scale 4G cm^{-1})

Figure 5.1

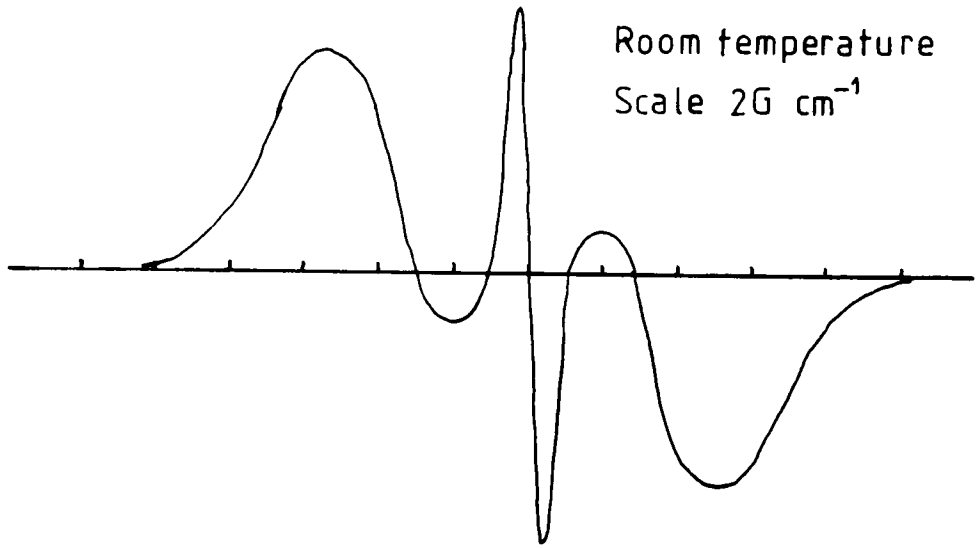

Figure 5.2 CW(derivative) spectrum for γ-AlOOH

(for the line less the central peak) is 17.5G[2].

A Fourier transform spectrometer was also used to produce absorption spectra. The instrument used was a Bruker CXP at the applications laboratory of Bruker-Physik AG at Karlsruhe, as discussed in Chapter 3. In Fourier transformation it is important that the time zero be correct if a true absorption spectrum is to be obtained by Fourier transformation of an FID. The initial part of the FID is lost in the instrument dead-time and the time zero has to be placed at the end of this. In work on liquids a negligible part of the total decay is lost and Fourier transformation is widely used. In work on solids, the dead-time (4 μs for the CXP) is an appreciable part of the total decay (10-40 μs) and the distortion of spectra obtained by Fourier transformation will therefore be greater. Use of the solid echo technique (114) to give a time zero outside the dead-time is attractive, but the echo decay has only been shown to be equivalent to the FID in a simple case (see section 2.7).

Fourier transformation of the off-resonance FID (with time zero at the end of the dead-time) for NH_4Cl gave, at room temperature, an approximately Gaussian lineshape with $\Delta B_{\frac{1}{2}} = 2.89G$. Assuming an accurately Gaussian lineshape, this corresponds to $\Delta B = 4.90G$, in fair agreement with continuous-wave results. The corresponding room temperature spectra for GaOOH and γ-AlOOH are shown in figure 5.3. For GaOOH the apparent separation of the two peaks of the poorly resolved doublet was 4.79G and for γ-AlOOH the doublet separation was 8.22G. The integrated intensities of the central spikes correspond to less than 1% of the total absorption signal. Spectra recorded at

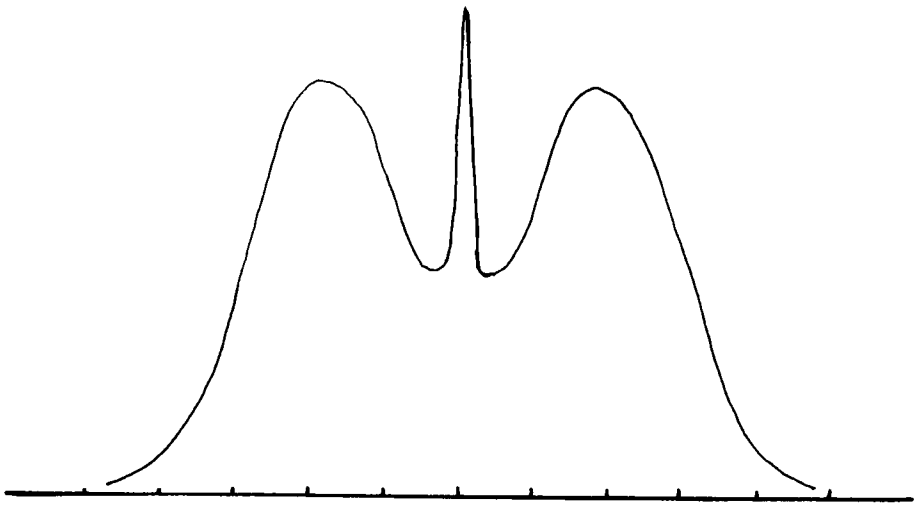

γ-AlOOH
(scale 2G cm^{-1})

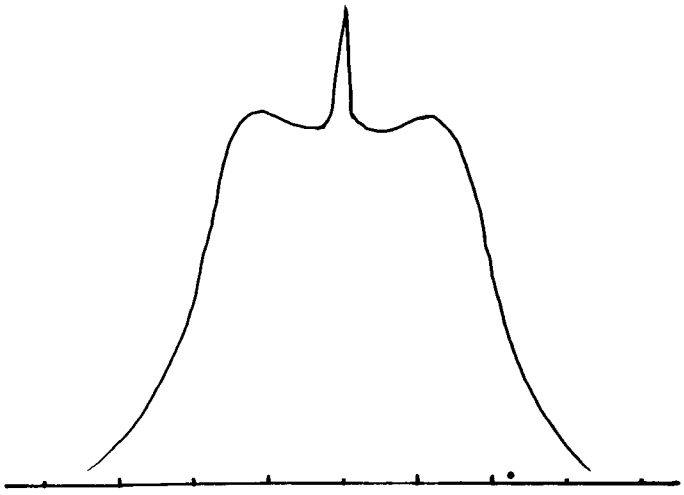

GaOOH
(scale 2G cm^{-1})

Absorption spectra (FT) at room temperature

Figure 5.3

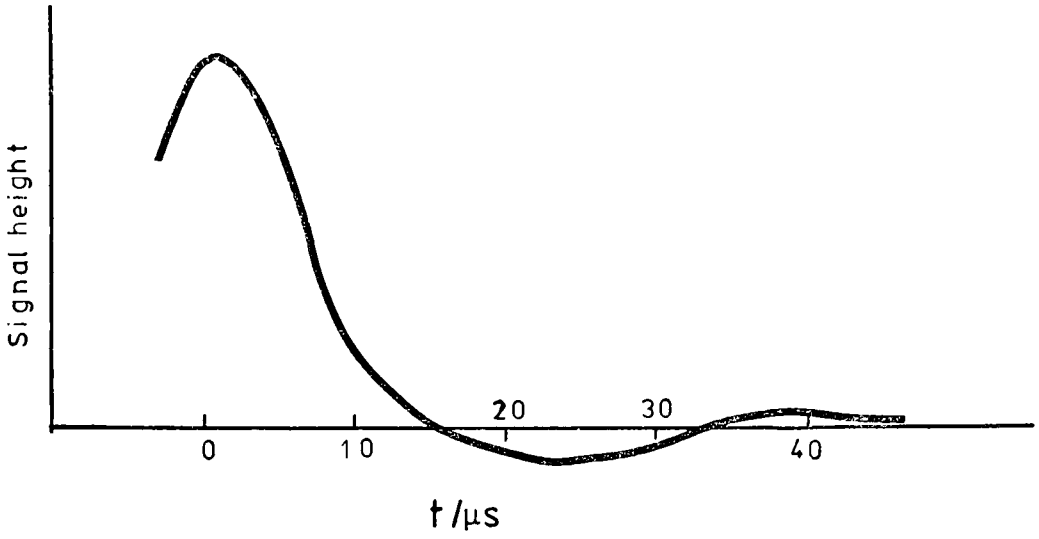

(a) γ-AlOOH

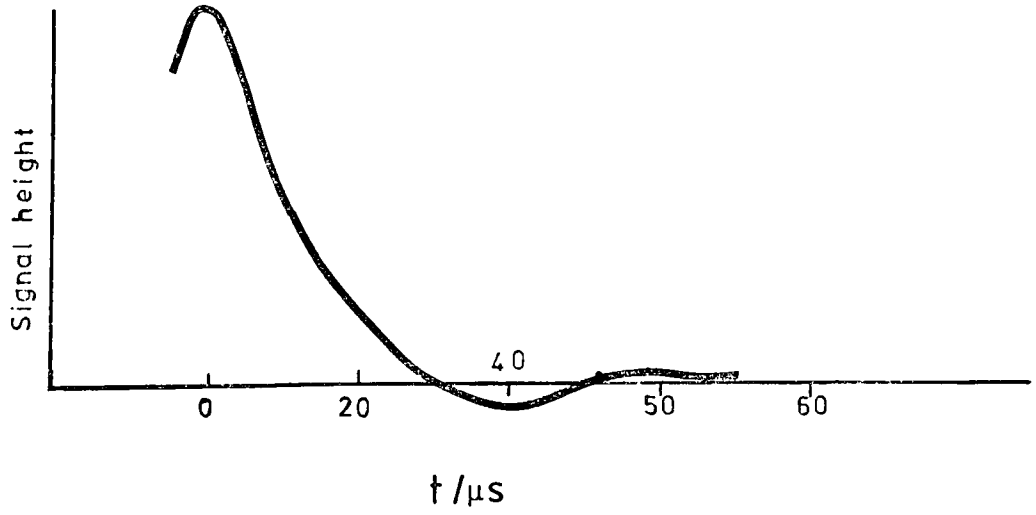

(b) GaOOH

Figure 5.4 Some solid echoes

120K showed no central spike. M_2 values calculated from these lineshapes were $11.6G^2$ and $21.1G^2$ for GaOOH and γ-AlOOH respectively. These values are larger than the true values (measured on CW instruments) as a result of the distortions discussed above. However, use of transformation to obtain M_2 values is not necessary as they are available from solid echo experiments (see section 2.7). The shapes of the absorption spectra are essentially correct, except that for GaOOH there was no evidence in the CW spectrum of the poorly resolved doublet.

Parallel experiments to those above were carried out using solid echoes for transformation (with time zero at the echo maximum). The spectrum of NH_4Cl was as before, as was that for γ-AlOOH with peak separation now 7.93G. The spectrum of GaOOH was similar in width to that obtained from the FID, but the shallow dip giving the apparent doublet structure had flattened to give shoulders around the central spike, which is consistent with the CW spectra. The solid echo transformation does, therefore, appear to give a truer lineshape.

On resonance room temperature solid echoes for GaOOH and γ-AlOOH were recorded by the author on the Polaron at York and on the CXP at Karlsruhe. The decays were similar on both instruments and are illustrated in figure 5.4. T_2 (defined as in section 2.8) was 15 μs and 9.3 μs for GaOOH and γ-AlOOH respectively. Fitting the top of the echo (as discussed in section 3.6) gave M_2 values of $8.1G^2$ for GaOOH and $18.1G^2$ for γ-AlOOH, in close agreement with the CW results.

5.2 Hydrogen molybdenum bronzes.

Measurements of the relaxation times T_2, T_1 and $T_{1\rho}$ were carried out on the compounds $H_{0.36}MoO_3$ and $H_{1.71}MoO_3$ using the Polaron instrument at York, as discussed in Chapter 3.

The signal to noise ratio for observed decays for the compound $H_{0.36}MoO_3$ was very poor and averaging was necessary to see any decay at all. Spin-spin relaxation was exponential in the line-narrowing region. The solid echo decay shape at lower temperatures is shown in figure 5.5. T_1 was measured by the progressive saturation method. Spin-lattice relaxation was non-exponential both for T_1 and $T_{1\rho}$ measurements, and the decays were analysed to give the time to decay to 1/e of the initial signal height and a least squares fit to two exponentials, as discussed in section 3.6. Tables 5.1-5.5 summarise the relaxation data for this compound.

The results of measurements on $H_{1.71}MoO_3$ are given in tables 5.6-5.9. Spin-spin relaxation was exponential in the line-narrowing region and figure 5.6 illustrates the solid echo decay shape at lower temperatures. T_1 was measured by the $90^\circ-\tau-90^\circ$ method, checks by the progressive saturation method giving similar results. At temperatures below 160K, spin-lattice relaxation was non-exponential and was analysed as for $H_{0.36}MoO_3$.

Figures 5.7-5.10 illustrate the data in tables 5.1-5.9 and are preceded by an explanatory key.

Room temperature measurements on $H_{0.36}MoO_3$ using the Jeol CW instrument gave a linewidth, ΔB, for the asymmetric line observed, of 0.4G. The signal to noise ratio for these measurements was very poor. Attempts to record spectra at lower temperatures were unsuccessful due to the signal disappearing under instrument noise.

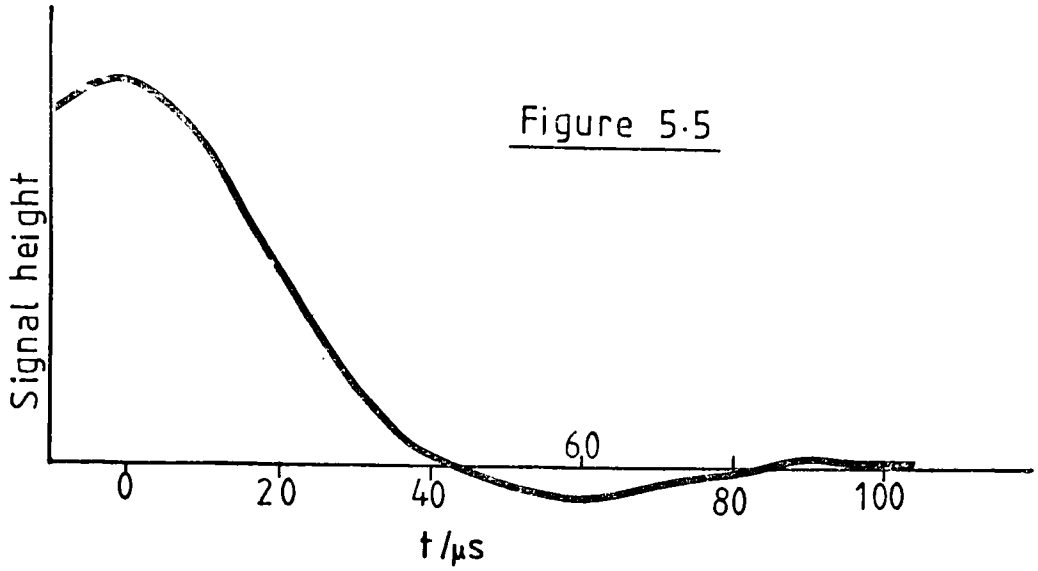

Figure 5·5

$H_{0.36}MoO_3$

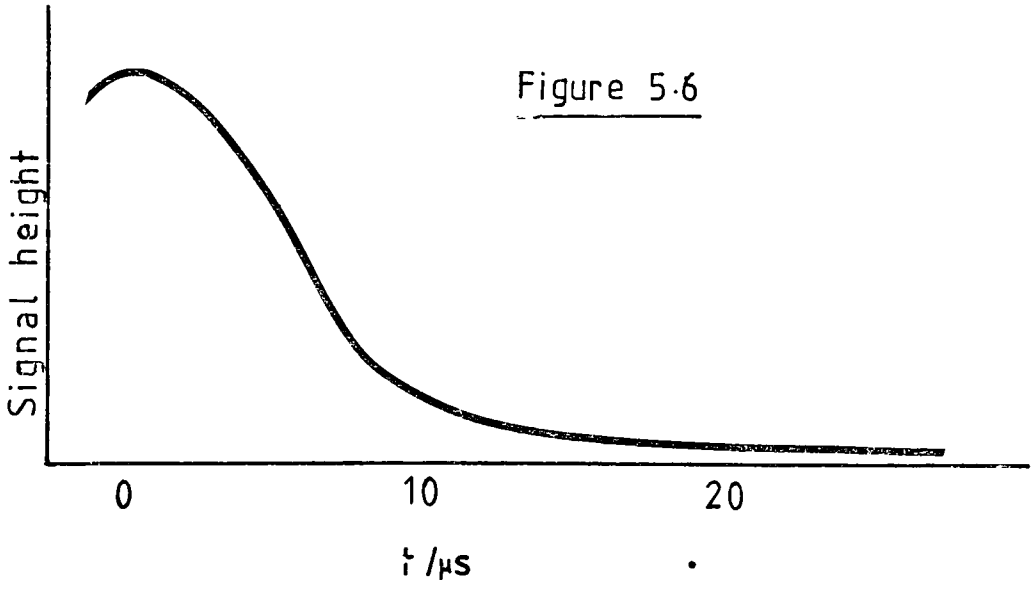

Figure 5·6

$H_{1.71}MoO_3$

Some solid echoes

Key to Figures 5.7-5.10

Figure 5.7 Relaxation times for $H_{1.71}MoO_3$ over a range of temperature. (Data from tables 5.6,5.7,5.9)

Figure 5.8 Relaxation times for $H_{1.71}MoO_3$ over a range of temperature. (Data from tables 5.6-5.9) Non-exponential spin-lattice relaxation is fitted by two exponentials.

Figure 5.9 Relaxation times for $H_{0.36}MoO_3$ over a range of temperature. (Data from tables 5.1,5.2,5.4)

Figure 5.10 Relaxation times for $H_{0.36}MoO_3$ over a range of temperature. (Data from tables 5.1,5.3) Non-exponential spin-lattice relaxation is fitted by two exponentials.

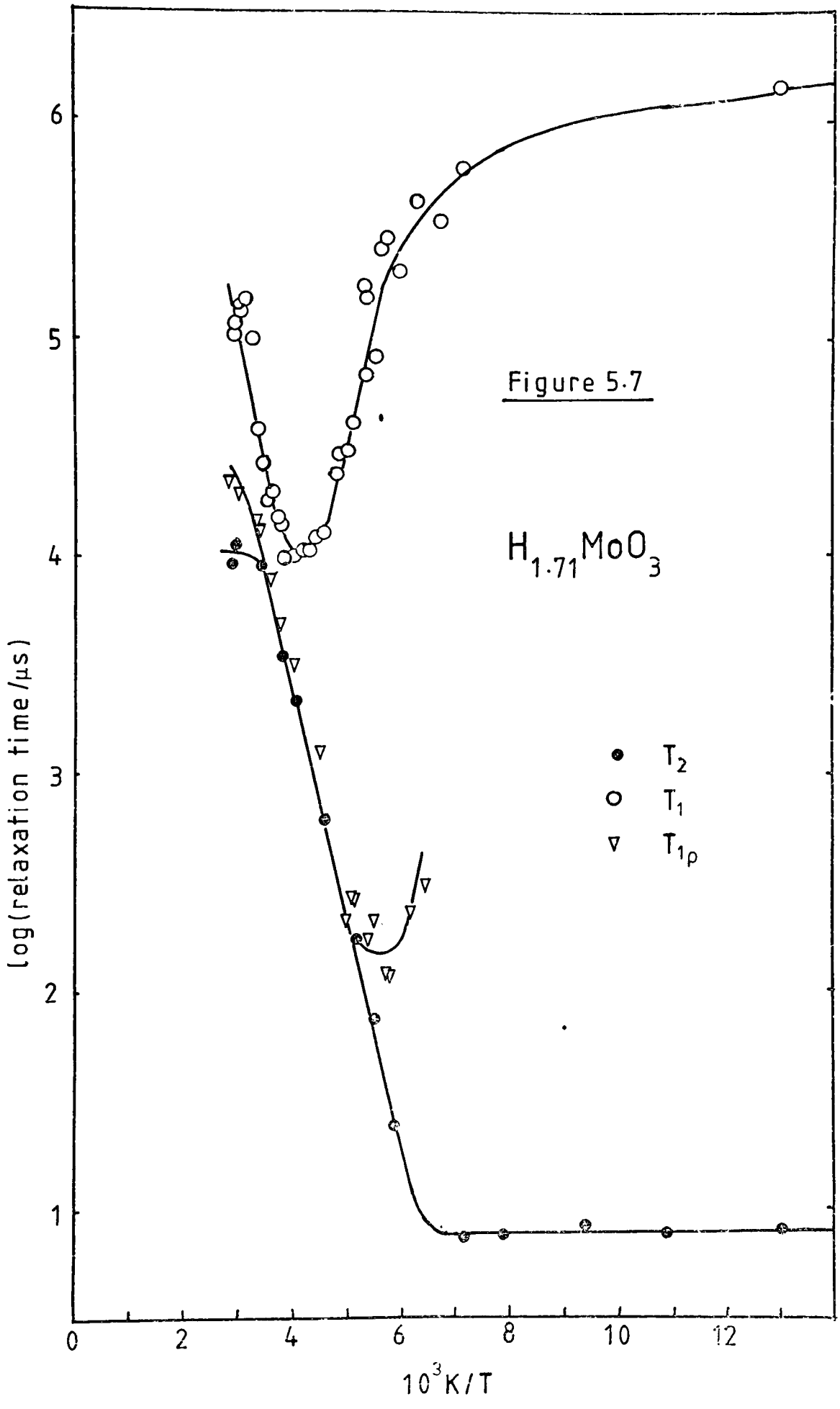
Figure 5.7
$H_{1.71}MoO_3$
T_2
T_1
$T_{1\rho}$
log(relaxation time/μs)
$10^3 K/T$
0
2
4
6
8
10
12
1
2
3
4
5
6

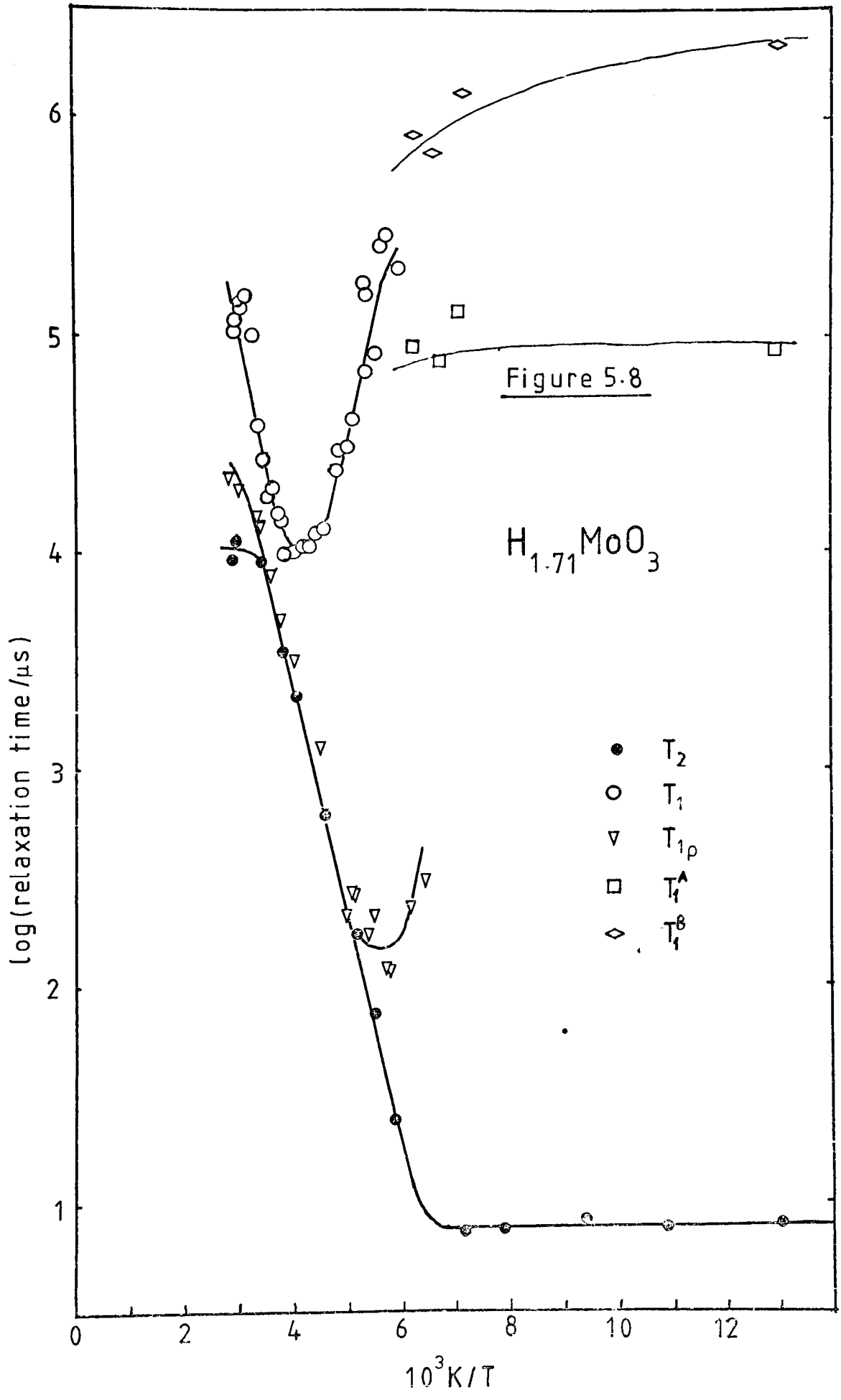
Figure 5.8
$H_{1.71}MoO_3$
T_2
T_1
$T_{1\rho}$
T_1^A
T_1^B
log(relaxation time/μs)
$10^3 K/T$
0
2
4
6
8
10
12
1
2
3
4
5
6

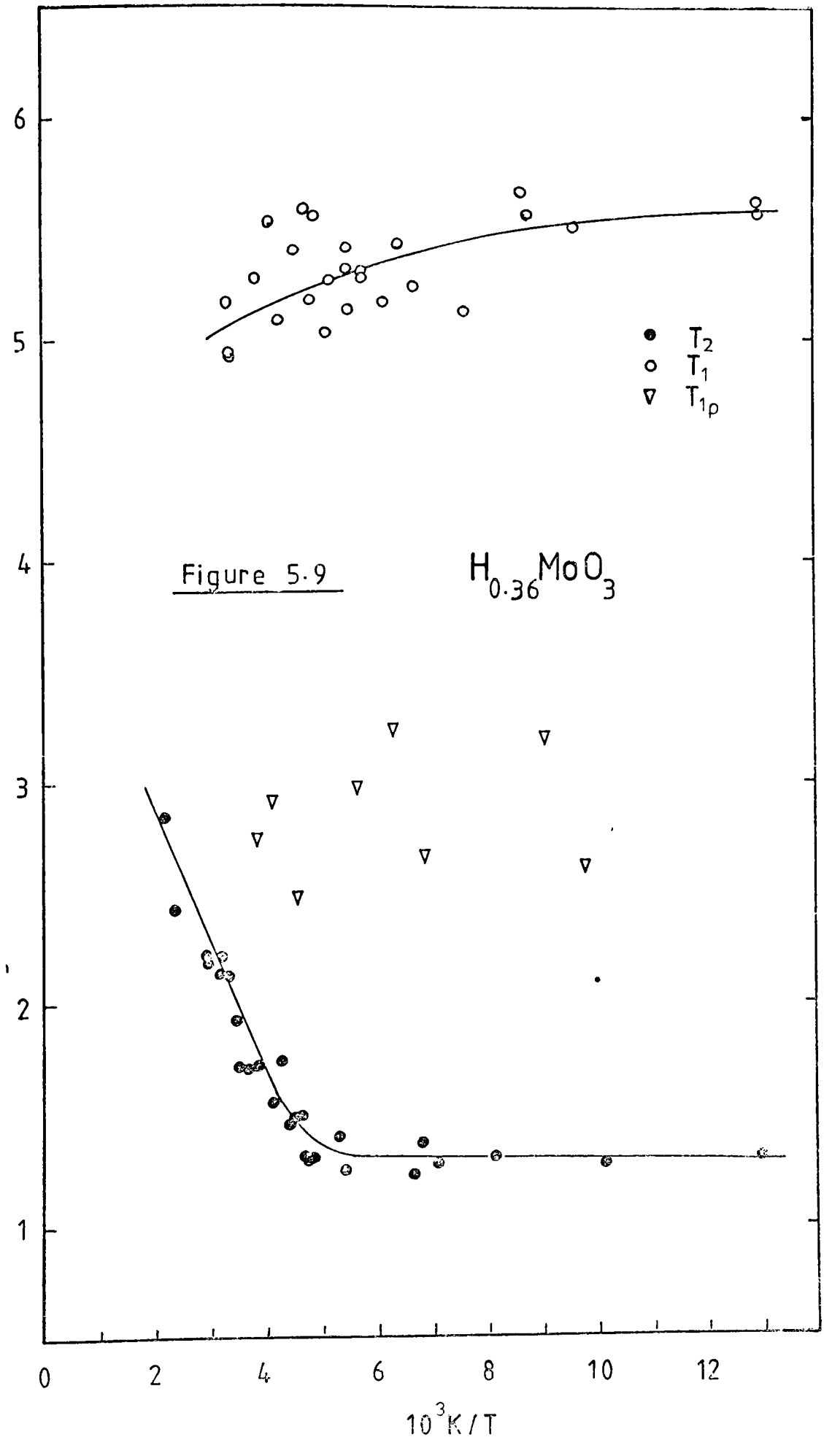

Figure 5.9

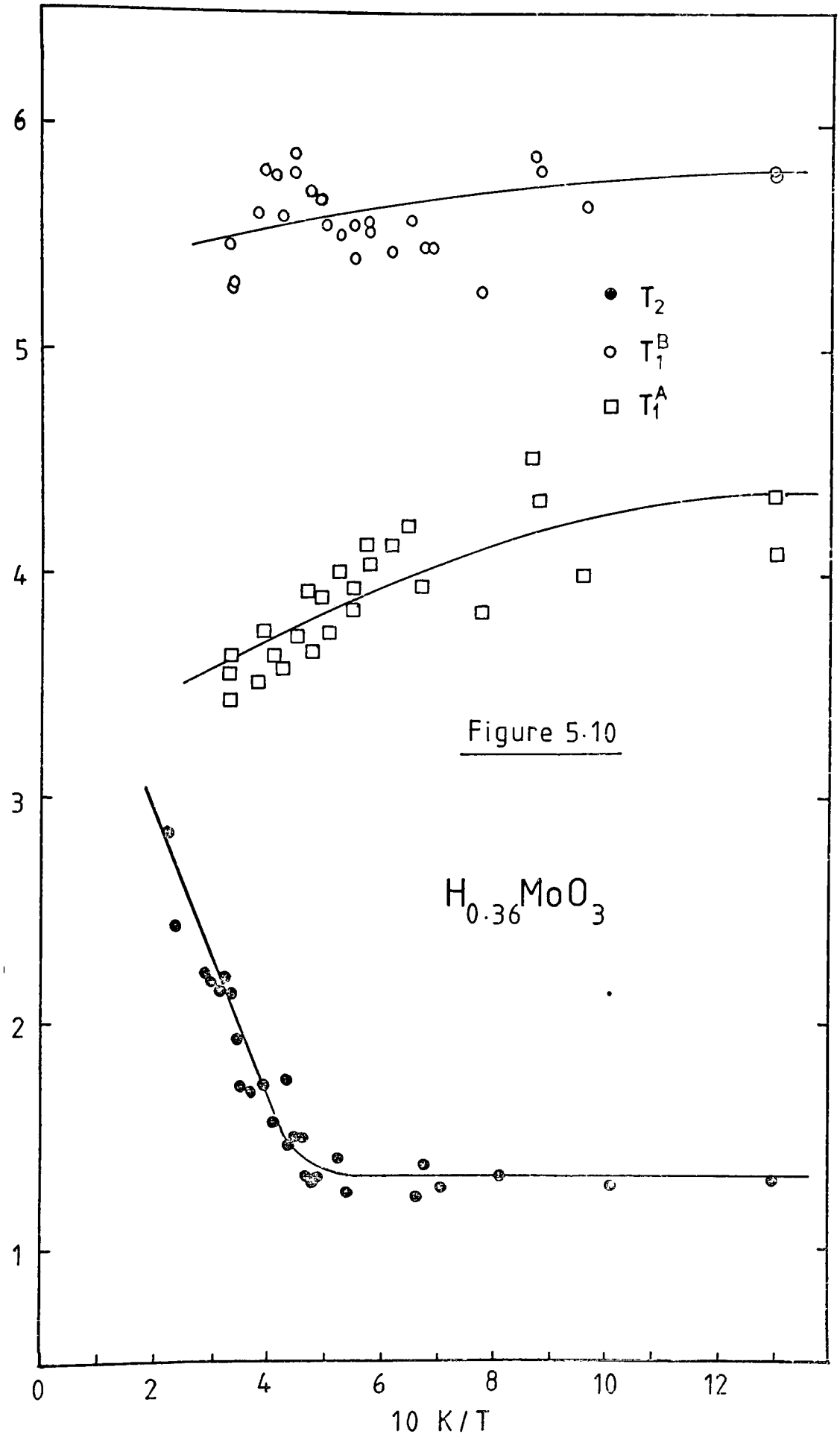

Figure 5·10

Further CW spectra on compounds $H_{0.34}MoO_3$ and $H_{1.68}MoO_3$ (prepared by J.J. Birtill (39)) were run at 100K and 15 MHz by B.G. Silbernagel of Exxon Research and Engineering Co., Linden, New Jersey. Typical derivative and integral spectra are given in figures 5.11 and 5.12. The signal to noise ratio is again very poor but it is possible to estimate M_2 values (corrected for modulation broadening) of $5G^2$ and $25G^2$ for $H_{0.34}MoO_3$ and $H_{1.68}MoO_3$ respectively. The smallest modulation width used was 0.63G. The derivative signals for both compounds show two components, a narrow signal and a broader one. For $H_{0.34}MoO_3$ the linewidth for the wider component is 6.8G and for $H_{1.68}MoO_3$ it is 10.8G.

Absorption spectra produced by Fourier transformation of the FID's (time zero at the end of the dead-time), using the Bruker CXP at 90MHz, are shown in figures 5.13 and 5.14. The room temperature lineshape for $H_{0.36}MoO_3$ is asymmetric, as observed on the Jeol instrument. The low temperature lineshape is similar to the CW spectrum, the structure being smoothed out by modulation in the latter case. The separation of the two smaller peaks is 4.1G. The room temperature lineshape for $H_{1.71}MoO_3$ is extremely narrow with shape characteristic of an axially symmetric chemical shielding tensor (95). The FID in this case is so long that distortions; due to loss of signal in the dead-time, are negligible. The low temperature lineshape for $H_{1.71}MoO_3$ is similar to that for $H_{0.36}MoO_3$ but considerably wider, the peak separation for the side peaks being about 11G. The lack of structure in the CW spectra is again presumably due to noise and modulation effects.

Second moment (M_2) values were estimated from the low

Figure 5·11

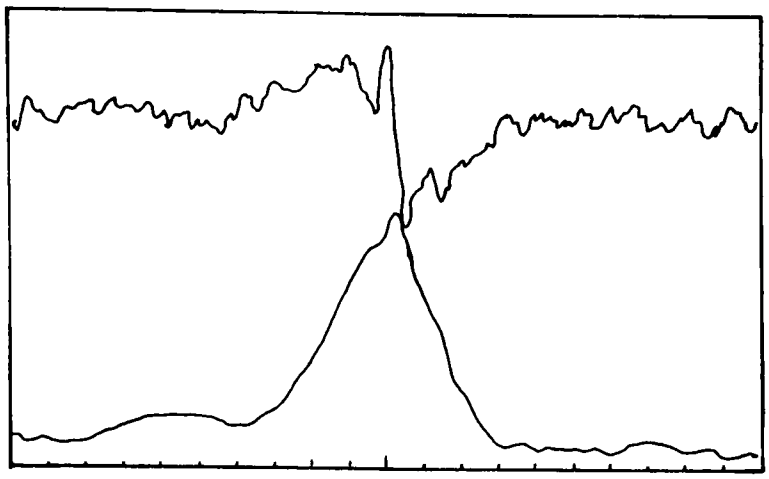

$H_{0.34}MoO_3$

Figure 5·12

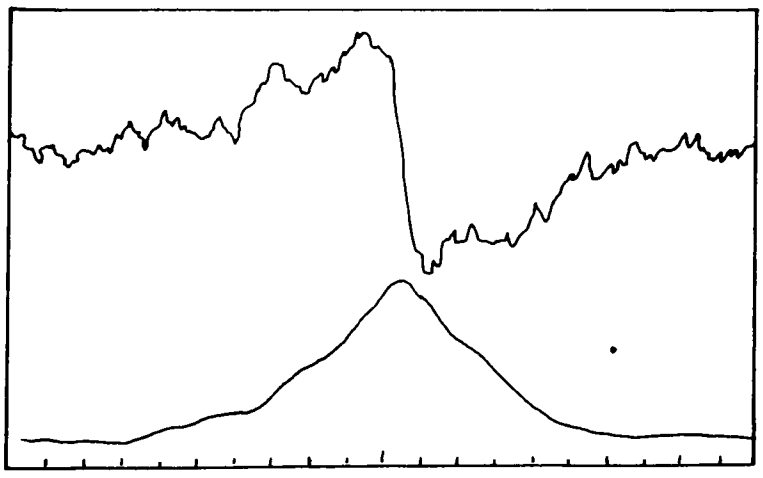

$H_{1.68}MoO_3$

CW Spectra (mod width = 0·63G)

(T = 100 K)

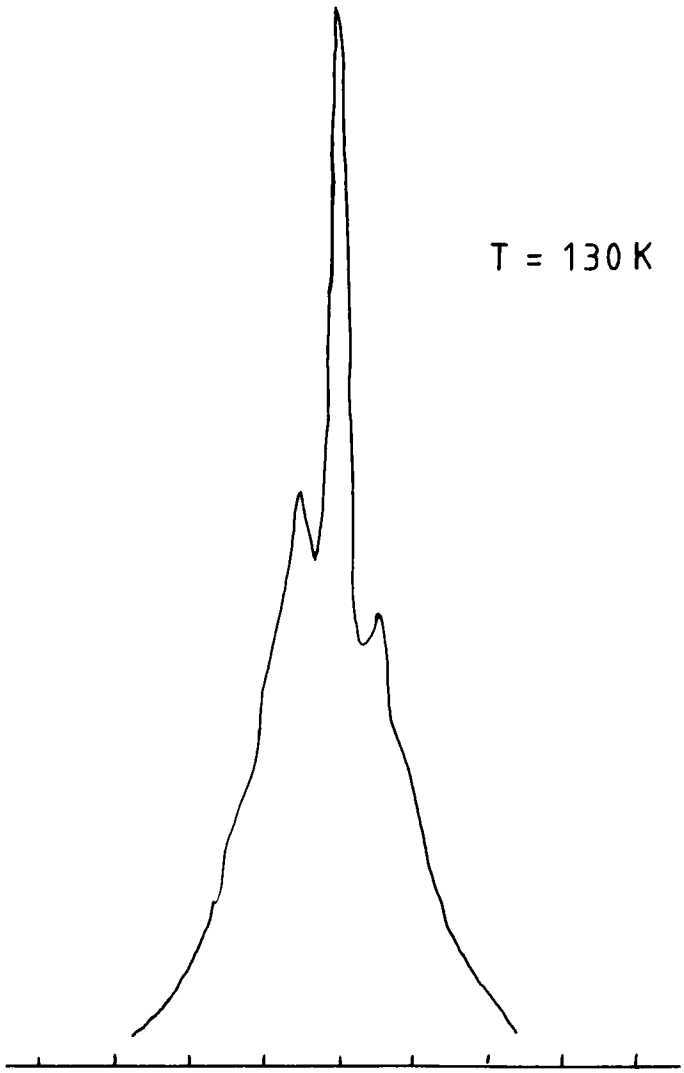

FT absorption spectrum for $H_{0.36}MoO_3$

Figure 5.13

Figure 5.14

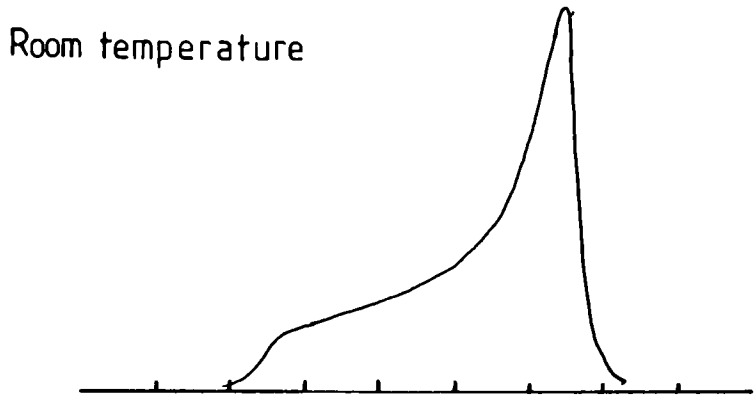

(scale 0·5 kHz cm^{-1})

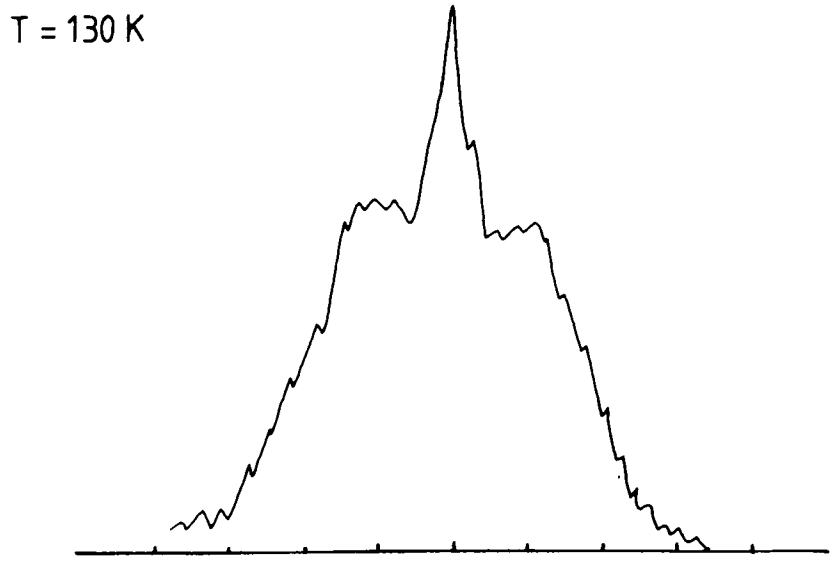

(scale 4 G cm^{-1})

FT absorption spectra for $H_{1.71}MoO_3$

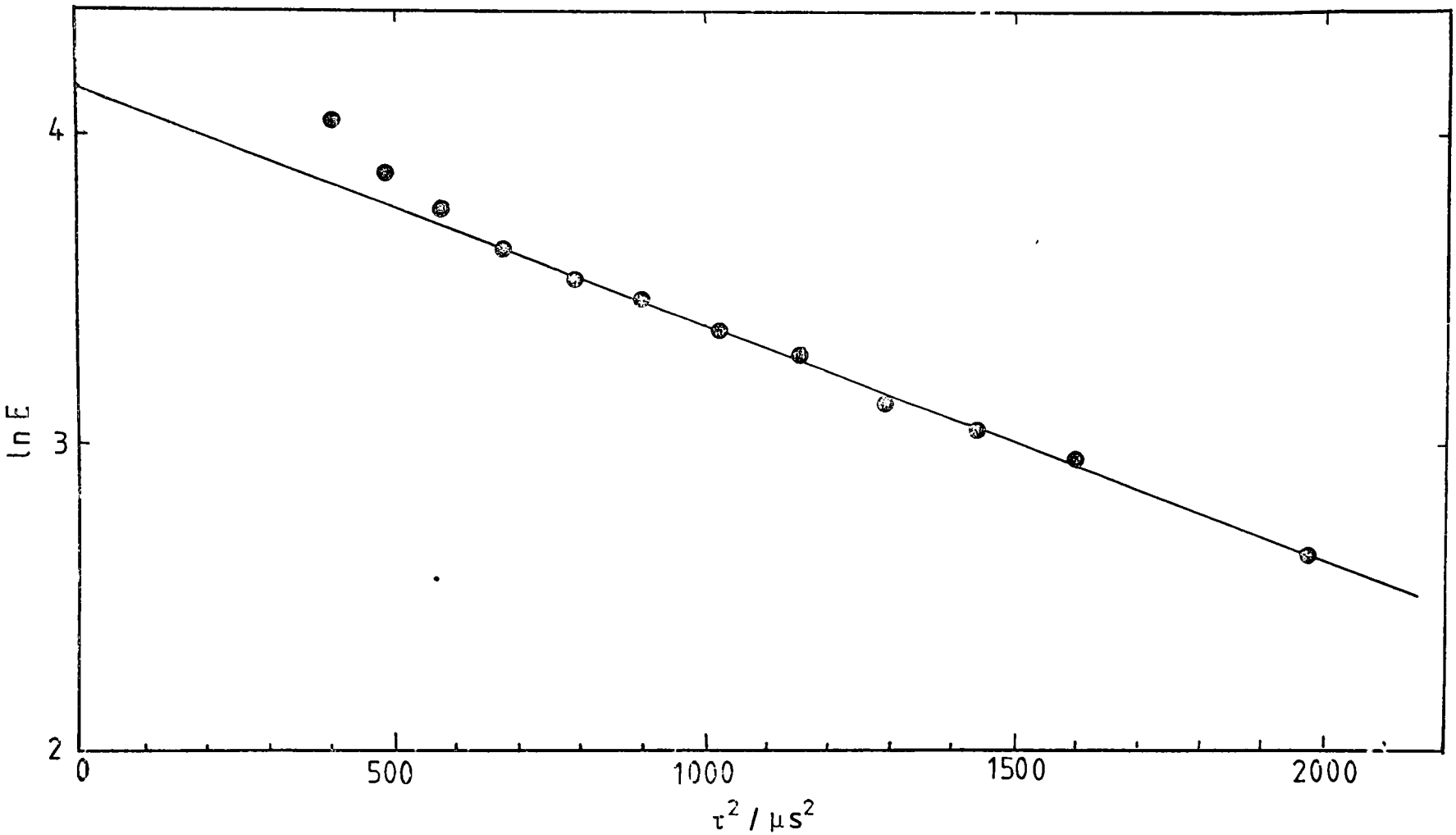

Figure 5.15 Solid echo amplitude for $H_{1.71}MoO_3$

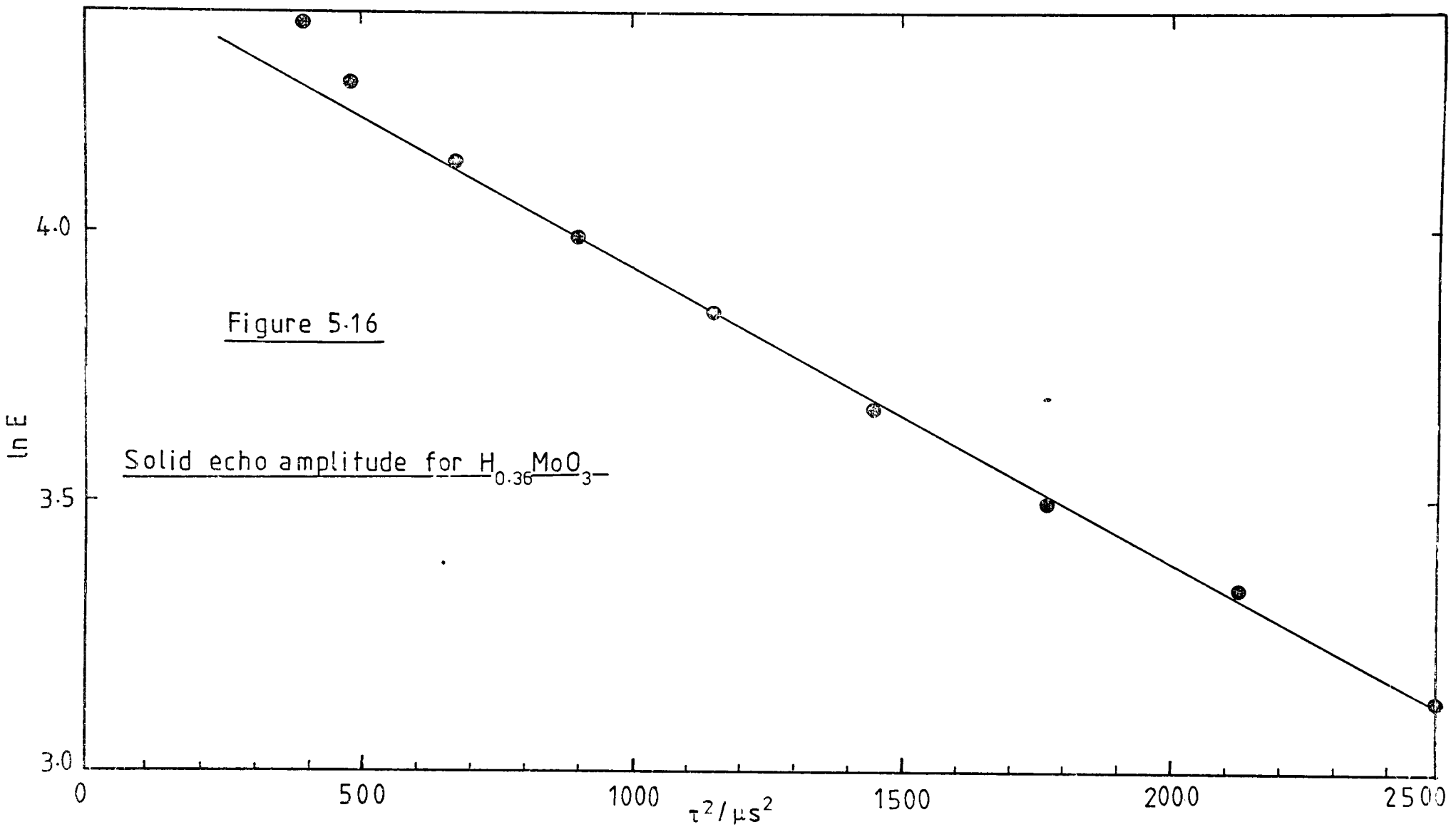

Figure 5·16

Solid echo amplitude for $H_{0.36}MoO_3$

temperature solid echoes (as discussed in section 3.6). For $H_{0.36}MoO_3$, M_2 had the value $5.7G^2$ and for $H_{1.71}MoO_3$ M_2 had the value $23G^2$. These are in close agreement with the CW estimates of Silbernagel.

The decay of the solid echo decay height, $E(\tau)$, as a function of pulse separation τ (see section 2.7) was followed for these compounds. The results are given in figures 5.15 and 5.16. The behaviour for both compounds is approximately Gaussian with values of M_2^{VV}(inter) of $1.71\pm.03\,G^2$ and $2.44\pm.06\,G^2$ obtained by least squares fitting for $H_{0.36}MoO_3$ and $H_{1.71}MoO_3$ respectively.

5.3 β-aluminas.

Measurements of T_1, T_2 and $T_{1\rho}$ for the materials NH_4^+ β-alumina and H_3O^+ β-alumina were made using the Polaron instrument at York. Some T_1 measurements on NH_4^+ β-alumina were carried out by Miss P. Fridd as part of her third-year undergraduate project at York. Confirmatory measurements were made by the author. T_1 measurements by the 90°-τ-90° and progressive saturation methods gave similar results.

NH_4^+ β-alumina showed exponential spin-spin relaxation in the line-narrowing region. Below 250K spin-lattice relaxation was non-exponential, data then being analysed both in terms of the time for decay to 1/e of the initial signal height and also in terms of two exponentials (as discussed in section 3.6). The results are summarised in tables 5.10-5.14.

The H_3O^+ β-alumina decays had a much poorer signal to noise ratio. T_2 behaviour in the line-narrowing region was exponential, but spin-lattice relaxation appeared non-exponential

Key to Figures 5.17-5.20

Figure 5.17 Relaxation times for NH_4^+ β-alumina over a range of temperature. (Data from tables 5.10,5.11,5.14).

Figure 5.18 Relaxation times for NH_4^+ β-alumina over a range of temperature. (Data from tables 5.10,5.12). Non-exponential spin-lattice relaxation is fitted by two exponentials.

Figure 5.19 Relaxation times for H_3O^+ β-alumina over a range of temperature. (Data from tables 5.15,5.16,5.18)

Figure 5.20 Relaxation times for H_3O^+ β-alumina over a range of temperature. (Data from tables 5.15,5.17). Non-exponential spin-lattice relaxation is fitted by two exponentials.

Figure 5.17

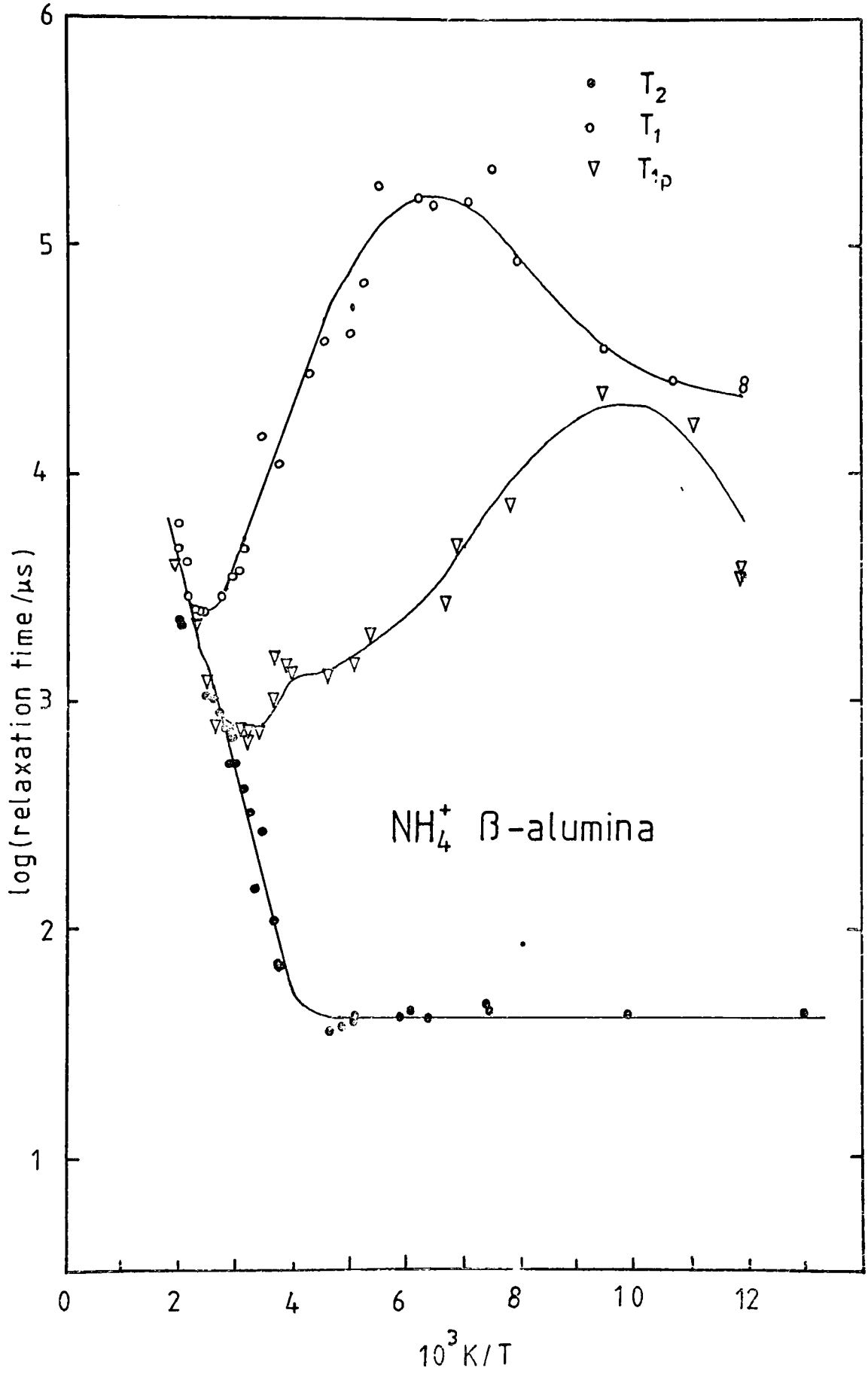
T_2
T_1
$T_{1\rho}$
NH_4^+ β-alumina
log(relaxation time/μs)
$10^3 K/T$
6
5
4
3
2
1
0
2
4
6
8
10
12

Figure 5.18

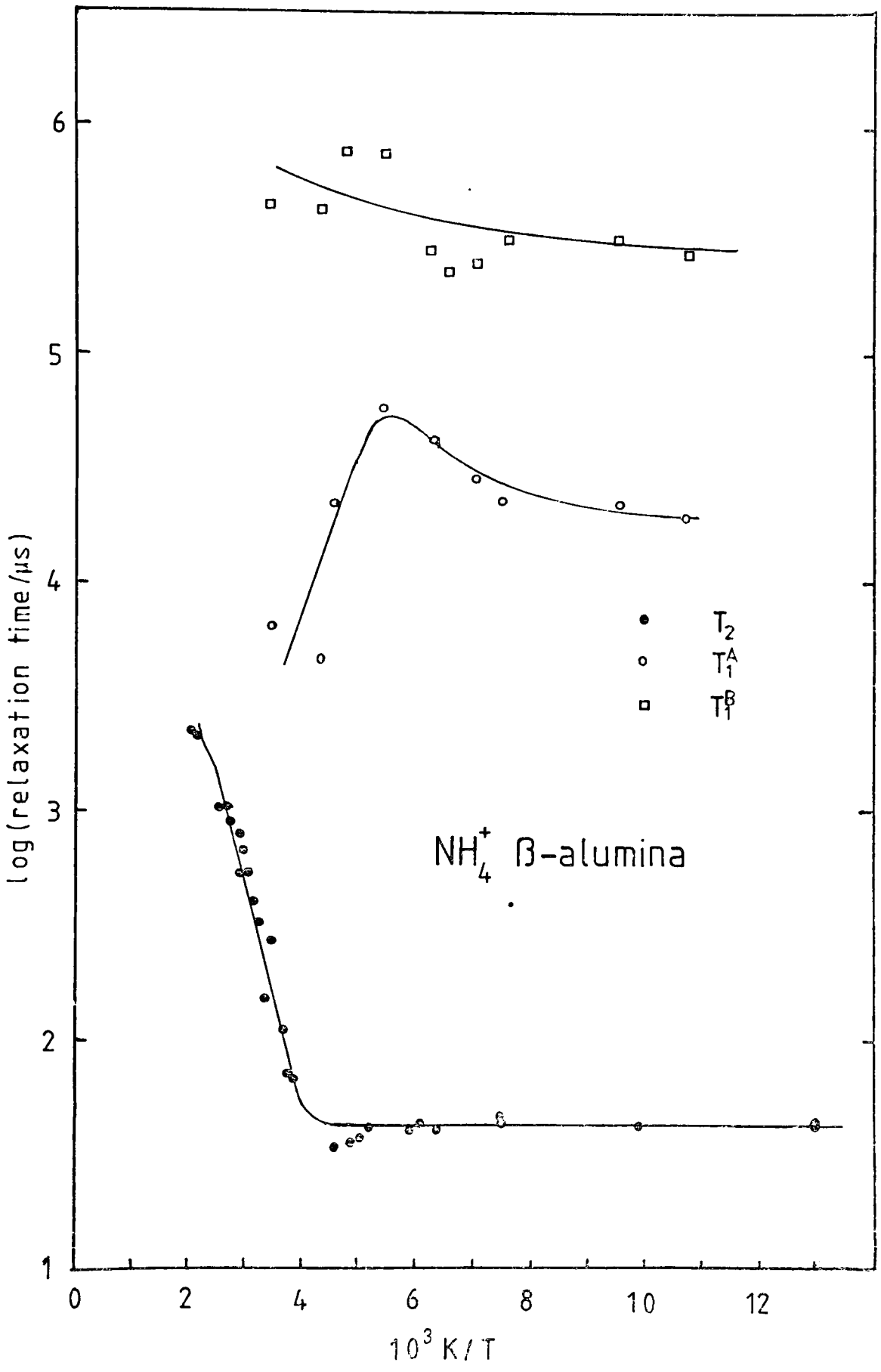
log (relaxation time/μs)
6
5
4
3
2
1
0
2
4
6
8
10
12
10³ K/T
T2
T1A
T1B
NH4+ β-alumina

Figure 5.19

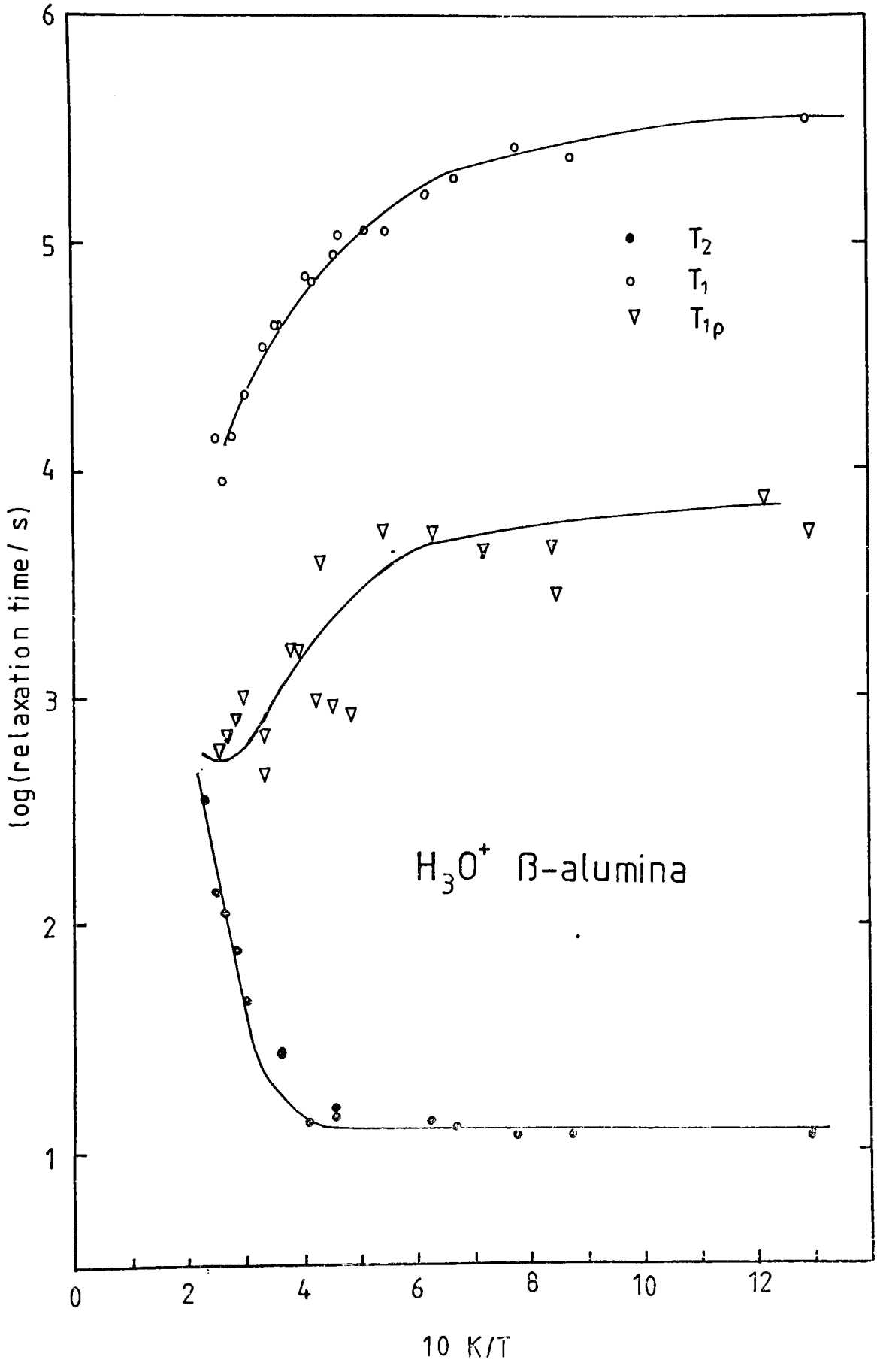
6
5
4
3
2
1
0
2
4
6
8
10
12
log(relaxation time / s)
10 K/T
T2
T1
T1ρ
H3O+ β-alumina

Figure 5·20

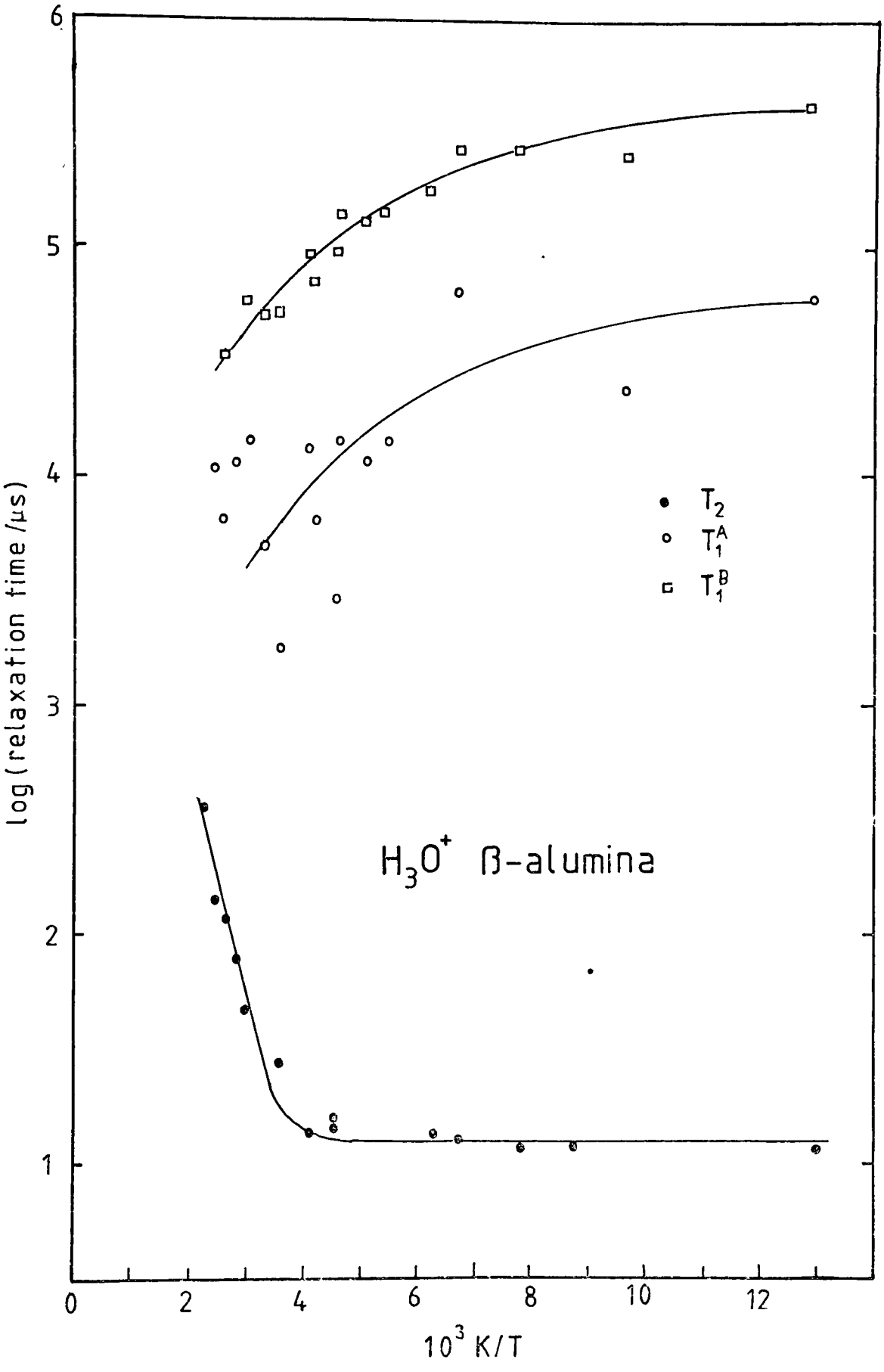
log (relaxation time /μs)
6
5
4
3
2
1
0
2
4
6
8
10
12
10³ K/T
T₂
T₁ᴬ
T₁ᴮ
H₃O⁺ β-alumina

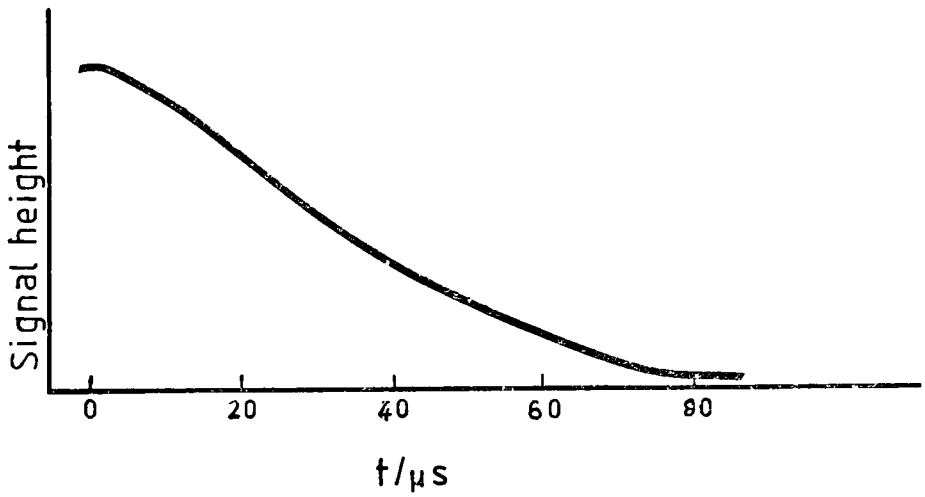

(a) NH_4^+ ß-alumina

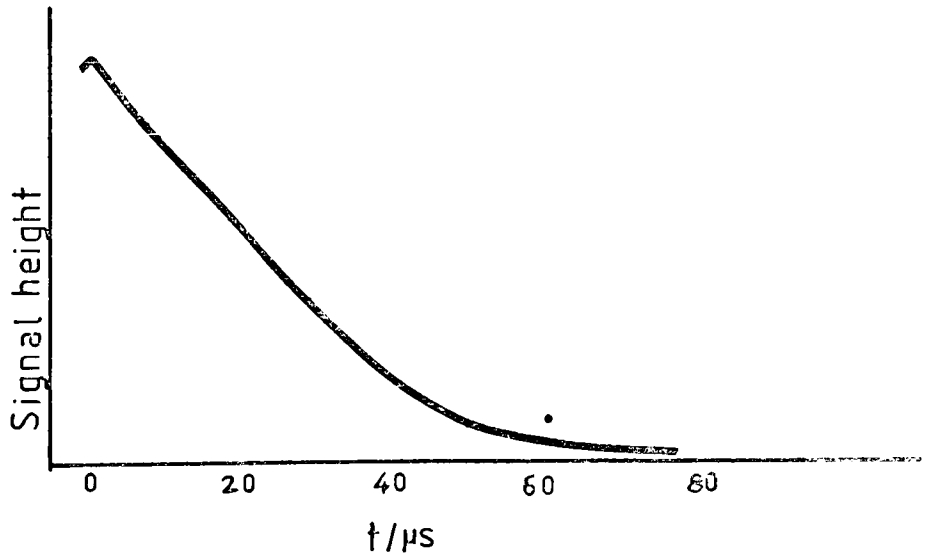

(b) H_3O^+ ß-alumina

Figure 5.21 Some solid echoes

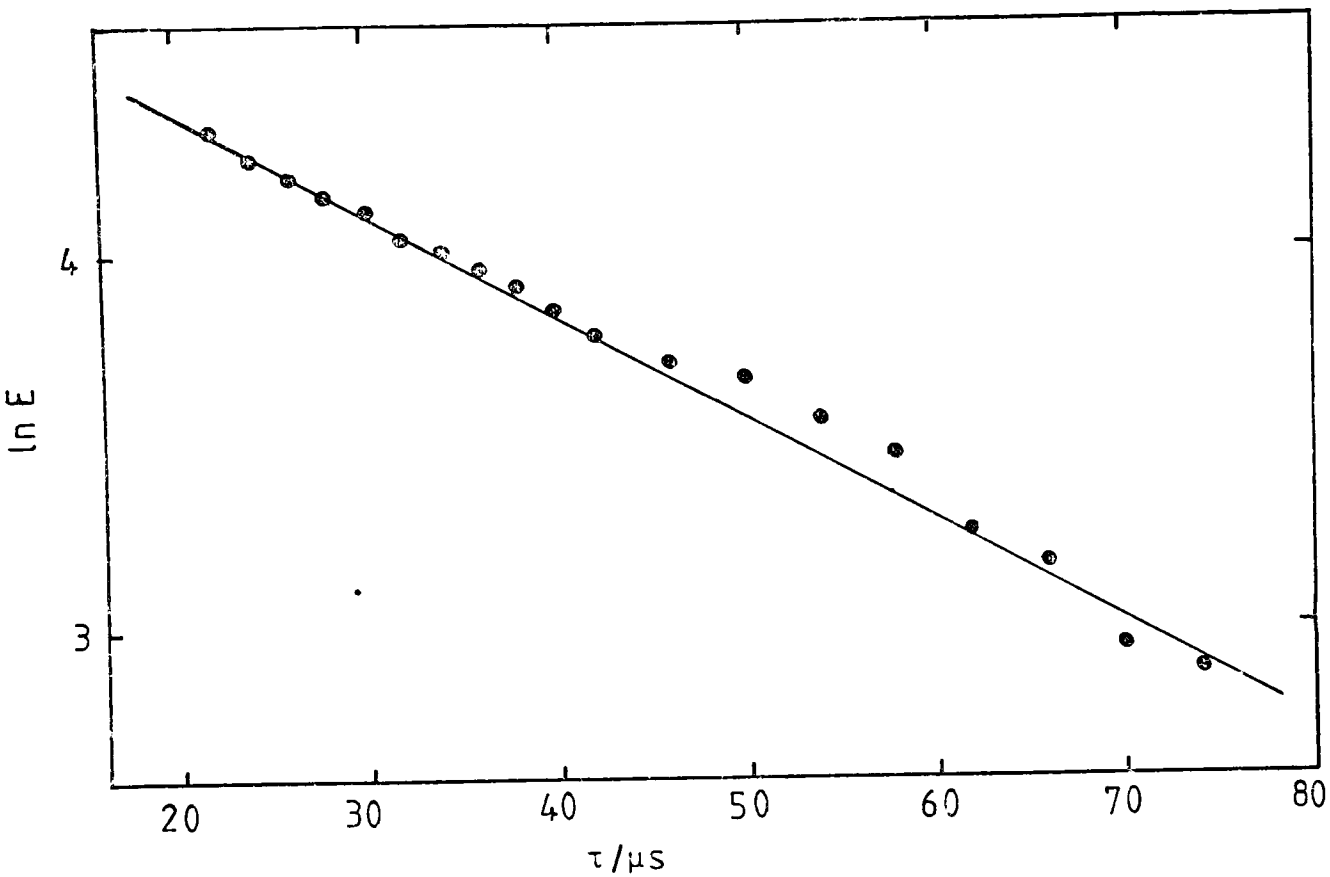

Figure 5·22 Solid echo amplitude for NH_4^+ β-alumina

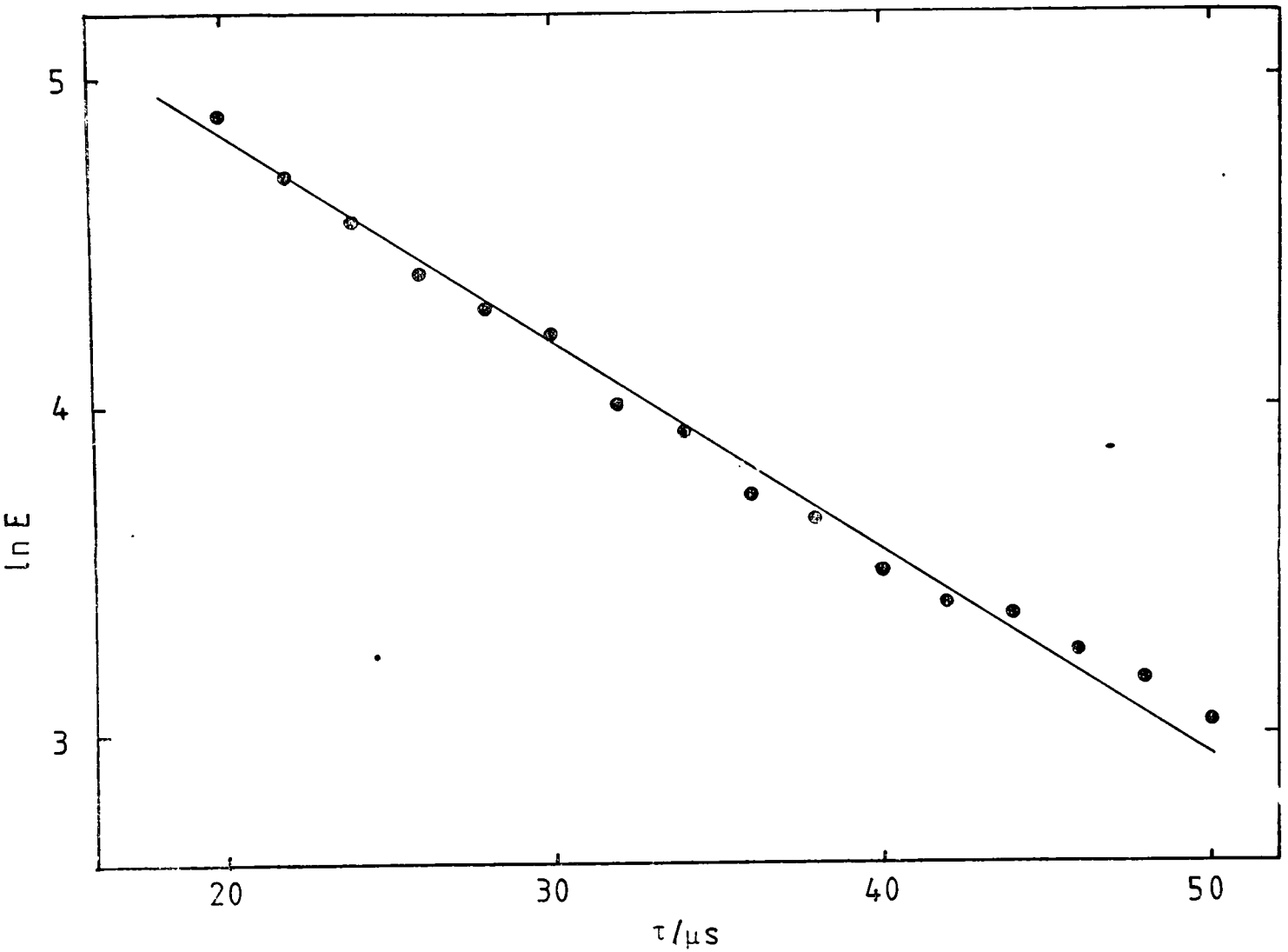

Figure 5·23 Solid echo amplitude for H_3O^+ β-alumina

throughout the temperature range studied, the data then being analysed as for NH_4^+ β-alumina. The results are summarised in tables 5.16-5.19.

Figures 5.17-5.20 illustrate the relaxation data in tables 5.10-5.19 and are preceded by an explanatory key.

The low temperature solid echo decay shapes for these compounds are illustrated in figure 5.21. Fitting the echo maxima (see section 3.6) gave M_2 values of $1.20G^2$ and $15.2G^2$ for NH_4^+ β-alumina and H_3O^+ β-alumina respectively. The decay of the echo amplitude, $E(\tau)$, with pulse separation τ (see section 2.7) was followed and the results are shown in figures 5.22 and 5.23. Neither compound showed Gaussian behaviour, but both showed an approximately exponential decay of $E(\tau)$ with τ.

Chapter 6

Interpretation and Conclusions

6.1 Oxide hydroxides.

The observation of absorption spectra consisting of a narrow central peak superimposed on a wide line is common for oxide hydroxides and hydroxides (157). The assignment of the central peak is a matter of debate. Glemser (158) assigned it to hydration water. Fraisard and Imelik (159) assigned it to surface water. In their studies of boehmite (γ-AlOOH), Fripiat and Touillaux (36) found the intensity of the peak to be independent of surface area and that it remained, even after outgassing under high vacuum at 160°C for several days. They concluded that there were constitutional protons in fast motion in boehmite and proposed that a number of protons were not in a zig-zag chain of hydroxyl groups but formed water molecules (OH_2 groups coordinated to aluminiums) capable of relatively free rotation. However, the rotation would be 180° flips of the water molecule about its C_2 axis and it is well known (160) that the Pake splitting for water (161) survives unchanged for this motion, no matter what the rate of flipping, provided that negligible time elapses during the flipping process. This would therefore not give the central peak observed.

In this work, the central peak has been shown (from the Fourier transform absorption spectra) to be $<1\%$ of the total absorption at room temperature. The central peak could be due to non-constitutional water molecules, trapped in the lattice during its formation and mobile at room temperature. Lowering the temperature will broaden this line towards that for the

static molecule and the central peak will eventually disappear under the main signal. This explains the decrease in intensity with temperature, as observed in the continuous-wave spectra, and the absence of the peak at lower temperatures. That the amount of occluded water is small is shown by its not being detected in the analyses. The amount will not depend on the surface area, but rather on the conditions of preparation.

The linewidth for GaOOH was constant over the entire temperature range and it follows (from the line-narrowing criterion $(\gamma^2 M_2)^{\frac{1}{2}}\tau_c < 1$) that $\tau_c > 10^{-5}$s at 200°C. In his exchange studies on the isostructural compound α-FeOOH, Gallagher (31) gives E_a = 34.3 kJ mol^{-1} and $D_o = 6.5 \times 10^{-13}$cm^{2}s^{-1}. It follows (see section 1.1) that $\tau_c^o \sim 10^{-4}$s and hence, at 200°C, $\tau_c \sim 1$s. Assuming τ_c at 200°C for GaOOH is similar to that in α-FeOOH, no line narrowing is expected, in agreement with the experimental results.

A value of M_2 for GaOOH of 6.34G^2 was calculated from the structure of GaOOD, as given by Pye, Birtill and Dickens (25). The experimental value obtained on the Jeol instrument was 8.3 ± 0.9G^2 and the other values obtained (7.7G^2 Bruker broad-line, 8.1G^2 from the solid echo) were within these error limits. The heavy atom coordinates (Ga,O) are likely to be the same in GaOOH and GaOOD and it therefore seems that the hydrogen atom coordinates in GaOOH differ from the deuterium atom coordinates in GaOOD. An O-H bond is typically 0.9-1.1Å in length and in general, for hydrogen bonds, the links O-H and H...O are not colinear, the angle between them commonly deviating from 180° by 10-20° and sometimes by as much as 40° or 50° (162). The author carried out calculations of M_2 for a range of r (the O-H bond length) and ϑ (see figure 6.1) values. The results are

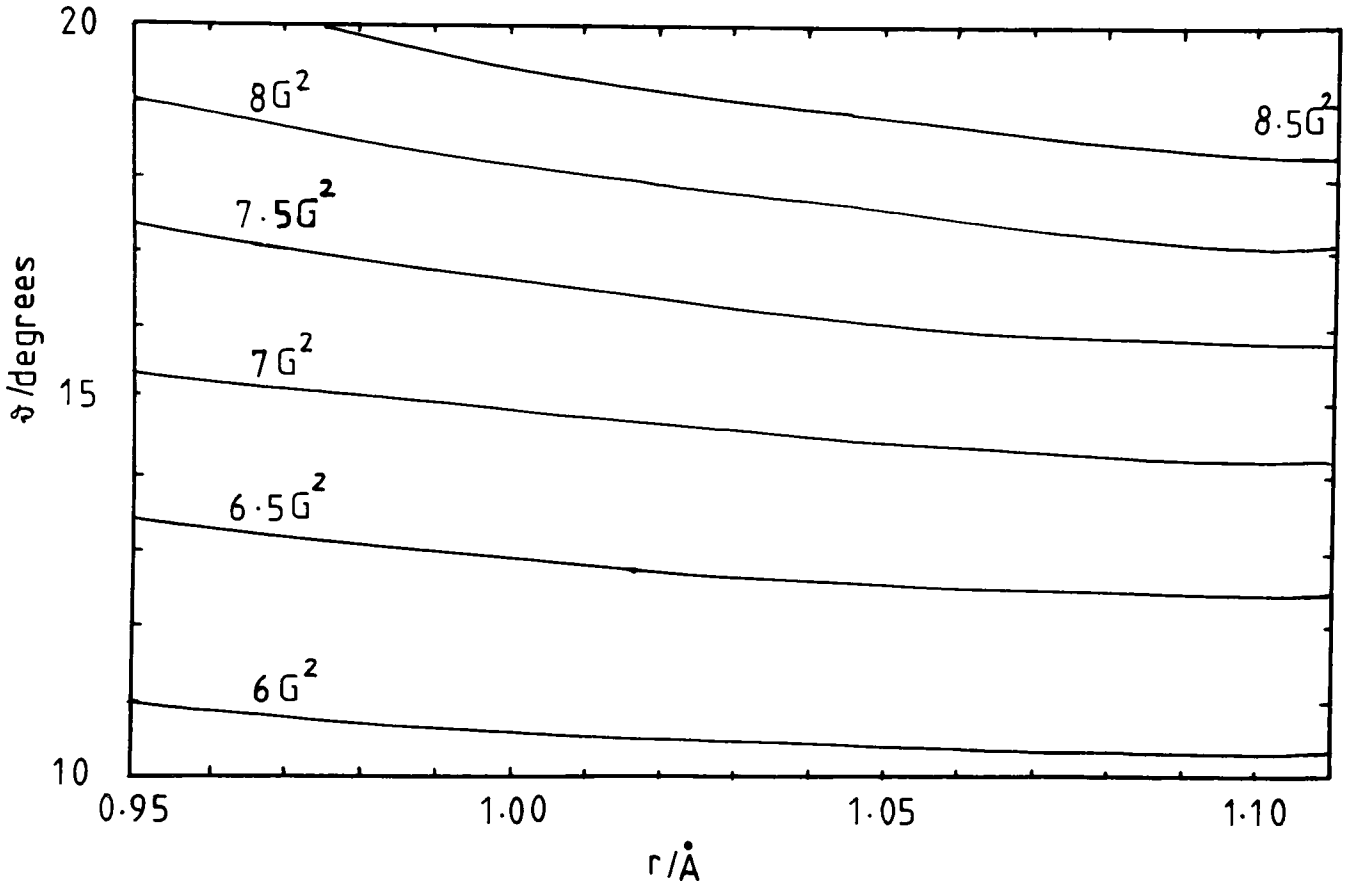

M_2 as a function of r and ϑ for GaOOH

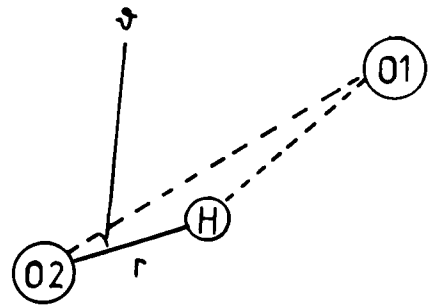

Figure 6·1

summarised in figure 6.1. In GaOOD, r = 0.996Å and $\vartheta = 12.5^{\circ}$. M_2 for GaOOH is seen to vary only slightly with r but to rise more steeply with ϑ. The experimental M_2 value shows that ϑ is greater in GaOOH than GaOOD. Taking the O-H and O-D bond lengths to be the same, ϑ(GaOOH) is 18°. This difference between GaOOH and GaOOD is significant, but not understood.

The absorption spectrum of boehmite (γ-AlOOH) is a Pake doublet, very like that observed for gypsum ($CaSO_4.2H_2O$, see ref 161). This is shown most clearly by the spectra obtained by Fourier transformation. The doublet shows that there are pairs of protons in the structure and is also evident in the spectra given by other workers (e.g. 36) who, however, have not commented upon it.

Previous nmr (2[illegible],36) and infra-red studies (29,30) of boehmite have been interpreted in terms of a zig-zag chain of hydroxyl groups. The infra-red spectrum (dry KBr pellet) recorded by the author using an SP1025 spectrometer is shown in figure 6.2. The doublet at high frequency (3280,3080 cm^{-1}) is due to the O-H stretching mode, that at low frequency (1160, 1080 cm^{-1}) is due to the O-H bending mode and the weak doublet (1970,2090 cm^{-1}) is presumably an overtone of this. Systems containing OH_2 groups, such as ice and the molybdic acids, have an intense absorption band at 1600 cm^{-1}, which is absent from the boehmite spectrum. The nmr doublet for boehmite therefore cannot be due to OH_2 groups, but must arise from pairing of hydrogens bonded to different oxygen atoms.

The occurrence of Pake doublets can be understood as follows. A pair of spin-$\frac{1}{2}$ nuclei gives an nmr spectrum which is a sharp doublet separated by a field δB where

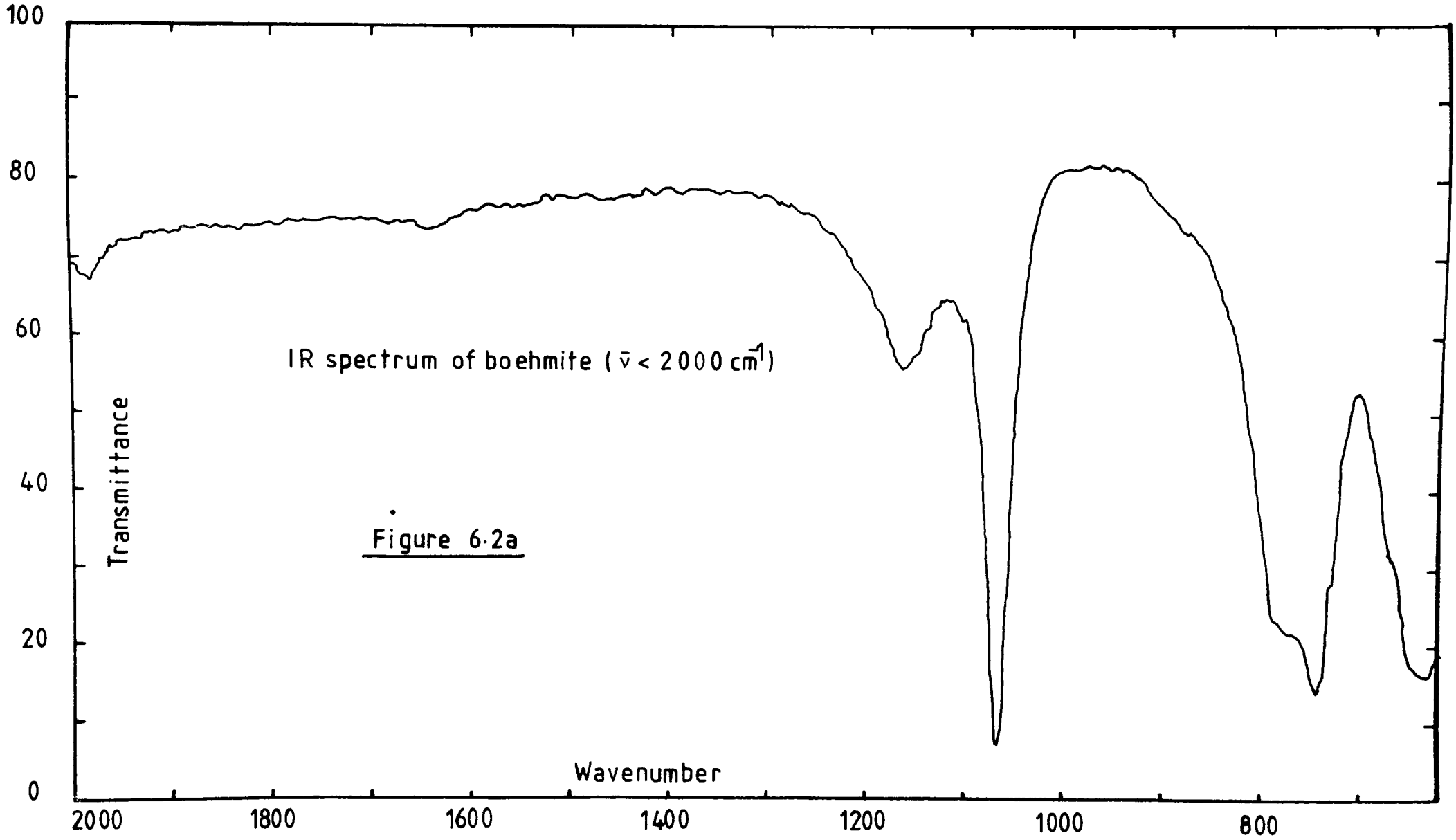
100
80
60
40
20
0
Transmittance
IR spectrum of boehmite ($\bar{\nu} < 2000\ cm^{-1}$)
Wavenumber
2000
1800
1600
1400
1200
1000
800

Figure 6·2a

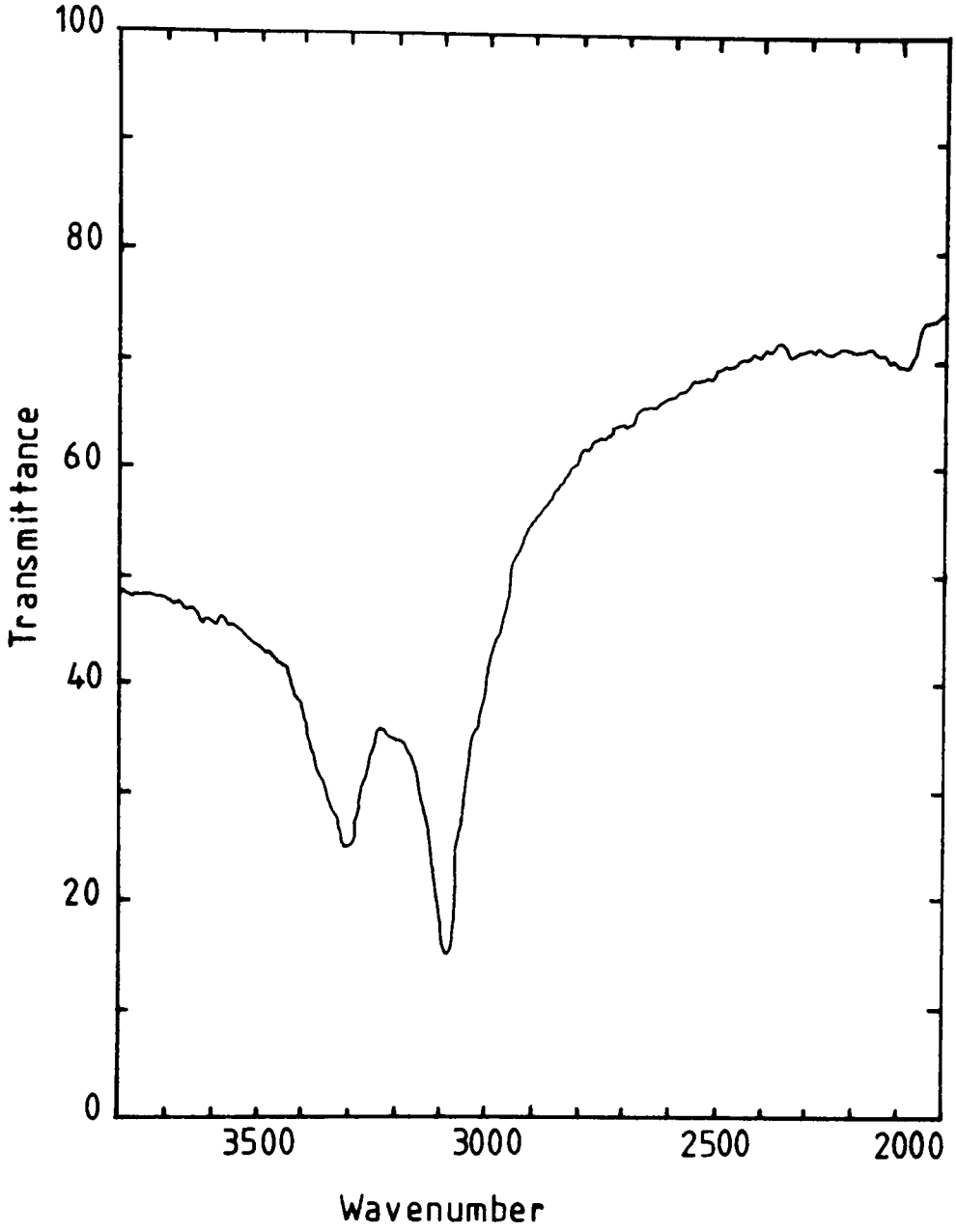

IR spectrum of boehmite ($3800 > \bar{\nu}/cm^{-1} > 2000$)

Figure 6·2b

$$\delta B = -2\alpha(3\cos^2\vartheta - 1)$$

and $$\alpha = \tfrac{1}{4}\gamma\hbar\left(\frac{\mu_0}{4\pi}\right) r^{-3}. \qquad (6.1)$$

r is the distance between the spins and ϑ the angle between the inter-spin line and the static field direction. In real crystals, the presence of other magnetic nuclei leads to broadening of these doublet lines, the broadening usually being assumed to be Gaussian. The broadening is, however, generally asymmetric and Holcomb and Pedersen (163,164) have shown that the separation of the centres of gravity of the left and right hand sides of the absorption spectrum gives the most reliable information about r. This approach is, however, only valid if the intra-pair interaction (giving δB) is much greater than the inter-pair interaction (giving the broadening), which is not true for all ϑ values. The method is therefore not extendable to powders, where all values of ϑ occur. Pake (161) fitted doublet lineshapes for powders assuming a Gaussian broadening function S(b) where

$$S(b) = (\beta\sqrt{2\pi})^{-1} \exp(-b^2/2\beta^2).$$

This broadening is independent of ϑ, which is strictly incorrect. M_2 is then, after fitting, given by

$$M_2 = \frac{4}{5}\alpha^2 + \beta^2$$

Gabuda et al.(165) give a method for extracting r to high accuracy using characteristic features of the absorption spectrum for powders. From the separation of points of maximum curvature, ΔB, and the doublet splitting, δB, $K(\beta/\alpha)$ is calculated where

$$K(\beta/\alpha) = (\Delta B - \delta B)/(\Delta B + \delta B).$$

β/α can then be read off a known graph of $K(\beta/\alpha)$ versus β/α and so $L(\beta/\alpha)$ can be read off another known graph where

$$L(\beta/\alpha) = 2\alpha/(\Delta B + \delta B).$$

α and β are therefore known and

$$r^3 = \tfrac{3}{4}\gamma\hbar\left(\frac{\mu_0}{4\pi}\right)\alpha^{-1}$$

and so for proton pairs

$$r^3 = 21.16/\alpha \quad \text{Å}^3\text{G}.$$

The boehmite derivative absorption spectrum (see figure 5.2) has ΔB = 10.93G and δB = 5.67G. Using Gabuda's method, these figures give α = 4.40G and β = 1.67G. M_2 calculated from these fitting parameters is $18.3G^2$, in good agreement with the experimental value ($17.5G^2$). r, for a pair in boehmite is therefore 1.69Å. The effect of motions, such as vibrations, on line shape is a complex problem. For crystal hydrates, the vibrations and librations of the water molecule have been shown (160) to cause r measured as above to be bigger than r_e (the equilibrium interproton distance) according to

$$r^{-3} = 0.839\ r_e^{-3}.$$

For boehmite the effects are not obvious, vibrations in the plane of the hydroxyl chain perhaps shortening r and vibrations out of the plane increasing r. The effects could therefore be self-compensating.

Some model structures for the hydroxyl chain in boehmite are shown in figure 6.3. Model 1 is that predicted using the unpublished neutron diffraction work of Pye and Wiseman (26,27) on γ-AlOOD. Each proton is equidistant from two others in this chain and hence there are no distinct pairs. Model 2 shows possible hydrogen positions that might be observed by neutron diffraction if the hydrogens lay on either side of the O-O line. There are twice as many hydrogen sites as given by Pye and Wiseman, but the space group is still Cmcm, which gives the best fit to the neutron diffraction data. Only one site per

Figure 6.3

The hydroxyl chain in boehmite

Model 1

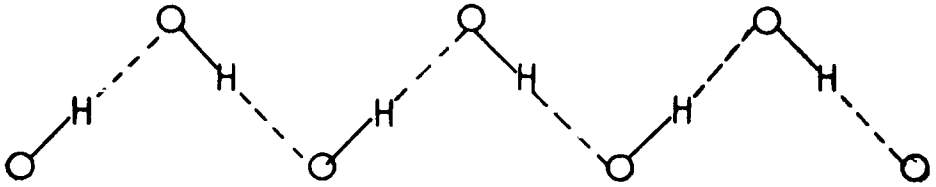

Model 2

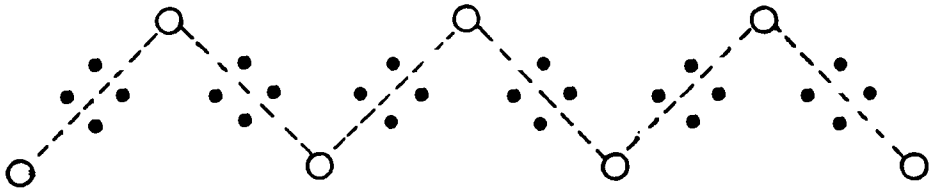

● = possible hydrogen site

Model 3

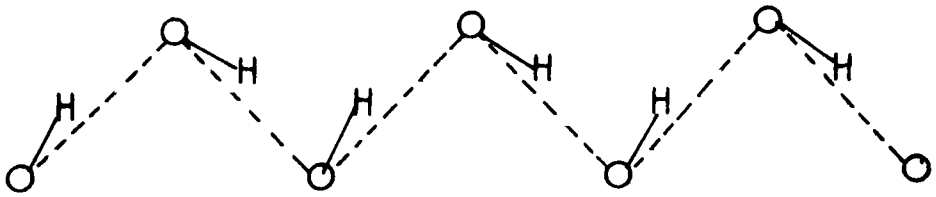

Figure 6.4

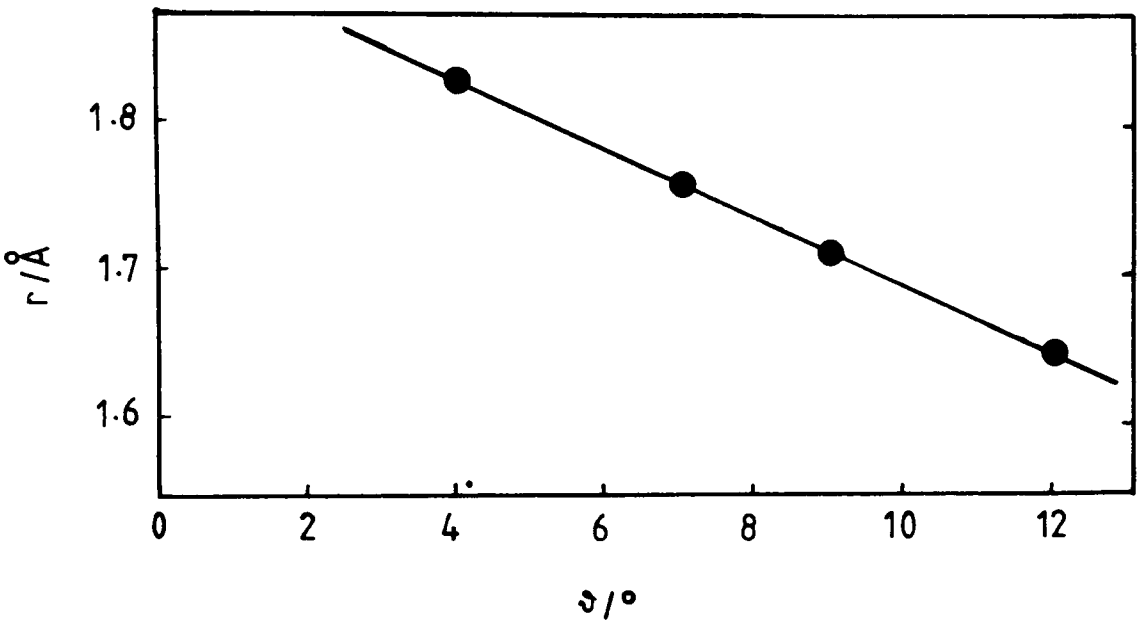

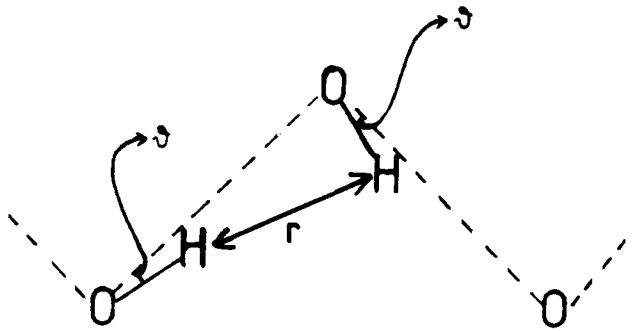

Model 3 for γ-AlOOH
(see text)

O-O line can be occupied. Model 3 has a hydroxyl chain (derived from Model 2) which contains distinct pairs. The nmr doublet shows that most of the protons are in pairs. The average unit cell is the result of disorders in the arrangements in different chains, in different layers and possibly domains in a given chain, domain boundaries consisting of a short stretch with the arrangement of Model 1.

Pye and Wiseman's (26,27) oxygen and aluminium coordinates, obtained by neutron diffraction, are likely to be more accurate than those from X-ray results (144,145) and the author used these for M_2 calculations. The van Vleck formula for boehmite is

$$M_2 = 358.1 \sum_{H} r_{H-H}^{-6} + 126.1 \sum_{Al} r_{Al-H}^{-6} \text{ Å}^6 G^2.$$

The author calculated these sums upto a radius of 4Å, further terms being negligibly small. Estimation of the contribution due to interactions between different chains (2.86Å apart) is awkward as there may be disorder in the polarities of neighbouring chains. This contribution was taken to be $0.5G^2$. Model 1 (with no pairs) gave $M_2 = 15.6G^2$. In calculations for Model 3, the O-H bond was taken to be 1Å andthe angle ϑ, of the protons off the O-O line was taken to be the same for both proton sites. The calculated variation of r, for the pairs, with ϑ is shown in figure 6.4. A value of $\vartheta = 10^{\circ}$ corresponds to r = 1.69Å, as found experimentally, and calculation assuming this angle gave $M_2 = 19.9G^2$ (M_2 being the mean for the non-equivalent hydrogens). As discussed earlier, the O-H...O linkage is commonly not linear.

Holm, Adams and Ibers (28) obtained an experimental, temperature independent, M_2 value for boehmite of $18 \pm 1G^2$, which is in agreement with the values obtained in this work (see

section 5.1). Model 1 might be consistent with this, with the hydrogen atom coordinates differing from the deuterium coordinates in γ-AlOOD, but does not give an nmr doublet. Model 3 is consistent both with the experimental M_2 value and with the nmr doublet. Further diffraction work would be necessary to confirm that Model 3 is the correct structure.

6.2 Hydrogen oxide bronzes.

Previous nmr studies of hydrogen oxide bronzes have been concerned with the hydrogen tungsten bronzes, H_xWO_3, and there has been some disagreement in the interpretation of the results. Vannice, Boudart and Fripiat (43) report the protons to be highly mobile with $\tau_c^o = 3.7 \times 10^{-12}$s and $E_A = 5.4$ kJ mol^{-1}. Their conclusions are based on a poorly defined T_1 minimum (700ms at 100K) in a temperature range where they find T_2 constant (in the range 16-32 μs). The lack of motional narrowing and the inconsistency of the value of the T_1 "minimum" with the rigid lattice T_2 value cast doubt on their interpretation. Dickens, Murphy and Halstead (42) measured relaxation times and linewidths and found line narrowing above 250K. A single motional process, with $\tau_c^o = 7 \times 10^{-8}$s and $E_A = 16$ kJ mol^{-1}, accounted for all the results and the low temperature M_2 value was consistent with the known structure of H_xWO_3 (37). The results of neutron elastic scattering studies (38) are consistent with the nmr interpretation of Dickens et al., but not with that of Vannice et al.. Nishimura (44) has studied proton mobility by following nmr linewidth as a function of temperature. He finds $E_A = 13$ kJ mol^{-1}, in fair agreement with Dickens et al., and $\tau_c^o = 1.1 \times 10^{-10}$s. The different τ_c^o value could result from different sample preparation techniques. Dickens et al. worked with reduced WO_3 crystals, whereas Nishimura worked with reduced WO_3 powder, which could contain some H_2O as electrochromic films do (see section 1.3). His data give a diffusion coefficient comparable to that deduced form bleaching current measurements on electrochromic films.

The positions for hydrogen atoms in $H_{1.71}MoO_3$ are unknown. Inelastic neutron scattering (41) indicates the presence of OH_2 groups in the coordination sphere of molybdenum atoms. The MoO_3 framework is illustrated in figure 6.5. In $H_{0.36}MoO_3$ the intra-layer sites shown in figure 6.5 are occupied. The presence of one hydrogen per O-O line within the layer would give the stoichiometry $H_{1.0}MoO_3$, so additional sites must be occupied in $H_{1.71}MoO_3$. It is unlikely that the OH_2 groups involve the bridging oxygens within the layers, as the layers might then be expected to cleave (by analogy with the structural relationship between MoO_3 and the molybdic acids, shown in figure 1.7). The OH_2 groups are probably derived from the terminal oxygens at the top and bottom of the MoO_3 layers. These can hydrogen bond to the next layer, possibly to bridging oxygens. That these sites are not occupied in $H_{0.36}MoO_3$ could be due to multiple bond character in the Mo-O terminal linkage, which is by far the shortest bond (1.67Å) in MoO_3 (39). Filling all possible terminal sites with OH_2 groups would give the stoichiometry $H_{2.0}MoO_3$, which is that of the most reduced bronze phase obtainable.

The nmr absorption spectrum for $H_{1.71}MoO_3$ at low temperatures is not consistent with all the hydrogen atoms being present as OH_2 groups, as a Pake doublet (discussed in the previous section) would then be expected. The separation of the side peaks is difficult to estimate, there being a large flat portion (see figure 5.14), but is about 11G, similar to that in gypsum ($CaSO_4.2H_2O$). These side peaks are therefore attributable to terminal OH_2 groups. The central peak may therefore arise from the remaining hydrogens, present as hydroxyl groups. Estimation of the areas under the absorption curve due to these 2 types of

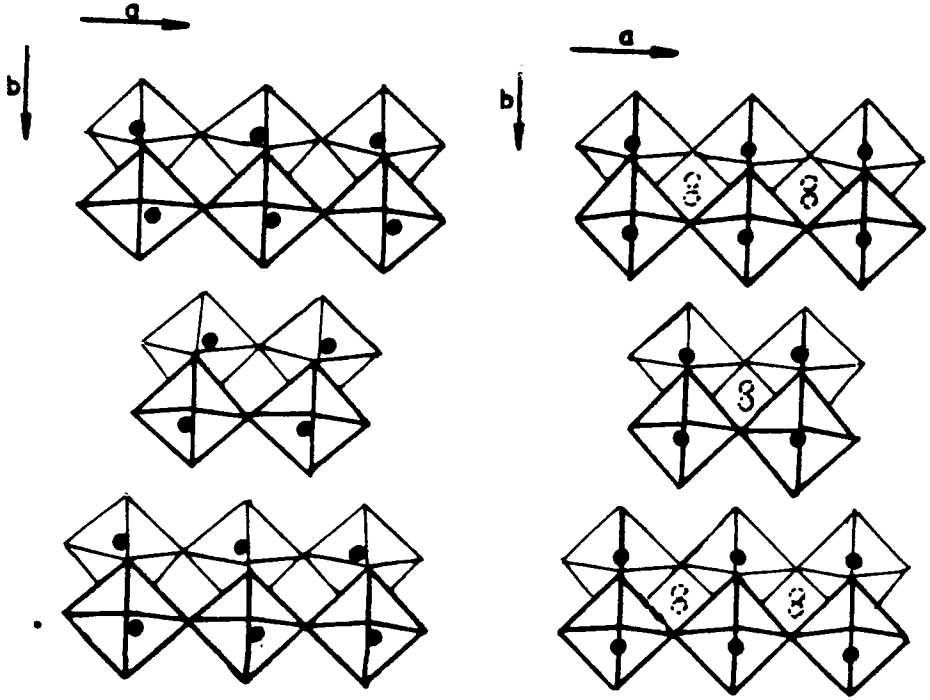

MoO_3 $H_{0.34}MoO_3$

Figure 6.5

hydrogen environment suggests that 89% of the protons are present in OH_2 groups. The position of the hydroxyl groups in the structure is uncertain. They could be in the intra-layer positions occupied in $H_{0.36}MoO_3$, could be rotated from this to point towards a terminal oxygen on a neighbouring layer or could be in the terminal positions. Any of these models could fit the experimental M_2 value.

The shape of the room temperature absorption spectrum for $H_{1.71}MoO_3$ is characteristic of the powder pattern resulting from axially symmetrical anisotropic chemical shielding (95). The anisotropy $(\sigma_\perp - \sigma_{//})$ is 22 ppm (2 kHz at 90MHz). This shows that the strong dipolar interaction between protons has been wiped out by diffusion of the hydrogens but that anisotropic chemical shielding has survived. Motion restricted to a plane (e.g. the interlayer region) within a crystallite would have this effect. Thus for a given crystallite, after averaging over a plane of sites, the average principal components of the shielding tensor would be $\langle\sigma\rangle_{xx} = \langle\sigma\rangle_{yy} \neq \langle\sigma\rangle_{zz}$.

For $H_{1.71}MoO_3$ motional narrowing occurs at temperatures >150K. The measured T_2 levels off at high temperatures (where $T_2 \simeq 10$ms) showing that some residual interaction has not been removed by both the Carr-Purcell-Meiboom-Gill (CPMG) pulse sequence and the diffusional motion. Chemical shielding, magnetic field inhomogeneity and interactions between unlike spins all transform under rotation in a rotating frame for a spin I in the same way as the operator $\hat{I}_z$ (95). The CPMG pulse sequence toggles $\hat{I}_z(t)$ between $+\hat{I}_z$ and $-\hat{I}_z$ and hence the time average of all these interactions vanishes leaving only those between like spins. The limit for the measured T_2 in this compound is evidence that the diffusion of protons is not completely isotropic and hence

does not totally remove the dipolar interactions. This could be due to lack of diffusion between different interlayer regions or because diffusion does not occur over a long range within a given interlayer region. As $T_2 \propto (M_2)^{-\frac{1}{2}}$ (see section 2.4) and the limiting T_2 value is 10^3 the rigid lattice value, the residual interaction is 10^{-6} times as strong as the dipolar interactions in the rigid lattice.

Measurement of T_2 from free induction decays (FID's) in a high homogeneity (high resolution) magnetic field would not have removed chemical shielding effects, the FID's then being the Fourier transform of the powder absorption lineshape. Thus, at sufficiently high temperatures, the relaxation time measured from the CPMG sequence, T_2^{CP}, will be greater than that from the absorption lineshape (or FID's), T_2^{LS}. The high temperature linewidth is 22 ppm, which corresponds (for measurements using a 16 MHz instrument) to $T_2^{LS} = 0.5$ms.

T_1, T_2^{CP} and $T_{1\rho}$ are all very similar for $H_{1.71}MoO_3$ at room temperature, confirming that there is rapid diffusion of hydrogen. The T_2 data in the line narrowing region give $E_A = 21.9 \pm 0.3$kJ mol^{-1} and an estimate of τ_c^o (from the line narrowing criterion $(\gamma^2 M_2)^{\frac{1}{2}} \tau_c = 1$) of 2.9×10^{-13}s. The $T_{1\rho}$ data give $E_A = 21.8 \pm 1.4$kJ mol^{-1} and least squares fitting of the T_1 minimum to BPP theory gives $E_A = 22.0 \pm 1.4$kJ mol^{-1} and $\tau_c^o = (0.9 \pm 0.65) \times 10^{-14}$s. The very close agreement of these values shows that they can all be interpreted in terms of one diffusive hydrogen motion.

The values $E_A \simeq 20$kJ mol^{-1} and $\tau_c^o \sim 10^{-13}$s are common for several different classes of materials showing fast hydrogen diffusion. This is true, for instance, of the compounds $H_{1.71}MoO_3$ (this work), $HUO_2PO_4.4H_2O$ (19) and $LaNi_5H_6$ (166).

Molecular/bond vibration frequencies are typically 1000-3000 cm^{-1} (i.e.~10^{13}Hz). τ_c^o, and hence the diffusion itself, may therefore arise from a bond vibration.

The T_1 minimum for $H_{1.71}MoO_3$ predicted from the low temperature M_2 value ($23G^2$) is 6.4 ms (BPP theory) or 7.0 ms (Torrey theory). The experimental minimum (from the least-squares fit) is 10.1 $\pm$ 0.6 ms and is thus higher than predicted by either of these models, reflecting their inadequacy for describing the motion.

A minimum in $T_{1\rho}$ for $H_{1.71}MoO_3$ occurs at about 110 μs, measurements then being currently difficult due to loss of most of the decay in the instrument dead time. In the weak collision case, and for the magnetic fields used in this work, the expected ratio $(T_1)_{min}/(T_{1\rho})_{min}$ is 250 (BPP theory) or 125 (Torrey theory). The experimental ratio is 90. The local field in the rotating frame, B_L' (given by $B_L' = (\frac{1}{3}M_2)^{\frac{1}{2}}$, see section 2.6) is 2.8G for $H_{1.71}MoO_3$ and this is not small compared with the B_1 field (8G). The $T_{1\rho}$ minimum is therefore not a weak collision (perturbation treatment) case.

At low temperatures (below 160K), T_1 for $H_{1.71}MoO_3$ deviates from the values predicted if motional modulation of the dipolar interproton interactions were the only relaxation mechanism. The temperature dependence of T_1 is then very slight and the relaxation non-exponential. This could be due to relaxation involving paramagnetic (impurity) centres then being more efficient (see section 2.8). This being the case, it follows that T_{1e} (the relaxation time of the paramagnetic centres) is $< 10^{-6}$s.

The structure of the compound $H_{0.36}MoO_3$ is known from neutron diffraction and is discussed in section 1.3. The hydrogen

Figure 6.6

The zig-zag chain in $H_{0.36}MoO_3$

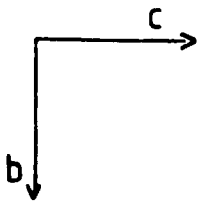

x = possible hydrogen site

O = oxygen atom

(a) Average structure

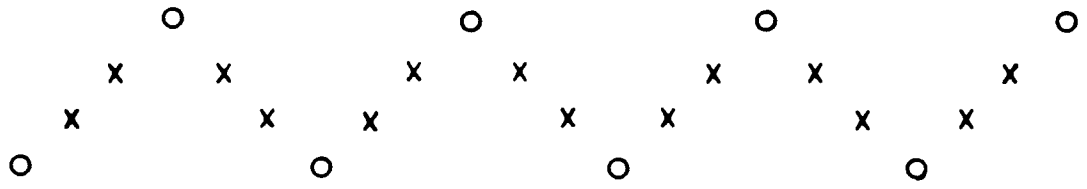

(b) Available sites near an occupied site

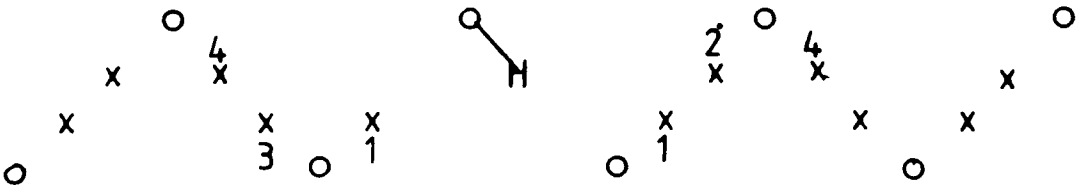

atoms are situated on sites within the layers and in a zig-zag chain of oxygen atoms, akin to that discussed for boehmite (section 6.1). The two sites on a given O-O line are too close for simultaneous occupation and neutron inelastic scattering (41) shows there are no OH_2 groups. The stoichiometry $H_{0.36}MoO_3$ corresponds to an average occupancy of 0.18 for the available hydrogen sites.

The experimental M_2 value for $H_{0.36}MoO_3$ is $5.7G^2$. Contributions to M_2 from interactions with molybdenum atoms (which have only 25% natural abundance of magnetic isotopes) and between protons in different chains (which are 3.887Å apart) are small. The possible hydrogen sites around a given hydroxyl group are shown in figure 6.6(b). The distances of the sites from the hydroxyl hydrogen are 1.912Å for type 1, 2.582Å for type 2, 3.076Å for type 3 and 3.736Å for type 4, these distances being calculated from Birtill's neutron diffraction results (39). M_2 is the mean of the M_2 values for the possible hydrogen distributions weighted according to the probability of each distribution. The contribution to M_2 of a proton is $6.68G^2$ for type 1 sites, $1.21G^2$ for type 2, $0.423G^2$ for type 3 and $0.132G^2$ for type 4. To explain the experimental M_2 value, most (about 85%) of the hydrogens must have a neighbouring type 1 site occupied. This does not correspond to a random distribution but suggests that most of the hydrogens are in pairs, the chance of three hydrogens getting close together being small.

The absorption spectrum of $H_{0.36}MoO_3$ has a wide doublet component with a doublet splitting, ΔB, of 4.1G. To a first approximation $\Delta B = 2\alpha$ (see equation 6.1) and this corresponds to a separation of 2.18Å for a pair of protons. This separation is close to that of nearest neighbour occupiable sites (1.94Å)

and the side peaks may therefore arise from those protons present in pairs. The central peak may arise from those protons not in pairs. Estimation of the areas under the absorption curves due to each type of hydrogen suggests that 88% of the hydrogen atoms are in pairs, in good agreement with the argument of the previous paragraph.

Line narrowing for $H_{0.36}MoO_3$ commences at 215K, as shown by the T_2 data. The signal to noise ratio was extremely poor for all measurements on this compound, this being due to the low hydrogen content and to RF skin effects, which arise from the high electronic conductivity of the material. Schoellhorn et al. (53) report a narrow line (1.1G wide) at room temperature, showing line narrowing, for their poorly characterised "$H_{0.5}MoO_3$" and Schroeder and Weitzel (40) report difficulty in obtaining absorption spectra for their $H_{0.31}MoO_3$.

The T_2 relaxation data for $H_{0.36}MoO_3$ in the line narrowing region gives $E_A = 11.2 \pm 0.9$ kJ mol^{-1} and an estimate of τ_c^o (from the line narrowing criterion $(\gamma^2 M_2)^{\frac{1}{2}}\tau_c = 1$) of 3×10^{-8}s. The corresponding figures for $H_{0.46}WO_3$ are $E_A = 16$ kJ mol^{-1} and $\tau_c^o = 7 \times 10^{-8}$s (42). The results are therefore very similar for these two compounds. τ_c^o is rather long and perhaps corresponds to a soft lattice mode.

The extremely poor signal to noise ratio for measurements on $H_{0.36}MoO_3$, together with the non-exponentiality of the spin-lattice relaxation (which was arbitrarily analysed as two exponentials), leads to a very large scatter in T_1 and $T_{1\rho}$ data, the very slight temperature dependence of which shows that motional modulation of dipolar interactions is not the most efficient relaxation process. The behaviour is like that for

$H_{1.71}MoO_3$ at low temperatures, the interpretation being that relaxation is occurring via paramagnetic (impurity) centres (see section 2.8). In order to derive motional information from T_1 and $T_{1\rho}$ measurements on $H_{0.36}MoO_3$, it would be necessary to greatly reduce the paramagnetic impurity concentration. However, high purity starting materials were used and a preparation starting from, say, ultra-high purity Mo metal would have to be attempted.

In both $H_{0.36}MoO_3$ and $H_{1.71}MoO_3$ most of the protons are present in pairs and it is therefore not surprising that the decay of the solid echo amplitude, $E(\tau)$, with pulse separation, τ, is approximately Gaussian (see section 2.7). For both compounds there is a slight curvature at short τ, this presumably being due to those protons not present in pairs. $M_2^{VV}(\text{inter})$ is larger for $H_{1.71}MoO_3$ than for $H_{0.36}MoO_3$, which is expected as the distance between pairs is smaller in the former compound. As these systems are more complex than the model systems considered theoretically, where all the protons are in pairs, the interpretation of the $M_2^{VV}(\text{inter})$ values is not obvious.

Self-diffusion coefficients for the protons in $H_{1.71}MoO_3$ and $H_{0.36}MoO_3$ can be estimated (see section 1.1). A possible model for diffusion in $H_{1.71}MoO_3$ is hopping along an O-O line, perhaps from a bridging oxygen to a terminal oxygen on a neighbouring layer (or vice-versa). The jump distance would be about 1Å and hence $D_o \sim 10^{-3} cm^2 s^{-1}$ and at room temperature $D \sim 10^{-7} cm^2 s^{-1}$, which would classify $H_{1.71}MoO_3$ as a superionic conductor. For $H_{0.36}MoO_3$, a possible model is hopping the zig-zag chain of bridging oxygens, the jump distance again being about 1Å. For this model $D_o \sim 3 \times 10^{-9} cm^2 s^{-1}$ and at

room temperature $D \sim 3 \times 10^{-11} cm^2 s^{-1}$, showing this material to have only a poor ionic conductivity. The corresponding room temperature ionic conductivities are $\sigma \sim 2 \times 10^{-2} ohm^{-1} cm^{-1}$ for $H_{1.71}MoO_3$ and $\sigma \sim 10^{-6} ohm^{-1} cm^{-1}$ for $H_{0.36}MoO_3$.

6.3 β-aluminas

Previous nmr studies of ionic motion in β-aluminas have been concerned with Na^+ ion motion in Na^+ β-alumina. Examination of the results of these studies gives information about motions in β-aluminas in general. Information has been obtained about site occupation and ordering, motional processes and activation barrier height distributions.

Absorption lineshape studies have given information about Na^+ site occupation in Na^+ β-alumina. Kline et al. (167) found that, in studies of powder samples, a number of different sites had to be occupied to account for spectra below 170K and Bailey et al. (168) found clear evidence in single crystals at 77K and 103K for occupation of a number of independent Na sites. This is in agreement with structure determinations by diffraction techniques (see section 1.4). Above 110K motional narrowing occurs due to jumping between these sites. Boilot et al. (169) studied single crystals at 300K, 100K and 4.2K and found a tendency for Na^+ to cluster in equilateral triangles at low temperatures ($\sim$100K). X-ray diffuse scattering studies (170) show that changes in ionic conductivity with temperature correlate with the degree of order among the conducting ions, a higher degree of order corresponding to a lower conductivity.

Information about Na^+ motion in Na^+ β-alumina has come from both linewidth and relaxation time studies. The dominant relaxation mechanism is quadrupolar interaction between the ^{23}Na ($I = 3/2$) nucleus and electric field gradients. Kline et al. (167) found sudden line narrowing in powder absorption spectra above 170K and deduced an activation energy $\sim$10 kJ mol^{-1}. Jerome and Boilot (171) also found $E_A \simeq$ 10 kJ mol^{-1} from T_1 measurements in the same

temperature range. Chung et al. (172) studied linewidths for single crystals and deduced E_A = 16 kJ mol^{-1}, in good agreement with the results of tracer diffusion and conductivity measurements. Bailey et al. (168) extended these measurements to include the dependence of linewidth on crystal orientation and obtained E_A = 10 kJ mol^{-1} and $\tau_c^o \simeq 7.5 \times 10^{-11}$s. Walstedt et al. (173) studied T_1 for single crystals prepared in different ways. They fitted T_1 data allowing for local variations in barrier heights at different sites and attributed different results from different samples to variations in the structure and/or charge defects. Evidence for a barrier height distribution also comes from conductivity dispersion measurements on single crystals (174). Bjorkstam and Wei (175) established the comparability of results from nmr and other studies. They identified two separate line narrowing mechanisms in the range $100K < T < 500K$. In the range $110K < T < 150K$, the line narrows with $E_A \simeq 5$ kJ mol^{-1}, but at higher temperatures a second mechanism is evident and, above 300K, E_A = 16 kJ mol^{-1}. The low temperature line narrowing is assigned to rapid local motion between mid-oxygen (mO) sites and Beevers-Ross (BR) sites (see section 1.4) and the additional narrowing at $T > 150K$ to long range sodium diffusion in the conduction plane over distances long compared to the correlation length of microdomains formed by spatially ordered Na^+ ions (see section 1.4).

The compounds NH_4^+ β-alumina and H_3O^+ β-alumina are said to be being studied for possible use as electrolytes in fuel cells, batteries and as constituents of hydrogen monitors (176). Until very recently, literature reports of investigations on these compounds have been very few in number.

Extensive studies of NH_4^+ β-alumina by electron and X-ray

diffraction, IR and Raman spectroscopy and some conductivity measurements have recently been reported by Colomban et al. (156). The structure of NH_4^+ β-alumina resembles that of Tl^+ β-alumina (177), which is not surprising in view of the similarity of the ionic radii (Tl^+= 1.50 Å, NH_4^+ is effectively 1.40 Å). The site occupancies are 72% BR, 21% mO, 7% aBR and the extra oxygens above the ideal stoichiometry is in mO sites bound by two Al^{3+} Frenkel defects (see section 1.4). Though X-ray diffraction does not give the positions of the hydrogen atoms, IR vibrational bands characteristic of the NH_4^+ ion are observed. The ammonium ion can form upto four hydrogen bonds in both the BR and mO sites, two with pillar oxygens and two with oxygens in the spinel blocks. Conductivity measurements are given for the range $400K < T < 620K$, these temperatures being generally higher than those for the nmr measurements in this work. The activation energy for conduction is 46 kJ mol^{-1}, the same as that obtained from dielectric loss measurements (92), and at 400K $\sigma \simeq 5 \times 10^{-5}$ $ohm^{-1}cm^{-1}$. NH_4^+ β-alumina is therefore a poorer ionic conductor than Na^+β-alumina. Colomban et al. state that the conducting species is the NH_4^+ ion and it is difficult to envisage an alternative long range charge transport mechanism.

Axe et al. (178) have studied NH_4^+ β-alumina using inelastic neutron scattering. They deduce that the correlation time for translational jumps of the NH_4^+ ion must be $> 6 \times 10^{-11}$s at temperatures less than 473K. They interpret the results in terms of rapid jump reorientation of NH_4^+ ions with correlation time $\sim 10^{-12}$s at room temperature. The results suggest that $E_A = 3.5 \pm 0.5$ kJ mol^{-1} and $\tau_c^o = 2.3 \times 10^{-13}$ s for the reorientation process.

The relaxation behaviour found for NH_4^+ β-alumina in this work will be considered in two different temperature ranges. At high

temperature (above 250K) line narrowing occurs and spin-lattice relaxation is exponential, minima being observed in T_1 and $T_{1\rho}$. Below 250K, T_2 is constant and spin-lattice relaxation is non-exponential.

Non-exponential spin-lattice relaxation can arise from a number of causes (see section 2.8). One cause, quantum mechanical tunnelling, is important in NH_4^+ compounds at very low temperatures (see e.g. ref 181). The barrier to NH_4^+ reorientation in NH_4^+ β-alumina is apparently low (178) and hence tunnelling splittings for restricted rotational energy levels could be large (180). However, it appears not to be necessary to postulate that tunnelling is an important relaxation mechanism in this work, in which the temperatures are higher than those usually involved in tunnelling studies. There are a number of possible different NH_4^+ ion sites in the conduction plane (see section 1.4), the reorientation rates for which, and hence the appropriate T_1's, differ. When the time τ_d between translational jumps of the NH_4^+ ion is greater than the relaxation time, non-exponential relaxation can result, but, when τ_d is much less than the relaxation time, an average exponential relaxation is observed. Analysis of non-exponential relaxation in terms of two exponentials is arbitrary and no help in explaining the results. T_1 at the lowest temperatures measured (see figure 5.17) appears to be decreasing to a low temperature minimum, which could be due to reorientation of the NH_4^+ ion. This minimum will be broad because of the different reorientation rates for the various sites. The motional parameters deduced from Axe et al.'s work (178) suggest a T_1 minimum at 41K, assuming BPP theory applies at that temperature. $T_{1\rho}$ could also be decreasing at the lowest temperatures toward a minimum due to reorientation.

The low temperature M_2 value (estimated to be 1.2 G^2 from solid echoes) is not the rigid lattice value for an ammonium compound (for which about 50 G^2 is typical (179)). This is due to random reorientation of the NH_4^+ ion removing the entire intra-ionic M_2 contribution. An estimate of the residual, inter-ionic, M_2 contribution can be made by assuming a model structure of stoichiometric NH_4^+ β-alumina with the NH_4^+ ions in Beevers-Ross (BR) sites, which are 5.6Å apart, and the protons placed at their average positions over the reorientation i.e. at the centre of the ions. This model gives an inter-ionic M_2 of 0.3 G^2. The compound has a larger inter-ionic M_2, this being due to the presence of more NH_4^+ ions than in the stoichiometric model and occupation of further sites, which lead to the NH_4^+ ions being closer together on average.

At temperatures greater than 250K line narrowing occurs, and above 450K $T_1 = T_2 = T_{1\rho}$, which is strong evidence for a translational diffusion mechanism. The observed T_1 minimum (2.6ms) at 390K corresponds to modulation of a second moment (M_2) of 57 G^2. Translational diffusion might be expected to modulate only the residual inter-ionic M_2, and hence a minimum at about 120ms might be expected (see section 2.6). The low temperature M_2 and the position of the T_1 minimum therefore appears to be a paradox. However, NH_4^+ ions coming very close together in the translational process could correspond to a strong interaction, absent at low temperature, which translation could modulate. Wang et al. (91) showed, in their calculations, that the ions might move in pairs, and this could be compatible with NH_4^+ ions coming close together.

The author analysed T_2 in the line narrowing region and T_1 around the T_1 minimum in terms of the BPP theory (see section 2.6).

The equations for T_1 and T_2 can be re-expressed in terms of the T_1 minimum : -

$$\frac{(T_1)_{min}}{T_1} = 0.702\,\omega\tau_c\left(\frac{1}{1+\omega^2\tau_c^2} + \frac{4}{1+4\omega^2\tau_c^2}\right)$$

$$\frac{(T_1)_{min}}{T_2} = 0.351\,\omega\tau_c\left(3 + \frac{5}{1+\omega^2\tau_c^2} + \frac{2}{1+4\omega^2\tau_c^2}\right)$$

The author evaluated τ_c at different temperatures from the T_2 and T_1 data. The results are shown in figures 6.7 and 6.8. The T_2 data are characterised by $E_A = 25.1 \pm 1.2$ kJ mol^{-1} and $\tau_c^o = 1.8 \times 10^{-11}$s, and the T_1 data by $E_A = 24.1 \pm 1.5$ kJ mol^{-1} and $\tau_c^o = 1.4 \times 10^{-11}$s. The attempt frequency $(1/\tau_c^o)$ is therefore of the same order as that for translation of Na^+ ions in Na^+ β-alumina (168,173) and presumably arises from the same process. E_A is considerably higher than for Na^+ β-alumina (16 kJ mol^{-1}) but is lower than that observed in conductivity and dielectric loss measurements (46 kJ mol^{-1}). The agreement between E_A for diffusion and E_A for dielectric loss is not good for K^+ β-alumina and Rb^+ β-alumina (92) and this could also be the case for NH_4^+ β-alumina. The temperature range of conductivity measurements (156) was $400K < T < 620K$ whereas the the temperature range giving motional information in this work is $250K < T < 500K$ and this could be the origin of the discrepancy of the E_A values. At 473K $\tau_c \sim 10^{-8}$s, which is consistent with Axe et al.'s conclusion (178) that, for translation, $\tau_c > 6 \times 10^{-11}$s at temperatures below 473K.

The diffusion mechanism for NH_4^+ ions in NH_4^+ β-alumina is unknown but could involve a jump directly from a BR site to an aBR site (jump distance 3.22Å) or via an intervening mO site (jump distance 1.61Å). Assuming the latter to be the case, the diffusion coefficient D is estimated (see section 1.1) to be 5×10^{-9} cm^{2}s^{-1}

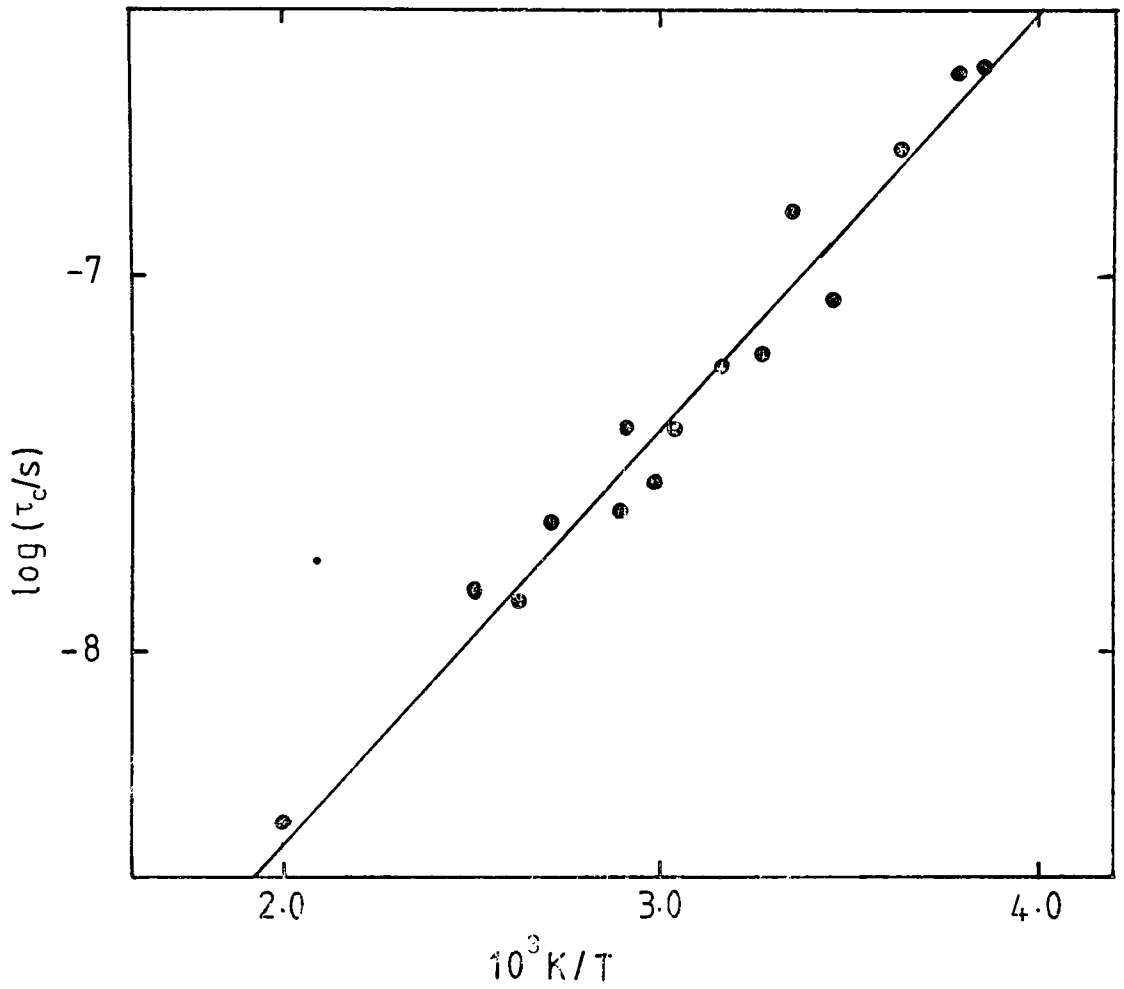

Figure 6·7

τ_c for NH_4^+ β-alumina

(deduced from T_2 data)

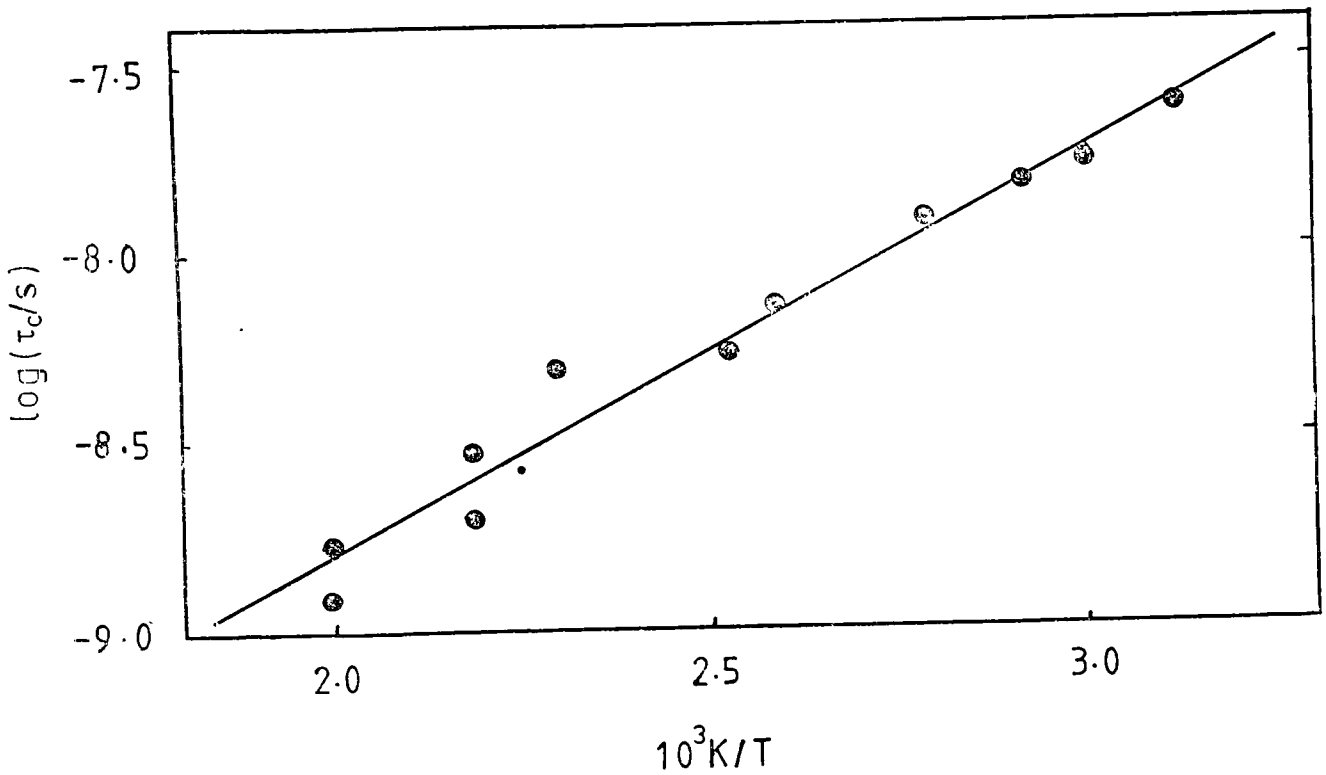

Figure 6·8

τ_c for NH_4^+ β-alumina

(deduced from T_1 data)

at 390K (the temperature of the T_1 minimum) and the corresponding ionic conductivity is 10^{-4}ohm^{-1}cm^{-1}, which is close to the experimental value (5×10^{-5}ohm^{-1}cm^{-1} at 400K, reference 156).

$T_{1\rho}$ for NH_4^+ β-alumina has a minimum (0.66ms) at 325K. The ratio $(T_1)_{min}/(T_{1\rho})_{min}$ is 4, far less than predicted by weak collision (BPP or Torrey) theories. However, assuming the minimum arises from the same process as the T_1 minimum, the local field in the rotating frame ($(\frac{1}{3}M_2)^{\frac{1}{2}}$) is 4.4 G, which is not small compared to the B_1 field (8 G) and this is therefore not a weak collision case.

H_3O^+ β-alumina has been the subject of three recent studies. Kato and Saalfeld (147) carried out an X-ray structure determination and found oxygen atoms in the BR sites. They suggested that, as in H^+ β-alumina (84), a hydrogen is bonded to a pillar oxygen and this is bonded to a water molecule on a BR site. Colomban et al. (183) found, by IR and Raman studies, that H_3O^+ ions are present together with some higher species such as $H_5O_2^+$ and $H_7O_3^+$. Unpublished conductivity studies (184) show that single crystal H_3O^+ β-alumina has $\sigma \sim 10^{-11}$ohm^{-1}cm^{-1} at 293K and this increases until 473K with E_A = 77 kJ mol^{-1}. H_3O^+ β-alumina is thus only a poor ionic conductor, the conductivity at 473K being similar to that for hydrogen bonded crystals (see section 1.2). The conduction mechanism is not known and the magnitude of E_A is not understood. There is possibly extensive hydrogen bonding between the conducting species and structural oxygens. There is no clear evidence for proton migration through the lattice independent of H_3O^+ motion, but exchange between conducting species may occur, perhaps via structural oxygens, at the unit cell level.

Measurements on small single crystals of H_3O^+ β"-alumina (185) show the conductivity $\sim 10^{-5}$ohm^{-1}cm^{-1} at 293K. This is larger than for H_3O^+ β-alumina and this is attributable to differences in the

structure of the conduction plane (see section 1.4). K^+ β"-alumina has similarly been found to have a higher conductivity than K^+ β-alumina (62).

Motions of the H_3O^+ ion have been studied by nmr (186,187) for hydroxonium perchlorate ($H_3O^+ClO_4^-$). The ion is a shallow pyramid with the H-O-H angle 118.5° and the O-H distance 1.01Å. Below 130K, M_2 is 31 G^2, corresponding to a static H_3O^+ ion. In the range $160K < T < 243K$, the observed M_2 is reduced to 10 G^2 by hindered rotation of the H_3O^+ about its C_3 axis. At higher temperatures, rapid isotropic reorientation removes the entire intra-ionic M_2 contribution and M_2 is 2.2 G^2.

Interpretation of the relaxation results for H_3O^+ β-alumina in this work is complicated by the sample being a mixture of β and β" phases (see section 4.3). Treatment of non-exponential spin-lattice relaxation in terms of two exponentials might be expected to separate the relaxation parameters for the two phases, but the situation does not appear to be that simple, the ratio of the amplitudes of the exponentials not being constant. This could be due to their being a number of proton-containing species and sites.

Motional narrowing is seen in the T_2 data above 270K, the data giving $E_A = 27.9 \pm 5.4$ kJ mol^{-1} and $\tau_c^o \sim 10^{-10}$s (estimated from the narrowing criterion $(\gamma^2 M_2)^{\frac{1}{2}} \tau_c = 1$). The proton motion is evidently not the conduction mechanism, which occurs far faster in the β" phase than in the β phase and would lead to non-exponential spin-spin relaxation, T_2 values for the two phases being different. The relaxation is exponential, showing the process to be equally fast in both phases. The ionic conductivity at 293K calculated assuming H_3O^+ transport is the conduction mechanism and is being observed is $\sim 10^{-7}$ ohm^{-1} cm^{-1}, several orders of magnitude greater

than observed experimentally for the β phase, showing the assumption to be wrong. The process could be proton exchange involving the species in the conduction plane and possibly the stuctural oxygens. In chloroauric acid tetrahydrate a proton hopping mechanism (within an unsymmetrical $H_5O_2^+$ ion) occurs with E_A = 24 kJ mol^{-1} (182), which is similar to E_A for this compound. T_2 is observed to increase by a factor of 20 from the low temperature value and, as $T_2 \propto (M_2)^{-\frac{1}{2}}$, protons which are initially close together are taken far apart by the exchange process.

The low temperature M_2 value observed for H_3O^+ β-alumina (estimated to be 15 G^2 from solid echoes) does not correspond to that observed for $H_3O^+ClO_4^-$ in any temperature range. The spin-lattice relaxation data show no sign of a low temperature T_1 minimum due to rotation of H_3O^+ ion. The levelling off of T_1 at low temperatures could be due to relaxation via paramagnetic impurities then being important. If the exchange process modulates the entire M_2, a T_1 minimum at about 10ms is expected (see section 2.6). T_1 at the highest temperatures studied is of this magnitude, and measurements at higher temperatures might show the presence of this minimum. The M_2 value suggests that a large fraction of the protons are not present in H_2O molecules or proton-containing ions, but are in hydroxyl groups. This is the case in gallium sulphate monohydrate ($(H_3O)Ga_3(OH)_6(SO_4)_2$), for which the observed M_2 is 15.3 G^2 (183).

The decay of the solid echo amplitude, $E(\tau)$, with pulse separation, τ, is not Gaussian for H_3O^+ β-alumina or H_4^+ β-alumina. This is not surprising, as neither compound contains proton pairs (see section 2.7).

References (Part A)

1. A.D. Le Claire in "Fast ion transport in solids", ed. W. van Gool (North-Holland, London, 1973)
2. P. McGeehin, A. Hooper, J. Mater. Sci, 21, 1 (1977)
3. P. McGeehin, A. Hooper, A.E. Hughes in ref. 6
4. A. Abragam, "The principles of nuclear magnetism", (Oxford University Press, London, 1961)
5. T.C. Farrar, E.D. Becker, "Pulse and Fourier transform nmr" (Academic Press, London, 1971)
6. G.D. Mahan, W.L. Roth (eds.), "Superionic conductors" (Plenum, New York, 1976)
7. T.H. Estell, S.N. Flengas, Chem. Rev., 70, 339 (1970)
8. T. Takahashi, T. Eseka, H. Iwahara, J. Appl. Electrochem., 5, 197 (1975)
9. A.B. Hart in "Chemistry and the needs of society", (The Chemical Society, London, 1974)
10. H.Y-P. Hong, Mater. Res. Bull., 11, 173 (1976)
11. J.B. Goodenough, H.Y-P. Hong, J.A. Kafalas, Mater. Res. Bull., 11, 203 (1976)
12. B.E. Taylor, A.D. English, T. Berzins, Mater. Res. Bull., 12, 171 (1977)
13. I.D. Raistrick, C. Ho, R.A. Huggins, Mater. Res. Bull., 11, 953 (1976)
14. D.K. Follstaedt, P.M. Richards, Phys. Rev. Lett., 37, 1571 (1976)
15. B.C.H. Steele in ref. 6
16. J. Bruinink, J. Appl. Electrochem., 2, 239 (1972)
17. L. Glasser, Chem. Rev., 75, 21 (1975)
18. M.G. Shilton, A.T. Howe, Mater. Res. Bull., 12, 701 (1977)
19. P.E. Childs, T.K. Halstead, to be published in Mater. Res. Bull.
20. I.F. Chang, B.L. Gilbert, T.I. Sun, J. Electrochem. Soc., 122, 955 (1975)
21. B.W. Faughnan, R.S. Crandall, P.M. Heyman, RCA Reviews, 36, 177 (1975)
22. P.G. Dickens, P.J. Wiseman, MTP International Reviews of Science, Inorganic Chemistry Series 2, vol 10 (1975)
23. A.F. Wells, "Structural Inorganic Chemistry", 4th Edn., (Oxford University Press, 1975)
24. W.R. Busing, H.A. Levy, Acta Crystallogr., 11, 798 (1958)

25. M.F. Pye, J.J. Birtill, P.G. Dickens, Acta Crystallogr., B33, 3224 (1977)
26. P.J. Wiseman, D.Phil thesis (Oxford, 1974)
27. M.F. Pye, Part II thesis (Oxford, 1975)
28. C.H. Holm, C.R. Adams, J.A. Ibers, J. Phys. Chem., 62, 992 (1958)
29. K.A. Wickersheim, G.K.Korpi, J.Chem. Phys, 42, 579 (1965)
30. J.J. Fripiat, H. Bosmans, P.G. Rouxhet, J. Phys. Chem., 71, 1097 (1967)
31. K.J. Gallagher, D.N. Phillips, Trans. Far. Soc., 64, 785 (1968)
32. A.M. Arjona, J.J. Fripiat, Trans. Far. Soc., 63, 236 (1967)
33. Y.K. Wei, R.B. Bernstein, J. Phys. Chem., 63, 738 (1959)
34. A. Mata, J.J.Fripiat, Trans. Far. Soc., 63, 2936 (1967)
35. M.F. Pye, private communication
36. J.J. Fripiat, R. Touillaux, Trans. Far. Soc., 65, 1236 (1969)
37. P.J. Wiseman, P.G. Dickens, J. Solid State Chem., 6, 374 (1973)
38. C.J. Wright, J. Solid State Chem., 20, 89 (1977)
39. J.J. Birtill, D.Phil thesis (Oxford, 1977)
40. F.A. Schroeder, H. Weitzel, Z. Anorg. Allg. Chem, 435, 247 (1977)
41. C.J. Wright, J.J. Birtill,P.G. Dickens, to be published
42. P.G. Dickens, D.J. Murphy, T.K. Halstead, J. Solid State Chem., 6, 370 (1973)
43. M.A. Vannice, M. Boudart, J.J. Fripiat, J. Catal., 17, 359 (1969)
44. K. Nishimura, Solid State Comm., 20, 523 (1976)
45. M.D. Mayers, T.A. Augurt, U.S. patent 3,708,220 (1973)
46. R. Hurditch, Electronics Letters, 11, 142 (1975)
47. M. Green, W.C. Smith, J.A. Weiner, Thin Solid Films, 38, 89 (1976)
48. O. Glemser, G. Lutz, Z. Anorg. Allg. Chem., 264, 17 (1951)
49. O. Glemser, Nachr. Akad. Wiss. Göttingen, Math. Phys. Chem. Abt. IIA, 121 (1955)
50. L. Kihlborg, G. Hägerström, A. Rönnquist, Acta Chem. Scand., 15, 1187 (1961)
51. K. Wilhelmi, Acta Chem. Scand., 23, 419 (1969)
52. I.D. Raistrick, Part II thesis (Oxford, 1969)

53. R. Schoellhorn, R. Kuhlmann, J.O. Besenhard, Mater. Res. Bull., 11, 83 (1976)
54. E. Schwarzmann, O. Glemser, Z. Anorg. Allg. Chem., 312, 45 (1961)
55. V.Y. Kabanov, V.F. Chuvaev, Russ. J. Phys. Chem., 38, 717 (1964)
56. M.L. Freedman, J. Amer. Chem. Soc., 81, 3834 (1959)
57. S. Maricic, J.A.S. Smith, J. Chem. Soc. (London), 886 (1958)
58. S. Abrink, B.G. Brandt, Chemica Scripta, 1, 169 (1971)
59. H.R. Oswald, J.R. Günter, E. Dubler, J. Solid State Chem., 13, 330 (1975)
60. N. Weber in ref. 6
61. C.A. Beevers, M.A.S. Ross, Z. Kristallogr., 97, 59 (1937)
62. J.T. Kummer, Progr. in Solid State Chem., 7, 141 (1972)
63. C.R. Peters, M. Bettman, J.W. Moore, M.D. Glick, Acta Crystallogr., B27, 1826 (1971)
64. M. Bettman, C.R. Peters, J. Phys. Chem., 73, 1774 (1969)
65. M. Bettman, L.L. Terner, Inorg. Chem., 10, 1442 (1971)
66. N. Weber, A.F. Venero, Tech. Report No. SR69-102, Ford Motor Company Publication 12/16/69
67. G. Yamaguchi, K. Suzuki, Bull. Chem. Soc. Japan, 41, 93 (1968)
68. R.J. Baughman, R.A. Lefever, Mater. Res. Bull., 10, 607 (1975)
69. R.C. De Vries, W.L. Roth, J. Am. Ceram. Soc., 52, 364(1969)
70. Y. Le Cars, J. Théry, R. Collongues, Compt. Rend. Acad. Sci. Paris, 274C, 4 (1972)
71. P.E.D. Morgan, Mater. Res. Bull., 11, 233 (1976)
72. W.L. Roth, R.C. De Vries, J. Solid State Chem., 20, 111 (1977)
73. R.J.D. Tilley in "Crystallography and crystal chemistry of materials with layered structures", ed. F. Levy, (Reidel, Dordrecht, 1976)
74. H. Harata, Mater. Res. Bull., 6, 401 (1971)
75. H. Sato, Y. Hirotsu, Mater. Res. Bull., 11, 1307 (1976)
76. W.L. Roth, J. Solid State Chem., 4, 60 (1972)
77. W.L. Roth, F. Reidinger, J. La Placa, in ref. 6
78. Y.Y. Yao, J.T. Kummer, J. Inorg. Nucl. Chem., 29, 2453 (1967)
79. H. Saalfeld, H. Matthies, S.A. Datta, Ber. Deut. Keram. Ges., 45, 212 (1968)

80. T. Nishikawa, T. Nishida, Y. Katsuyama, Y. Kawakita, I. Uei, Nippon Kagaku Kaishi, 6, 1048 (1974)
81. P. McGeehin, B.C. Tofield, private communication
82. T. Kodama, G. Muto, J. Solid State Chem., 17, 61 (1976)
83. T. Kodama, G. Muto, J. Solid State Chem., 19, 35 (1976)
84. W.A. England, A.J. Jacobson, B.C. Tofield, J.C.S. Chem. Comm., 895 (1976)
85. K. Kato, H. Saalfeld, Acta Crystallogr., B33, 1596 (1977)
86. R.D. Shannon, C.T. Prewitt, Acta Crystallogr., B26, 1076 (1970)
87. M.S. Whittingham, Electrochemica Acta, 20, 575 (1975)
88. H. Sato, R. Kikuchi, J. Chem. Phys., 55, 677 (1971)
89. M.J. Rice, W.L. Roth, J. Solid State Chem., 4, 294 (1972)
90. W. van Gool, P.H. Bottelberghs, J. Solid State Chem., 7, 59 (1973)
91. J.C. Wang, M. Gaffari, S. Choi, J. Chem. Phys., 2, 772 (1975)
92. R.H. Radzilowski, Y.F. Yao, J.T. Kummer, J. Appl. Phys., 40, 4716 (1969)
93. C.P. Slichter, "Principles of magnetic resonance", (Harper and Row, New York, 1963)
94. F. Bloch, Phys. Rev., 70, 460 (1946)
95. U. Haeberlen, "High resolution nmr in solids: selective averaging", Adv. Mag. Res. supplement (1976)
96. M. Mehring, " High resolution nmr spectroscopy in solids", (Springer-Verlag, Berlin, 1976)
97. E.R. Andrew in MTP International Reviews of Science, Physical Chemistry Series 2, vol. 4 (1976)
98. J.S. Waugh, L.M. Huber, U. Haeberlen, Phys. Rev. Lett., 20, 180 (1968)
99. C.P. Slichter, D.C. Ailion, Phys. Rev., 135, A1099 (1964)
100. E.R. Andrew, "Nuclear magnetic resonance" (Cambridge University Press, 1955)
101. J.H. van Vleck, Phys. Rev., 74, 1168 (1948)
102. N. Bloembergen, E.M. Purcell, R.V. Pound, Phys. Rev., 73, 679 (1948)
103. R. Kubo, K. Tomita, J. Phys. Soc. Japan, 9, 888 (1954)
104. A.G. Redfield, Adv. Mag. Res., 1, 1 (1965)
105. P.D. Buckley, K.W. Jolley, D.N. Pinder, Progress in nmr spectroscopy, 10, 1 (1975)

106. H.C. Torrey, Phys. Rev., 92, 962 (1953)
107. H.C. Torrey, Phys. Rev., 96, 690 (1954)
108. H.C. Torrey, Phys. Rev., 104, 563 (1956)
109. H.A. Resing, H.C. Torrey, Phys. Rev., 131, 1102 (1963)
110. G.P. Jones, Phys. Rev., 148, 332 (1966)
111. D.C. Look, I.J. Lowe, J. Chem. Phys., 14, 2995 (1966)
112. J.S. Blicharski, Acta Phys. Pol., A41, 223 (1972)
113. D. Wolf, P. Jung, Phys. Rev., 12, B3596 (1975)
114. J.G.Powles, J.H. Strange, Proc. Phys. Soc., 82, 6 (1963)
115. P. Mansfield, Phys. Rev., 137, A961 (1965)
116. E.L. Hahn, Phys. Rev.,80, 580 (1950)
117. I. Solomon, Phys. Rev., 110, 61 (1958)
118. N. Boden, N. Mortimer, Chem. Phys. Lett., 21, 538(1973)
119. N. Boden, Y.K. Levine, R.T. Squires, Chem. Phys. Lett., 28, 523 (1974)
120. N. Boden, M. Gibb, Y.K. Levine, M. Mortimer, J. Mag. Res., 16, 471 (1974)
121. D.J. Murphy, D.Phil thesis (Oxford, 1971)
122. B.I. Hunt, J.G. Powles, Proc. Phys. Soc., 88, 513 (1966)
123. D. Wolf, J. Mag. Res., 17, 1 (1975)
124. P.S. Allen in MTP International Reviews of Science, Physical Chemistry Series 1, vol. 4 (1972)
125. H.S. Gutowsky, G.E. Pake, R. Bersohn, J. Chem. Phys., 22, 643 (1954)
126. D.E. O'Reilly, T. Tsung, J. Chem. Phys., 46, 1291 (1967)
127. N.A. Abood, D.Phil thesis (York, 1976)
128. R.L. Hilt, P.S. Hubbard, Phys. Rev., 134, A392 (1964)
129. S. Clough, J. Phys. C, 9, 1553 (1976)
130. K. Morimoto, J. Phys. Soc. Japan, 40, 804 (1976)
131. R. Srinivasan in MTP International Reviews of Science, Physical Chemistry Series 2, vol. 4 (1976)
132. H.Y. Carr, E.M. Purcell, Phys. Rev., 94, 630 (1954)
133. S. Meiboom, D. Gill, Rev. Sci. Instr., 29, 688 (1958)
134. G.E. Pake, Solid State Physics, 2, 1 (1956)
135. D.C. Look, D.R. Locker, Rev. Sci. Instr., 41, 250 (1970)
136. D.C. Look, D.R. Locker, Phys. Rev. Lett, 20, 987 (1968)
137. R. Freeman, H.D.W. Hill, J. Chem. Phys., 53, 4103 (1970)
138. S.R. Hartmann, E.L. Hahn, Phys. Rev., 128, 2042 (1962)
139. D.C. Ailion, Adv. Mag. Res., 5, 177 (1971)
140. P.R. Bevington, "Data reduction and error analysis for the physical sciences" (McGraw-Hill, New York, 1969)

141. R. Roy, V.G. Hill, E.F. Osborn, J. Amer. Chem. Soc., 74, 719 (1952)
142. J. Böhm, G. Kahan, Z. Anorg. Chem., 238, 350 (1938)
143. V.G. Hill, R. Roy, E.F. Osborn, J. Am. Ceram. Soc., 35, 135 (1952)
144. P.P. Reichertz, W.J. Yost, J. Chem. Phys., 14, 495 (1946)
145. W.O. Milligan, R.L. McAtee, J. Phys. Chem., 60, 273 (1956)
146. C. Choain, F. Marion, Bull. Chim. Soc. France, 212 (1963)
147. K. Kato, H. Saalfeld, Acta Crystallogr., B33, 1596 (1977)
148. A.S.T.M. X-ray powder diffraction file.
149. H.A. Resing, Advances in molecular relaxation processes, 3, 199 (1972)
150. H. Pfeiffer, NMR - basic principles and progress, 7, 53 (1972)
151. H.A. Resing, J. Chem. Phys., 46, 2876 (1967)
152. D. Sames, Ann. d. Phys., 15, 363 (1965)
153. J. Jeener, P. Broekaert, Phys. Rev., 157, 232 (1967)
154. D.C. Ailion, Adv. Mag. Res, 5, 177 (1971)
155. G.C. Farrington, J.L. Duffy, M.W. Breiter, W.L. Roth, to be published in J. Solid State Chem.
156. Ph. Colomban, J.P. Boilot, A. Kahn, C. Lucazeau, Nouveau Journal de Chimie, 2, 21 (1977)
157. M.A. Fitzgibbon, Part II thesis (Oxford, 1972)
158. O. Glemser, Nature, 183, 143 (1959)
159. J. Fraisard, B. Imelik, J. Chem. Phys., 63, 607 (1966)
160. L.W. Reeves, Progress in nmr spectroscopy, 4, 193 (1969)
161. G.E. Pake, J. Chem. Phys., 16, 327 (1948)
162. H.D. Megaw, "Crystal structures: a working approach", (Saunders, London, 1973)
163. D.F. Holcomb, B. Pedersen, J. Chem. Phys., 38, 54 (1963)
164. B. Pedersen, D.F. Holcomb, J. Chem. Phys., 38, 61 (1963)
165. S.P. Gabuda, Yu.G. Kriger, N.K. Moroz, J. Struct. Chem., 17, 297 (1976)
166. T.K. Halstead, N.A. Abood, K.H.J. Buschow, Solid State Comm., 19, 425 (1976)

167. D. Kline, M.S. Story, .L. Roth, J. Chem. Phys., 57, 5180 (1972)

168. W. Bailey, S. Glowinkowski, M. Story, W.L. Roth, J. Chem. Phys., 61, 4126 (1976)

169. J.P. Boilot, L. Zuppiroli, G. Delplanque, L. Jerome, Philos. Mag., 32, 343 (1975)

170. J.P. Boilot, G. Collin, R. Comes, J. Thery, R. Colongues, A. Guinier in reference 6

171. D. Jerome, J.P. Boilot, J. Phys. Paris, 36, L129 (1974)

172. I. Chung, M.S. Story, W.L. Roth, J. Chem. Phys., 11, 4093 (1975)

173. R.E. Walstedt, R. Dupree, J.P. Remeika, A. Rodriguez, Phys. Rev. B, 15, 3442 (1977)

174. R.J. Grant, I.... Hodge, M.D. Ingram, A.R. West, Nature, 266, 42 (1977)

175. J.L. Bjorkstam, C.H. Wei, XIXth Congress Ampere, Heidelberg (October 1976)

176. T. Takahashi in reference 6

177. G. Collin, J.P. Boilot, A. Kahn, J. Thery, R. Comes, J. Solid State Chem., 21, 283 (1977)

178. J.D. Axe, L.M. Corliss, J.M. Hastings, W.L. Roth, O. Muller, J. Phys. Chem. Solids, 39, 155 (1978)

179. A. Watton, D.C. Reynhardt, H.E. Petch, J. Chem. Phys., 65, 4370 (1976)

180. C.A. McDowell, P. Raghunathan, R. Srinivasan, Mol. Phys., 29, 815 (1975)

181. M. Punkinnen, J. Mag. Res., 19, 222 (1975)

182. D.E. O'Reilly, E.M. Peterson, C.E. Scheie, J.M. Williams, J. Chem. Phys., 55, 5629 (1971)

183. Ph. Colomban, G. Lucazeau, R. Mercier, A. Novak, J. Chem. Phys., 67, 5244 (1977)

184. G.C. Farrington, J.L. Duffy, M.W. Breiter, W.L. Roth, to be published in J. Solid State Chem.

185. G.C. Farrington, Fall Electrochemical Society meeting, Atlanta (October 1977)

186. D.E. O'Reilly, E.M. Peters, J.A. Williams, J. Chem. Phys., 54, 96 (1971)

187. J.W. Hennel, M. Polish-Stachura, Acta Phys. Polon, 35, 239 (1969)

188. R.T. Thompson, D.W. Aydon, J. Chem. Phys., 61, 1813 (1974)

PART B

ELECTRONIC STRUCTURE OF MOLECULES

Chapter 7

Wave Functions and Molecular Shape

7.1 Molecular wave functions and electron densities.

The electronic wave function, Ψ, for a molecule with a fixed nuclear framework is a solution of the time independent Schroedinger equation for that molecule.

$$\hat{H}\Psi = E\Psi \qquad (7.1)$$

$\hat{H}$ is the Hamiltonian operator for the system and E is the electronic energy corresponding to the stationary state with electronic wave function, Ψ. $\hat{H}$ contains terms corresponding to the electronic kinetic energy and the electronic potential energy, which arises from electron-electron and electron-nucleus interactions. Born and Oppenheimer (1) showed that treatment of a total molecular wave function as a product of nuclear and electronic wave functions is a good approximation because of the large ratio between electronic and nuclear masses. The solutions of (7.1) depend on nuclear positions and a separate calculation must be performed for each assumed molecular geometry. The equilibrium geometry for any electronic state is that with the lowest total (nuclear + electronic) energy.

The electronic wave function for an N-electron molecule, $\Psi(1,2....N)$, has the following interpretation. The probability of finding electron 1 in dv_1 (with spatial coordinates between $\underline{r}_1 + d\underline{r}_1$, and spin variable between s_1 and $s_1 + ds_1$), electron 2 in dv_2.....etc. is given by

$$\Psi(1,2...N)^* \Psi(1,2...N)\, dv_1 dv_2 ... dv_N \qquad (7.2)$$

for a normalised wave function. The probability of finding electron 1 in dv_1 and electrons 2 to N anywhere is obtained by

summing the probabilities (7.2), keeping the coordinates of electron 1 fixed. The indistinguishability of electrons ensures that all electrons have the same probability of being in dv_1 :-

$$P_1(v_1)\, dv_1 = N\left(\int \Psi(1,2\ldots N)^* \Psi(1,2\ldots N)\, dv_2 dv_3 \ldots dv_N\right) dv_1.$$

The probability of finding an electron in $d\underline{r}_1$ irrespective of spin is thus

$$\rho_1(\underline{r}_1)\, d\underline{r}_1 = \left(\int P_1(v_1)\, ds_1\right) d\underline{r}_1 \qquad (7.3)$$

ρ_1 is the electron density function measured by crystallographers. This function has only three spatial coordinates, whereas the electronic wave function is a function of $3N$ spatial coordinates and N spin coordinates. A knowledge of the electron density is essential in understanding the chemical behaviour of a molecule.

Many of the equations of quantum mechanics are considerably simplified if expressed in atomic units (see e.g. ref 2). Atomic units are used throughout this work.

7.2 The orbital approximation.

In the absence of electron repulsion terms, the Schroedinger equation for an N-electron system could be solved by writing the N-electron wave function as a product of one-electron functions.

$$\Psi(1,2\ldots N) = \chi_a(1)\, \chi_b(2) \ldots\ldots \chi_k(N) \qquad (7.4)$$

The Schroedinger equation would then be separable into a set of equations, each involving the coordinates of only one electron and the solutions being the functions χ. The electron repulsion terms in the Hamiltonian prevent this separation of variables and make it impossible to obtain an exact solution to the Schroedinger equation.

An orbital is simply a useful one-electron wave function for constructing approximate many-electron wave functions. It is an eigenfunction of a one-electron operator, which is not directly related to the complete Hamiltonian except through some approximation involving averaging of the electron-electron interactions. The spin orbitals, χ, are combined space functions, ψ, and spin functions, η, permissible forms of the latter being only α or β (as $m_s = \pm \frac{1}{2}$ for electrons). The Pauli principle requires the many-electron wave function to be antisymmetric with respect to interchange of electrons. Functions of the type (7.4) are thus unsatisfactory, but on writing $\Psi(1,2...N)$ as a Slater determinant of spin-orbitals a satisfactory function is obtained.

$$\Psi(1,2...N) = (N!)^{-\frac{1}{2}} \begin{vmatrix} \chi_a(1)\chi_b(1)...\chi_k(1) \\ \vdots \\ \chi_a(N)\chi_b(N)...\chi_k(N) \end{vmatrix} = |\chi_a \chi_b ... \chi_k| \quad (7.5)$$

The electron density $\rho_1(\underline{r}_1)$ at $\underline{r}_1$, as given in (7.3), can be shown, for a closed shell electronic configuration, to be the sum of the electron densities in the molecular orbitals.

i.e. $\rho_1(\underline{r}) = \sum_i n_i \psi_i^2(\underline{r})$

where n_i is the number of electrons in the orbital ψ_i (i.e. having the spatial wave function ψ_i).

The electronic Hamiltonian for a molecule may be written

$$\hat{H} = \sum_i \hat{h}^c(i) + \sum_{i<j} \frac{1}{r_{ij}}$$

where $\hat{h}_c(i)$ is the so-called core Hamiltonian consisting of the kinetic energy operator and electron-nucleus interaction terms. Operation on the Slater determinant of orthonormal spin-orbitals (7.5) gives the electronic energy E_{el} where

$$E_{el} = \sum_{r=a}^{k} h^c_{rr} + \sum_{pairs} (J_{rs} - K_{rs}) \qquad (7.6)$$

where h^c_{rr}, J_{rs} and K_{rs} are matrix elements of the core Hamiltonian, Coulomb and exchange operators respectively and are given by

$$h^c_{rr} = \int \chi^*_r \hat{h}^c \chi_r \, d\tau$$

$$J_{rs} = \int \chi_r(i)^* \chi_s(j)^* \frac{1}{r_{ij}} \chi_r(i) \chi_s(j) \, d\tau_i \, d\tau_j$$

$$K_{rs} = \int \chi_r(i)^* \chi_s(j)^* \frac{1}{r_{ij}} \chi_s(i) \chi_r(j) \, d\tau_i \, d\tau_j.$$

Application of the variation theorem to the determinantal wave function defines orbitals known as Hartree-Fock self-consistent field (SCF) orbitals. For Ψ to be the best wave function of its type, the spin orbitals χ must be eigenfunctions of the Fock operator $\hat{F}$ where

$$\hat{F} = \hat{h}^c + \sum_{s=a}^{k} (\hat{J}_s - \hat{K}_s) = \hat{h}^c + \hat{G} \qquad (7.7)$$

$\hat{J}_s$ and $\hat{K}_s$ are the Coulomb and exchange operators respectively. The operator $\hat{F}$ is strange in that it depends on its own eigenfunctions.

The eigenvalues of $\hat{F}$ are called orbital energies, ϵ_r.

$$\epsilon_r = F_{rr} = h^c_{rr} + \sum_{s=a}^{k} (J_{rs} - K_{rs}).$$

It follows that the molecular electronic energy, E_{el}, is given by

$$E_{el} = \sum_{r=a}^{k} \epsilon_r - \sum_{pairs} (J_{rs} - K_{rs}).$$

For a function of the type (7.5) the total molecular energy is thus not just the sum of orbital energies plus nuclear repulsion energy. The potential governing the SCF orbitals consists of a core potential and Coulomb and exchange potentials for each electron. Since these latter two depend on the orbitals themselves, an iteration procedure has to be adopted in calculating SCF orbitals.

Removal of an electron from a spin-orbital χ_a, leavin the wave functions for the other orbitals unchanged, gives a positive ion of electronic energy E^+ where

$$E^+ = \sum_{r=b}^{k} h^c_{rr} + \sum_{\substack{\text{pairs} \\ r\neq a, s\neq a}} (J_{rs} - K_{rs})$$

and it follows that

$$E^+ = E_{el} - h^c_{aa} - \sum_{s=a}^{k} (J_{as} - K_{as}) = E - \varepsilon_a$$

Thus $-\varepsilon_a$ can be equated to the ionization potential $(E^+ - E_{el})$, measured experimentally by photoelectron spectroscopy, providing the ionization process is adequately represented without change in the wave functions of the other electrons or the nuclear positions. This is known as Koopmans' theorem.

7.3 Localised orbitals.

Information about chemical bonding in terms of traditional concepts (bonds, lone pairs etc.) is masked by the delocalised multicentre nature of molecular orbitals. Although a delocalised description is very useful for some purposes (e.g. classification of symmetry species, discussion of electronic transitions), an alternative localised description can be achieved by a unitary transformation of the orbitals (3). The individual orbitals are then concentrated in different regions of the molecule. The total electronic wave function (a Slater determinant) is invariant to such a transformation and hence so are the total electron density and molecular energy. Thus a closed shell atomic configuration of s and three p orbitals, whose total electron density is spherical, can be transformed into an equivalent description in terms of four tetrahedral hybrids of the type sp^3. The freedom to transform to a localised description is a consequence

(a) Total electron density in the plane of the molecule.

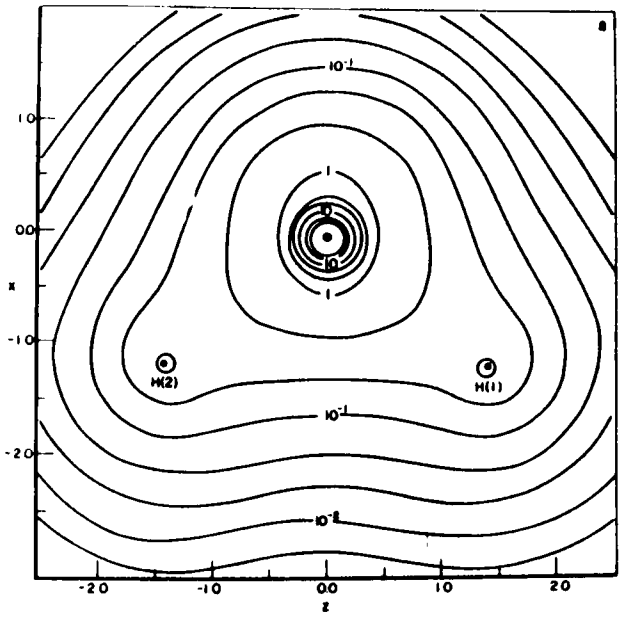

(b) One-electron density for the lone pair orbital.

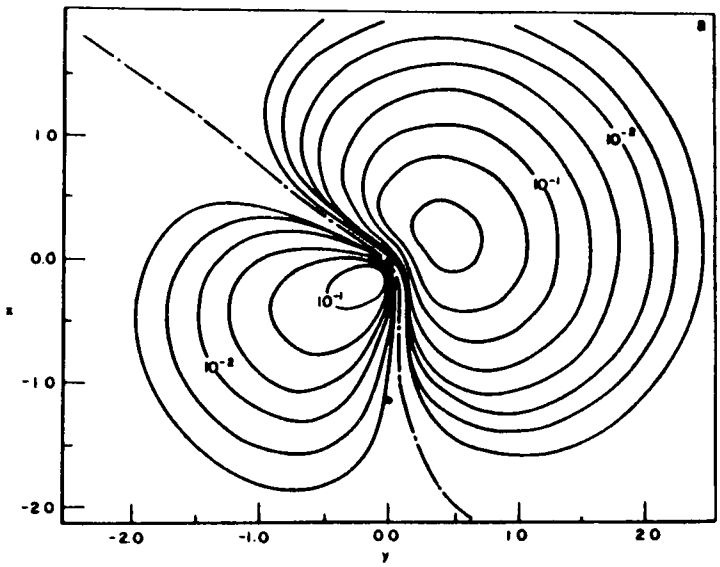

Figure 7.1 Some calculated electron density maps for water.

(c) One-electron density for the bonding orbital.

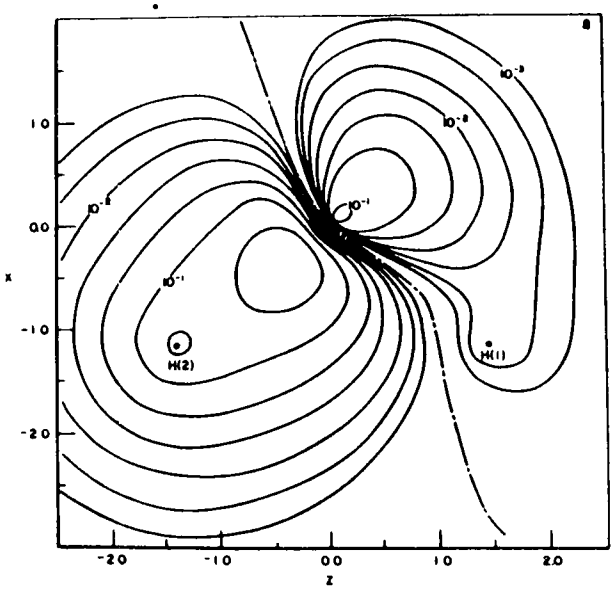

of the Pauli principle, which requires the total electronic wave function to be a determinant rather than a simple product.

Several criteria have been proposed for the localisation of molecular orbitals (4-8) and all give rather similar localised orbitals. A consequence of the conventional expansion of molecular orbitals in terms of orbitals centred on the various atomic centres (the LCAO method) is that transformation of molecular orbitals will not result in orbitals that are completely localised (4,9), as the orthogonality of the localised orbitals then requires that they have contributions from all the atomic centres. One criterion (5) for the localisation of electrons in pairs is the maximisation of the total self-energy, D, where

$$D = \sum_{n=1}^{N/2} J_{nn}.$$

and the sum is over the localised space orbitals. Figure 7.1 illustrates the results of Liang (10) and Taylor (11) who used this criterion for their calculations on the water molecule.

7.4 Binding regions and forces.

A modern emphasis is on the molecular charge distribution and chemical binding (12-14). The Hellmann-Feynman theorem (15,16) states that the force on any nucleus in a molecule is the sum of the electrostatic forces due to the other nuclei and to the electronic charge distribution treated as a continuous charge density by classical methods. Berlin (17) divided the space in a molecule into binding and anti-binding regions. Electron density placed in a binding region binds the nuclei together whereas electron density in an anti-binding region tends to separate them. It follows that there must be a

concentration of electronic charge between the nuclei (i.e. in the binding region) for electrostatic equilibrium.

It is a consequence of the Pauli principle that no two electrons can occupy the same spin-orbital, as two columns of the total determinantal wave function would then be equal and the wave function would vanish. Were this not true, all the electrons in a molecule would crowd into the orbital of lowest energy and would thus concentrate in the binding region. The Pauli principle can thus be considered to force electrons into regions of space where they are remote from some of the nuclei.

7.5 Molecular shapes.

The two most important qualitative molecular shape models are the valence shell electron-pair repulsion (VSEPR) scheme and the use of Walsh-Mulliken diagrams. These continue to provide the conceptual framework for understanding molecular shape, even though far more rigorous quantum mechanical solutions are available for many molecules.

7.5.1 The VSEPR model.

Sidgwick and Powell (18) were the first to relate the angular arrangement of electrons around a central atom to the number of electrons in its valence shell. They put the number of electron pairs in a one-to-one correspondence with molecular shape: two pairs linear, three pairs a planar triangle, four pairs tetrahedral, five pairs a trigonal bipyramid and six an octahedron. These same results are given by the simpler model of point charges on a spherical surface interacting with the force law $(1/r)^n$ whatever the value of n (19). The simplicity of the charges on a sphere model has led to the impression that

electrostatic repulsion between electron pairs is the basic origin of inorganic stereochemistry.

Gillespie and Nyholm (20) recognized a distinction between bonding and lone pairs. The latter are closer to the central nucleus than the former and this leads to the rule for electrostatic interactions: lone pair - lone pair > lone pair - bond pair > bond pair - bond pair. Thus the angle between the bond pairs in ammonia will be less than the tetrahedral angle due to distortion of the tetrahedron in accordance with this rule. The tetrahedral angle is 109.5^{o} and the bond angle in ammonia, 107^{o}, is smaller as predicted. By bringing together existing experimental data and further refining the model, Gillespie has systematised a large body of structural knowledge (21-23).

The total energy of a molecule, E_{tot}, can be partitioned into the following components:-

$$E_{tot} = T + V_{nn} + V_{ne} + V_{ee} \qquad (7.8)$$

where T is the total kinetic energy, V_{nn} is the nucleus-nucleus repulsion energy, V_{ne} the nucleus-electron attraction energy and V_{ee} the electron-electron repulsion energy. The equilibrium configuration is said (24) largely to depend on V_{ee}, this apparently providing the theoretical basis for the VSEPR scheme. This interaction can be visualised classically, in a localised orbital description, in terms of interactions among bond pairs and lone pairs. However V_{ee} is mostly due to repulsions between electrons in the same orbital, repulsions between different orbitals being small in comparison, and it would be surprising if these latter small energy terms were responsible for molecular shape (as determined by the minimum in E_{tot}).

Naleway and Schwartz (25) have considered the VSEPR model for water, using localised orbitals derived from LCAO-SCF molecular orbitals, and find some agreement with the physical ideas of VSEPR theory, though, significantly, no minimum is found in V_{ee} between 90^{o} and 180^{o}. Their localised orbitals were not completely localised however, for the reasons discussed in section 7.3.

Lennard-Jones (26) and, in his later writings (23), Gillespie have urged that the effects of the Pauli principle are much more powerful than electrostatic forces in determining the shapes and properties of molecules.

7.5.2 Walsh-Mulliken diagrams.

A molecular orbital description of molecular shape is embodied in a set of principles known as Walsh's rules (27,28). The basis of the model is the correlation diagram, which is a plot of valence "orbital energies" as a function of a geometrical variable (e.g. bond angle). The assumption is made that the same diagram is applicable to all systems within a given class (e.g. AH_2 molecules). Walsh (27) and Mulliken (28) worked out these diagrams using empirical data and simple assumptions concerning mixing and weighting of atomic orbitals. The diagrams are used to predict molecular shape by filling up the orbitals with pairs of electrons and finding the bond angle giving the smallest sum of "orbital energies".

The precise nature of Walsh's "orbital energies" is a matter of debate. Coulson and Neilson (29) suggested they were "partitioned energies" whose sum (including the core electrons) equalled the total electronic energy. Bingel (30) used the one-electron energies of his united atom Hamiltonian. Schmidtke and Preuss (31) used the eigenvalues of a one-electron Hamiltonian

where the electron-electron interactions are replaced by an effective central field. However, correlation diagrams based on these approaches are in qualitative agreement with Walsh's only for AH_2 and AH_3 molecules. Coulson and Deb (32) have interpreted Walsh's rules in terms of the Hellman-Feynman theorem and have constructed Walsh-type diagrams using calculations of force in terms of valence angle, keeping the central atom fixed. They conclude that the force formulation provides a satisfactory pictorial basis for understanding molecular geometry, but, in the absence of highly accurate electron densities, the approach is unsuitable for quantitative predictions. Peyerimhoff et al. (33) proposed the use of the Hartree-Fock energies, ε_i, as the "orbital energies". The sum of the valence shell Hartree-Fock energies, E_{val}^{HF}, is grossly different from the total molecular energy, E_{tot}. However, E_{val}^{HF} could be a criterion for molecular geometry provided $\partial E_{val}^{HF}/\partial \vartheta$ and $\partial E_{tot}/\partial \vartheta$ maintain similar signs as the valence angle ϑ varies. Unfortunately this is not always true (34), especially for polar molecules. Ruedenberg (35) has shown that, at the molecular equilibrium configuration, a simple approximate relationship exists between E_{tot} and the energies ε_i, this relationship being

$$E_{tot} = \frac{3}{2} \sum_i n_i \varepsilon_i$$

where the sum is over all the occupied orbitals and n_i is the number of electrons in orbital i. Use of the same summation to discuss molecular geometry is not satisfactory, Anno and Sakai (36) having shown that there may be no minimum at the equilibrium configuration.

Allen (37) has attempted to link together the VSEPR scheme and Walsh-Mulliken diagrams by pointing out that the same single determinant wave function giving the Hartree-Fock ε_i values can be transformed to give a localised description which can be discussed in terms of the VSEPR scheme.

7.6 The present work.

Electron-electron repulsions are commonly believed to be important in determining the electron distributions, and hence the molecular geometry, for small molecules. In this work, the importance of these interactions, and other effects discussed in section 7.5, is assessed using the water molecule as a simple model system.

The hydride molecules of the elements of the first short period can be regarded as derived from the neon atom by removal of the appropriate number of protons from the central nucleus and placing them at the appropriate coordinates for the individual molecules. This could be regarded as a two stage process. The first stage is production of a spherical electronic charge cloud by smearing the proton charges over a thin spherical shell of radius the A-H distance for the molecule (where A is the central atom) and the second being the localisation of the protons. The hypothetical spherical entity produced by the first stage is termed a molecular puff.

Single determinant electronic wave functions for molecules and molecular puffs can be obtained by SCF methods, which give the best (lowest energy) wave functions of this type. Perturbation of a molecular puff by localisation of the protons, making no allowance for changes in electron-electron interactions,

gives an approximation to the SCF orbitals. Comparison of the two wave functions (in terms of energies, electron distributions etc.) for the molecule shows the effect of the terms neglected in the perturbation and hence their role in determining molecular geometry.

The one-centre expansion (OCE) method (38,39), where the molecular orbitals are expressed in terms of functions centred on a single origin, is used throughout this work. The molecular puff is itself a single centre system and the OCE method has been applied (38) to first row hydrides, with the origin at the nucleus of the central atom. Perturbation of a molecular puff to give a hydride molecule is akin to the treatments used in ligand field theory, where attention is focussed on the effect of the perturbing charges on the orbitals of the central atom. An advantage of the OCE method is that truly localised orbitals can be obtained, orthogonality being satisfied without contributions from around all the nuclei present (see section 7.3).

All calculations in this work were carried out on the Oxford University Computing Laboratory ICL 1906A computer using programs written by the author. Some of these programs are listed on microfiche in the programs appendix.

Chapter 8

The One-Centre Calculations

8.1 The matrix formulation of SCF theory.

Molecular orbitals are commonly represented as linear combinations of known one-electron functions. From a basis set of m linearly independent functions, ϕ, m linearly independent orbitals, ψ, can be constructed.

$$\psi_j = \sum_{i=1}^{m} c_{ij} \phi_i .$$

The electronic energy (equation 7.6) for an N-electron system is then a function of the expansion coefficients, c_{ij}, of the N/2 occupied orbitals, and variational minimisation gives m equations of the form

$$\sum_{j=i}^{m} (F_{ij} - \varepsilon S_{ij}) c_{ij} = 0$$

where $F_{ij} = \langle \phi_i | \hat{F} | \phi_j \rangle$ and $S_{ij} = \langle \phi_i | \phi_j \rangle$. These equations are known as Roothaan's equations (40,41) and can be written in matrix form as

$$FC = \varepsilon SC$$

where F and S are mxm matrices, with elements F_{ij} and S_{ij}, and C is a column vector with elements c_{ij}. Solution of the matrix equation

$$(F - \varepsilon S)C = 0$$

gives m approximate SCF orbitals and corresponding orbital energies. The (m - N/2) solutions in addition to the N/2 occupied orbitals are termed virtual orbitals and describe the states of a test electron moving in the field of the whole neutral molecule. Increasing the number of basis functions leads to better approximations to a larger number of orbitals.

The Fock operator (equation 7.7) may be written as

$$\hat{F} = \hat{h}^c + \hat{G}$$

and hence

$$F = H + G$$

where H and G are matrices with elements H_{ij} ($\langle \phi_i | \hat{h}^c | \phi_j \rangle$) and G_{ij} ($\langle \phi_i | \hat{G} | \phi_j \rangle$) respectively. A matrix T containing the column vectors of the occupied orbitals can be written

$$T = (C_A | C_B | \ldots\ldots)$$

and a matrix R is related to this by

$$R = TT^+$$

where T^+ is the transpose of T. The molecular electronic energy is given by

$$E_{el} = 2 \text{ tr } (RH) + \text{tr } (RG) \qquad (8.1)$$

where tr denotes the trace (sum of the diagonal elements) of a matrix.

In the matrix formulation, F is a function of the expansion coefficients c_{ij} and the eigenvalue equation has to be solved iteratively. An initial Fock matrix, F^o, is calculated from a suitably chosen initial coefficient matrix, T^o, and the new coefficient matrix, T^1, is calculated from F^o. This iterative cycle is continued until the solutions converge in accord with some criterion. Commonly used criteria (2,24,42) are the matrices T or R or the eigenvalues ϵ being the same, to a required accuracy, on successive cycles. In this work, a simple linear extrapolation procedure was used where

$$F_{ij}^{n+1} = F_{ij}^{calc} + \delta (F_{ij}^{calc} - F_{ij}^{n})$$

and F_{ij}^{calc} is that calculated using T^{n+1} and δ is an extrapolation parameter (taken to be 1/3). This extrapolation procedure ensured more rapid convergence than unconstrained iteration. The criterion for self-consistency was taken as the convergence

of E_{el}, as given by

$$E_{el} = 2tr\ (R^n H^{n-1}) + tr\ (R^n G^{n-1})$$

to within 10^{-6} hartrees on successive cycles. This generally occurred before the twentieth cycle.

8.2 The one-centre expansion method.

The one-centre expansion (OCE) method (38,39) uses, as a basis set for the expansion of a wave function, functions centred on a common origin, usually a nuclear position. The principal advantage of the method is that, though many more basis functions are needed than in conventional methods, the difficult task of evaluating multi-centre integrals is avoided. The basis set of orbitals may have no natural association with the problem itself but the resulting molecular orbitals can be transformed to truly localised orbitals.

A one-centre wave function is most in error close to off-centre nuclei, where cusp conditions are difficult to fulfil. Cohen and Coulson (43) have considered the H_2^+ molecule ion and find OCE functions good except at the hydrogen nuclei, where no cusps are produced. Electron density maps of Saturno and Parr's (44,45) one-centre function for methane show no maxima at the hydrogen nuclei. The errors are least when the off-centre nuclei have small charges and it is for this reason that the hydrides AH_n are the most suitable for one-centre (the heavy atom nucleus) calculations.

Moccia (46) used one-centre basis sets for extensive calculations on hydride molecules. Not only were equilibrium internuclear distances and bond angles computed very well, but also the dipole moments. The functions used were Slater-type

orbitals (STO's) of s,p,d and f type centred on the heavy atom. STO's have the functional form

$$\phi_{n,l,m} = Nr^{n-1} \exp(-Ur)\, Y_l^m$$

where N is a normalising constant given by

$$N = (2U)^{n+\frac{1}{2}}/((2n)!)^{\frac{1}{2}},$$

U is the orbital exponent and Y_l^m is a spherical harmonic normalised to unity.

In this work, Moccia's basis set for water (46) is taken as the best of its type and used for molecular puff and perturbation calculations. Further SCF molecular and molecular puff and perturbation calculations were carried out using a subset of Moccia's basis set, the functions chosen being the principal contributors to Moccia's molecular orbitals for water. Table 8.1 gives the basis functions used in each case. Moccia's notation is used and requires that the dependence on the angular coordinate ϕ be $\sin(m\phi)$ when m is negative and $\cos(m\phi)$ when ϕ is positive.

8.3 The potential due to the protons.

The potential, V, due to the hydrogen nuclei in hydride molecules can be expanded as a series of spherical harmonics centred on the central atom (47,48). It is convenient to work in polar coordinates and express V as

$$V = \sum_k \sum_q a_k^q R^k(r)\, Y_l^m(\vartheta,\phi).$$

a_k^q are expansion coefficients, $R^k(r)$ are radial functions and Y_k^q are spherical harmonics in their complex form, normalised to unity. The spherical harmonics used in this work had the "natural" choice of phase (49,50).

i.e. $Y_l^m(\vartheta,\phi) = (-1)^m Y_l^{-m}(\vartheta,\phi)$.

Table 8.1

Basis set of STO's for water

n	l	m	U	Function label: Complete set	Function label: Smaller set
1	0	0	12.60	1	
1	0	0	7.45	2	s_1
2	0	0	2.20	3	s_2
2	0	0	3.24	4	
2	0	0	1.28	5	
2	1	0	1.51	6	p_z
2	1	0	2.44	7	
2	1	0	3.92	8	
3	2	0	1.60	9	d_{z^2}
3	2	0	2.40	10	
3	2	2	1.60	11	$d_{x^2-y^2}$
3	2	2	2.40	12	
4	3	0	1.95	13	
4	3	2	1.95	14	
2	1	-1	1.51	15	p_y
2	1	-1	2.44	16	
2	1	-1	3.92	17	
3	2	-1	1.60	18	d_{yz}
3	2	-1	2.40	19	
4	3	-1	1.95	20	
4	3	-3	1.95	21	
2	1	1	1.51	22	p_x
2	1	1	2.44	23	
2	1	1	3.92	24	
3	2	1	1.60	25	d_{xz}
3	2	1	2.40	26	
4	3	1	1.95	27	
4	3	3	1.95	28	

An effective termination of the series can be imposed by symmetry. In evaluating matrix elements of V, terms of the form $\langle A_1 | Y_k^q | A_2 \rangle$ arise, where A denotes the angular part of a basis function. If any of these integrals vanish identically, there is no point in knowing the associated radial functions or expansion coefficients. The angular parts of the basis functions in this work (STO's) are spherical harmonics. The integrals $\langle Y_{l'}^{m'} | Y_k^q | Y_l^m \rangle$ vanish unless a vector triangle can be constructed from the suffices l, l', k. In this work the maximum value of l used is 3 and hence only terms with k upto and including 6 need be considered.

The expansion coefficients, a_k^q, are given by

$$a_k^q = \frac{4\pi}{2k+1} \sum_n Y_k^{q*}(\vartheta_i, \phi_i)$$

where the sum is over the n hydrogen nuclei. The radial functions, $R^k(r)$, are defined by

$$R^k(r) = r^k/a^{k+1} \quad \text{for } r < a$$
$$= a^k/r^{k+1} \quad \text{for } r > a$$

where a is the O-H bond length. Evaluation of the radial part of a matrix element of V has thus to be done in two parts.

The first term, V_o, in the expansion of V has a particularly simple interpretation

$$V_o = n 4\pi Y_o^o R^o(r) Y_o^o$$
$$= \frac{n}{a} \text{ for } r < a \text{ and } \frac{n}{r} \text{ for } r > a.$$

This is simply the potential due to a thin spherical shell of radius a and total charge n. V for the water molecule can thus be written as the sum of two terms.

$$V = V_o + V_{C_{2v}} \qquad (8.2)$$

$V_{C_{2v}}$ is the potential due to the further terms in the expansion, which impart C_{2v} symmetry to the molecule.

8.4 Molecular puffs and the perturbation method.

The orbitals calculated by SCF methods are eigenfunctions of the Fock operator appropriate to the molecule or molecular puff. For a hydride molecule this operator is given by

$$\hat{F}_{mol} = \hat{h}^{c}_{mol} + \hat{G}_{mol}$$
$$= -\tfrac{1}{2}\nabla^2 - \frac{Z}{r} - V + \hat{G}_{mol}$$

where $\hat{G}_{mol}$ is found interatively, r is the distance of the electron from the central nucleus and Z the charge on this nucleus. V for water can be written (equation 8.2) as $V_o + V_{C_{2v}}$. The Fock operator for the corresponding molecular puff (see section 7.6) is

$$\hat{F}_{puff} = \hat{h}^{c}_{puff} + \hat{G}_{puff}$$
$$= -\tfrac{1}{2}\nabla^2 - \frac{Z}{r} - V_o + \hat{G}_{puff}$$

where $\hat{G}_{puff}$ is found iteratively and will differ from $\hat{G}_{mol}$ as the electron-electron interactions in a molecular puff and a molecule differ.

The perturbation method used in this work consists in saying that the molecular orbitals of the molecule are eigenfunctions of the one-electron operator $\hat{P}$ where

$$\hat{P} = \hat{F}_{puff} + V_{C_{2v}}$$
$$= \hat{h}^{c}_{mol} + \hat{G}_{puff}$$

This can be regarded as an approximation to the true molecular Fock operator with the electron-electron interactions taken to be the same in the spherical molecular puff and the C_{2v} water molecule (*i.e.* $\hat{G}_{puff} = \hat{G}_{mol}$). $\hat{F}_{puff}$ depends on the expansion

coefficients of the orbitals for the molecular puff and is found by SCF methods. The molecular orbitals are then calculated by solving the matrix equation

$$(P - \varepsilon S)C = 0$$

As $\hat{P}$ is known exactly, no iteration is necessary. The molecular electronic energy, E_{el}, corresponding to a wave function built-up from molecular orbitals calculated by this perturbation method is calculated using equation 8.1

$$E_{el} = 2tr(RH) + tr(RG).$$

R is calculated from the molecular orbital coefficients, $H_{ij} = \langle \phi_i | \hat{h}^c_{mol} | \phi_j \rangle$ and G_{ij} are calculated using the calculated molecular orbital coefficients. G_{ij} values differ *from* those for the molecular puff or the SCF molecule.

Comparison of molecular wave functions calculated by the SCF and perturbation methods allows an assessment of the importance of the differences in $\hat{G}_{puff}$ and $\hat{G}_{mol}$ in determining molecular geometry and hence also of the role of electron-electron interactions in this.

8.5 Matrix element evaluation.

Matrix elements were evaluated using exact analytical formulae. The author's computer programs, including these calculations, are listed on microfiche in the programs appendix.

The matrix element F_{ij} can be written as (51)

$$F_{ij} = \langle \phi_i | \hat{F} | \phi_j \rangle = H_{ij} + G_{ij}$$
$$= H_{ij} + 2 \sum_{k=1}^{m} \sum_{l=1}^{m} R_{kl} (2 \langle ik|q|jl \rangle - \langle ik|q|lj \rangle)$$

where $\langle ab|q|cd \rangle = \iint \phi^*_a(1)\phi^*_b(2) \frac{1}{r_{12}} \phi_c(1)\phi_d(2)\, d\underline{r}_1\, d\underline{r}_2$.

The integrals $\langle ab|q|cd \rangle$ can be shown (49) to be given by

$$\langle ab|q|cd \rangle = \delta(m_a+m_b, m_c+m_d) \sum_{k=|m|}^{\infty} c^k(l_a m_a l_c m_c)\, c^k(l_d m_d l_b m_b)\, R^k(n_a l_a n_b l_b, n_c l_c n_d l_d) \quad (8.3)$$

where n_i, l_i, m_i are determined by the basis functions and

$$|m| = m_a - m_c = m_d - m_b.$$

Gaunt (52) has given general formulae for the coefficients $c^k(lm\ l'm')$. Computer routines for evaluation of these coefficients were given by D.F. Mayers of the Oxford University Computing Service. The radial integrals are given by

$$R^k(n_a l_a n_b l_b, n_c l_c n_d l_d) = \int\int \frac{r_<^k}{r_>^{k+1}} R_a(1) R_b(2) R_c(1) R_d(2)\, dr_1 dr_2$$

where R_i is the radial part of the basis function ϕ_i, $r_<$ is the lesser of r_1 and r_2 and $r_>$ the greater of the two. For $c^k(lml'm')$ to be non-zero the conditions

$$k + l + l' = 2g \quad (g \text{ integral})$$

$$|l - l'| \leq k \leq l + l'$$

must be satisfied, this limiting the necessary range of the summation in equation 8.3.

The elements H_{ij} can be written as

$$H_{ij} = \langle \phi_i | -\tfrac{1}{2}\nabla^2 - \frac{Z}{r} - V | \phi_j \rangle$$

$$= \langle \phi_i | -\tfrac{1}{2}\nabla^2 - \frac{Z}{r} | \phi_j \rangle - V_{ij}$$

where $V_{ij} = \langle \phi_i | V | \phi_j \rangle = \langle R_i Y_i | \sum_p \sum_q c_q^p R^p(r) Y_p^q | R_j Y_j \rangle$

$$= \sum_p \sum_q c_p^q \langle R_i | R^p(r) | R_j \rangle \langle Y_i | Y_p^q | Y_j \rangle$$

The angular integral is simply related to a Gaunt coefficient by

$$\langle Y_i | Y_p^q | Y_j \rangle = \delta(q, m_i - m_j) \cdot \frac{2p+1}{4\pi} \cdot c^p(l_i m_i, l_j m_j).$$

The radial integral has to be evaluated in two parts, as discussed in section 8.3.

8.6 The virial theorem and scaling.

The virial theorem for a stationary state of a system of electrons and nuclei interacting only through electrostatic forces is

$$2\langle T \rangle + \langle V \rangle = 0$$

where $\langle T \rangle$ and $\langle V \rangle$ are the expectation values of the total kinetic and potential energies. The total energy is

$$E_{tot} = \langle T \rangle + \langle V \rangle$$

and hence

$$E_{tot} = - \langle T \rangle .$$

In the Born-Oppenheimer approximation these equations are strictly only valid for the equilibrium configuration of a molecule or for separate atoms. The theorem is satisfied by exact eigenfunctions of the molecular Hamiltonian, and by certain classes of approximate wave functions, including accurate Hartree-Fock functions.

An approximate wave function can be made to satisfy the virial theorem by a scaling procedure, which is commonly used (53,54). A scale factor, λ, is defined by

$$\lambda = - \langle V \rangle / 2 \langle T \rangle$$

and a new wave function can be defined with total energy, E'_{tot}, where

$$E'_{tot} = \lambda^2 \langle T \rangle + \lambda \langle V \rangle .$$

The new scaled electronic wave function $\Psi'(\underline{r})$ is related to the unscaled wave function $\Psi(\underline{r})$ by

$$\Psi'(\underline{r}) = \lambda^{3N/2} \Psi(\lambda \underline{r})$$

and satisfies the virial theorem. $\Psi'(\underline{r})$ is a wave function applicable to a system where the internuclear distances are λ those used to calculate the unscaled wave functions.

In this work, the variation of terms included in E_{tot} is followed as a function of the bond angle for the water molecule using a basis set of only 9 one-centre functions (STO's) to give an approximate electronic wave function. The energy terms considered are those in equation 7.8 and are scaled to

satisfy the virial theorem. Kaleway and Schwartz (25) also scaled the various energy terms in their work. In this work

$$E'_{tot} = \lambda^2 \langle T \rangle + \lambda \langle V \rangle$$
$$= \langle T \rangle' + \langle V \rangle'_{nn} + \langle V \rangle'_{ne} + \langle V \rangle'_{ee}$$
$$= - \langle T \rangle'$$

where $\langle T \rangle' = 2\lambda^2 \text{ tr } (RA) \quad (A_{ij} = \langle \phi_i | -\frac{1}{2}\nabla^2 | \phi_j \rangle)$

$\langle V \rangle'_{ne} = 2\lambda \text{ tr } (RB) \quad (B_{ij} = \langle \phi_i | -\frac{Z}{r} - V | \phi_j \rangle)$

$\langle V \rangle'_{ee} = \lambda \text{ tr } (RG)$

$\langle V \rangle'_{nn} = \frac{16\lambda}{r_{O-H}} + \frac{\lambda}{r_{H-H}}$ for the molecule $= \frac{17\lambda}{r_{O-H}}$ for the puff.

8.7 Orbital localisation and the dipole moment.

A number of different localisation criteria have been proposed (see section 7.3). The two most commonly used are the maximum total self-energy criterion of Edmiston and Ruedenberg (5) and the maximum electron distance method of Boys (55,56). The former maximises the sum $\sum_i \langle l_i l_i | \frac{1}{r_{12}} | l_i l_i \rangle$ over the occupied orbitals, l_i, and involves calculation of two-electron integrals, m^4 of them for a basis set of m functions. Boys' method maximises the term $\sum_i \langle l_i | \underline{r} | l_i \rangle . \langle l_i | \underline{r} | l_i \rangle$, needing the calculation of only m^2 one -electron integrals, and has the additional advantage that the centroids of the localised orbitals are calculated as part of the localisation procedure. Boys' method was therefore used in this work.

The point group for the water molecule is C_{2v} and the molecule is placed in the YZ plane. The valence shell molecular orbitals are $2a_1, 3a_1, 1b_2$ and $1b_1$. The localised orbitals, l_i, can be written

$$l_i = d_{i1}\psi_{2a_1} + d_{i2}\psi_{3a_1} + d_{i3}\psi_{1b_1} + d_{i4}\psi_{1b_2}$$

and these equations are summarised in the matrix equation

$$L = D\underline{\psi}$$

where $\underline{\psi}$ is the column vector of molecular orbitals. If l_1 and l_2 are bonding orbitals and l_3 and l_4 are lone pair orbitals, it follows from the symmetry and orthormality of the localised orbitals that

$$d_{13} = d_{23} = d_{34} = d_{44} = 0$$
$$d_{14} = d_{24} = d_{33} = d_{43} = 1/\sqrt{2}$$
$$d_{12} = d_{22} = (\tfrac{1}{2} - d_{11}^2)^{\frac{1}{2}} = (\tfrac{1}{2} - d_{21}^2)^{\frac{1}{2}}$$
$$\frac{d_{11}}{d_{12}} = \frac{d_{21}}{d_{22}} = -\frac{d_{32}}{d_{31}} = -\frac{d_{42}}{d_{41}}$$

Fixing a value for d_{11} determines all the other unknown coefficients. As $\underline{\psi} = T\underline{\phi}$ (see section 8.1), the localised orbitals are related to the basis functions by the equation

$$L = DT\,\underline{\phi} = K\,\underline{\phi}$$

where k_{ij} are the expansion coefficients of the localised orbitals.

Boys' localisation minimises I where

$$I = \sum_a \langle l_a l_a | r_{12}^2 | l_a l_a \rangle$$
$$= -2 \sum_a R_a^2 + 2 \sum_a \langle l_a | r_1^2 | l_a \rangle$$

and $\underline{R}_a = \langle l_a | \underline{r} | l_a \rangle$ and $R_a^2 = \underline{R}_a . \underline{R}_a$. The second term is invariant to all unitary transformations and minimisation of I therefore corresponds to maximisation of S where

$$S = \sum_a \langle l_a | \underline{r} | l_a \rangle . \langle l_a | \underline{r} | l_a \rangle$$

(as discussed previously). S can be expanded in terms of the expectation values of the components of the dipole moment operator for the localised orbitals.

$$S = \sum_a \langle l_a | x | l_a \rangle^2 + \langle l_a | y | l_a \rangle^2 + \langle l_a | z | l_a \rangle^2$$
$$= \sum_a \langle x \rangle_a^2 + \langle y \rangle_a^2 + \langle z \rangle_a^2$$

The coordinates of the centroids of the localised orbitals are $(\langle x \rangle_a, \langle y \rangle_a, \langle z \rangle_a)$, and Boys' criterion therefore involves maximisation of the sum of the squares of the distances between localised orbital centroids. It is easily shown that

$$\langle x \rangle_a = \sum_i k_{ai}^2 x_{ii} + 2 \sum_{i<j} \sum k_{ai} k_{aj} x_{ij}$$

where $x_{ij} = \langle \phi_i | x | \phi_j \rangle$, and there are similar formulae for $\langle y \rangle_a$ and $\langle z \rangle_a$.

In this work, S was calculated over a range of d_{11} values. The maximum S was then found by cubical curve fitting to four points around the maximum, the value of d_{11} there giving orbitals localised according to Boys' criterion.

The electronic dipole moment, μ_e, for a molecule is

$$\mu_e = -2 \sum_i \langle z \rangle_i$$

where the sum is over all the occupied orbitals. Calculation of μ_e is therefore akin to the localisation procedure. μ_e is a molecular property and is invariant to unitary transformations of the orbitals. It can therefore be evaluated with the valence shell in either a localised or a molecular orbital description, this providing an internal check of the author's computer programs.

8.8 Electron density maps.

The concepts involved in discussion of electron density are best presented visually. An electron density map for any plane in a molecule can be produced. Streitweiser and Owens (57) have compiled a book of computer drawn molecular orbital contour diagrams for small molecules.

For a molecule with a closed shell configuration, the electron density at $\underline{r}$ is given by

$$\rho_1(\underline{r}) = 2 \sum_i \psi_i(\underline{r})^* \psi_i(\underline{r})$$

where the sum is over the i occupied orbitals. Electron densities for orbitals (molecular or localised) and filled valence shells can also be considered, the former considering only one term in the sum and the latter only terms involving the valence shell.

In this work, electron density maps for various molecular planes and functions (molecular/valence/orbital) were produced by the author using the Calcomp-GPCP (58) contouring package at the Oxford University computing laboratory. Difference maps, showing changes in electron density in going from molecular puff to molecule, were also calculated. Data points were generated (by the author's programs) over a square grid of 625 points and the contouring package then produced smooth contours using a 20 point interpolation procedure.

Chapter 9

Results of one-centre calculations

9.1 Quality of basis sets.

Moccia's single determinant one-centre SCF calculations on the water molecule (46) give a molecular energy of -75.9225, very close to the estimated Hartree-Fock limit of -76.088. The more complicated one-centre configuration interaction calculations of Bishop and Randic (59), using 19 determinants, give a molecular energy of -75.8611, not as good as Moccia's value. Moccia's basis set is thus very good for calculations on water, the best of its kind. Single determinant LCAO calculations, with extended basis sets on all the nuclear centres, can get closer to the Hartree-Fock limit (e.g. -76.0631, ref.60).

In this work, Moccia's basis set was used for high accuracy calculations involving the water molecular puff and perturbation of this to give a wave function for the water molecule. In addition, a subset of this was used in calculations at a variety of bond angles by both perturbation and SCF methods. The functions chosen for this were of the types 1s,2s,2p and 3d and were the principal contributors to the molecular orbitals in Moccia's SCF calculations (see section 8.2). Inclusion of functions of d symmetry was essential if the final electron density was not to be spherical, as it was in some of Bishop's calculations (61). Use of the smaller basis set results in less accurate energies than calculations using Moccia's full basis set. In all calculations, the O-H bond length, and hence the radius of the molecular puff also, was taken to be 1.814, Moccia's value for the equilibrium bond length.

9.2 The molecular puff.

Table 9.1 summarises the molecular orbitals and energies calculated for the water molecular puff using Moccia's basis set. The orbitals obtained using the smaller basis set are given in Appendix 2.

Calculations involving molecular puffs have been carried out by a number of workers (61-63). Bishop (61) has calculated wave functions for water which give a spherical electron density. The name "molecular puff", for the system of a central nucleus and a thin spherical shell of positive charge was first used by Hauk, Parr and Hameka (62), who used a molecular puff as a first stage in their one-centre calculation of molecular energies.

The molecular electronic energy for the molecular puff was calculated to be -84.8289 using Moccia's basis set and -84.4658 using the smaller basis set. The molecular puff is a spherical problem, best treated by one-centre methods, and thus, in view of the quality of Moccia's basis set, the former value is likely to be close to the Hartree-Fock limit.

Figures 9.1 and 9.2 illustrate electron densities calculated, using Moccia's basis set, for the molecular puff. Figure 9.1 shows the electron density for the valence shell, the dashed line being equal in length to the radius of the thin spherical shell. Figure 9.2 shows the electron density for a pair of electrons in an sp^3 hybrid orbital.

Table 9.1

The H_2O molecular puff

Function	1s	2s	$2p_z$	$2p_y$	$2p_x$
1	0.05169	0.02009			
2	0.94639	-0.26516			
3	-0.01739	0.79780			
4	0.02550	0.10821			
5	0.00498	0.15997			
6			0.81838		
7			0.02045		
8			0.24524		
15				0.81838	
16				0.02045	
17				0.24524	
22					0.81838
23					0.02045
24					0.24524
Eigenvalues	-20.4537	-1.2527	-0.5304	-0.5304	-0.5304

E_{tot} = -75.457326 E_{el} = -84.828881

V_{nn} = 9.371555 T = 75.910904

V_{ne} = -198.973621 V_{ee} = 38.233836

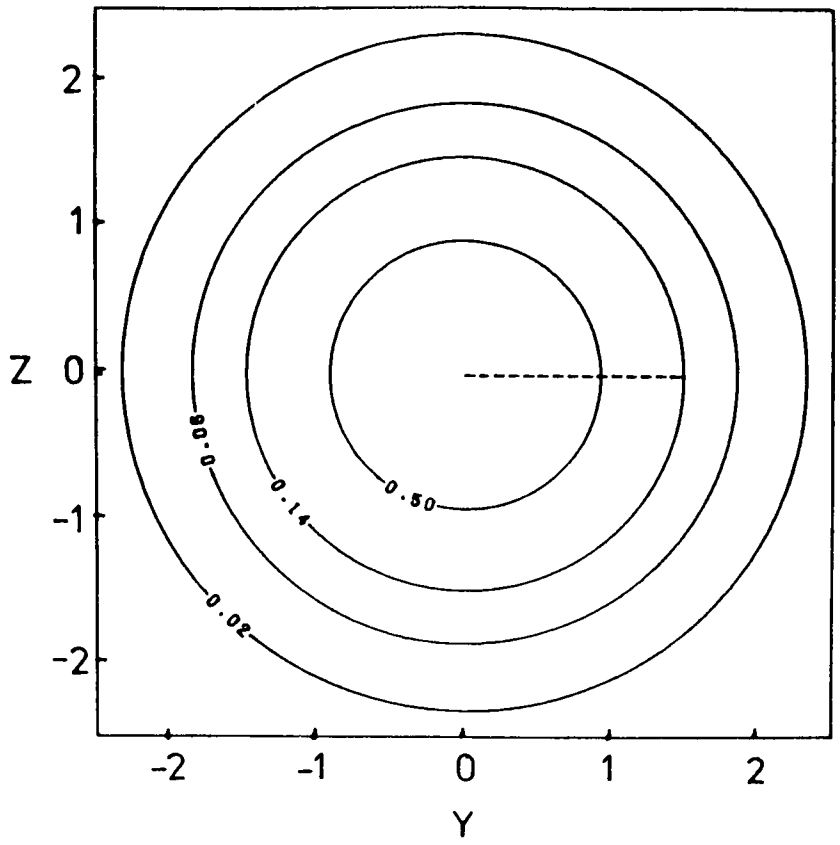

Figure 9.1 Valence shell electron density for the molecular puff

Figure 9.2 Electron density for a doubly occupied sp^3 hybrid

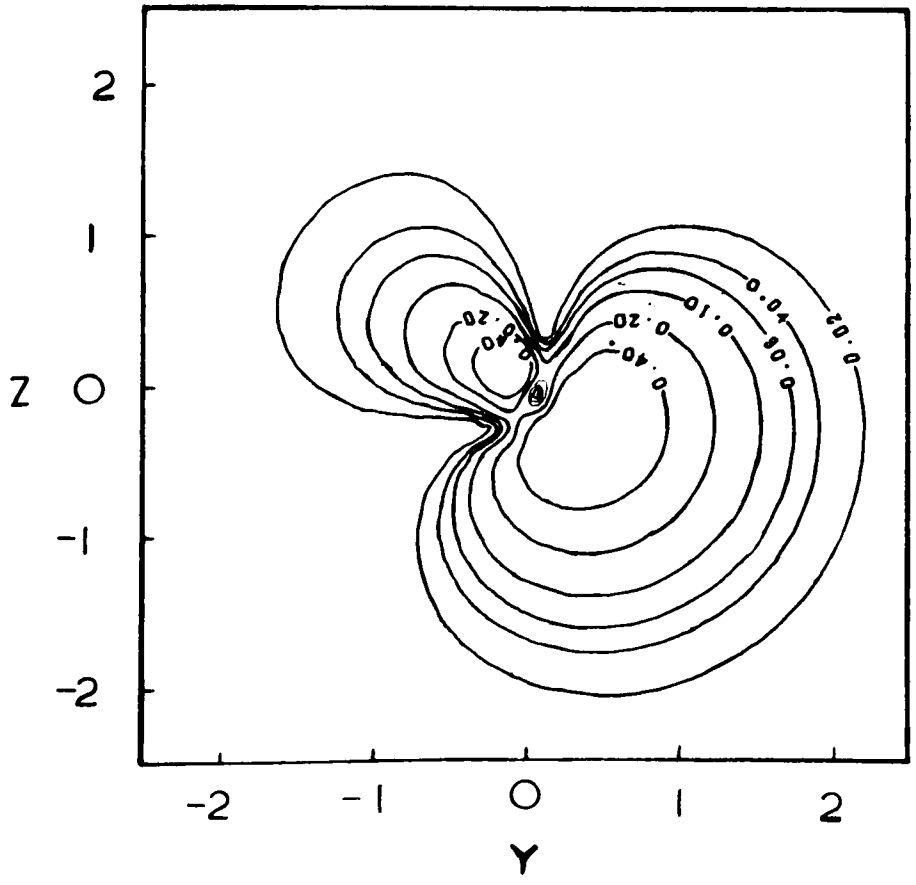

9.3 SCF and perturbation calculations.

The perturbation method used in this work is similar to those of Hauk, Parr and Hameka (62) and Kim and Parr (63). In these methods, the molecular wave function is calculated, numerically rather than analytically as in this work, assuming each molecular puff orbital is independently perturbed by the one-electron perturbing (nuclear localisation) potential (see section 8.4). The energy increment, on going from the molecular puff to the molecule, is then calculated using integral Hellmann-Feynman theorem (64).

Table 9.2 summarises the molecular orbitals calculated in this work for a bond angle of 106.54° (Moccia's equilibrium bond angle) using the perturbation method.

Table 9.3 summarises the energy terms, calculated using the author's computer programs, for the molecular wave function, the results for both Moccia's SCF calculation and the perturbation method being given. Moccia does not give values for V_{ne}, V_{ee} or T. The energy terms calculated in this work differ only very slightly from those he gives (e.g. in the fourth figure after the decimal point for E_{tot}), the differences being due to different rounding errors in the computer programs used.

Table 9.4 gives details of the calculated centroids of the localised orbitals; r is the distance of the centroid from the oxygen nucleus and ϑ the angle subtended at it by equivalent centroids (e.g. by two bonding pairs). The centroid of an sp^3 hybrid for the molecular puff is also given.

Table 7.2

Molecular orbitals for H_2O by the perturbation method

Function	$1a_1$	$2a_1$	$3a_1$	$1b_2$	$1b_1$
1	0.05169	0.01757	-0.00980		
2	0.94638	-0.24655	0.09785		
3	-0.01741	0.76063	-0.29907		
4	0.02552	0.08683	-0.06023		
5	0.00498	0.16956	0.05598		
6	0.00110	0.22450	0.81639		
7	-0.00231	0.05993	-0.03377		
8	0.00363	0.05751	0.24712		
9	-0.00002	0.01120	0.08162		
10	0.00002	0.00760	0.01104		
11	0.00019	-0.04834	-0.04951		
12	-0.00029	-0.01413	0.01250		
13	-0.00001	-0.02050	-0.00589		
14	-0.00002	-0.04864	-0.04797		
15				0.86941	
16				-0.04751	
17				0.23378	
18				0.19725	
19				-0.00096	
20				0.05805	
21				-0.05596	
22					0.75052
23					0.03924
24					0.25268
25					0.07312
26					0.01129
27					0.01284
28					-0.02694
Eigenvalues	-20.5836	-1.3332	-0.5762	-0.6991	-0.4999
(Moccia SCF Values	-20.5249	-1.3261	-0.5561	-0.6814	-0.4954)

Table 3.3

Energy terms for H_2O

Energy term	Boccia SCF	Perturbation
E_{tot}	-75.922809	-75.904903
E_{el}	-85.087009	-85.069103
V_{nn}	9.164200	9.164200
V_{ne}	-198.943172	-198.320599
V_{ee}	37.917464	37.685117
T	75.938699	75.566396

Table 3.4

Localised orbitals for H_2O

System	Orbital	r	ϑ /°
Puff	Valence sp^3	0.6335	109.47
SCF molecule (d_{11}= 0.5741)	bond pair	0.9492	101.4
	lone pair	0.5570	123.4
Perturbation molecule (d_{11}= 0.6103)	bond pair	0.8738	98.8
	lone pair	0.5528	127.3

The electronic energy of the molecular puff is 99.70% that of the SCF molecule. The perturbation method gives orbitals for the molecule which have very similar eigenvalues to the SCF molecular orbitals and a total molecular electronic energy which is 99.98% that obtained by the SCF method. The perturbation method thus gives 95% of the total change in going from the molecular puff to the SCF molecule. The numerical results of the SCF and perturbation method calculations are similar in all respects.

The effect on the total electron density of going from the molecular puff to the molecule can be discussed in terms of the centroids of the localised orbitals of the valence shell. In the molecule, the angle between lone pairs is considerably wider than, and the the angle between the bonding pairs considerably less than, the tetrahedral angle between the sp^3 hybrids of the molecular puff. The lone pair is more tightly bound (closer) to the oxygen nucleus than the puff sp^3 hybrid, and the bonding orbitals are drawn out towards the hydrogen nuclei. The bonding pair centroids are inside the bond angle, which is expected as charge is thus concentrated in the binding region (see section 7.4). The effect of the changes in electron-electron interactions between molecular puff and the molecule, which are neglected in the perturbation method, is to move the bonding orbital centroids nearer to the hydrogen nuclei.

It is worth noting that the order for $1/r_{ij}$, where i and j are centroids of localised orbitals, is

lone pair - lone pair > lone pair - bond pair > bond pair - bond pair

which is the order postulated for repulsion energies in the VSEPR scheme.

The calculated electronic dipole moments, μ_e, are -1.3493 for the SCF molecule and -1.2942 for the perturbation method molecule, which correspond to molecular moments, μ_{mol}, of 0.8204 and 0.8755 respectively. The experimental value of μ_{mol} is 0.725 and the calculated values are larger because of the inability of a one-centre basis set to give a high electron density far from the expansion centre.

All the main features of the electron distribution for water, as calculated by Moccia, are also present in that calculated by the perturbation method. This is seen most clearly in electron density maps.

Figures 9.5-9.6 show the electron densities for doubly occupied valence shell molecular orbitals, as calculated from Moccia's functions. They are very similar to those given elsewhere (e.g. ref. 2). Dotted lines in these diagrams join oxygen and hydrogen nuclei.

Figures 9.7 and 9.8 show the valence shell electron density calculated from Moccia's functions and are very nearly identical to figures 9.9 and 9.10, the corresponding diagrams for the results of the perturbation method calculations. Figures 9.11-9.14 show the same to be true for lone pair and bonding orbitals calculated by the two methods.

Figure 9.15 is a difference density map showing the difference in valence shell electron density on going from the molecular puff to the molecule (SCF functions being used). Solid lines denote positive difference density and short-dashed lines denote negative difference density. There is a build-up of density around the hydrogen nuclei, as might be expected, and there is also a small build-up of charge behind the oxygen nucleus

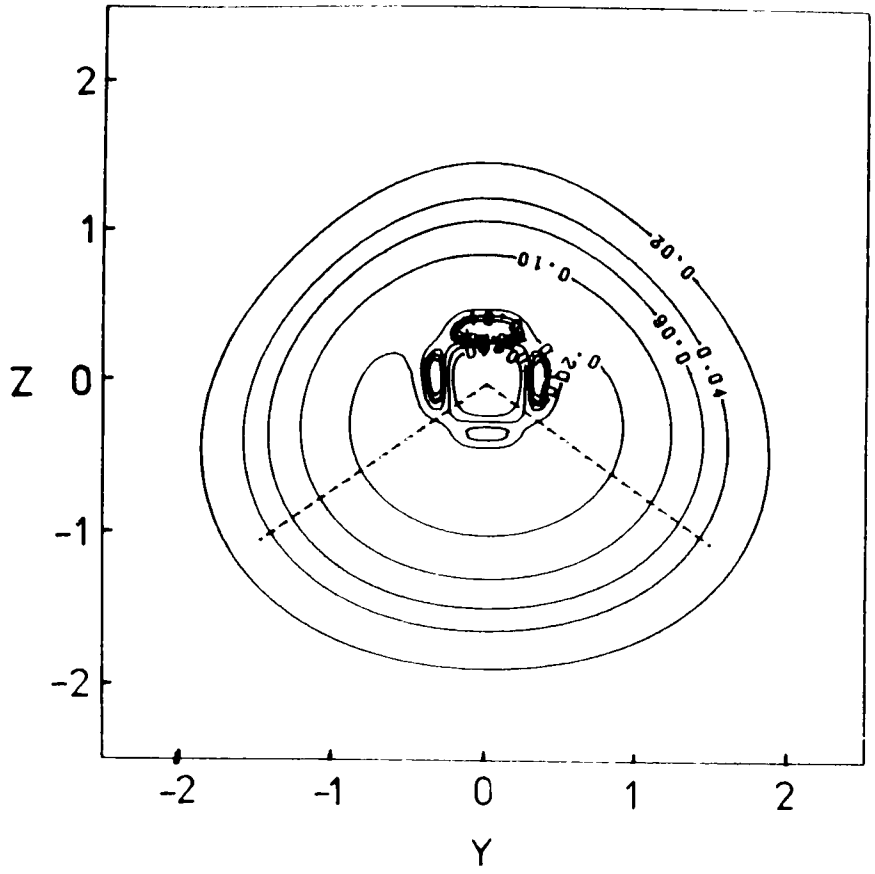

Figure 9.3 The $2a_1$ orbital for water

Figure 9.4 The $3a_1$ orbital for water

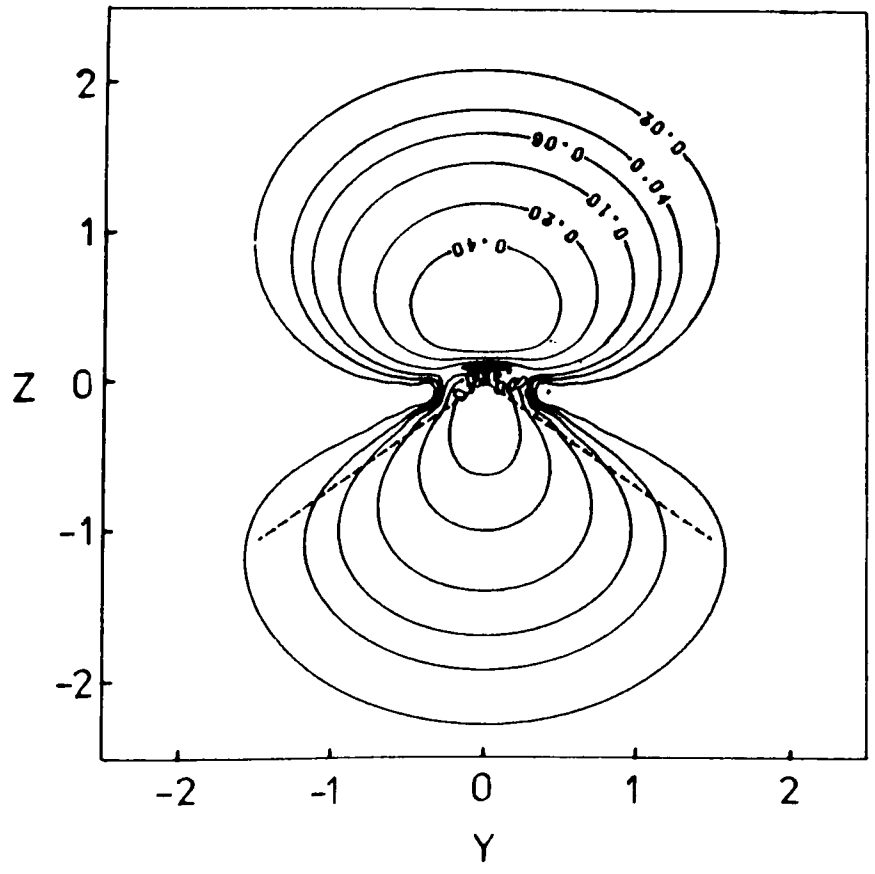

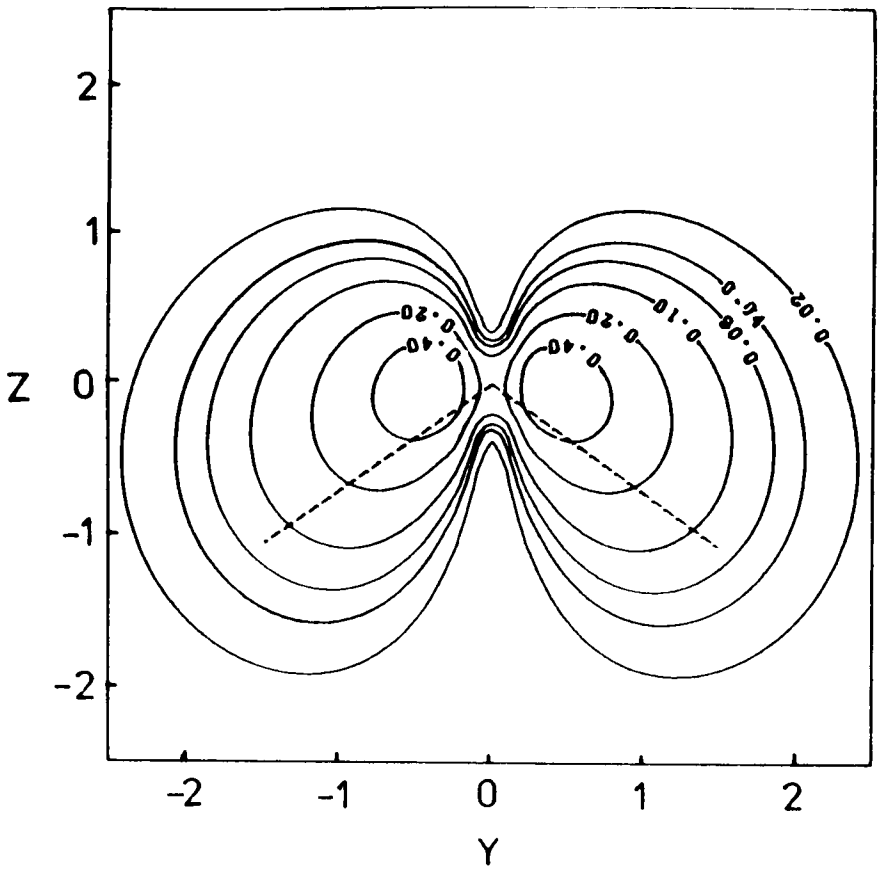

Figure 9.5 The $1b_2$ orbital for water

Figure 9.6 The $1b_1$ orbital for water

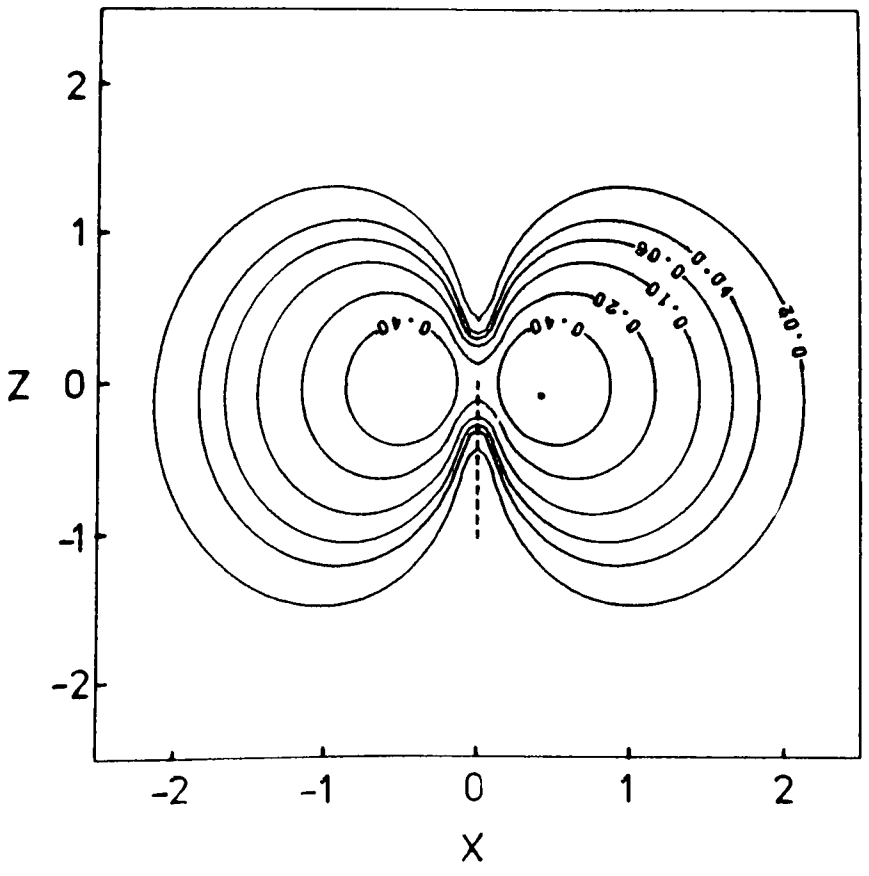

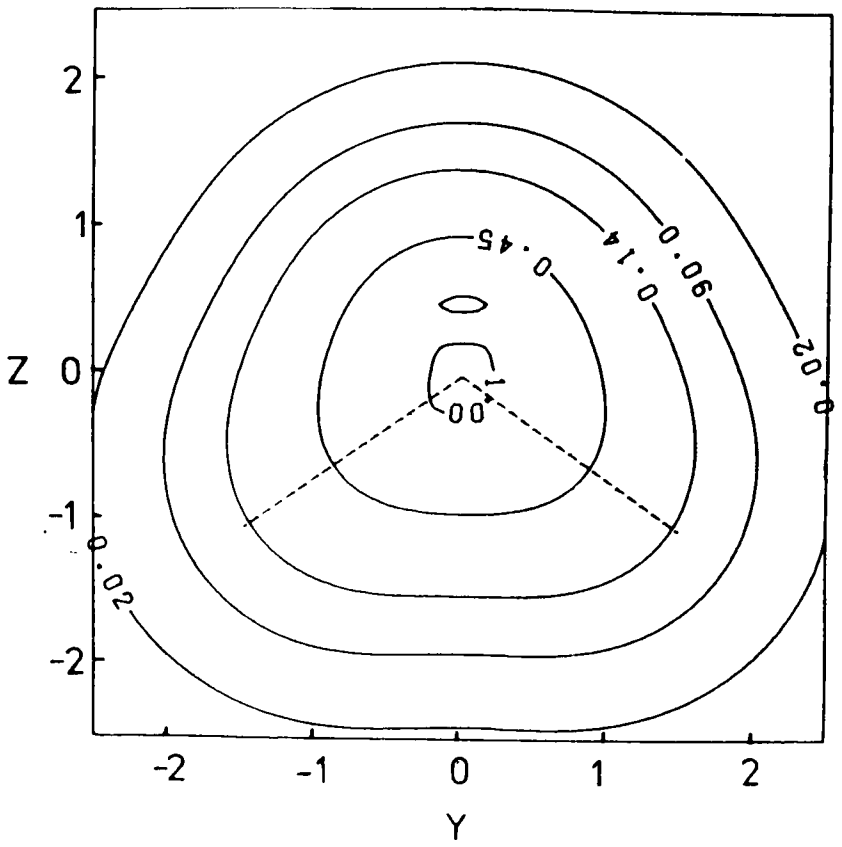

Figure 9.7 Valence shell for the water molecule (SCF) (YZ plane)

Figure 9.8 Valence shell for the water molecule (SCF) (XZ plane)

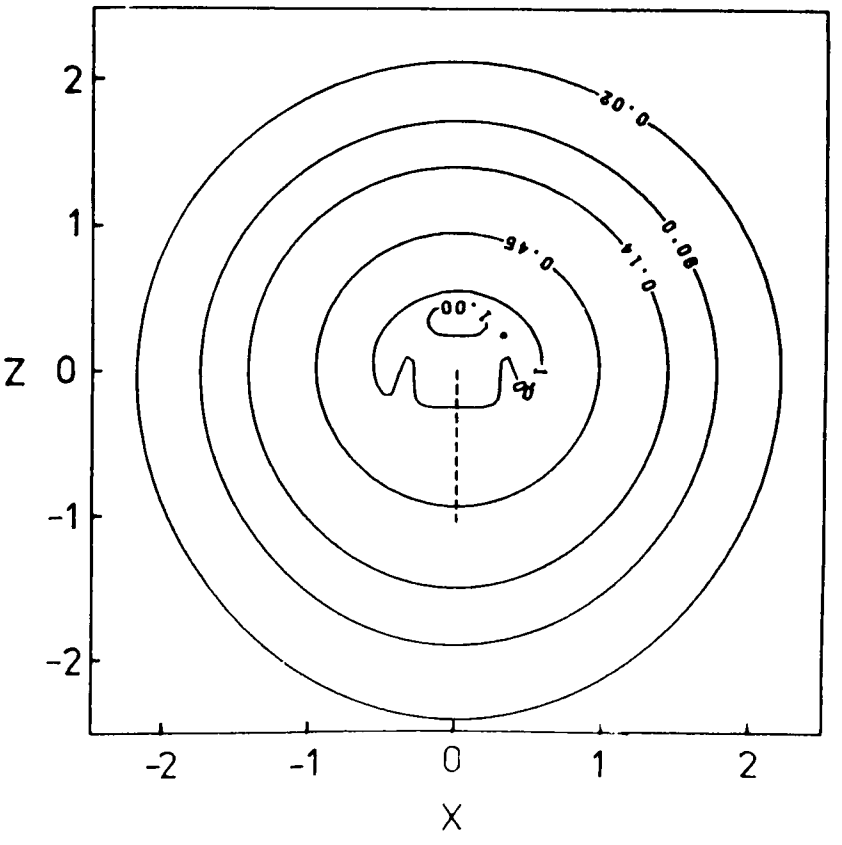

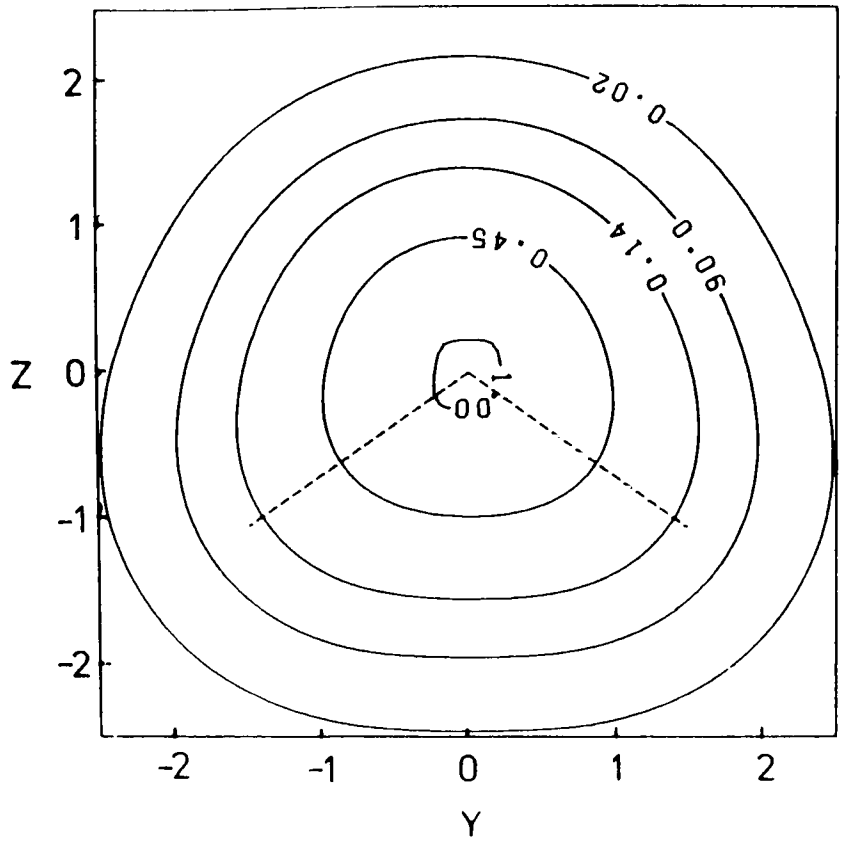

Figure 9.9 Valence shell for water (perturbation method) (YZ plane)

Figure 9.10 Valence shell for water (perturbation method) (XZ plane)

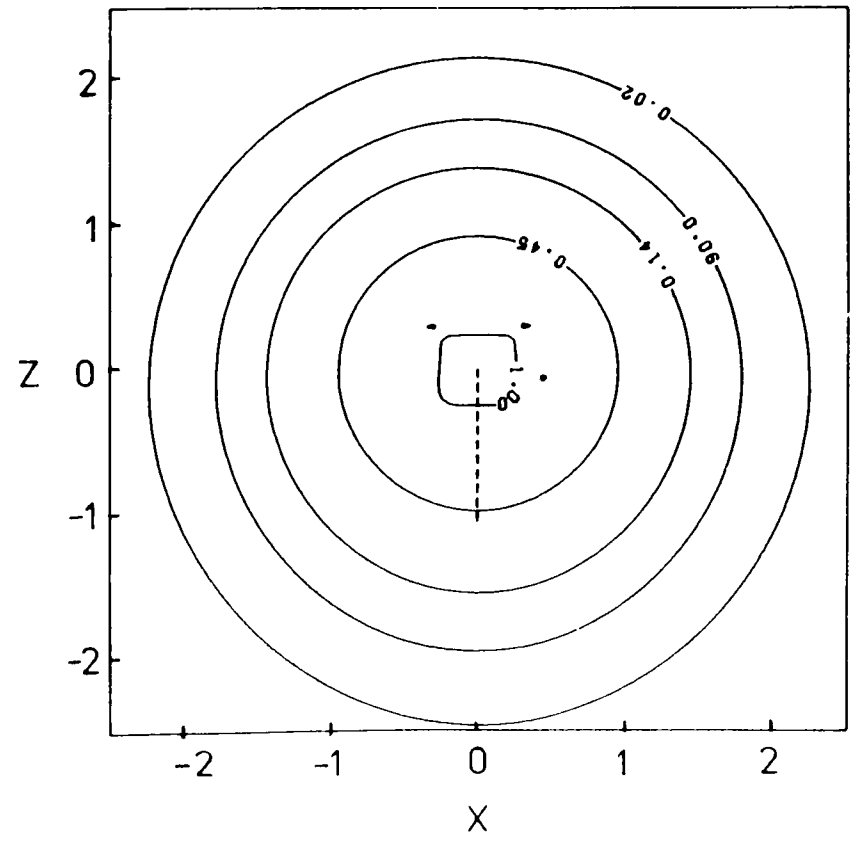

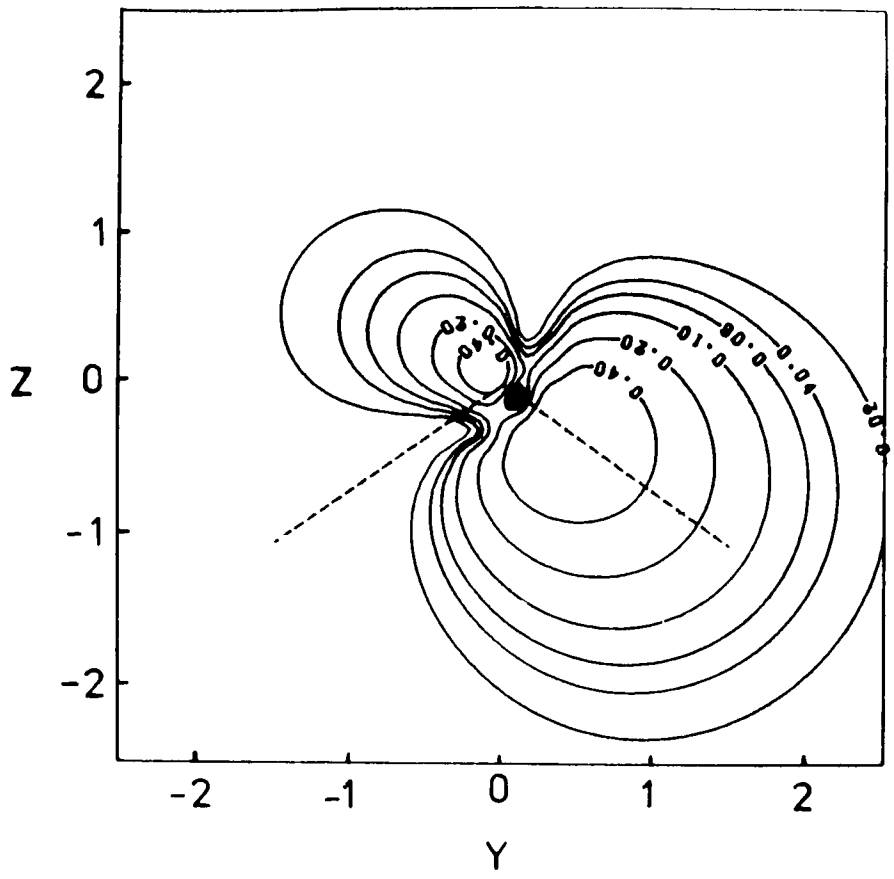

Figure 9.11 Bonding pair for water (SCF)

Figure 9.12 Lone pair for water (SCF)

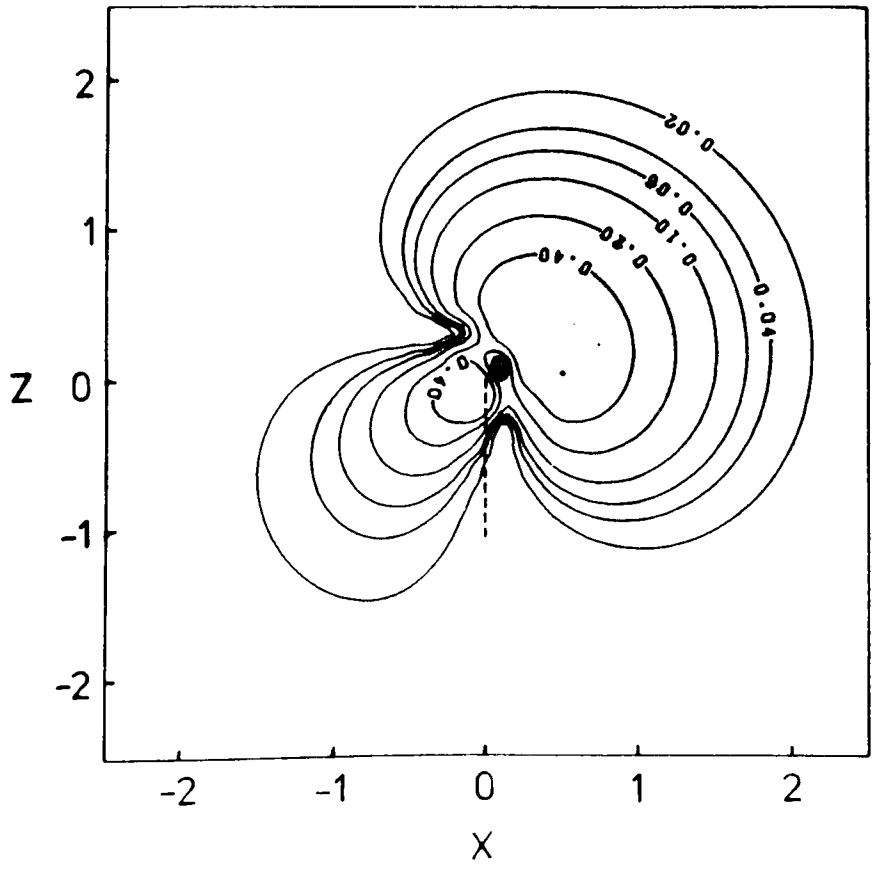

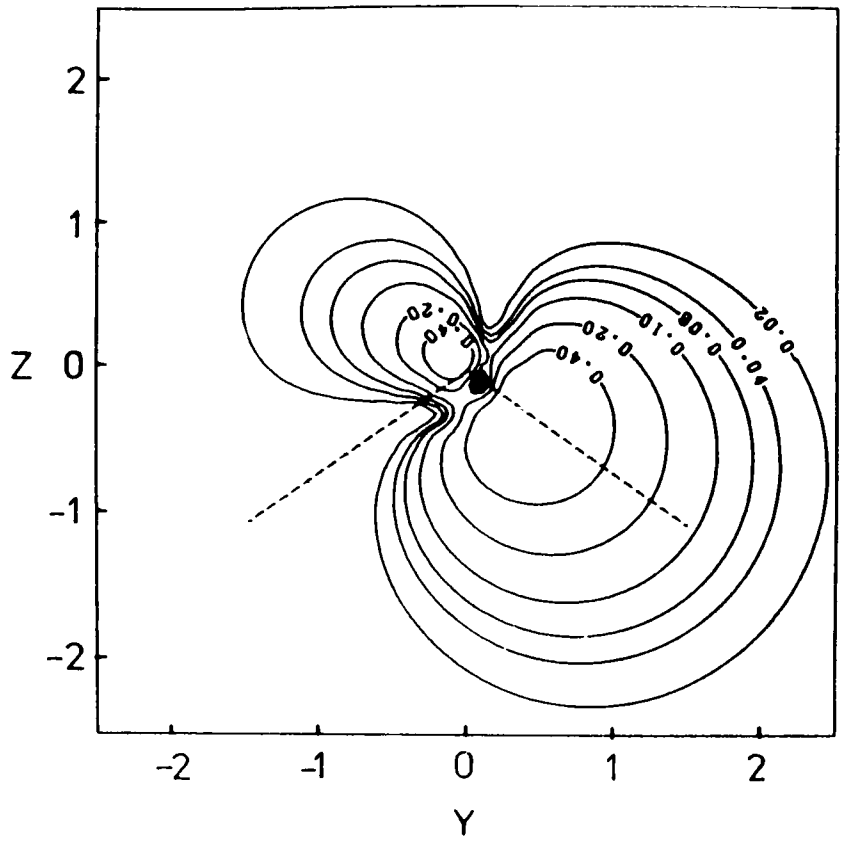

Figure 9.13 Bonding pair for water (perturbation method)

Figure 9.14 Lone pair for water (perturbation method)

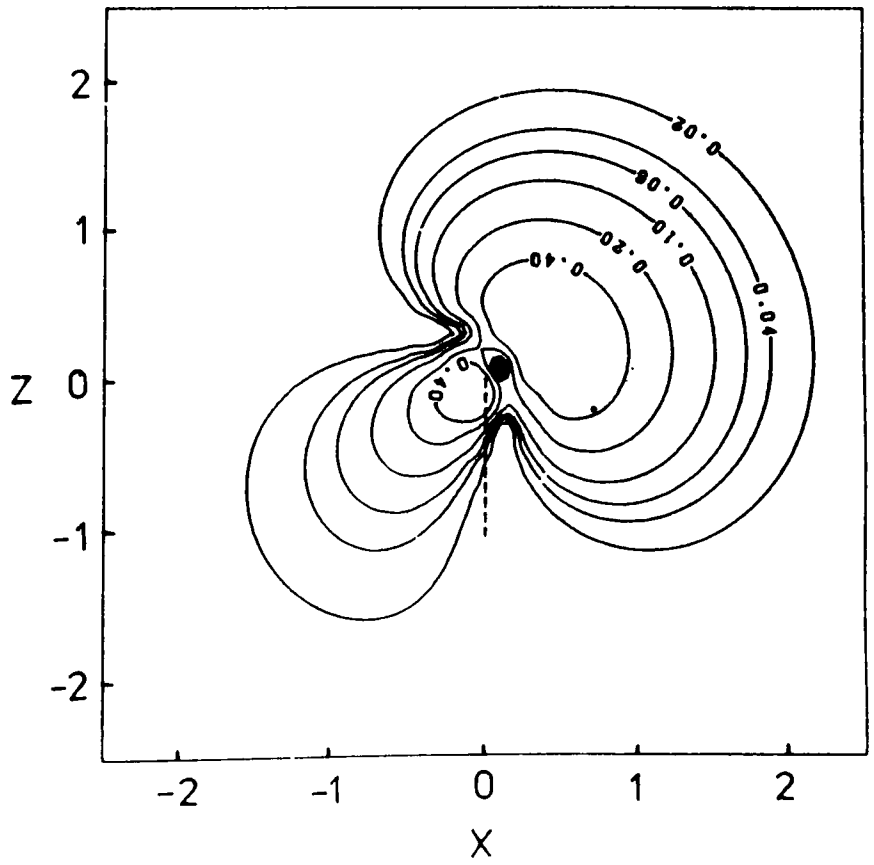

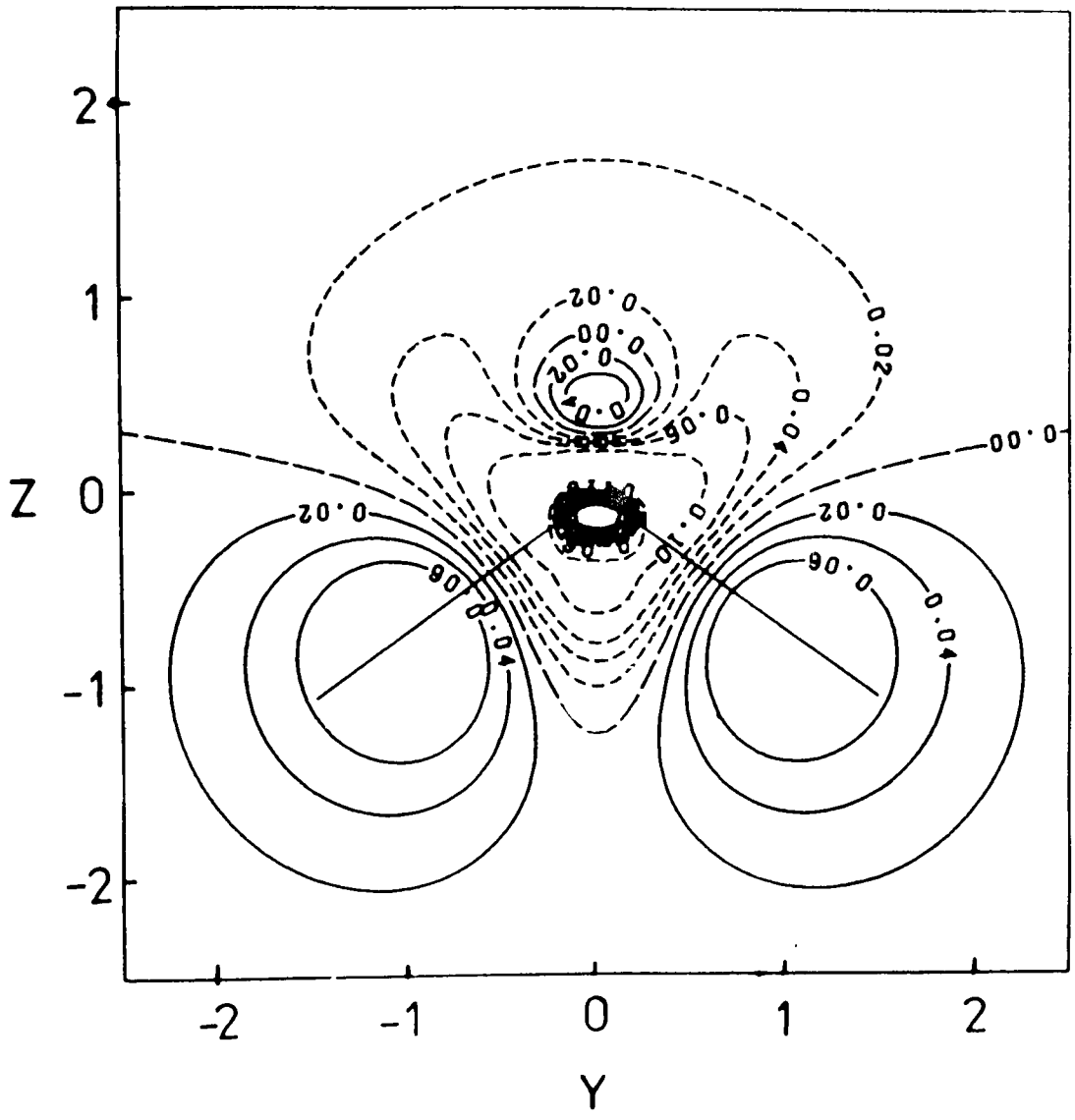

Figure 9.15 Valence shell difference map on going from the molecular puff to the CCF molecule

i.e. outside the binding region (see section 7.4). This has also been noted in difference maps showing total molecular electron density less the sum of the individual atomic densities. Bader, Henneker and Cade (14), for instance, noted this latter effect for the Li_2 and N_2 molecular. This is a manifestation of the Pauli exclusion principle, not all the electrons being able to crowd into the binding region (see section 7.4).

9.4 Variation of bond angle.

Calculations were carried out over a wide range of bond angle, α, using the small basis set. The calculated wave functions are given in Appendix 2. Tables 9.5-9.9 summarise the results of these calculations.

The results of SCF and perturbation method calculations are very similar at each molecular geometry. The effects discussed in section 9.3, for the more accurate wave functions, are reproduced at each molecular geometry by the less accurate wave functions of this section.

The total molecular energy, E_{tot}, has a minimum at 101.5°, close to the experimental bond angle (104.5°). None of the energy terms V_{nn}, V_{ne}, V_{ee} has a minimum, this showing that none of these terms is solely responsible for the equilibrium molecular geometry, which is the result of a delicate balance of energy terms. Figure 9.16 shows the angular minimum in E_{tot}. The solid line denotes the SCF calculations and the dotted line the perturbation method calculations.

Figure 9.17 is a Walsh-type correlation diagram for the valence shell molecular orbitals. It compares very well in form with those from far more accurate calculations (e.g. ref. 54).

Table V.5

Scaled energy terms for H_2O

α/°	$T(=-E_{tot})$	$-E_{el}$	V_{nn}	$-V_{ne}$	V_{ee}
Puff	74.6546	84.4658	9.8112	194.1404	35.0200
SCF method					
90	75.0717	84.7395	9.6677	194.8151	35.0039
95	75.0756	84.7269	9.6514	194.8081	35.0056
100	75.0772	84.7140	9.6369	194.7984	35.0072
104.5	75.0768	84.7020	9.6252	194.7876	35.0088
106.54	75.0761	84.6964	9.6203	194.7822	35.0096
109.46	75.0746	84.6883	9.6137	194.7737	35.0108
140	75.0330	84.5911	9.5662	194.6639	35.0318
170	74.9912	84.5367	9.5475	194.5852	35.0554
Perturbation method					
90	75.0641	84.7312	9.6671	194.8107	35.0154
95	75.0677	84.7184	9.6507	194.8068	35.0206
100	75.0691	84.7054	9.6363	194.8000	35.0255
104.5	75.0687	84.6933	9.6246	194.7917	35.0297
106.54	75.0681	84.6878	9.6197	194.7874	35.0315
109.46	75.0666	84.6797	9.6131	194.7804	35.0341
140	75.0271	84.5926	9.5655	194.6771	35.0573
170	74.9888	84.5354	9.5466	194.5939	35.0697

Table 3.6

Orbital energy as a function of bond angle

(signs omitted)

α/°	$1a_1$	$2a_1$	$3a_1$	$1b_2$	$1b_1$
Puff	21.6704	1.6431	0.6331	0.6331	0.6331
SCF method					
90	21.7065	1.6947	0.6855	0.7556	0.5411
95	21.0751	1.6908	0.6711	0.7700	0.5400
100	21.7036	1.6873	0.6570	0.7854	0.5390
104.5	21.7022	1.6845	0.6447	0.7945	0.5380
106.54	21.7015	1.6833	0.6393	0.7992	0.5375
109.46	21.7006	1.6817	0.6316	0.8056	0.5369
140	21.6902	1.6704	0.5697	0.8476	0.5301
170	21.6830	1.6660	0.5278	0.8577	0.5255
Perturbation method					
90	21.7075	1.6832	0.6927	0.7512	0.5385
95	21.7052	1.6800	0.6772	0.7653	0.5374
100	21.7029	1.6772	0.6621	0.7784	0.5363
104.5	21.7007	1.6750	0.6489	0.7893	0.5353
106.54	21.6998	1.6741	0.6431	0.7939	0.5348
109.46	21.6984	1.6729	0.6348	0.8003	0.5341
140	21.6855	1.6658	0.5632	0.8434	0.5281
170	21.6789	1.6643	0.5270	0.8559	0.5247

Table 9.7

Orbital energy sums as a function of angle

α/°	$-E^{HF}_{val}$	$-\frac{1}{2}\sum_i n_i \varepsilon_i$
Puff	7.0848	75.6384
SCF method		
90	7.3538	76.1502
95	7.3438	76.1310
100	7.3354	76.1109
104.5	7.3254	76.0917
106.54	7.3186	76.0824
109.46	7.3116	76.0692
140	7.2236	75.9060
170	7.1540	75.7800
Perturbation method		
90	7.3312	76.1193
95	7.3198	76.0953
100	7.3080	76.0707
104.5	7.2970	76.0476
106.54	7.2918	76.0371
109.46	7.2842	75.9945
140	7.2010	75.8580
170	7.1438	75.7524

Table 9.8

Centroids of localised orbitals for H_2O

$\alpha/^\circ$	Bonding r	Bonding $\vartheta/^\circ$	Lone pair r	Lone pair $\vartheta/^\circ$
Puff	0.628	109.47	0.628	109.47
SCF method				
90	0.870	91.4	0.599	130.0
95	0.873	93.6	0.597	128.4
100	0.875	95.8	0.596	126.8
104.5	0.875	97.7	0.594	125.4
106.54	0.875	98.6	0.593	124.8
109.46	0.874	99.8	0.592	123.9
140	0.839	112.4	0.573	115.0
170	0.760	123.4	0.538	106.4
Perturbation method				
90	0.841	88.0	0.571	137.3
95	0.841	90.0	0.570	135.5
100	0.841	92.0	0.569	133.7
104.5	0.840	93.8	0.577	132.0
106.54	0.839	94.6	0.567	131.2
109.46	0.837	95.8	0.566	130.2
140	0.800	108.1	0.557	118.9
170	0.733	119.8	0.548	108.1

Table 9.9

Dipole moments for H_2O

$\alpha/^\circ$	SCF method μ_e	SCF method μ_{mol}	Perturbation method μ_e	Perturbation method μ_{mol}
90	-1.417	1.148	-1.586	0.979
95	-1.351	1.100	-1.516	0.935
100	-1.280	1.052	-1.442	0.890
104.5	-1.213	1.008	-1.371	0.850
106.54	-1.183	0.987	-1.339	0.831
109.46	-1.137	0.958	-1.291	.804
140	-0.695	0.606	-0.745	0.496
170	-0.153	0.163	-0.185	0.131

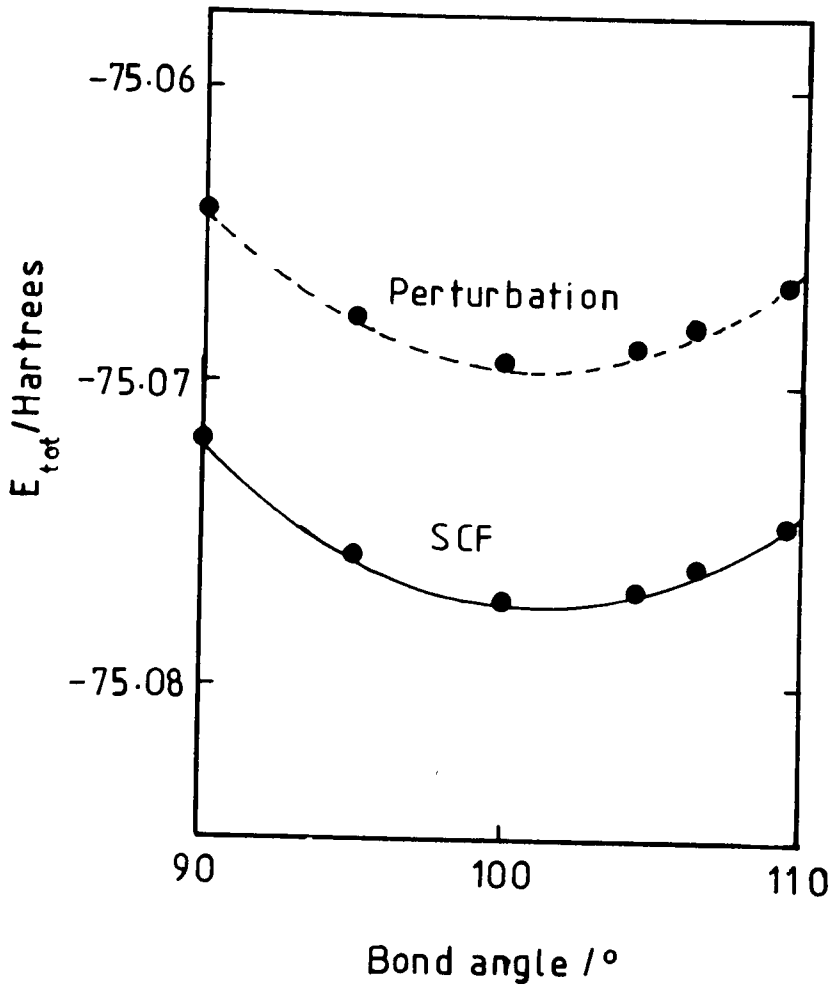
-75·06
-75·07
-75·08
E_{tot}/Hartrees
Perturbation
SCF
90
100
110
Bond angle /°

Figure 9·16

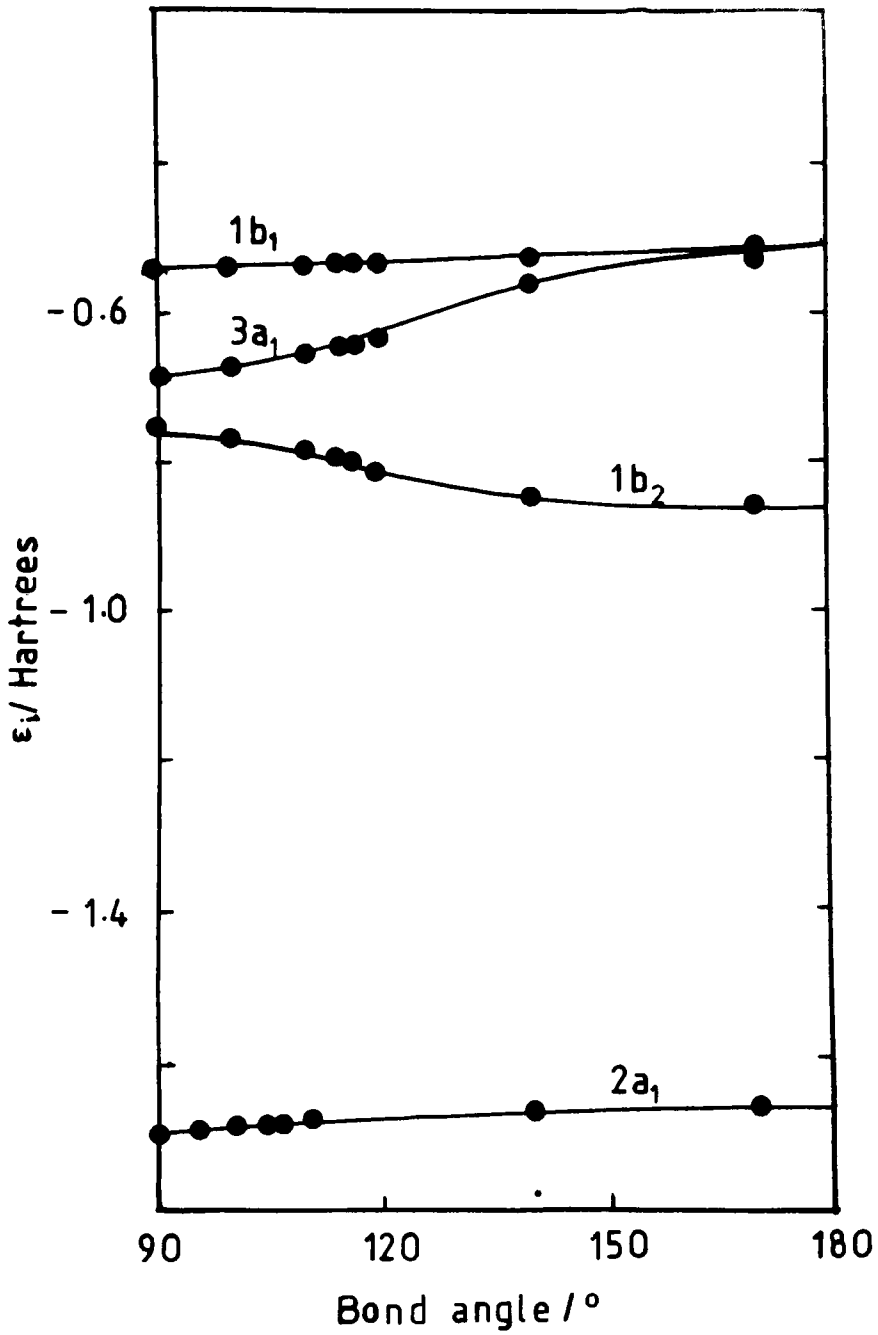

"Walsh"diagram for water (SCF)

Figure 9·17

The orbitals $1b_1$ and $3a_1$ become equivalent at $\alpha = 180^\circ$. They are derived from the molecular puff $2p_x$ and $2p_z$ functions and then lie in the plane perpendicular to the linear molecular axis. $1b_2$ is derived from the puff $2p_y$ and is lower in energy at $\alpha = 180^\circ$ as it then "points" directly at the hydrogen nuclei. Neither of the orbital energy sums E_{val}^{HF} or $\frac{1}{2}\sum_i n_i \epsilon_i$ (discussed in section 7.5.2) shows a minimum. Both do, however, decrease as α decreases from 180°, correctly indicating that water is a bent, rather than a linear, molecule.

Chapter 10

Discussion and conclusions

10.1 SCF and perturbation method calculations.

The very close agreement between calculations by SCF and perturbation methods in this work is evidence that the most important terms in changing the electron density from that in the spherical molecular puff to that in the molecule, and hence in determining molecular geometry, are included by the perturbation approach. The perturbation method allows no change in the electron-electron interaction operator from that in the molecular puff in computing the molecular wave function and hence these interactions do not bear primary responsibility for molecular shape.

10.2 Comparison to other work.

The results in this work can be compared to the work of Frost (65), Naleway and Schwartz (25), Bader (13) and Maclagan and Schnuelle (66).

Frost (65) described the electronic structure of an N-electron molecule in a closed-shell state by N/2 doubly occupied orbitals, each of which was represented by a single normalised spherical Gaussian orbital (see e.g. ref. 2). The valence shell orbitals were lone pair and bonding pair orbitals, their radii and positions being determined by variational minimisation of the molecular energy, E_{tot}. The orbitals were not orthogonal. The extreme simplicity of the basis set results in molecular energies (for water E_{tot} = -64.288, only 85% of the Hartree-Fock limit) which are very poor compared to those calculated in this work (98.6% of the limit using the small basis set). Frost's calculated equilibrium bond angle (88.4°) is rather small, but the bond

length (1.666) is reasonable. The angle, ϑ, subtended at the oxygen nucleus by the orbital centroids is 81.8° for the bond pairs and 204.8° for the lone pairs. The angles ϑ therefore differ from the tetrahedral and bond angles in the same sense as in this work, but that for the lone pairs is much too large, reflecting the non-orthogonality of the orbitals. The distances, r, of the centroids from the oxygen nucleus are 0.56 for bonding orbitals and 0.10 for the lone pair, the same distances being 0.87 and 0.59 in this work. Frost's model thus correctly predicts that the lone pair is more tightly bound than the bonding pair, but the electron density is poor.

Naleway and Schwartz (25) considered the VSEPR model by a localised molecular orbital study of water, similar to some of the calculations in this work, using the maximum total self-energy criterion (5) for localisation of the resulting LCAO-SCF molecular orbitals. The molecular energy was calculated, using extended basis sets, to a high accuracy (-76.03122 at the equilibrium angle α = 104.52°). The orbitals were not, however, truly localised two-centre orbitals (see section 7.3). They calculated interaction energies and energy terms for their localised orbitals, finding good agreement between their results and the predictions of the VSEPR scheme, and examined the behaviour of various energy sums as a function of bond angle. Significantly, most of the sums showing a minimum included V_{nn}, the total nucleus-nucleus interaction energy, but no minimum was found in V_{ee}, the total electron-electron interaction energy, just as in this work. Neither E^{HF}_{val} nor $\frac{3}{2}\sum_i n_i \varepsilon_i$ (see section 7.5.2) showed a minimum, despite the high accuracy of the calculations, in common with this work. Other high

accuracy calculations have however found a minimum in the latter term (34).

A necessary requirement for electrostatic equilibrium is that charge be concentrated in the binding region (see section 7.4). Bader (13) argues that, for a molecular wave function built-up using both orbitals centred on the oxygen and orbitals centred on the hydrogens, an acceptable electron density distribution must have oxygen lone pair orbitals which are close to sp hydrids and the oxygen orbitals overlapping the hydrogen orbitals must be close to pure 2p orbitals. The angle between these latter bonding hybrids on the oxygen will therefore be considerably less than the bond angle (i.e. the bonds will be bent). Maclagan and Schnuelle (66) found this to be true in minimal STO (Slater-type orbital) basis set valence-bond calculations for water. The angle between the bonding hybrids remained constant (93 ± 1^{o}) while the bond angle varied over 30^{o}. In this work, the centroids of the bonding orbitals are consistently inside the bond angle, concentrating charge in the binding region. The angle between the bonding orbitals does, however, alter as the bond angle is varied, this being a consequence of the one-centre method in which there are no functions centred on the hydrogen nuclei.

10.3 A simple classical model.

A simple classical model of the electron-pair repulsions in the valence shell, as suggested by the VSEPR scheme, is as follows. Two electrons (a pair) are placed at each of the localised orbital centroids. As remarked in section 9.3, the Gillespie-Nyholm order of repulsion energies applies. The

Table 10.1

Electron-pair repulsion model calculations

$\alpha/^{\circ}$	E_r
Puff	23.3991
SCF method	
90	20.3133
95	20.2431
100	20.2025
104.5	20.1908
106.54	20.1932
109.46	20.2050
140	20.9355
170	22.9030
Perturbation method	
90	21.3015
95	21.2439
100	21.2094
104.5	21.1983
106.54	21.1994
109.46	21.2077
140	21.7674
170	23.1074
Results of Section 5.3	
Puff	23.2005
SCF	19.7417
Perturbation	20.8329

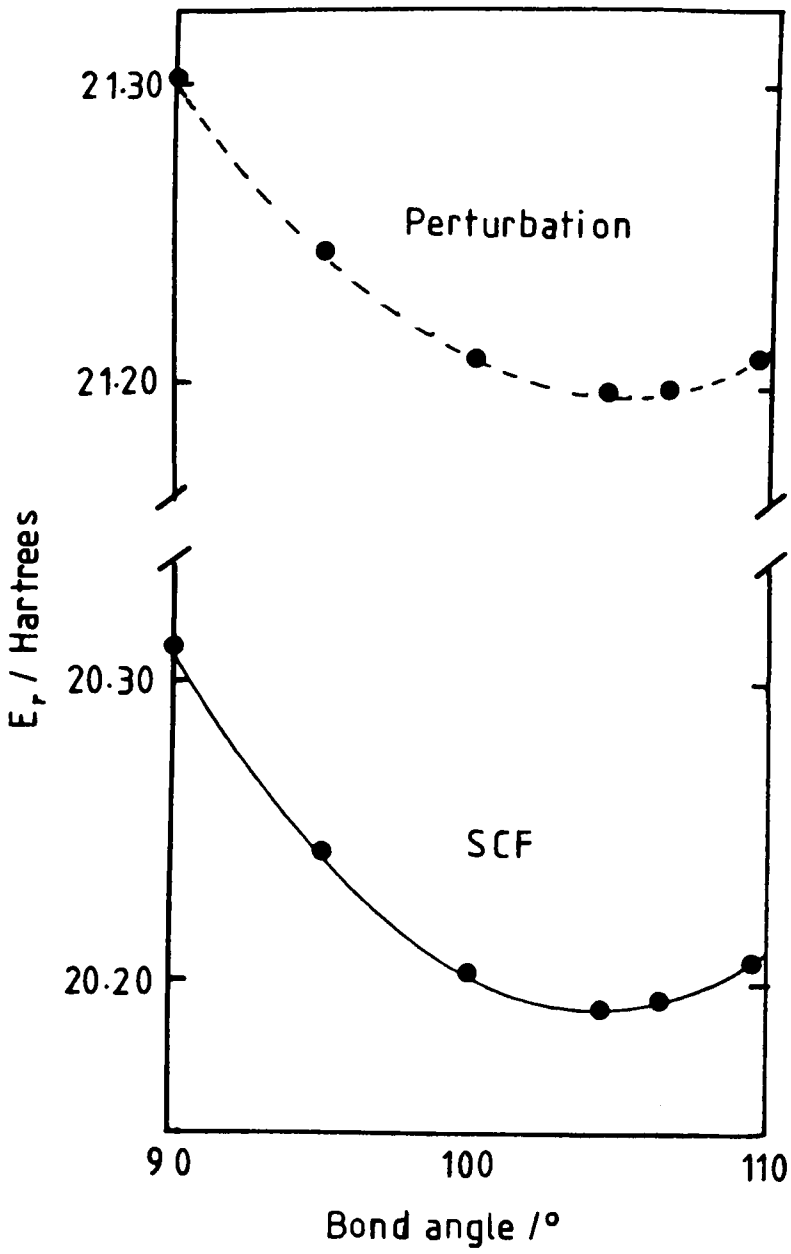
21·30
21·20
Perturbation
20·30
20·20
SCF
E_r / Hartrees
9 0
100
110
Bond angle /°

Figure 10.1

"total repulsion energy", E_r, is given by

$$E_r = \sum_{i<j} \frac{1}{r_{ij}}$$

where r_{ij} is the distance between centroids i and j.

Table 10.1 gives the results of calculations using this model and figure 10.1 illustrates the variation in E_r with bond angle, α. E_r is smaller for the molecule than for the molecular puff and is also smaller from SCF calculations than from perturbation method calculations. Neglect of changes in electron-electron interactions between the molecular puff and the molecule causes the bonding orbital centroids to be too close together.

A minimum in E_r occurs close to the equilibrium geometry. This does not mean that E_r, arising from an unrealistic classical model, can be said to determine molecular geometry. Rather, this shows that the effects responsible for molecular geometry produce an electron distribution that fits the VSEPR scheme and thus appears to be due to electron-electron interactions.

Naleway and Schwartz (25) note that there is a maximum in the sum of distances between their localised orbital centroids. Their results also fit the simple classical model presented here.

10.4 Final discussion.

The salient features of the VSEPR and Walsh-Mulliken schemes have been reproduced in this work using one-centre calculations by both SCF and perturbation methods.

There is no minimum in the molecular electron repulsion energy, V_{ee}, at the equilibrium geometry, though this is widely assumed in qualitative discussions (e.g. ref. 24). Further it has been demonstrated in this work that electron-electron interactions cannot be primarily responsible for molecular shape, which is the result of a delicate balance of energy terms.

The success of the VSEPR scheme is due to a correlation between its predictions and the consequences of the effects which actually determine molecular shape. This correlation does not imply a causal relationship.

References (Part B)

1. M. Born, J.R. Oppenheimer, Ann. d. Phys., 84, 457 (1927)
2. E. Steiner, "The determination and interpretation of molecular wave functions", Cambridge University Press (Cambridge,1976)
3. P.H. Millie, B. Levy, G. Berthier in "Localisation and delocalisation in quantum chemistry" vol.1, O. Chalvet, R. Daudel, S. Diner, J.P. Malrieu (eds.), Reidel (Dordrecht,1975)
4. J. Lennard-Jones, J.A. Pople, Proc. Roy. Soc. (London), A202, 166 (1950)
5. C. Edmiston, K. Ruedenberg, Rev. Mod. Phys., 35, 457 (1963)
6. S.F. Boys, Rev. Mod. Phys., 32, 296 (1960)
7. V. Magnasco, A. Perico, J. Chem. Phys., 47, 971 (1967)
8. W. von Niessen, J. Chem. Phys., 56, 4290 (1972)
9. C.A. Coulson, "Valence" (2nd edition), Oxford University Press (London,1961)
10. J.H. Liang, Ph.D thesis, Ohio State University (1970)
11. W.J. Taylor, J. Chem. Phys., 48, 2385 (1968)
12. R.F.W. Bader, G.A. Jones, Can. J. Chem., 41, 586 (1962)
13. R.F.W. Bader, J. Am. Chem. Soc., 86, 5070 (1964)
14. R.F.W. Bader, W.H. Henneker, P.E. Cade, J. Chem. Phys., 46, 3341 (1967)
15. R.P. Feynman, Phys. Rev., 56, 340 (1939)
16. B.M. Deb, Rev. Mod. Phys., 45, 22 (1973)
17. T. Berlin, J. Chem. Phys., 19, 214 (1951)
18. N.V. Sidgwick, H.M. Powell, Proc. Roy. Soc. (London), A176, 153 (1940)
19. R.J. Gillespie, Can. J. Chem., 38, 818 (1960)
20. R.J. Gillespie, R.S. Nyholm, Chem. Soc. Quart. Rev., 11, 339 (1957)
21. R.J. Gillespie, Angew. Chem., 6, 819 (1967)
22. R.J. Gillespie, J. Chem. Educ., 47, 18 (1970)
23. R.J. Gillespie, "Molecular geometry", Van Nostrand Rheinhold (London,1972)
24. R. McWeeny, B.T. Sutcliffe, "Methods of molecular quantum mechanics", Academic Press (London,1976)
25. C.A. Naleway, M.E. Schwartz, J. Am. Chem. Soc., 95, 8235 (1973)
26. J. Lennard-Jones, Advancement of Science, 11, 143 (1954)

27. A.D. Walsh, J. Chem. Soc., 2260 (1953)
28. R.S. Mulliken, Rev. Mod. Phys., 14, 204 (1942)
29. C.A. Coulson, A.H. Neilson, Discuss. Faraday Soc., 35, 71 (1963)
30. W.A. Bingel in "Molecular orbitals in chemistry, physics and biology", P.-O. Lowdin, B. Pullman (eds.), Academic Press (New York,1964)
31. H.H. Schmidtke, H. Preuss, Z. Naturforsch., 16a, 790 (1961)
32. C.A. Coulson, B.M. Deb, Int. J. Quantum Chem., 5, 411 (1971)
33. S.D. Peyerimhoff, R.J. Buenker, L.C. Allen, J. Chem. Phys., 45, 734 (1966)
34. R.J. Buenker, S.D. Peyerimhoff, Chem. Rev., 74, 127 (1974)
35. K. Ruedenberg, J. Chem. Phys., 66, 375 (1977)
36. T. Anno, Y. Sakai, J. Chem. Phys., 67, 4771 (1977)
37. L.C. Allen, Theor. Chim. Acta, 24, 117 (1972)
38. R.G. Parr in "Molecular orbitals in chemistry, physics and biology", P.-O. Lowdin, B. Pullman (eds.), Academic Press (New York,1964)
39. D.M. Bishop, Adv. Quantum Chem., 2, 25 (1967)
40. C.C.J. Roothaan, Rev. Mod. Phys., 23, 69 (1951)
41. C.C.J. Roothaan, Rev. Mod. Phys., 32, 179 (1960)
42. D.B. Cook, "Ab initio valence calculations in chemistry", Butterworth (London,1974)
43. M. Cohen, C.A. Coulson, Proc. Cam. Phil. Soc., 57, 96 (1961)
44. A.F. Saturno, R.G. Parr, J. Chem. Phys., 33, 22 (1960)
45. A.G. Turner, A.F. Saturno, R.G. Parr, J. Chem. Phys., 40, 1919 (1964)
46. R. Moccia, J. Chem. Phys., 40, 2164 (1964)
47. M. Gerloch, R.C. Slade, "Ligand field parameters", Cambridge University Press (Cambridge,1973)
48. C.J. Ballhausen, "Introduction to ligand field theory", McGraw-Hill (New York,1962)
49. E.U. Condon, G.H. Shortley, "The theory of atomic spectra", Cambridge University Press (Cambridge,1935)
50. J.C. Slater, "Quantum theory of atomic structure" vol.1, McGraw-Hill (New York,1960)
51. G. Doggett, "The electronic structure of molecules, theory and applications to inorganic molecules", Pergamon (Oxford,1
52. J.A. Gaunt, Phil. Trans. Roy. Soc. (London), A228, 151 (1

53. P.-O. Lowdin, J. Mol. Spectrosc., 3, 46 (1959)
54. A.D. McLean, J. Chem. Phys., 40, 2774 (1964)
55. J.M. Foster, S.F. Boys, Rev. Mod. Phys., 32, 300 (1960)
56. S.F. Boys in "Quantum theory of atoms, molecules and the solid state", ed. P.-O. Lowdin, Academic Press (New York,1966)
57. A. Streitweiser Jr., P.H. Owens, "Orbital and electron density diagrams", Macmillan (Riverside, N.J.,1973)
58. California computers, GPCP manual (available at OUCL)
59. D.M. Bishop, M. Randic, Mol. Phys., 10, 517 (1966)
60. C.W. Kern, M. Karplus in "Water - a comprehensive treatise" vol.1, Plenum (New York,1972)
61. D.M. Bishop, J.R. Hoyland, R.G. Parr, Mol. Phys., 6, 467 (1963)
62. P. Hauk, R.G. Parr, H.F. Hameka, J. Chem. Phys., 39, 2085 (1964)
63. H. Kim, R.G. Parr, J. Chem. Phys., 49, 3071 (1968)
64. H. Kim, R.G. Parr, J. Chem. Phys., 41, 2892 (1964)
65. A.A. Frost, J. Phys. Chem., 72, 1289 (1968)
66. R.G.A.R. Maclagan, G.W. Schnuelle, Theor. Chim. Acta, 46, 165 (1977)

APPENDICES

Appendix 1

Tabulated results of relaxation time measurements

Table 5.1

T_2 Measurements on $H_{0.36}MoO_3$

T/K	10^3K/T	T_2/μs	$\log_{10}(T_2/\mu s)$	Mode
77	12.99	20	1.301	SE*
99	10.10	19	1.279	SE*
123	8.13	21	1.322	SE*
142	7.04	19	1.279	SE*
147	6.80	22	1.342	SE*
151	6.62	17.5	1.243	SE*
184	5.43	18	1.255	SE*
191	5.24	15	1.176	SE*
198	5.05	22	1.342	SE
205	4.88	21.1	1.324	FID
207	4.83	20.7	1.317	FID
214	4.67	21.1	1.324	FID
216	4.63	31.2	1.494	FID
219	4.57	31.2	1.494	FID
225	4.44	29.2	1.465	FID
232	4.31	56.5	1.752	FID
243	4.12	36.9	1.567	FID
261	3.83	55.6	1.745	FID
266	3.76	51.3	1.710	FID
281	3.56	53.9	1.732	FID
288	3.47	88.4	1.946	FID
295	3.39	141	2.148	FID
311	3.22	165	2.218	FID
319	3.13	142	2.152	FID
336	2.98	157	2.195	FID
350	2.86	168	2.225	FID
435	2.30	267	2.427	FID
455	2.20	651	2.814	FID

SE = Solid echo
FID = Free induction decay
* = Non-exponential.

Table 5.2

T_1 Measurements on $H_{0.36}MoO_3$

(decay to 1/e of initial signal)

T/K	10^3K/T	T_1/ms	$\log_{10}(T_1/ms)$
77	12.99	370	2.568
77	12.99	412	2.614
104	9.62	325	2.512
114	8.77	390	2.591
115	8.70	478	2.680
131	7.63	137	2.137
148	6.76	177	2.247
155	6.45	281	2.448
162	6.17	154	2.188
174	5.75	182	2.259
174	5.75	208	2.317
179	5.59	158	2.148
180	5.56	216	2.335
180	5.56	272	2.434
191	5.24	192	2.283
198	5.05	107.4	2.031
201	4.96	292	2.466
207	4.83	148	2.170
212	4.72	386	2.587
218	4.59	257	2.410
234	4.27	126	2.100
243	4.12	324	2.511
253	3.95	387	2.587
261	3.83	184	2.264
298	3.36	82.0	1.919
298	3.36	80.1	1.904
300	3.33	153	2.183

Table 5.3

T_1 Measurements for $H_{0.36}MoO_3$

(fit to two exponentials)

T/K	10^3K/T	T_1/ms		A/A+B
		Decay A	Decay B	
77	12.99	12.3	609	0.28
77	12.99	23.6	614	0.33
104	9.62	10.1	435	0.34
114	8.77	20.7	656	0.34
115	8.70	33.4	735	0.30
131	7.63	7.03	186	0.26
148	6.76	8.83	298	0.34
155	6.45	16.8	390	0.25
162	6.17	13.4	281	0.38
174	5.75	14.2	384	0.41
174	5.75	11.5	353	0.33
179	5.59	8.85	260	0.34
180	5.56	6.92	375	0.35
180	5.56	6.91	375	0.35
191	5.24	10.6	329	0.34
198	5.05	5.54	365	0.51
201	4.98	8.38	486	0.37
207	4.83	4.83	516	0.51
212	4.72	8.63	790	0.40
218	4.59	5.49	580	0.43
234	4.27	5.77	404	0.60
243	4.12	4.46	600	0.50
253	3.95	6.11	643	0.33
261	3.83	5.33	425	0.44
298	3.36	4.39	190	0.43
298	3.36	2.55	188	0.50
300	3.33	3.62	315	0.41

Table 5.4

$T_{1\rho}$ Measurements on $H_{0.36}MoO_3$

(decay to 1/e of initial signal)

T/K	10^3K/T	$T_{1\rho}$ /μs	$\log_{10}(T_{1\rho}$ /μs)
102	9.80	432	2.635
109	9.17	1730	3.239
144	6.94	491	2.691
159	6.29	1810	3.257
176	5.68	974	2.989
218	4.59	315	2.498
244	4.10	847	2.928
255	3.92	584	2.767

Table 5.5

$T_{1\rho}$ Measurements on $H_{0.36}MoO_3$

(fit to two exponentials)

T/K	10^3K/T	$T_{1\rho}$ /μs		A/A+B
		Decay A	Decay B	
102	9.80	37.2	6140	0.76
109	9.17	42.8	9870	0.65
144	6.94	39.9	2320	0.70
159	6.29	120	5790	0.50
176	5.68	77.3	1520	0.30
218	4.59	63.0	604	0.38
244	4.10	246	1240	0.29
255	3.92	65.3	907	0.30

Table 5.6

T_2 Measurements on $H_{1.71}MoO_3$

T/K	10^3K/T	T_2/μs	$\log_{10}(T_2/\mu s)$	Mode
77	12.99	7.8	0.892	SE*
92	10.87	7.7	0.886	SE*
106	9.43	8.4	0.924	SE*
126	7.94	7.75	0.889	SE*
139	7.19	7.4	0.869	SE*
171	5.85	42.7	1.630	FID
181	5.52	74.8	1.874	FID
193	5.18	177	2.248	FID
218	4.59	625	2.796	CP
249	4.02	2210	3.344	CP
260	3.85	3540	3.549	CP
293	3.41	9280	3.968	CP
331	3.02	11300	4.053	CP
342	2.92	9270	3.967	CP

SE = Solid echo

FID = Free induction decay

CP = Carr-Purcell-Meiboom-Gill

* = Non-exponential.

Table 5.7

T_1 Measurements on $H_{1.71}MoO_3$

T/K	10^3K/T	T_1/ms	$\log_{10}(T_1/ms)$	
77	12.99	1440	3.158	*
140	7.14	600	2.778	*
148	6.76	354	2.549	*
160	6.25	437	2.640	*
169	5.92	203	2.307	
175	5.71	298	2.474	
177	5.65	263	2.420	
180	5.56	84.2	1.925	
185	5.41	158	2.199	
187	5.35	69.0	1.839	
188	5.32	171	2.234	
196	5.10	42.1	1.624	
200	5.00	30.8	1.489	
203	4.93	28.8	1.459	
205	4.88	28.8	1.459	
207	4.83	23.8	1.377	
212	4.72	29.0	1.462	
219	4.57	12.2	1.086	
225	4.44	11.9	1.076	
231	4.33	10.8	1.033	
240	4.17	10.6	1.025	
249	4.02	16.0	1.204	
249	4.02	10.2	1.009	
260	3.85	9.75	0.989	
263	3.80	14.2	1.152	
266	3.76	15.0	1.176	
275	3.64	35.6	1.551	
285	3.51	32.5	1.512	
292	3.42	49.0	1.690	
293	3.41	40.4	1.606	
308	3.25	102	2.009	
320	3.13	151	2.179	
328	3.05	133	2.124	
330	3.03	131	2.117	
343	2.92	151	2.179	

* Non exponential (fitted value given for decay to 1/e).

Table 5.8

T_1 Measurements on $H_{1.71}MoO_3$

(fit to two exponentials)

T/K	10^3K/T	T_1/ms		A/A+B
		Decay A	Decay B	
77	12.99	90.8	2160	0.28
140	7.14	134	1300	0.42
148	6.76	76.4	692	0.40
160	6.25	90.8	847	0.39

Table 5.9

$T_{1\rho}$ Measurements on $H_{1.71}MoO_3$

T/K	10^3K/T	$T_{1\rho}$ /μs	$\log_{10}(T_{1\rho}$ /μs)
155	6.45	304	2.483
162	6.17	233	2.367
173	5.78	111	2.045
174	5.75	117	2.068
181	5.52	206	2.314
188	5.32	171	2.233
193	5.18	252	2.401
195	5.13	268	2.428
199	5.03	243	2.386
204	4.90	212	2.326
209	4.78	750	2.875
221	4.52	1240	3.093
249	4.02	3230	3.509
264	3.79	5010	3.700
277	3.61	7840	3.894
287	3.48	13300	4.124
293	3.41	14400	4.157
331	3.02	19500	4.290
343	2.92	20900	4.319

Table 5.10

T_2 Measurements on NH_4^+ β-alumina

T/K	10^3K/T	T_2/μs	$\log_{10}(T_2/\mu s)$	Mode
77	12.99	44	1.643	SE*
101	9.90	43	1.633	SE*
133	7.52	42	1.623	SE*
134	7.46	47	1.672	SE*
157	6.37	40	1.602	SE*
165	6.06	43	1.633	SE*
171	5.85	40	1.602	SE*
177	5.65	46	1.663	SE*
189	5.29	40	1.602	SE*
194	5.16	42	1.623	SE*
197	5.08	39	1.591	SE*
202	4.95	35.5	1.550	SE*
216	4.63	35	1.544	SE*
217	4.61	35	1.544	SE*
256	3.86	68.6	1.836	FID
264	3.79	69.7	1.843	FID
275	3.64	111	2.046	FID
294	3.46	280	2.448	FID
298	3.36	158	2.199	FID
305	3.28	370	2.508	CP
315	3.17	401	2.603	CP
329	3.04	539	2.731	CP
335	2.99	691	2.840	CP
344	2.91	531	2.725	CP
345	2.90	776	2.890	CP
369	2.71	812	2.960	CP
381	2.62	1030	3.014	CP
398	2.51	1010	3.008	CP
456	2.19	2190	3.339	CP
500	2.00	2267	3.356	CP

SE = Solid echo

FID = Free induction decay

CP = Carr-Purcell-Meiboom-Gill

* = Non-exponential.

Table 5.11

T_1 Measurements on NH_4^+ β-alumina

(decay to 1/e of initial signal)

T/K	10^3K/T	T_1/ms	$\log_{10}(T_1/ms)$	
77	12.99	23.6	1.373	
77	12.99	26.0	1.415	
93	10.75	26.6	1.425	*
105	9.52	36.2	1.559	*
125	8.00	93.1	1.969	*
133	7.52	227	2.356	*
141	7.09	163	2.212	*
153	6.54	151	2.179	*
157	6.37	167	2.223	*
182	5.49	190	2.279	*
189	5.29	65.7	1.817	*
200	5.00	43.5	1.638	
218	4.59	37.6	1.598	*
230	4.35	27.9	1.446	*
263	3.80	11.3	1.053	
291	3.44	15.4	1.187	*
321	3.12	4.80	0.681	
337	3.01	3.80	0.580	
342	2.92	3.50	0.544	
358	2.79	3.06	0.486	
386	2.59	2.58	0.412	
396	2.53	2.58	0.412	
435	2.30	2.62	0.418	
456	2.19	4.26	0.629	
456	2.19	3.13	0.495	
500	2.00	4.70	0.672	
500	2.00	6.17	0.790	

* Non-exponential.

Table 5.12

T_1 Measurements on NH_4^+ β-alumina
(fit to two exponentials)

T/K	10^3K/T	T_1/ms		A/A+B
		Decay A	Decay B	
93	10.75	19.2	282	0.86
105	9.52	21.9	321	0.77
125	8.00	24.0	107	0.13
133	7.52	21.6	333	0.31
141	7.09	29.9	254	0.31
153	6.54		232	0.30
157	6.37	42.7	303	0.38
182	5.49	60.7	769	0.56
218	4.59	23.8	753	0.77
230	4.35	4.76	453	0.65
291	3.44	6.47	488	0.69

Table 5.13

$T_{1\rho}$ Measurements on NH_4^+ β-alumina

T/K	10^3K/T	$T_{1\rho}$/ms		A/A+B
		Decay A	Decay B	
77	12.99	3.46	22.7	0.51
77	12.99	1.29	13.6	0.32
90	11.11	3.64	33.4	0.41
105	9.42	2.77	35.8	0.27
160	6.25	0.968	5.14	0.45
185	5.41	0.601	3.58	0.40
195	5.13	0.307	2.24	0.41
201	4.98	0.650	7.43	0.70
213	4.69	0.549	2.37	0.45
249	4.02	1.150	17.4	0.88

Table 5.14

$T_{1\rho}$ Measurements on NH_4^+ β-alumina

T/K	10^3K/T	$T_{1\rho}$/ms	$\log_{10}(T_{1\rho}/ms)$	
77	12.99	9.07	0.958	*
77	12.99	8.40	0.924	*
90	11.11	16.3	1.212	*
105	9.52	24.5	1.389	*
128	7.81	7.20	0.858	
146	6.85	4.58	0.661	
160	6.75	2.62	0.418	*
185	5.41	1.95	0.289	*
195	5.13	1.12	0.150	*
213	4.69	1.28	0.108	*
249	4.02	1.41	0.150	*
251	3.98	1.47	0.167	
270	3.70	0.846	-0.013	
272	3.68	1.59	0.201	
294	3.40	0.722	-0.141	
298	3.36	0.758	-0.120	
305	3.28	0.688	-0.162	
315	3.17	0.710	-0.149	
329	3.04	0.668	-0.175	
330	3.03	0.668	-0.175	
347	2.88	0.752	-0.124	
351	2.85	0.771	-0.113	
381	2.62	0.780	-0.108	
401	2.49	1.143	0.058	
456	2.19	2.185	0.339	
500	2.00	4.02	0.604	
500	2.00	4.08	0.611	

* Non-exponential.

Table 5.15

T_2 Measurements on H_3O^+ β-alumina

T/K	10^3K/T	T_2/μs	$\log_{10}(T_2/\mu s)$	Mode
77	12.99	12	1.079	SE*
114	8.77	12	1.079	SE*
128	7.81	12	1.079	SE*
148	6.76	13	1.114	SE*
161	6.21	14	1.146	SE*
183	5.46	14	1.146	SE*
216	4.63	16	1.204	SE*
217	4.61	15	1.176	SE*
239	4.18	14	1.146	SE*
276	3.62	27	1.431	SE
328	3.05	47.3	1.626	FID
351	2.85	78.3	1.894	FID
375	2.67	115	2.058	FID
407	2.46	144	2.157	FID
436	2.29	357	2.553	CP

FID = Free induction decay
* = Non-exponential.
SE = Solid echo
CP = Carr-Purcell

Table 5.16

T_1 Measurements for H_3O^+ β-alumina

(decay to 1/e of initial signal height)

T/K	10^3K/T	T_1/ms	$\log_{10}(T_1/ms)$
77	12.99	365	2.563
114	8.77	237	2.375
128	7.81	259	2.414
148	6.76	198	2.296
161	6.21	161	2.208
182	5.49	116	2.066
195	5.13	113	2.052
215	4.65	109	2.036
217	4.61	83.0	1.919
235	4.26	66.7	1.824
240	4.17	72.5	1.860
276	3.62	43.9	1.642
298	3.36	34.3	1.536
328	3.05	27.1	1.434
353	2.83	14.7	1.168
376	2.66	9.08	0.958
399	2.57	14.6	1.164

Table 5.17

T_1 Measurements on H_3O^+ β-alumina

T/K	10^3K/T	T_1/ms		A/A+B
		Decay A	Decay B	
77	12.99	58.6	413	0.11
114	8.77	23.2	241	0.11
128	7.81	(8.73)	274	0.06
148	6.76	53.4	272	0.26
161	6.21	(4.97)	178	0.09
182	5.49	14.0	142	0.17
195	5.13	11.6	131	0.13
215	4.65	14.9	141	0.21
217	4.61	2.92	96.1	0.13
235	4.26	6.68	75.0	0.11
240	4.17	14.0	96.6	0.23
276	3.62	1.70	50.9	0.14
298	3.34	5.16	50.4	0.27
328	3.05	14.9	58.2	0.56
353	2.83	11.6		0.88
376	2.66	6.31	35.0	0.76
399	2.51	10.8		0.86

Table 5.18

$T_{1\rho}$ Measurements on H_3O^+ β-alumina
(decay to 1/e of initial signal height)

T/K	10^3K/T	$T_{1\rho}$ /μs	$\log_{10}(T_{1\rho}$ /μs)
79	12.66	5280	3.722
82	12.20	7900	3.897
118	8.47	2660	3.426
119	8.40	4970	3.696
139	7.19	4340	3.637
157	6.37	5480	3.739
183	5.46	5051	3.703
204	4.90	845	2.927
222	4.50	908	2.958
228	4.39	4010	3.603
238	4.20	954	2.980
251	3.98	1660	3.221
256	3.91	1830	3.262
295	3.39	448	2.651
299	3.34	614	2.788
323	3.10	1000	3.001
355	2.82	798	2.902
373	2.68	670	2.826
379	2.64	643	2.808

Table 5.19

$T_{1\rho}$ Measurements on H_3O^+ β-alumina
(fit to two exponentials)

T/K	10^3K/T	$T_{1\rho}$/ms		A/A+B
		Decay A	Decay B	
79	12.66	1030	10500	0.36
82	12.20	1110	14400	0.36
118	8.47	52.4	6380	0.44
119	8.40	42.4	14800	0.49
139	7.19	32.6	5800	0.42
157	6.37	39.9	6050	0.42
183	5.46	33.1	7590	0.43
204	4.90	40.6	3030	0.51
222	4.50	68.3	3110	0.51
228	4.39	146	7180	0.35
238	4.20	47.1	2090	0.42
251	3.98	72.5	3500	0.44
256	3.91	95.6	4410	0.44
295	3.39	71.8	1250	0.48
299	3.34	103	1670	0.47
323	3.10	212	4910	0.56
355	2.82	238	5320	0.60
373	2.68	248	4720	0.63
379	2.64	217	4230	0.61

Appendix 2

Small basis set molecular orbitals for H_2O

This appendix details the molecular orbitals discussed in section 9.2. α is the bond angle. The basis functions are as in Table 8.1. d_{11} is discussed in section 8.6 and defines localised orbitals obtained by Boys' method.

(1) The molecular puff

Function	1s	2s	$2p_x$	$2p_y$	$2p_z$
S_1	1.0006	-0.2574			
S_2	-0.0026	1.0284			
p_x			1.0000		
p_y				1.0000	
p_z					1.0000

(2) SCF calculations

Function	$1a_1$	$2a_1$	$3a_1$	$1b_2$	$1b_1$
$\alpha = 90^\circ$					
S_1	1.0006	-0.2551	0.0440		
S_2	-0.0026	1.0097	-0.1918		
p_z	0.0003	0.1815	0.9744		
d_{z^2}	0.0000	0.0354	0.1122		
$d_{x^2-y^2}$	0.0000	-0.0448	-0.0561		
p_y				0.9714	
d_{yz}				0.2373	
p_x					0.9970
d_{xz}					0.0778

$d_{11} = 0.562$

$\alpha = 95^{\circ}$

1.0006	-0.2355	0.0415		
-0.0026	1.0116	-0.1807		
0.0003	0.1713	0.9776		
0.0000	0.0252	0.0991		
0.0000	-0.0484	-0.0597		
			0.9717	
			0.2363	
				0.9972
				0.0741

$d_{11} = 0.561$

$\alpha = 100^{\circ}$

1.0006	-0.2339	0.0390		
-0.0026	1.0133	-0.1701		
0.0003	0.1614	0.9804		
0.0000	0.0173	0.0866		
0.0000	-0.0521	-0.0829		
			0.9724	
			0.2335	
				0.9975
				0.0704

$d_{11} = 0.560$

$\alpha = 104.5^{\circ}$

1.0006	-0.2342	0.0369		
-0.0026	1.0147	-0.1608		
0.0002	0.1525	0.9826		
0.0000	0.0105	0.0758		
0.0000	-0.0554	-0.0654		
			0.9733	
			0.2293	
				0.9978
				0.0670

$d_{11} = 0.560$

$\alpha = 106.54^{\circ}$

1.0006	-0.2343	0.0359		
-0.0026	1.0152	-0.1566		
0.0002	0.1485	0.9835		
0.0000	0.0075	0.0711		
0.0000	-0.0569	-0.0664		
			0.9739	
			0.2270	
				0.9979
				0.0655

$d_{11} = 0.560$

$\alpha = 109.46^{\circ}$

1.0006	-0.2345	0.0346		
-0.0026	1.0160	-0.1508		
0.0002	0.1428	0.9848		
0.0000	0.0033	0.0646		
0.0000	-0.0591	-0.0676		
			0.9748	
			0.2231	
				0.9980
				0.0633

$d_{11} = 0.560$

$\alpha = 140^{\circ}$

1.0006	-0.2357	0.0208		
-0.0026	1.0209	-0.0908		
0.0002	0.0836	0.9939		
0.0000	-0.0334	0.0143		
0.0000	-0.0796	-0.0641		
			0.9886	
			0.1506	
				0.9993
				0.0386

$d_{11} = 0.560$

$\alpha = 170^{\circ}$

1.0006	-0.2360	0.0056		
-0.0026	1.0224	-0.0243		
0.0000	0.0216	0.9995		
0.0000	-0.0520	-0.0002		
0.0000	-0.0915	-0.0210		
			0.9992	
			0.0405	
				0.9999
				0.0102

$d_{11} = 0.560$

(3) Perturbation method calculations

Function	$1a_1$	$2a_1$	$3a_1$	$1b_2$	$1b_1$
$\alpha = 90^{\circ}$					
S_1	1.00006	-0.2291	0.0618		
S_2	-0.0025	0.9918	-0.2702		
p_z	0.0006	0.2582	0.9541		
$d_z 2$	0.0000	0.0410	0.1402		
$d_{x^2-y^2}$	0.0000	-0.0387	-0.0321		
p_y				0.9759	
d_{yz}				0.2183	
p_x					0.9936
d_{xz}					0.1127

$d_{11} = 0.588$

$\alpha = 95^{\circ}$

1.0006	-0.2300	0.0583.		
-0.0025	0.9957	-0.2551		
0.0006	0.2444	0.9594		
0.0000	0.0328	0.1296		
0.0000	-0.0417	-0.0338		
			0.9765	
			0.2153	
				0.9942
				0.1074

$d_{11} = 0.586$

$\alpha = 100^{\circ}$

1.0006	-0.2308	0.0549		
-0.0025	0.9993	-0.2401		
0.0006	0.2305	0.9644		
0.0000	0.0249	0.1190		
0.0000	-0.0447	-0.0354		
			0.9775	
			0.2109	
				0.9948
				0.1019

$d_{11} = 0.583$

$\alpha = 104.5^{\circ}$

1.0006	-0.2315	0.0518		
-0.0025	1.0023	-0.2265		
0.0005	0.2179	0.9686		
0.0000	0.0181	0.1097		
0.0000	-0.0474	-0.0365		
			0.9786	
			0.2058	
				0.9953
				0.0968

$d_{11} = 0.581$

$\alpha = 106.54^{\circ}$

1.0006	-0.2318	0.0504		
-0.0025	1.0036	-0.2204		
0.0005	0.2121	0.9703		
0.0000	0.0150	0.1055		
0.0000	-0.0486	-0.0369		
			0.9792	
			0.2031	
				0.9955
				0.0944

$d_{11} = 0.580$

$\alpha = 109.46^{\circ}$

1.0006	-0.2322	0.0484		
-0.0025	1.0054	-0.2117		
0.0005	0.2039	0.9728		
0.0000	0.0108	0.0996		
0.0000	-0.0503	-0.0373		
			0.9800	
			0.1988	
				0.9958
				0.0910

$d_{11} = 0.579$

$\alpha = 140^{\circ}$

1.0006	-0.2352	0.0276		
-0.0026	1.0188	-0.1210		
0.0003	0.1166	0.9914		
0.0000	-0.0250	0.0458		
0.0000	-0.0662	-0.0350		
			0.9915	
			0.1302	
				0.9986
				0.0531

$d_{11} = 0.566$

$\alpha = 170^{\circ}$

1.0006	-0.2364	0.0070		
-0.0026	1.0241	-0.0306		
0.0001	0.0293	0.9995		
0.0000	-0.0424	0.0097		
0.0000	-0.0748	-0.0102		
			0.9994	
			0.0344	
				0.9999
				0.0134

$d_{11} = 0.553$